UNIVERSIDAD DE ALCALÁ

ESCUELA POLITÉCNICA SUPERIOR

DEPARTAMENTO DE ELECTRÓNICA

Doctoral Thesis

Subspace-Based Methodologies for the Non-Cooperative Identification of Aircraft by Means of a Synthetic Database of Radar Signatures

Patricia López Rodríguez

2016

UNIVERSIDAD DE ALCALÁ

ESCUELA POLITÉCNICA SUPERIOR

DEPARTAMENTO DE ELECTRÓNICA

Subspace-Based Methodologies for the Non-Cooperative Identification of Aircraft by Means of a Synthetic Database of Radar Signatures

Author

Patricia López Rodríguez

Advisors

Ignacio Bravo Muñoz y Raúl Fernández Recio

2016

Doctoral Thesis

A Escoti y a Olga

Acknowledgements

Aquí me encuentro, varios dias después de dar por finalizada la escritura, un domingo por la tarde enfrente del ordenador una vez más y la verdad es que no sé muy bien cómo empezar. Durante estos días me ha dado tiempo a reflexionar y a pensar en la gran cantidad de personas que no sólo me han ayudado en la elaboración de este trabajo sino que también me han apoyado mucho a lo largo de todo este largo proyecto de cuatro años y pico.

Sin lugar a dudas tengo que mencionar en primer lugar a mi familia, mis padres y mi hermano que siempre han estado en los momentos más difíciles y siempre estarán y a María José que fue la que me abrió el gusanillo de empezar esta aventura y que además ha sido un modelo de perseverancia y esfuerzo.

Por supuesto tengo mucho que agradecer a mis directores de tesis, Raúl y Nacho. A Raúl porque aunque no haya estado tan presente estos dos últimos años, sin él esta tesis no habría sido gestada ni salido adelante y a Nacho por su esfuerzo, su ilusión y sobre todo por su apoyo y buenas vibraciones que me transmite siempre y por animarme y encontrar financiación para realizar la estancia.

Al INTA por concederme esta oportunidad y sobre todo a mis compañeros y amigos, los que estuvieron y los que están, por hacerme sentir una más desde el primer día y por los buenos ratos: Juan Ángel, Edu, Juan, Jesús, Noe, Borja, Óscar, Poyatos, Olga y Escoti.

A mis *Kollegen* del Fraunhofer, Marian, Fabio, Fernando, Tanja y Stefan por acogerme durante 3 meses y por hacerme sentir una más del equipo y sobre todo a mis *payicos* Jorge, Zlatan e Ignacio por hacerme sentir como en casa y por los grandes momentos que hemos pasado juntos, en Alemania, en Croacia y en Murcia.

No me puedo olvidar de los amigos que han estado a mi lado al pie del cañón durante estos años, mis compañeros del máster: Chema, Vero, César y Raúl y mis compis de piso que siempre han estado ahí después de un día duro: Edu, Ana y Chusi. Al Trevi, cómo no, que se ha tenido que tragar mil historias de cómo va la tesis y que me espera en Murcia con los brazos abiertos cada vez que voy. Y las dos personas que más apoyo me han dado, pues son las que más cerca han estado de una manera u otra, a Ana Roncero pues sabe muy bien lo que es hacer un doctorado y porque siempre está ahí cuando la necesito incluso aunque viva a 10 horas de aquí, y a Albert que en estos últimos dos años siempre me ha apoyado y ha sabido darme ánimos y sacarme una sonrisa en los momentos más duros.

Por último, quiero agradecer especialmente a Escoti y a Olga su esfuerzo y dedicación, ya que realmente también forman parte de esta tesis y sin los cuales no hubiera sido posible acabarla: Escoti, mi *tercer director* siempre ayudándome y dándome buenos consejos y Olga, mi segundo cerebro. Sin vuestro esfuerzo y ayuda... a saber cómo habría acabado esto!!

No he podido evitar emocinarme mientras escribía pues la verdad es que las palabras se quedan cortas para expresar lo que siento en este momento, pero al menos lo intentaré mandando un eterno gracias a todos.

Resumen

Una de las principales preocupaciones dentro del mundo de la aviación es la identificación rápida, eficaz y fiable de cualquier objeto observado que se encuentre a cualquier distancia y bajo cualquier condición atmosférica.

Gracias a los avances en tecnología radar, esto se ha conseguido. De hecho, los radares son los sensores más adecuados para el reconocimiento de blancos en vuelo ya que pueden operar en escenarios de baja visibilidad, como malas condiciones atmosféricas, niebla, polvo, etc.

El reconocimiento de blancos mediante radar se puede dividir en dos técnicas principales: las llamadas técnicas cooperativas o no cooperativas. Las primeras, también conocidas por sus siglas en inglés como IFF (Identification friend or foe), requieren de una comunicación activa entre el blanco iluminado y el radar, mientras que las no cooperativas, llamadas NCTI (Non-cooperative target identification), no necesitan de comunicación directa sino que se basan en la comparación del blanco observado con una base de datos de blancos conocidos previamente observados en las mismas condiciones.

Los sistemas IFF se basan en un escenario de Pregunta-Respuesta, esto es, el blanco a identificar recibe una pregunta desde el sistema radar en forma de señal encriptada y éste, si es amigo, será capaz de descifrarla y enviarla de vuelta al sistema radar interrogador, o en su defecto será identificado como hostil. Estos sistemas se encuentran operativos hoy en día, sin embargo esta necesidad de establecer comunicación directa con el blanco presenta un punto débil. De hecho, a lo largo de los años han existido casos donde los sistemas IFF han fallado provocando una serie de accidentes que han hecho aflorar la búsqueda de alternativas o sistemas de refuerzo. De ahí que naciera la curiosidad de explorar sistemas no cooperativos, en los que se puede obtener información del blanco iluminado incluso si éste no esta dispuesto a colaborar.

Para la obtención de esta información acerca de los blancos, los sistemas NCTI hacen uso de radares de alta resolución. Éstos ven los blancos como compuestos por diversos puntos que dispersan la energía emitida por el radar, generando así una imagen de la reflectividad de un blanco, lo que se ha llamado su firma radar. Comparando dicha firma radar con una base de datos de firmas radar de blancos conocidos es posible establecer, mediante una serie de algoritmos de identificación, el tipo de blanco iluminado por el radar.

Sin embargo, uno de los temas más cuestionados es cómo poblar y actualizar esta base de datos de firmas radar. De manera ideal, la base de datos debería de contener medidas de blancos reales en vuelo; sin embargo, para garantizar una cierta confianza en el reconocimiento del blanco, esto implica la recopilación de una gran cantidad de firmas radar de la mayoría de aviones existentes. Desafortunadamente, la principal desventaja de esta estrategia radica en la dificultad de obtener firmas radar de aviones neutrales o enemigos, los cuales, muy probablemente no estén dispuestos a colaborar en campañas de medida.

Por esta razón, esta tesis propone utilizar firmas radar de blancos ideales, generadas mediante simulaciones electromagneticas, como base de datos. Con el avance de las herramientas de predicción

electromagnética se es capaz de obtener de manera rápida y a bajo coste firmas radar de cualquier blanco deseado, en cualquier orientación así como en cualquiera de sus diferentes configuraciones. Así, la base de datos podrá ser tan amplia como sea necesario y la actualización de ésta sólo implicaría el modelado CAD de nuevos blancos y su simulación, en lugar de planificar campañas de medida que son en general costosas, tediosas y largas en el tiempo. Además, ya que no es fácil encontrar libremente conjuntos de datos que dispongan de estas firmas radar, ésta es una buena aproximación para el entrenamiento y evaluación de nuevos algoritmos para la identificación.

De este modo, el principal objetivo de esta tesis yace en el desarrollo de algoritmos eficientes de identificación de aeronaves en vuelo de manera no cooperativa, con altas tasas de acierto y empleando una base de datos de blancos obtenida mediante simulación electromagnética. El escenario propuesto consistirá, pues, en la comparación de firmas radar reales obtenidas en una campaña de medidas con una base de datos compuesta por firmas radar simuladas, con ello se pretende por un lado, simular un escenario más realista, en el que las firmas de los blancos recogidas por el radar no tienen porqué tener la misma calidad que aquellas de la base de datos y por otro, comprobar que la identificación de un avión real mediante simulaciones es posible.

Para ello, se diseñará toda la metodología de identificación, la cual consta del correcto procesado de las firmas radar de alta resolución, la aplicación de las técnicas necesarias para extraer sus principales características, el desarrollo de nuevos algoritmos de identificación y por último la evaluación de éstos teniendo en cuenta las tasas de identificación obtenidas.

Abstract

One of the current concerns in the actual world of aviation is the lack of quick and reliable identification of any observed object unambiguously, at long distances and under any weather conditions.

Thanks to the advances in modern radar technologies, these requirements have been achieved. Indeed, radars are the most suitable sensors for a rapid and reliable recognition of targets as they can operate in scenarios where visibility is very poor, such as bad weather conditions, smoky and dusty environments, etc.

Target recognition using radar sensors can be divided into two techniques: cooperative and non-cooperative. Cooperative techniques, known as identification friend or foe (IFF), require the communication between target and radar, while non-cooperative techniques, so-called non-cooperative target identification (NCTI), do not establish any communication with them but rely on the comparison of the measured targets with a reference database.

IFF systems are Question-Answer schemes, where the unidentified aircraft receives a question from the interrogator system in the form of an encrypted signal and the target will be able to decipher it in case of being a friend, otherwise it will be categorized as foe. These systems are operative nowadays, however, the need of establishing direct communication with the target is a weak point of this technology. Along the years, cases where IFF systems did not work properly have caused tragedies that have highlighted the need for alternatives to these cooperative systems. Non-cooperative identification systems provide, in principle, enough information to identify targets without their cooperation, even if they are not aware of being observed.

These non-cooperative systems take advantage of high resolution radar data. To high resolution radars, a target is composed of several points that reflect the emitted radar signal, therefore, high resolution radars provide an image of the reflectivity of a target, that is, its signature. By comparison of the acquired signature with a database of known potential targets, the identification systems apply a number of algorithms in order to compare the observed target data with this database and to determine its class.

One of the most challenging aspects is the question of the assembly and update of the database of potential targets. Ideally, the database should be populated with measurements of real target signatures, nevertheless in order to guarantee a reliable recognition, it implies the previous collection of a vast number of signatures of the majority of the existing aircraft. Unfortunately, the main drawback of this approach is the unavailability of these radar signatures for neutral and adversary assets.

Thus, this thesis proposes the use of a database of ideal targets generated by electromagnetic simulations. Electromagnetic prediction codes provide a relatively cheap way of generating target signatures of any target in any aspect angle and configuration so the database can be as wide as required, the database population would be fast and low-cost and its update would just imply the modelling of new targets and simulation instead of planning expensive and lengthy cooperative measurement campaigns. Additionally, since finding datasets of actual signatures is not straightforward, this approach is also very useful for the

training and assessment of new algorithms.

This thesis has as a main objective the development of efficient algorithms for aircraft identification in a non-cooperative way, with high success rates and employing a database populated with information from electromagnetic simulations. The proposed scenario consists in the comparison of actual signatures with a database of simulated ones, this way, a more real scenario is emulated where the collected signatures may not have the same high SNR as the ones in the database of potential targets.

To accomplish this, the complete identification methodology will be designed, consisting in the correct processing of the high resolution radar signatures, the application of techniques to extract their main features, the development of new identification algorithms and finally their evaluation according to the identification rates obtained for the observed aircraft with a certain degree of confidence.

Contents

List of Figures

List of Tables

List of Acronyms

1-NN	1-Nearest Neighbour
AGC	Automatic Gain Control
ATC	Air-Traffic Control
ATR	Automatic Target Recognition
AWGN	Additive White Gaussian Noise
CAD	Computer-Aided Design
CMSM	Constrained Mutual Subspace Method
CSM	Conventional Subspace Method
FDTD	Finite Difference Time Domain
FEM	Finite Element Method
FPI	Formación del Personal Investigador
gMSM	generalized Mutual Subspace Method
GTD	Geometrical Theory of Diffraction
HERM	Helicopter Rotor Modulation
HMM	Hidden Markov Models
HRR	High Resolution Radar
HRRP	High Resolution Range Profile
IDFT	Inverse Discrete Fourier Transform
IFF	Identification Friend of Foe
IFFT	Inverse Fast Fourier Transform
INTA	Instituto Nacional de Técnica Aeroespacial
ISAR	Inverse Synthetic Aperture Radar
JEM	Jet Engine Modulation
LDA	Linear Discriminant Analysis
LOS	Line of Sight
MLP	Multi-Layer Perceptron
MoM	Method of Moments
MSM	Mutual Subspace Method
MTRC	Motion Through Resolution Cells
NCTI	Non-Cooperative Target Identification
NCTR	Non-Cooperative Target Recognition
NURBS	Non-Uniform Rational B-Splines
PCA	Principal Component Analysis

PDF	Probability Density Function
PEC	Perfect Electric Conductor
PO	Physical Optics
PRF	pulse repetition frequency
PTD	Physical Theory of Diffraction
RCS	Radar Cross Section
RDI	Range-Doppler Imaging
RRM	Rotational Range Migration
SBR	Shooting and Bouncing Ray
SNR	Signal to Noise Ratio
SSR	Secondary Surveillance Radar
SVD	Singular Value Decomposition
SVM	Support Vector Machines
TRM	Translational Range Migration
UAH	Universidad de Alcalá
UTD	Uniform Theory of Diffraction

Chapter 1

Introduction

One of the current issues in today's military frameworks as well as in the civil world is the lack of quick and reliable identification of any object under observation unambiguously, at long distances and under any weather conditions.

Until recently, radar has been mainly used as a detector and tracker of objects since only limited information could be extracted from the radar signal reflected back from the targets. The poor resolution (several tens of meters) made it difficult to define a proper signature of the target and thus, targets were represented as moving spots onto the radar display. The evolution of radar since World War II along with the development of microwave components and the increase of computer processing speed, has enabled the possibility to obtain high resolution signatures of targets. Considering that nowadays fighter aircraft have a comparable shape and may also fly at comparable supersonic velocities, these radar signatures can make them distinguishable.

One approach for aircraft recognition is the obvious one, to let the aircraft identify itself, that is, a cooperative identification where both agents take part in it. Early in World War I, fratricides motivated the drawing of national insignia on the wings and fuselages of aircraft, and were also part of the reason why some pilots resorted to paint their fighters in loud colors, like the well-known pilot 'Red Baron' and his red fighter. With the advent of higher range weapons and considering battlefields with low visibility the real problem lied in the identification beyond visual range. In 1928, the British speculated on the possible use of sirens or whistles to create a signal that could be heard even if the aircraft could not be seen, but it became unsuccessful since it also informed the enemy force about their approaching.

In those days, radar developers foresaw that radar could be used as a device for identifying aircraft. Their first attempt was to alter the radar returns of friendly aircraft in some way that the ground operator would know about them being one of them. In this regard, in 1937, the British mounted a few test aircraft with an antenna wire along the fuselage. By switching the antenna on and off in a regular pattern, the radar cross-section of the aircraft was effectively changed. Tests on individual aircraft were successful but the system did not work with groups of aircraft since their synchronization was a difficult but essential task. Another attempt, in this case from the U.S. Navy, was to add a set of half-wavelength rods on a pole, where a motor rotated it changing the orientation of the rods and hence their radar returns, unfortunately, this simple system was also unsuccessful [1].

The limitations of these attempts for passive recognition techniques led the researchers to explore new fields in which aircraft could identify themselves cooperatively via transponders, where the ground station could send a question or a *challenge* (a coded signal) and the friend force, the aircraft, could reply with a specific coded signal. The first transponders or *Identification Friend of Foe (IFF)* systems, the Mark I

and Mark II, scanned all radar frequencies that were under use and when a radar pulse was detected, the transponder would transmit its own pulse back at the same frequency. As the radar frequencies were not many, this approach was useful at that time, although it rapidly became obsolete with the introduction of new radar frequencies [1, 2].

The Mark I and II established the basis of all the cooperative IFF systems that followed and that are still used nowadays, which are no more than Question-Answer systems, where the unidentified aircraft receives a *"Who are you?"* question from the interrogator system in the form of an encrypted signal; the target, equipped with a transponder, would decipher the *challenge* and generate an answer containing an identification code, implying it is a friend, otherwise it would be classified as hostile, or foe.

The civil aviation also takes advantage of these systems, they are the base of the *Air-Traffic Control (ATC)*, and since it was introduced as an adjunct to the primary radar, in the civil aviation, the IFF system is also known as the *Secondary Surveillance Radar (SSR)* [3], which not only provides information about the aircraft identity, but also about its altitude and in an enhanced mode it can also provide information such as the ground speed or the track angle [4].

Nevertheless, IFF systems have some drawbacks. The most evident is the need of an active response from the observed target, that is, the need of cooperation. There exist some situations where the transponder of an aircraft would fail to answer a request: the system might be malfunctioning, it might be jammed or damaged by the hostile forces, military codes might be broken or compromised by espionage, the *challenge* or the interrogation might be lost or even the system might be turned off in some warlike or hijacking scenarios. Additionally, since the SSR transponders meet international standards, hostile military forces might also use these transponders to pretend to be civil aircraft, deceiving the allied force.

In fact, non-operating IFF systems have been the source of several mistakes during the last decades. For example, a British aircraft was shot down by a US PAC-2 Patriot Missile in Iraq in 2003; the investigation report concluded that the fighter was mistaken for an enemy aircraft after a failure of the IFF systems. This and similar events have highlighted the need for alternatives to cooperative identification systems [5, 6].

1.1. Motivation

IFF is still nowadays a powerful and very useful tool for target recognition, and although all the aircraft are equipped with these transponders, as noted it is not infallible, should the question-answer loop be interrupted for any reason, the interrogated target will be classified as hostile, leading to a possible case of fratricide. Thus, it is important to also have an autonomous backup system that could identify targets without their cooperation, that is, non-cooperatively and in such short time that an appropriate defensive action could be taken. The *Non-Cooperative Target Identification (NCTI)* or *Non-Cooperative Target Recognition (NCTR)* is, in principle, the only methodology capable of solving the aforementioned problems. It must me noted that usually, the terms "recognition" and "identification" tend to be used along the literature interchangeably when assigning the target type and the same criteria will be used along this text, hence both terms NCTI and NCTR are frequently found with the same meaning.

High Resolution Radar (HRR) data have been shown to provide plenty of information to identify unknown targets and under conditions of poor visibility, such as night, fog, rain, etc [7–11]. HRR measurements can provide an image of target reflectivity, namely a radar signature, that depends upon the target structure. The basic idea of NCTI is to find the features of each aircraft signature that can be used to discriminate it from others. When the measured signature matches a pre-stored template,

and without establishing any communication with it, the target will be identified. The basic mode of operation of these systems is shown in Figure 1.1, where a high resolution radar illuminates an unknown target. When the emitted signal reaches the target it gets reflected and scattered back by the different parts of its structure, and those parts which have higher reflectivity, called *scattering centres* or just *scatterers* will be those that return more energy; at a given orientation of the target, namely the *aspect angle*, each *scatterer* reflects energy at a certain amplitude and phase, thus, the backscattered energy collected by the radar contains information relative to the target geometry, that is, its signature. By comparison of the acquired signature with a database of pre-stored and known potential targets, the identification systems work with a number of algorithms in order to compare the observed target data with this database and to determine the best match.

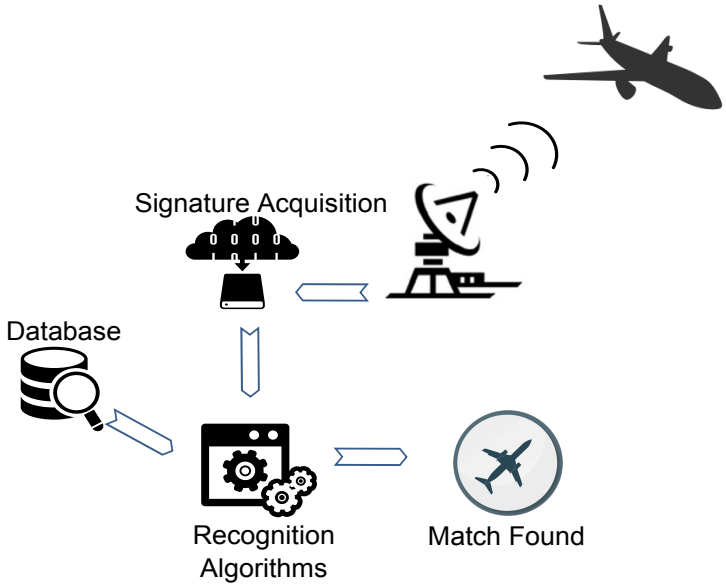

Figure 1.1: Basic concept of NCTI systems

With these non-cooperative techniques, an aircraft may not be aware that its signature is being measured for recognition purposes, thus, in any situation, even if the target wants to pass unnoticed, identification could be achieved if the database is well enough populated.

Different types of signatures can be employed to perform target recognition, such as *Jet Engine Modulation (JEM)*, *Helicopter Rotor Modulation (HERM)*, *High Resolution Range Profiles (HRRPs)*, *Inverse Synthetic Aperture Radar (ISAR)* images or *Range-Doppler Imaging (RDI)*.

JEM signatures are based on the blades of a jet aircraft, which modulate the radar returns, and HERM on the rotating parts, such as propellers or rotors of helicopters, that also cause modulation in the backscattered radar signal; while the former needs a frequency domain analysis, in the latter detection occurs in the time domain. Both cases do not require high range resolution signals but a high frequency resolution waveform with high pulse repetition frequency is required to obtain proper signatures. On the other hand, HRRP, ISAR and RDI are mainly imaging techniques since the signature consists on an actual image of the target, one or two dimensional, such that information of its geometry can be retrieved. When referring to one-dimensional radar image the signature is called a range profile (HRRP), which is just a representation of the different scaterring centres of a target along the radar *Line of Sight (LOS)*. Taking advantage of the motion of the aircraft under certain circumstances, also information in the direction perpendicular to the radar LOS can be extracted to form two-dimensional images, in range (ISAR) or in Doppler (RDI) [12]. These imaging techniques are needed of high resolution in range.

The JEM technique has been proven to be a powerful tool for the non-cooperative identification of aircraft, as the ensemble of papers from the NATO RTO groups [13] present. However, JEM techniques do not provide an all-aspect NCTR capability since, on the one hand, the target must be illuminated near nose-on aspects in order to allow the radar energy to couple to the engine duct, and on the other hand, the *Signal to Noise Ratio (SNR)* must be sufficiently high to be able to determine the different frequency contribution of the blades. This implies that JEM can only be operative at short distances [14]. Hence, early in the 90's [13], radar imaging techniques were proposed as a promising alternative since they do provide an all-aspect capability, do not demand such high SNR and more features of the illuminated aircraft can be inferred. Still these imaging techniques are under research and are thought to be the next step in the development of operative NCTI systems.

One of the most challenging aspects is the question of the assembly and update of the database of potential targets, this question has been in mind since NCTI was first considered [13]. It is important to develop a recognition system in which the database holds the generalization capability, that is, a database with information about the vast majority of existing targets in as many trajectories as possible. The complexity of this database will depend on the type of signature needed by the classification system. The simplest database population would be the one of JEM which only needs to store the blade count number for various compressor stages of the jet engine for nose-on aspect angles. Since the blade count is independent of target aspect, only one or two numbers are needed to be stored. However, in the case of the imaging techniques, it implies the generation of these images in all aspect angles.

There exist a few procedures available to accomplish the database population. They include: measurements of real in-flight target signatures, measurements of scale models in anechoic chambers and electromagnetic modelling of aircraft through prediction codes.

In principle, the measurements of real target signatures would be the best option to perform classification, nevertheless in order to guarantee the right recognition, it implies the previous collection of information in costly and lengthy measurement campaigns, from a great number of flying targets in different aspect angles and configurations, which is theoretically possible for friendly aircraft but mostly improbable for neutral and adversary assets.

The idea of obtaining measurements of scale models from knowledge of the target's dimensions and materials avoids the measurement campaigns of real in-flight targets, but it is highly dependent upon the scale model being a high integrity representation of the target, moreover, to collect proper signatures, wideband millimetre of submillimetre waves are needed in order to scale the actual radar frequencies. Thus, other solutions are sought. Electromagnetic prediction codes provide a relatively cheap way of generating target signatures of any target in any aspect angle and configuration so the database can be as wide as required, the database population would be fast and low-cost and its update would just imply *Computer-Aided Design (CAD)* modelling and simulation instead of planning expensive and lengthy cooperative measurements campaigns. The main drawback lies in the fact that due to the idealism and the approximations of the codes utilized for the simulations[1] and the aircraft models, the signatures obtained by these means are normally very "clean" [12].

The database arrangement is a recurring issue in NCTR, nevertheless, the true problem is not populating it with the most realistic signatures that can be afforded, but to establish the degree of realism that is required to developed a robust NCTR algorithm. A system that relies on a database of extremely accurate images of all the targets of interest will not be particularly robust since any slight, unanticipated variation will not be recognised.

[1]For the simulation of targets of great dimensions such as aircraft, asymptotic methods are usually utilized, like PO,GO and UTD, which introduce a series of approximations. For the rigorous ones, such as FDTD, the problem is so electrically large that a very powerful machine and a high unacceptable amount of time would be needed for their simulation

1.2. Scope

This thesis has been developed at *Instituto Nacional de Técnica Aeroespacial (INTA)* (Spanish National Institute for Aerospace Technology) in the Detectability and Electronic Warfare Laboratory where the author has mainly developed her thesis thanks to a *Formación del Personal Investigador (FPI)* grant.

Although young, since its inception in 1997, the Laboratory has been taking part in different NATO research groups related to NCTI and *Radar Cross Section (RCS)* estimation and its main goals are to acquire, maintain and update knowledge, as well as to procure innovative technologies and services, in the fields of radar and electronic warfare for defense and security applications.

Along the years, the Laboratory has specialized in the analysis, control and exploitation of radar signatures as well as in the development of light equipment for electronic warfare. In its facilities, a laboratory of radiofrequency and microwaves fully equipped is found, with vector network analyzers, signal generators, osciloscopes, power sources, electronic prototyping machines, anechoic chamber, etc. Additionally, specific software tools for electromagnetic simulation based on both rigorous and asymptotic techniques are also available; which are mainly used to give support to the main lines of investigation of the Laboratory and other dependencies of the Institute.

In this framework, as said, one of the main lines of investigation in which the Laboratory is involved consists on NCTR and fruit of it are the numerous articles published and two doctoral thesis (being the present doctoral thesis one of it). After the first doctoral thesis about NCTR presented by a former member of the Laboratory, a number of questions arose from it, therefore, this thesis was conceived with the idea of continuing the work proposed on it: an operative system for aircraft identification based on ISAR images.

Consequently, the first idea of this present research was to continue with the exploitation of the advantages that ISAR images could provide for aircraft identification and try to implement in a hardware platform a classifier prototype. However, after a first study about the computational burden it involved, in the form of a master thesis and in a later article (Appendix A), it was decided that working with range profiles would be a more achievable idea. Thus, the path of this thesis slightly changed its course, although the main subject was still maintained: the reliable non-cooperative identification of actual flying aircraft with a database of simulated signatures.

1.3. Objectives

As well as IFF, NCTR was also first thought to be developed for military purposes, however, as noted, civil systems will also be able to benefit from this technology, for example to avoid accidental shot down aircraft, to find hijacked airliners, for coastal surveillance, etc.

Just as the technology of automatic speech recognition and transcription has required decades of effort and research since its beginning until it could reach the commercial market, the problem of NCTR also needs a wide range of research before an operative and completely trustworthy system can be deployed. Due to the potential applications, the area is extremely interesting and great effort is being made nowadays to develop novel and efficient recognition algorithms [8, 9, 15–20].

This thesis has as a main objective the development of efficient algorithms for aircraft identification in a non-cooperative way, with high success rates and employing a database populated with information from electromagnetic simulations[2]. To do so, the complete identification methodology should be designed, consisting in the correct processing of the high resolution radar signatures, the application of the

[2]This approach is barely seen in the literature but of high interest as will be discussed in the following chapters

appropriate techniques to extract their main features, the development of some identification algorithms and finally the identification of the aircraft with a certain degree of confidence.

1.4. Outline

The organization of this thesis is as follows:

Chapter 1. Introduction. In this very first chapter a quick review about the dilemma of aircraft identification and the evolution of different methods utilized for its accomplishment is given; followed by the scope of the thesis and their objectives. Finally, the structure of the thesis is presented.

Chapter 2. State of the Art. This chapter is dedicated to set the reader in the context of non-cooperative aircraft identification. To do so, different techniques are reviewed and compared first and a decision on which one to use along the rest of the text is drawn, HRRPs. After this decision the rest of the chapter revises the different feature extraction techniques along with different algorithms utilized along the years in the literature to perform NCTR. In the last part of the chapter, the problem of the database assembly is presented.

Chapter 3. Radar Range Profiles for NCTI. It is focused on HRRPs, it presents their principal characteristics, how they are extracted from a high resolution radar measurement, the advantages and disadvantages in their usage and their processing to obtain suitable profiles for NCTR.

Chapter 4. Datasets. This fourth chapter introduces the datasets that are utilized along the thesis to validate the performance of the algorithms that will be proposed and also the specific processing that is applied to these different datasets. The chapter ends with a comparison of the given datasets with graphical examples.

Chapter 5. Algorithms for range profiles classification. The fifth chapter begins with the feature extraction techniques chosen for this research. After that, the definition of the three algorithms based on angle between subspaces is provided, where they are defined incrementally, that is, each algorithm presents an evolution with respect to the previous one. It is seen that each of the algorithms have a tuning parameter, which value should be optimized. In the case of the first two presented algorithms, F_u and F_w, the tuning parameter consists in finding the optimum subspace dimensionality, which is found by an energy threshold η; on the other hand, for the last proposed algorithm, gMSM, the parameter to be found, m, is the eigenvalue that will weight the rest of them to construct a vector of what we have called *softweights*. Finally, a first discussion on the performance of the three algorithms is given.

Chapter 6. Experiments and Results. This long chapter presents the results obtained in the aircraft recognition utilizing the algorithms defined in Chapter 5 with the datasets presented in Chapter 4 and it is divided into three main sections: the first one is the definition of the different test cases that are used to evaluate the algorithms, accordingly, two test cases are defined with their corresponding subcases. The following section, provides a study on the variation of the recognition performance of algorithms F_u and F_w with the signal subspace dimensionality controlled by parameter η; thus, a sweep in η is carried out for the different subcases and some conclusions about the best value and the robustness of the algorithms are drawn. The third section, evaluates the performance of algorithm gMSM by studying the change in the success rates according to the values of the selected *softweights*, which are modulated by parameter m; therefore, equally to the prior section, a sweep of m is done to assess the performance of gMSM and to decide its

optimum value. Finally, the chapter ends with a discussion on the obtained results as well as with a comparison of these proposed algorithms with others given in the literature.

Chapter 7. Conclusions and future research. The last chapter of this thesis summarizes the main contributions made by this thesis and enumerates the potential future research lines.

Appendix A. Computational Burden of an ISAR image identification system. This Appendix presents a study which addresses the computational burden needed in an ISAR-based NCTI system.

Chapter 2

State of the Art

The subject of *Non-Cooperative Target Identification (NCTI)* (or *Non-Cooperative Target Recognition (NCTR)*) using radar has been under research for many years and thus, many relevant research papers and textbooks can be found. As said in the introductory chapter, high resolution radar data are the most appropriate to accomplish this kind of identification. There are different ways of exploitation of these data leading to different techniques for NCTI; all of them have two things in common, firstly, the search of features that can discriminate one aircraft from the rest and secondly, as every pattern recognition or identification problem, the comparison with a database of templates to finally assign a class to the illuminated aircraft.

This chapter provides an insight about the state of the art of the technology applied to airborne target recognition, focusing this review in three main key areas which align to the main objectives of this thesis. These are:

- Different NCTR techniques
- Feature extraction and classification methods
- Datasets for NCTR

2.1. Non-Cooperative Target Identification Techniques

In Chapter 1 it was noted that different target signatures can be used to achieve NCTR. Roughly, these techniques can be divided into imaging techniques and non-imaging techniques.

Non-imaging techniques are based on the modulation of the radar returns by the rotation of aircraft engines or rotors of helicopters, while imaging techniques entail the creation of a one or a two dimensional image of the target through the processing of the radar returns.

In the following subsections, a review of these techniques will be given, extending the information given in the previous chapter. All these approaches have pros and cons and even if their concepts may be relatively simple in theory, it is the many detailed issues that have challenged researchers over a number of years.

2.1.1. Non-imaging techniques

Jet Engine Modulation (JEM) exploits the rotating parts of an aircraft, mainly their engines, to estimate the type of aircraft seen by the radar. This technique provides an estimate of the number of

blades located on the different stages of a jet engine. It is a frequency domain technique and a high frequency resolution waveform with a high *pulse repetition frequency (PRF)* is needed to obtain a high integrity JEM spectrum. Much of the discussion about JEM is gathered by Tait in [3]. The phenomenon occurs when a radar observes a jet airplane at approximately nose-on or tail-on aspect angles; then, the electromagnetic radiation enters the jet engine and is scattered back from the moving parts of its compressor and blade assembly. To acquire the JEM signal the operation is based on the spectral analysis of the returned target signal in order to extract the Doppler information caused by the rotational motion of the jet engine components[21].

This phenomenon was first noticed by Gardner [22], who measured the Doppler spectra of propeller-driven and turbojet aircraft at S-Band. He found numerous spectral lines, caused by the relative motion of the propellers with respect to the radar, as well as a strong modulation sideband due to the engine compressor blades in turbojet aircraft.

Even though the engines are usually enclosed, it was noticed that there is enough energy propagation down the ducts in such manner that the blades of the different stages of the engine can modulate this energy. These modulation sidebands produced by the blades are easily distinguished in the backstattered energy spectra and, depending upon aspect angle and transmitter frequency, can be sufficiently strong to provide the blade count of the first engine stages.

Cuomo and Pellegrini have deeply studied JEM. In [23] they make use of data obtained from experimental measurements on ATC Radar Systems relative to different civilian aircraft in different conditions (aspect angles and trajectories). They found out that in S- C- or X-band radars is possible to extract the JEM spectral analysis for nose-on aspect angles between -60° and 60° and also for tail-on aspects from -120° to 120°. In [24, 25], they validate the actual data with a simulation model, showing a good degree of accordance in the modeled spectra for S-band radar data.

Recently, JEM has been thought of as a micro-Doppler phenomenon and the application of time-frequency analysis is being also examined. Accordingly, Lim *et al.* [26] analyse via the short-time Fourier transform (STFT), the micro-Doppler signatures from four CAD and one experimental aircraft engine models. The obtained spectrograms show that additional information beyond traditional frequency analysis such as the length of the blades or whether their number is odd or even can be retrieved. In [27] a modified Hilbert-Huang transform (HHT) is applied to improve the previous results. The modified HHT allows the calculation of the spool period and the blade period, while the number of blades is estimated using these two parameters.

Even though its simple computation and maturity, JEM does have its limitations. It requires a specific radar waveform, target aspect angle and high SNR. The waveform needed to perform JEM requires high frequency resolution with a high PRF in order to penetrate into the engine and to provide the unambiguous Doppler returns caused by the blades; high SNR is desired, so the modulation can be detected and measured, in cases of low SNR the JEM spectrum is degraded and the spectral lines needed to infer the blade count might be masked; therefore, to apply this technique, the range at which the aircraft is illuminated is limited. Finally, the right aircraft aspect angle is required for the radar energy to be scattered by the engines and not by other parts. Figure 2.1 (extracted from [12]) depicts the ideal JEM spectrum of a jet engine, where the main chopping lines, intermodulation products and spool lines are seen. The ratio of the first stage chopping frequency (N/T) and the engine rotational period frequency (1/T) determines the first stage blade count (N). Similarly, if the second stage chopping frequency (M/T) can be determined, the second stage blade count (M), can be found.

But, undoubtedly, the main drawback of JEM is basically that it identifies types of engines instead of aircraft and unfortunately, different planes can be equipped with the same engines or different engines

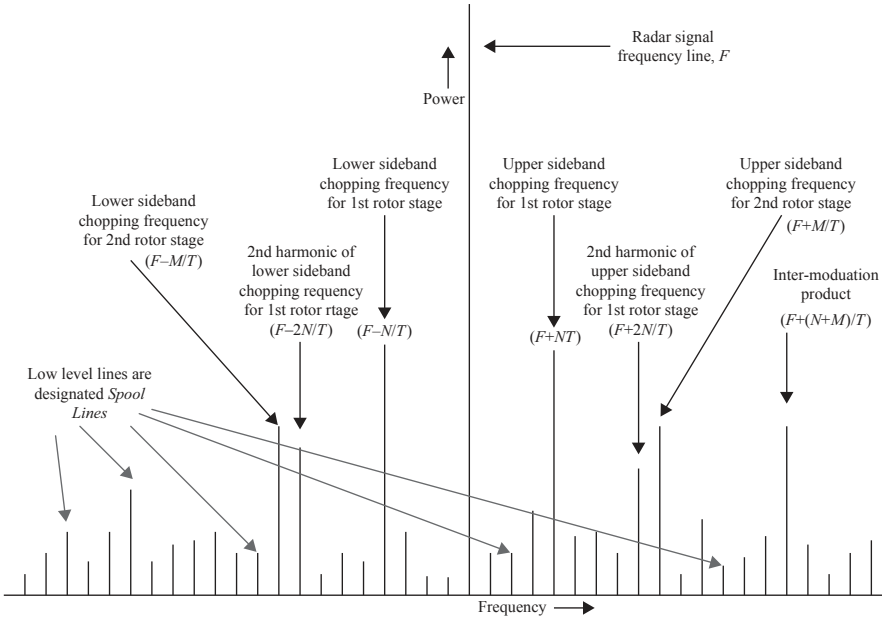

Figure 2.1: Ideal JEM spectrum [12]

can power the same planes; for example the engine F100 from Pratt and Whitney is used in the F-15 and F-16 fighter, and the airliner Airbus A310 is either powered by a CF6-80C2 from General Electric or a PW4000 from Pratt and Whitney [28–30]. At any means, JEM should be able to distinguish between fighters and transport aircraft since they use very different engines.

Another non-imaging technique for aircraft recognition is HERM. Its mode of operation is similar to JEM since it also measures the modulation in the backscattered radar signal, but this time, this modulation is generated by the rotors of helicopters. The collected features tend to be impulses from the blades, known as blade flash, and are normally detected in the time domain, so there is no necessity to provide high range resolution. To achieve identification, HERM uses information about the odd or even number of blades of an helicopter and the period between blade flashes. Therefore, the main drawback of this technique is that it works only for a small class of targets and just like JEM, it is capable of determining the type of engine of an helicopter instead of the true helicopter type [12].

2.1.2. Imaging Techniques

Imaging techniques do demand high resolution in range, unlike the JEM, where only a high resolution spectrum was needed. With a sufficiently wide bandwidth, radar can achieve high resolution in the collected data, providing target signatures with enough information to infer their structure. This time, contrary to JEM, the type of an illuminated aircraft can be inferred, not just its engine.

To high resolution radars, targets appear as composed of individual scattering points, also called scattering centers, backscatter sources or just scatterers, that have a strong radar reflection. High resolution radars have the ability to discern the different scattering centers of a target in both the propagation and the transversal direction of the transmitted energy; being able, therefore, to identify the geometry of a target. Thus, resolution of these radars is defined in two dimensions, on the one hand there is the *slant-range* resolution, which depends on the radar bandwidth and is defined as the ability to resolve

scatterers in the direction of the radar *Line of Sight (LOS)*; and on the other hand, there is the *cross-range* resolution which depends on the wavelength of the emitted signal and the angular sweep made during the illumination time. The cross-range resolution is defined as the ability to resolve scatterers in the normal direction to the plane containing the radar line of sight and the target rotation angle [31].

High resolution radar images can be one dimensional, known as *High Resolution Range Profiles (HRRPs)*, or two dimensional, called *Inverse Synthetic Aperture Radar (ISAR)* images and *Range-Doppler Imaging (RDI)*.

High Resolution Range Profiles

A *HRRP* is the projection onto the dimension of the radar line of sight of the radar energy scattered back by the different parts of an aircraft, that is, HRRPs represent the energy reflected by every *scatterer* in a moving target as a function of distance. Each profile consists of range bins that contain the distribution of the scattering centers of a target providing information about target structure such as its size, location of engines, etc., and it is defined as the squared magnitude of the coherent complex radar returns. An example of the correspondence between the scattering centers of a target and its range profile is shown in Figure 2.2.

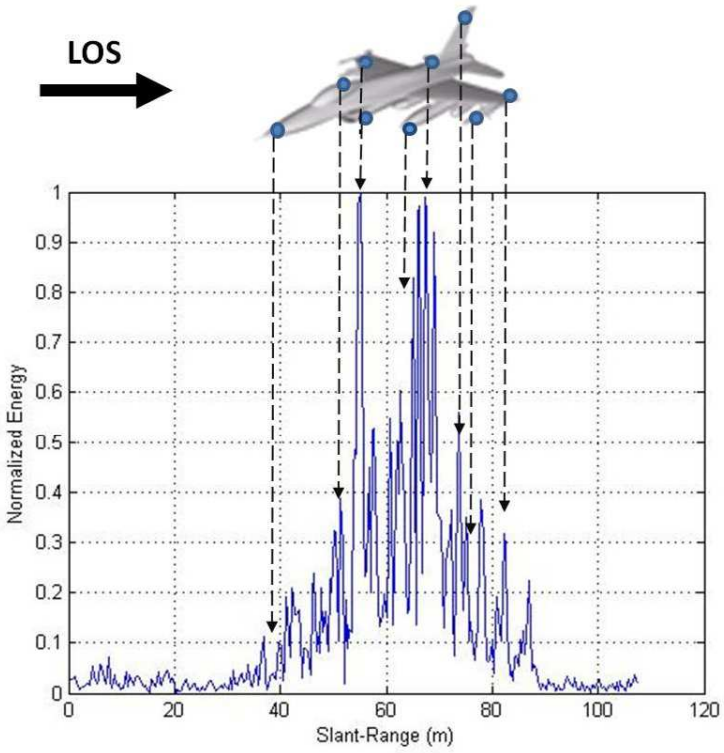

Figure 2.2: Example of the *scattering centers* of a HRRP

Signal processing needed to extract the HRRPs of a target is not very complex and also, since typically, no phase is present, working with them is quite simple; however, since the aircraft will be moving while collecting range profiles, they are very sensitive to the target viewing angle (aspect angle). This causes that range profiles may suffer from occlusion of scatterers or other unwanted effects that may cause that the scattering centers move from one range profile to the next; among these effects it is found the speckle effect, rotational range migration (RRM) or translational range migration (TRM) and thus, some algorithms for their compensation should be applied, hindering the complete HRRP extraction process.

Due to their simplicity and all the information they gather, the use of HRRPs for target identification has been a key research domain in the Defense industry and the radar *Automatic Target Recognition (ATR)*[1] and NCTI community during the last three decades.

Early in the 90's, Li and Yang used range profiles in [15] as the feature vectors for data representation. Five targets were chosen as the known targets and their scaled models were measured so as to retrieve the HRRPs. They could identify the targets with the measured scale models using a decision rule based on matching scores.

Bhatnagar *et al.* [16] in 1998, employed HRRPs for the identification of ground targets. They created a database of HRRP templates to help with the identification of simulated targets. Starting the new millennium, in 2001 Kim *et al.* [17] located the highest peaks in the range profiles using five different methods and the resulting small dimensional feature vectors were classified via a Bayes classifier. Zwart, van der Heiden *et al.* [8] tried to improve the classification performance of a system based on HRRP through the analysis of different methods for profile alignment and the suggestion of a new one, since the profile alignment is critical in the compensation of the translational range migration.

In 2007, in [9] it was stated that the phase of the range profiles may contain valuable target information and thus, the use of complex HRRP for identification is suggested in their study, achieving very good recognition results. In [18], the authors use the self-correlation function of range profiles as features for target recognition. Templates and test data are created using measured data and the results show that the self-correlation function is valid, regarding recognition performance, and robust against noise. Finally, more recently, in 2013, new methodologies as fuzzy logic are applied to recognize air targets with HRRP [19], and still nowadays, the investigation on HRRPs as base for NCTR is an open field.

Inverse Synthetic Aperture Radar

Inverse Synthetic Aperture Radar (ISAR) systems use the relative target-radar motion to obtain information in the cross-range direction and afterwards create an image of the illuminated target. In ISAR, the radar is stationary: it is the motion of a manoeuvring target that allows for the formulation of an image. The cross-range resolution for ISAR is generated by the target's motion, which provides the required large synthetic aperture. ISAR images contain information of consecutive HRRPs with small angular variation; these images display the distribution of scattering centers within a target in the perpendicular direction of the target's rotation plane [31,32]. Thus, for the creation of ISAR images the first step is the extraction of the HRRPs.

Figure 2.3 depicts the fact that ISAR images present the scattering centers of a target in two dimensions. The aircraft displayed in this figure correspond to a Fokker-100 and as depicted, each part of the aircraft is clearly noticeable in the ISAR. Signal processing needed to achieve ISAR images is complex and implies higher computational burden than that needed for the generation of HRRPs. The example shown in Figure 2.3 is a quite clear image, but to retrieve it, a number of motion compensation algorithms are required.

As stated, target motion with respect to the radar makes it possible to achieve ISAR images; nevertheless, not every movement is desired; there exist some actions that may cause blurring in the obtained images. In order to avoid this defocusing, motion compensation techniques must be applied [32, 33]. Generally speaking, target motion can be decomposed into translational and rotational [34,35]. In order to get focused images both the translational and rotational motion must be compensated. Translational motion causes consecutive profiles to be misaligned, so in order to compensate it an alignment of profiles must be completed, this procedure is also called range bin alignment. In addition to profile alignment, a

[1] ATR also includes the recognition of ground targets non-cooperatively. However, the term ATR can be found in the literature to allude either to ground or air targets recognition

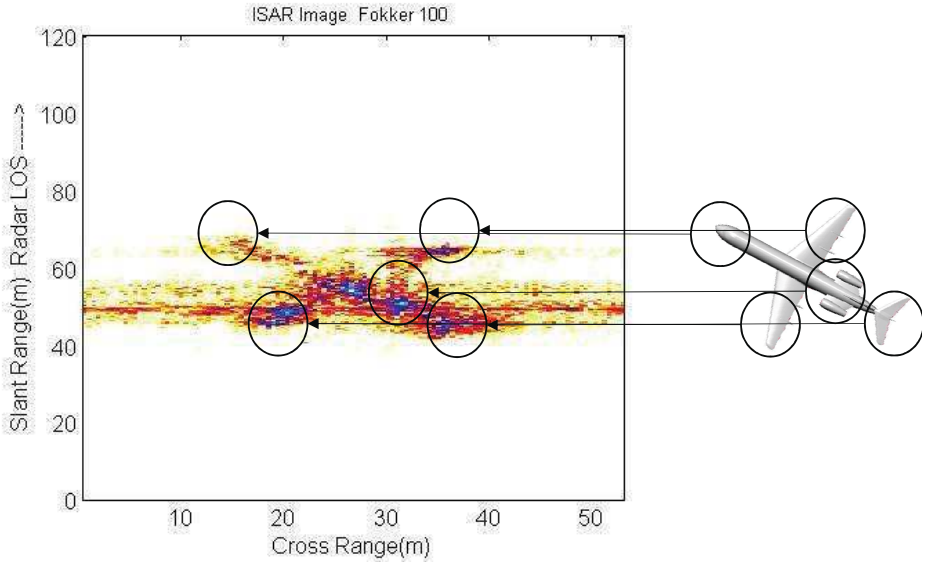

Figure 2.3: Example of an ISAR image

phase adjustment procedure must be applied in order to refer every measurement to the same origin. On the other hand, rotational motion causes *Motion Through Resolution Cells (MTRC)* [36] which produces the scatterers to move from bin to bin in slant- or cross-range. This effect is present when the rotational velocity of the target is sufficiently high to produce the scattering centers to move from one range bin to the next, hence, it can be ignored provided that the target is small or the required resolution is coarse [35].

For palliating these effects many algorithms have been proposed in the literature for motion compensation in ISAR imaging. Range bin alignment methods are rather standard, including centroid tracking [37, 38], envelope correlation [34], contrast/entropy based methods [39], prominent point processing or dominant scatterer algorithm [40], zero phase representation [8], etc. To compensate the MTRC the Polar Formatting Algorithm is frequently used [41], however, this technique can only be applied when both the distance between the target's center of rotation and the radar, and the variation of the aspect angle of the target are known; the main problem is that these data are, in principle, unknown for non cooperative targets.

Since the processing of ISAR is more complex and more computationally intensive, the use of ISAR images for aircraft identification is not as extended in the literature as the use of HRRPs. The literature is more focused on motion compensation techniques and on novel algorithms that will allow for better ISAR image resolution and thus, higher recognition rates [39, 42–47]. Nevertheless, there exist a few authors that focus their efforts in achieving NCTR with ISAR.

Rosenbach and Schiller [48] study the recognition rates obtained with a classifier based on HRRPs and on ISAR as a function of signal bandwidth. They reduce the bandwidth of the measurements from 800 MHz to 100 MHz concluding that with the reduction of the bandwidth and consequently reduction in slant range resolution, the identification with ISAR images is still possible and achieves good recognition rates since it provides the information in cross-range, which is missing in the HRRPs. In [49], the authors extract the scatterers of the targets from their ISAR images and according to their geometric

relationships they generate a set of geometric invariants to recognize aircraft. They add noise and rotation to the target models to variate the detected scatterer positions. The resulting identification rates show that the method is robust against noise but, even though the method has the advantage of a simple recognition database, it lacks of robustness against target rotation. Jurado *et al.*[50] face the NCTI problem by applying a two stage recognition procedure, first they obtain the class of the aircraft using neural networks applied to HRRPs (with the term class they refer to groups of targets with similar features, such as civilian airplane, military aircraft, Unmanned Aerial Vehicle, etc.). After the class in known, they extract the ISAR images and compare them with a database of synthetic images by means of the correlation function. Although the method obtains a good performance it suffer from high computational burden. Martorella *et al.* [51] propose a method based on the use of polarimetric ISAR images. They measure point-like targets models in a turntable in an anechoic chamber and compare them with the 2D point-like polarimetric ISAR images obtained. The results show good performance against noise and target orientation angle estimation errors. However, the experiments are run in an ideal scheme, and it is needed to run experiments with real targets to further prove the benefits of this method. In [52], a neural network classifier is exploited to recognize aircraft extracted from ISAR images. With the combination of two image processing techniques, they improve the shape and extract the features of the images. Then, Invariant Fourier descriptors are computed and used as input features to the neural network system.

Intuitively, a two dimensional image offers much more information about a target than a range profile and therefore, it should lead to a higher recognition performance. However, it has not been concluded whether the effort invested in achieving focused ISAR images is worth it in terms of performance and time consumption. In fact, Appendix A shows a study on the computational complexity of a recognition system based on ISAR images made by the author of this thesis, and which was the starting point of this whole study. On the one hand, it is proven that the creation of a fairly focused ISAR is a very time consuming task, where translational motion compensation is achieved with an envelope correlation algorithm and reaches a computational burden of order $O(N \cdot M^2)$ (with N and M being the number of profiles and the number of frequencies in a stepped-frequency waveform respectively). On the other hand, the identification task, a template matching algorithm based on the normalized cross correlation, have a computational complexity of order $O(C \cdot N^2)$ (with C being a constant). Although the system presented in the Appendix is not the most efficient, it is a good example of how cumbersome ISAR image identification can be.

Range Doppler Imaging

In *Range-Doppler Imaging (RDI)*, a two dimensional range-Doppler image of a target is formed by utilizing a waveform that should be on the one hand, of enough bandwidth to provide high range resolution and on the other hand, of the coherent pulse-Doppler type to obtain high resolution in the frequency domain, such as chirps or impulses. RDI is somehow similar to ISAR; in the latter, the cross-range resolution is generated by the target's motion, which provides the large synthetic aperture required; but in RDI, that effect can be seen as if the different parts of the target were in slightly different aspect angles from the radar and hence, had different values of Doppler frequency. Applying a high resolution Doppler waveform, the different parts of the target at the same range fall into different Doppler cells, which correspond to different cross-range cells, obtaining a 2D image. An example of an RDI of a civil airliner in a tail-on aspect angle can be seen in Figure 2.4 (extracted from [12]). As seen, the JEM lines can be distinguished in an RDI since the needed waveform also meets the requirements for JEM, and with this, the location of the engines in range can be determined.

RDI has not been widely explored, although it has high potential due to the use of both range and frequency data; this property has benefits in being able to localize the aircraft propulsion systems along

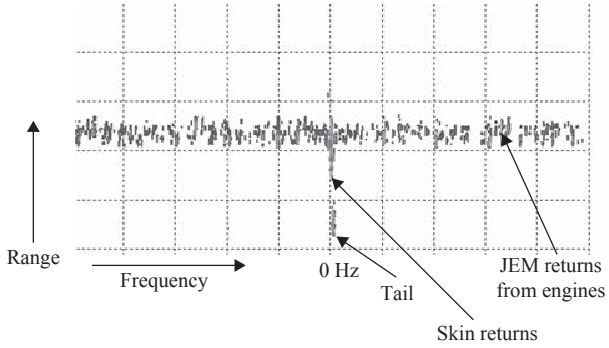

Figure 2.4: Example of a RDI image [12]

the profiles. However, the requirements on the waveform, make this technique difficult to implement and thus, it is not as well known as the other imaging techniques [12].

2.1.3. Comparison of NCTI Techniques

This section has provided an overview of different identification techniques used in the literature for NCTI, including JEM, HRRP and ISAR, and the two less explored, HERM and RDI.

As remarked, JEM is a mature technology, which is applied nowadays in some operational systems. Despite the small and simple database needed and the relatively short time the target needs to be illuminated by the radar to take measurements, JEM strongly depends on the aspect angle, that is, on a proper geometry between radar and target; if the radar signal cannot penetrate the engines, the identification will not be possible. Moreover, high SNR is also needed to detect the spectral lines and finally, JEM identifies engines instead of aircraft, and as mentioned, some aircraft may use the same engines and vice versa. The case of HERM is quite similar, it can only be used to identify helicopters, and as JEM ,it only provides the count of blades and thus, it can only be used to know how the helicopter is being powered.

These difficulties have made researchers to focus their attention on imaging techniques. Although ISAR images return information in two dimensions providing more knowledge about target geometry, the technology is not as mature as others and for the image extraction, the target must have a rotational component perpendicular to the line of sight. Additionally, the motion compensation needed to obtain an ISAR image is complex, not robust and computationally burdensome and also, since real-world 3D targets are mapped onto an image plane to form 2D ISAR images, this image projection plane, which is strongly dependent on the radar-target geometry and kinematics, should also be estimated [53]. RDI on the other hand, seems to have more information since it exploits not only the range information but also the Doppler, however, as seen, due to the high requirements on the radar waveform, this technique is not as utilized and well-known as the rest.

HRRPs have been under study for many years and are thought to be the next operational NCTI technique. Although range profiles only present scatter information on the dimension of the radar line of sight, they have been shown to achieve classification at any aspect angle and with a relatively short target illumination time. The only requisite for collecting range profiles is a radar waveform with large enough bandwidth. The main drawback is their dependency on the aspect angle: changes of few degrees mean changes in the shape of the HRRPs. Despite this, a HRRP can always be collected whereas ISAR or JEM require special conditions for data collection. However, since HRRPs are not inherently suitable for a radar operator interpretation, their automatic classification is desired.

In this thesis identification of range profiles have been opted since they present more advantages than other methods; therefore, the rest of it will be focused on HRRP-based NCTI. However, the use of HRRPs for classification purposes is still a challenging task since they suffer from target-aspect, amplitude-scale and time-shift sensitivity. Consequently, some processing techniques will be needed in order to deal with these issues. In general, HRRPs may not provide the best signature of a target, but their guaranteed accessibility makes them very useful when other techniques are not available. Additionally, when feasible, not only is it much easier to obtain reliable range profiles than focused 2D radar images, but also, the computational time needed to obtain a recognition output is much shorter.

The rest of the thesis will focus the attention on range profiles, their processing and the formulation of novel algorithms for aircraft identification. According to this, next section gives a brief revision of the different feature extraction and classification methods utilized for identifying aircraft non cooperatively with high resolution range profiles.

2.2. Feature extraction and Classification Methods

The classification of non cooperative observed objects from features measured by radar is a sub-field of the global problem of pattern recognition. An excellent guide about pattern recognition is the one authored by Duda *et al.*[54], in which the basic steps of the process of pattern recognition are explained in the introductory chapter with a simple example of classification of two classes of fish. After that example, it is concluded that the design of a pattern recognition system essentially involves the following aspects: 1) data acquisition and preprocessing, 2) data representation or feature extraction, and 3) decision making, that is, classification. According to this, Figure 2.5 redefines the system previously presented in Figure 1.1 seen in the previous chapter where the basis of a NCTI system is described. As depicted, the signature acquisition includes a preprocessing step, in which profiles will be applied a series of techniques to enhance their properties and a feature extraction step, in which discriminating parameters will be selected. These features will be the input to the classifier, which will make use of a number of algorithms to check the similarity of each input with the database of potential targets in order to assign each of them a class.

During the preprocessing stage, the raw data is prepared for a later feature extraction phase before the classification is performed. Preprocessing techniques are mainly used to improve the quality of the range profiles since they are very sensitive to the aircraft motion. The usual preprocessing techniques applied to HRRPs will be reviewed in Chapter 3 which is dedicated specially to range profiles, their extraction and their processing problems. Hence, the rest of this subsection will be dedicated to feature extraction and classification methods that are utilized for identification or range profiles.

2.2.1. Feature extraction

After the application of preprocessing techniques to improve the quality of profiles and in order to preserve relevant information, remove redundancies and capture significant attributes of aircraft in the range profiles, feature extraction techniques (that include dimensionality reduction) are usually needed before the identification process takes place. Feature extraction takes a sample as input and produces feature values as output. The number of extracted features is normally chosen to be fewer than the total necessary to describe the target, this causes a reduction in the initial input information. Reducing the dimensionality of the input samples results in faster classifiers and mitigates the curse of dimensionality[2]. Additionally, some transformed features may provide better discrimination ability, although due to

[2]High dimensional data is difficult to work with and, contrary to what can seem obvious, adding more features could increase the noise and hence the error

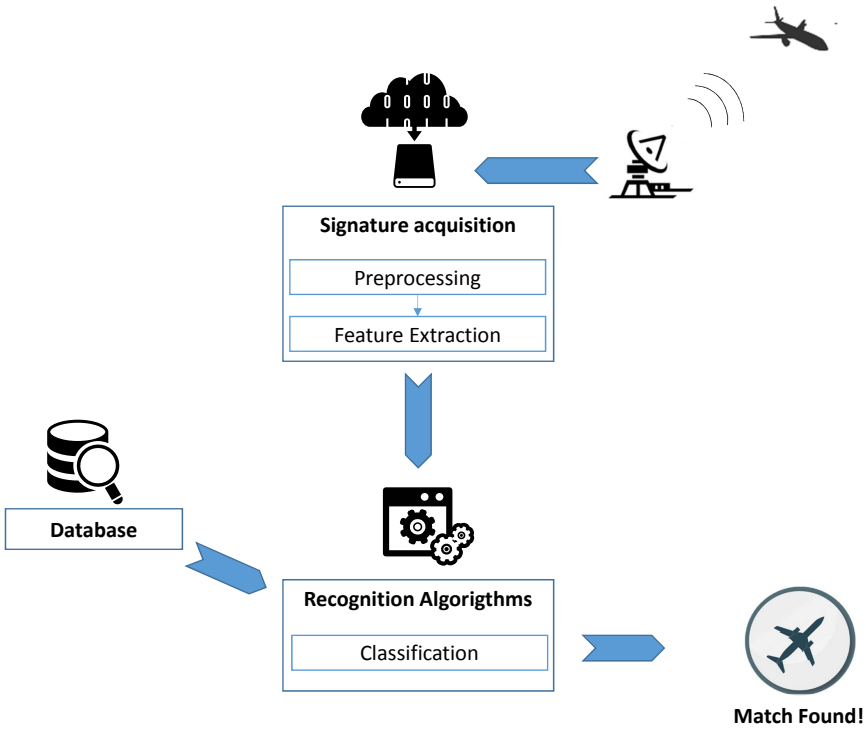

Figure 2.5: Steps of NCTR systems

transformation, they may not have a proper physical meaning. With feature extraction, redundant information that range profiles may have is removed and only a reduced representation of data will be needed to perform classification. Thus, non cooperative target recognition will get less computationally intensive and may have potential for real time processing. However, it must be noted that a great reduction of features may lead to a loss in the recognition system accuracy.

There exist several feature extraction and dimensionality reduction algorithms and in this section, the most frequently utilized techniques in NCTI along with some examples seen in the literature are discussed.

Principal Component Analysis (PCA) is perhaps one of the most widely used linear feature extractor, not only in NCTR but in many other disciplines. PCA computes the eigendecomposition of the covariance matrix of range profiles and keeps the eigenvectors with the highest eigenvalues as features. Examples of the application of PCA in HRRP-based target recognition can be observed in [9], where the authors select the PCA feature subspace that hold the 99% of the energy of the whole feature subspace to project a complex HRRP onto it and try to classify it; or in [55], where PCA is applied to complex range profiles to compress them before application of a minimal euclid distance classification.

A PCA related method, the Kernel PCA (KPCA) which is a type of nonlinear PCA, maps the feature from its original space to a high dimensional feature space via a nonlinear function, and then solves the eigenvalue problem. Chen *et al.* [56] compare the performance of PCA and KPCA, concluding that KPCA outperforms PCA although the selection of the best kernel is not straightforward.

Singular Value Decomposition (SVD) is another tool also used to perform PCA for feature extraction and dimensionality reduction, as in [16], where SVD is used to create templates for HRRP matching, or in [57], where it is used to represent target classes as subspaces.

Linear Discriminant Analysis (LDA) is used to find a low-dimensional representation of the data which preserves the differences between classes, so that a classifier can be designed in the feature domain. It is often referred to as Fisher Discriminant Analysis since the Fisher criterion is maximised. The projections with maximum class separability information are the eigenvectors corresponding to the largest eigenvalues of the product of the inverse of the within-class scatter matrix and the between-class scatter matrix. An example where LDA is used for HRRP feature extraction can be found in [58], where four different variations of the Fisher discriminant analysis are evaluated, or in [59], where it is used to further reduce the dimensionality of the feature vectors.

Other techniques can be also applied to extract features, but are less common in NCTI, like the wavelet transformation, which is found very often in speech recognition. In [60], a Haar wavelet is applied iteratively to HRRPs to obtain features of better quality on each iteration. Huether [61] also developed a wavelet denoising method to increase classification rates of an aircraft classification scenario based on HRRPs.

Other approaches focus on extracting translation-invariant features, thus avoiding the time-shift sensitivity of the range profiles. The most common translation-invariant features used in the literature include the magnitude of the FFT of a range profile [59, 62], utilization of the frequency spectra taken from the raw data obtained by the radar [63], the autocorrelation function of an HRRP [18] or computing the central moment features of range profiles produced by the MUSIC algorithm [64]. In [65], they use the autoregressive model and its autoregressive coefficients as well as the partial correlation coefficients as features for classification since, as the authors state, they are invariant to initial-phase, translation and scale. The power spectrum, which is the Fourier transform of the correlation function of average profiles is used in [66], while in [67] the differential power spectrum is introduced to extract translation-invariant features from range profiles.

More recent papers, even propose the exploitation of the micro-Doppler caused by the rotating turbine blades. Molchanov *et al.* [68] compare 4 different feature extraction methods, the first two, the magnitude of the FFT and the 20 first central moments, are frequently utilized in the literature and are based on the information of target structure contained in the HRRPs, on the contrary, a bicoherence estimation of the micro-Doppler content in radar returns and the cepstrum, which are time-frequency based methods, exploit the phase coupling caused by the rotating parts of the aircraft. They find that the time-frequency methods show robustness with the aspect angle variations but the central moments show more immunity against noise, concluding that micro-Doppler features can be successfully used to identify aircraft.

As seen, many feature extraction methods exist, ones are more used than others, sometimes mainly due to simplicity or for the requirements of the classifier. This subsection has been focused on the most common methods found in HRRP-based NCTR, but others exist that can also be applied to other disciplines. The selection of the best feature extractor will eventually depend on the nature of the input data, the user criteria and the classifier used.

2.2.2. Classifiers

Once the features have been selected, a classifier should be designed to determine a decision boundary such that the extracted features can be assigned to their true class. Different approaches have been identified for designing a classifier and in this section, a revision of the different classifiers used in the frame of HRRP-based NCTI is provided.

The most fundamental approach is through the Bayes decision theory but the application of this approach requires that the problem is fully formulated in probabilistic terms. Given the *Probability*

Density Function (PDF) of a class, it is possible to know the optimal decision boundaries for classification. The requirement of the full probabilistic knowledge of the problem is very restrictive since only in very idealized cases the exact PDF of the classes will be known. In the best case, general knowledge about the PDF may be available, together with a collection of samples from each class, the training samples. The problem is then to find a way to estimate the PDFs using this information since they usually require substantial training data. A number of studies are found in the literature that estimate the PDFs of different HRRP classes for classification. Kim *et al.* [64], after the extraction of the HRRP features, assume that the training data set has a multivariate normal distribution, and the *a priori* probability is the same for each class, the results show that the assumed distribution is appropriate for their extracted features. On the other hand, the research reported in [62] seeks a noise-robust statistical recognition method for complex HRRP. Given the FFT-magnitude features extracted from the HRRPs, they model each target via multitask Factor Analysis and employ the variational Bayesian inference for the recognition stage. Their experiments show that the model has a good recognition performance even with small training data and is robust to noise. The same authors described in [69] another method for HRRP statistical recognition when SNR of test samples is lower than that of the training samples. To achieve that, they model the HRRPs with a Probabilistic Principal Component Analysis (PPCA) while the noise is assumed independent Gaussian distributed. Other models to describe the statistical distribution of an HRRP include Gamma model [70] or the two-distribution compounded model comprising Gamma distribution and Gaussian mixture distribution.

A more intuitive approach is that of the distance classifiers, that are based on the concept of similarity; two patterns that are similar should be assigned the same class, then after defining a metric for calculating the similarity, two samples can be classified simply by template matching or minimum distance. The main problem of this matching technique is the definition of an adequate template that could undoubtedly represent a class. The most common metrics used to perform classification are the Euclidean distance and the cross-correlation of templates. When applying template matching to HRRP-based NCTI, sometimes the raw HRRPs are taken as inputs of the classification system without first extracting the main features. Such approach can be seen in [16], where after obtaining the templates of the HRRPs applying SVD, the correlation between an input HRRP and each template is used for recognition. On the other hand, [18] utilizes the self-correlation to define both the templates and the test samples.

The *1-Nearest Neighbour (1-NN)* decision rule is one of the most used distance classifiers since it provides a quite good classification performance and it is very simple. It can be seen as an extension of the minimum distance classifier, with the difference that now no templates are defined as such; in a set of training samples, whose classes are known, 1-NN assigns the input sample to the class of its nearest neighbour. This method is sub-optimal; the unknown input must be checked with all the training samples, implying that the number of operations increase with the number of samples, moreover, it will lead to an error generally greater than the Bayes error. However, with an unlimited number of samples, the error rate is never worse than twice the Bayes rate [54]. The generalization of the 1-NN is the k-NN decision rule, being k the number of neighbours checked to assign a class. Application of the 1-NN is quite common in the literature, especially when no computation restrictions exist, as an example, Zwart and Heiden [8] validate their HRRP alignment methodology with the study of the recognition performance obtained with the 1-NN classifier.

Subspace methods can be also considered as distance classifiers since ultimately they optimize a distance metric. Each class is defined as a subspace, and the test sample (a feature vector, an HRRP or another subspace) is projected onto the class subspace to find the distance between them. The distance metric is defined for each classification problem. Du *et al.* [9] define each class of aircraft as a subspace and find the minimum reconstruction error between an input profile and these subspaces by comparing

the input HRRP with its reconstruction according to the projection onto them. In the work presented by Pisane *et al.* [57] a subspace method for classifying aircraft based on the projections of a vector z into each one of the class subspaces is evaluated. They carry out three different tests, projection based on the energy, the orthogonal projection of the vector onto the subspace and the reconstruction of the original vector from its projection; the combination of the tests results according to a majority voting procedure shows a recognition rate between 70 and 90 %. More sophisticated subspace methods can be found in the literature mainly for identification of objects in static images or face recognition. Such is the case of the *Mutual Subspace Method (MSM)* or *Constrained Mutual Subspace Method (CMSM)* and their variants [71, 72], that present subspace methods based on principal angles. These latter techniques are barely seen in the literature for radar target recognition based on HRRP, although Maki and Fukui [73] have applied CMSM to ISAR image recognition proving these methods can also be useful for NCTI.

Another approach is the use of neural networks. Neural networks are inspired in the way biological systems work, more specifically, in the way the brain works. These networks are formed by simple processing units (called neurons) interconnected forming layers; the basic model of a neuron was introduced by McCulloch and Pitts in 1943 [74]. Three types of layers define a neural network: the input layer, the hidden layer and the output layer; all neurons in one layer are connected to all neurons in the next layer and transmit their value via the synaptic weight and the activation function. The most common neural networks are called *Multi-Layer Perceptrons (MLPs)*.

An example of a MLP applied to the classification of flying aircraft can be found in [75], where 5 different aircraft are classified using a MLP with 2 hidden layers using backpropagation training. Two architectures are tested, the first one has five outputs according to the 5 aircraft, while the second has two outputs according to the two big classes into which the 5 aircraft can be divided. They also study the optimal number of neurons in the input layer and as a result it is shown that for a better performance the number of input neurons should be equal to the number of range bins of each HRRP; additionally, they find that for their recognition problem, better recognition results are obtained with two outputs, concluding that their net is useful for a big class identification, such as civilian aircraft or unmanned aerial vehicle, but for a more specific classification further methods or a better training is needed. In [67], a feed-forward neural network trained with backpropagation is used as classifier of four aircraft models; the input layer is composed of 256 neurons with linear transfer function, 22 neurons form the hidden layer with log-sigmoid transfer function and the output layer is made up of 2 neurons with log-sigmoid transfer function. In this case, they extract the differential power spectrum and the product spectrum of HRRPs as input features; they use six different algorithms to train the network: four variations of the conjugate gradient algorithms, the resilient propagation and the simulated annealing resilient propagation algorithm. They found that, for their experiment, the latter training algorithm provides the best recognition rates.

An alternative for MLP is the use of Radial Basis Function (RBF) networks. Application of RBF to aircraft recognition can be found in [66], where a template matching method and RBF are compared to evaluate the recognition performance of higher order spectra features. In [76], a study of different evolutionary algorithms for selecting the input features is provided, while in the classification stage they use three methods, kNN, MLP and RBF.

Speech recognition is still dominated by *Hidden Markov Models (HMM)* but with the evolution of the feature extraction techniques HMM have also been applied to NCTI, although not as extensively as other methods. In HMM a finite set of states exist, each of which is associated with a probability distribution. The transitions between states are governed by a set of transition probabilities. The main difficulty is how to adjust the HMM parameters, so that the training set is represented by the model. Since an HRRP usually has more than 100 range bins, it is hard to apply a HMM to process that amount of information

directly, thus feature extraction plays a very important role especially when HMM are involved. The work in [77] is an example where 9 different scenarios using HMM are applied to classify flying targets. The study presented in [78] combines an eigen template match filtering method and hidden Markov modeling for classification of range profiles, improving with this combination the average recognition rate.

The *Support Vector Machines (SVM)* technique offers a possibility to train generalizable, nonlinear classifiers, in high dimensional spaces using a small training set. It maximizes the distance between classes by selecting support vectors determined by solving a constrained quadratic problem. A binary classification is made for the inputs of the SVM, although the extension of the binary classification problem to a multi classification one is possible by applying a one-against-all approach [79]. Recently, the use of SVMs in NCTI problems has increased, [80] and [81] are examples where SVMs return better recognition rates than those obtained with other methods such as RBF or maximum likelihood algorightms, nevertheless the time taken to construct an optimized SVM classifier could be too long for some applications.

Several classifiers used in NCTI have been reviewed, nevertheless, the choice of a classifier is a difficult problem and it is often based on which one is available, best known to the user or on computational requirements.

2.2.3. Discussion

In this section, a summary of different feature extraction methods and classifiers, which are applied in problems of pattern recognition based on high resolution radar data, has been presented.

Feature extraction is mainly employed to reduce dimensionality and discard redundant information. Several methods have been presented here that are frequently used in the frame of NCTI based on range profiles. PCA, SVD and KPCA are very similar since they are based on eigendecomposition; they are very common, well known and easy to use and best suited for gaussian distributed data, the main drawback probably lies in the decision of how much information to keep as "important", that is, the number of eigenvectors taken as a subspace. LDA is also based on eigendecomposition, it computes the linear discriminants that maximize the separation between multiple classes. It is also a well known procedure, but when the number of samples per class is relatively small LDA is not so well suited for the problem. Wavelets, that are time-frequency transformations, have also been applied to radar target recognition although their most common use is in the speech recognition domain. Researchers have found that wavelet methods can improve the probability of correct classification, however a thorough study about the appropriate wavelet family needed for a specific recognition problem is usually requested. Finally, it has been shown that translation invariant features are also powerful even when sometimes, extracting invariant features does not mean a reduction in dimensionality.

Classifiers reviewed in the section can be grouped into five approaches: statistical classifiers, that need an estimation of the probability distribution of the features, which is not always easy; distance classifiers, which are simple classifiers that with a distance measure they assign a class to the test sample; neural networks, with a computationally expensive training phase but with the advantage that this can be done off-line; hidden Markov models, with the additional drawback of adjusting the parameters of the models; and support vector machines, that are essentially binary classifiers that can be extended to multi-class scenarios.

To decide the best classifier an extensive comparison over many different problems should be carried out. With this purpose, the European Commission started the StatLog project [82], where twelve different real world datasets were classified using symbolic learning, statistical and neural networks classifiers. The results showed a large variability, illustrating that there exist no optimal classification rule, or quoting the authors:

> *There is no single best algorithm, and it is a case of "horses for courses". The best algorithm for a particular dataset depends crucially on features of that dataset.*

According to this, the question of which classifier to use should be more oriented to practical questions such as ease of implementation, quality of decision, time consumption in training and decision phases, adaptability to new scenarios or memory consumption and computational complexity.

Keeping this in mind and after the review of feature extraction methods and classifiers given in this chapter, a decision should be made. On the one hand, regarding the classifiers, SVM have a big limitation concerning the choice of a proper kernel, additionally, their high algorithmic complexity demands extensive memory requirements. HMM presents poor transparency in their implementation, where the modelling of the relationship between the hidden states and the observations is not trivial. Neural networks need of loads of samples to train the net and as will be seen, the number of available samples in this thesis is limited; additionally, the definition of the number of hidden layers and neurons needs also of a thorough study and may change from one scenario to another. Statistical classifiers may be a good option but always in the case of knowing the probability distribution of the features utilized. Distance classifiers, on the contrary, provide an easy approach, they can be used for classification of small sets of samples and its simplicity in implementation and adaptation to new scenarios makes them quite suitable for this study. Among the distance classifiers, it has been proven in different papers, that the subspace methods provide good performance in the field of face recognition, although small research on the field of NCI with range profiles is done. If we consider a matrix of range profiles as an image, like in face recognition, subspace methods should also provide good recognition performance. Therefore, in this thesis this latter type of classifiers have been chosen and some new algorithms will be developed in the following chapters.

On the other hand, regarding feature extraction methods, these are usually highly related to the selected type of classifier. Since the chosen classifiers belong to the family of subspace methods, among the reviewed feature extraction techniques, it seems reasonable to use some of the PCA-related feature extraction methods, since they transform the input subspace into another subspace, the feature subspace; this feature subspace provide the ability to reduce the data dimensionality and to work in a transformed subspace domain. Among the PCA-related feature extraction methods, PCA via SVD and via the typical eigendecomposition is selected in this study. Both ways, via eigendecomposition or SVD are equivalent, but maybe, SVD returns more stable results, as will be seen in the following chapters.

The ease of implementation of these techniques is one of the main reasons for their selection, but there are other reasons for selecting PCA over others. The problem of utilizing KPCA, as said, is the selection of the best kernel, which is not straightforward and may change between datasets, this will only add complexity to the identification problem, involving an additional parameter. In the case of LDA, although it might be thought, that LDA would always outperform PCA, since it deals directly with class discrimination, this assumption is not always true [83]. Indeed, when the number of samples per class is small or when the probability distributions of the different classes is not known *a priori*, PCA usually outperforms LDA. Therefore, PCA is chosen in the first place as the feature extraction method for the developed classifiers.

2.3. Datasets and database assembly

One of the main challenges in NCTI after years of research, apart from deciding which are the optimal features and classifiers, is the question of the database construction: what kind of measurements, or features extracted from these measurements, should populate the database to obtain an appropriate recognition performance and a good generalization capability.

It is accepted that a database should contain signatures of every allied target and preferably of a vast number of hostile and neutral platforms. For this reason, it was thought that a NATO-central NCTI database could be a wise alternative [84], nevertheless the type of classifier defines the database needed and vice versa; this implies that if the intention is to make a NATO database of air targets, then a corresponding NATO classifier should be developed as well, making this approach not as suitable as thought in principle.

Up to now three different approaches have been employed to assemble a database [3, 85]: the most obvious method, and the best option, should be to perform measurements of the real targets to be identified at all aspect angles, which is not only expensive but highly improbable for hostile targets. These real measurements can be performed in flight or mounting the targets on rotating turntables; the drawback of turntables is that the near-field measurements obtained can differ from the far-field measurements acquired from the air and also, effects of ground clutter that do not exist in the air will be present in the measurement. When choosing to acquire measurements of actual in-flight targets, this can be done by illuminating targets of opportunity that fly over a specific zone, or by scheduling cooperative measurements campaigns, where the type of aircraft and the flightplan as well as other parameters, like velocity, are known in advance. In both cases, the orientation of the aircraft and its associated aspect angle with respect to the radar should be determined accurately; additionally, both approaches involve several lengthy and expensive campaigns. However, although theoretically possible for friendly targets, it is unlikely that hostile nations will participate in these campaigns to release the radar signature of their most modern aircraft.

To alleviate this, the idea of using scale models and measure their signatures at a scaled frequency in anechoic chambers came up. This depends upon knowing the target physical characteristics in detail and even upon the use of representative materials. Although scale modelling is less expensive than planning cooperative measurement campaigns, it is still costly since it depends on the modelling and on the availability of the facility to measure it.

The third approach is the electromagnetic simulation of the target which also depends on its physical characteristics (it should be designed as a 3D CAD model) and on the integrity of the prediction codes used to extract the target signature. The techniques used to determine the radar scattering characteristics are based on various approaches that can be used to solve Maxwell's equations for incident signals. These methods are rather complex and not always the complete combination of electromagnetic effects that occur in reality can be considered, however this kind of software is commercially available, making the design and prediction of a target signature to be highly accessible. Using synthetic signatures might relieve the need for measuring signatures of hostile and neutral aircraft and might facilitate the database population due to the ease of adding new targets and aspect angles.

Whatever technique chosen for the database construction, it should be noted that it is important to develop a recognition system with a database of targets that holds the generalization capability, that is, a database with information about the vast majority of existing targets in as many trajectories as possible. Moreover, the associated classifier should be designed to be robust enough to compensate the deficiencies of the database.

In order to check the performance of the developed recognition algorithms the best option will be then to use a test set of actual HRRP measurements and compare them with a database of potential targets previously collected via cooperative measurements. This is one common approach found in the literature since the early 90's, when the interest in NCTI proliferated, to nowadays [9,63,86–88]; however, as noted, the availability of actual signatures is not very high due, mainly, to the difficulty of planning measurement campaigns and also to their common military character, which makes the signatures not available for many civilian researchers. Thus, when this approach is found, the signatures are usually collected by

the researchers with experimental radars or, on the contrary, they use signatures of certain measurement campaigns that have been released to certain purposes, hence it is very common to find studies using the same datasets. Given the difficulty with the availability of these actual measurements and with the evolution of software prediction codes, the approach of using simulated or synthetic signatures as both test set and database for validate the classifiers emerged in the late 90's and still nowadays is also applied in the literature [16,55,60,89]. Nevertheless, when utilizing equivalently produced signatures as both the input samples and database, that is, actual measurements vs. actual measurements or simulated profiles vs. simulated profiles, the results may be biased and the evaluated performance of a classifier may be considerably exaggerated compared with a system operating in the actual conditions. In both cases, the test samples and the database samples have similar nature and usually a similar high SNR resulting in very good recognition results. However, in a real hostile situation, *e.g.* at battle time, the range profiles of an unknown target are usually collected in a scene where high SNR cannot be guaranteed due to the measurement collection conditions, like long radar distance, and therefore, the collected actual target signatures (the test samples) will be less clear than those in the database. Additionally, in order to guarantee the right recognition, the unknown target must have been previously measured in a similar aspect angle and configuration (pods, missiles, *etc.*) and loaded to the target database, otherwise the classification would be erroneous.

Keeping this in mind, the interest of using predicted profiles as recognition database while using actual measurements as test samples arose in 1998 at the RTO SCI Symposium on "Non-Cooperative Air Target Identification Using Radar" held in Mannheim, Germany [13], where different studies on NCTI as well as simulation codes were presented.

The use of predicted profiles as database is very interesting: as noted, it is impossible to fill a database only with measured profiles since among other reasons, aircraft from hostile nations will never participate in measurement campaigns. Populating a database with synthetic target signatures has certain advantages: target signatures of any target in any aspect angle and configuration can be obtained with the use of RCS-prediction software so the database can be as wide as required, the database population is fast and low-cost and its update (addition of new targets, configurations or aspect angles) only implies CAD modeling and simulation, instead of planning expensive and lengthy cooperative measurement campaigns. On the other hand, it also has disadvantages: simulations are run in ideal environments, software simulation tools may not take into account all electromagnetic effects and aircraft models may not be exact replicas of real ones. These imply that synthetic signatures will be very clean compared to an actual measurement of the same target, hindering the identification process. Thus, the identification algorithms to be developed must be robust with the difference in shape and SNR between test and training samples.

The approach of comparing actual vs. predicted profiles is barely seen in the open literature [8,50,90] but as noted, it is a very interesting field due to the ease in the database population and the fast evaluation of algorithms. In [8], the authors classify a test set of range profiles coming from an actual measurement campaign with a database of simulated range profiles predicted using a software called *RAPPORT*. However, they were only interested in the performance of different alignment methods for HRRPs and they just chose the Euclidean distance as a metric, trivializing the recognition performance. On the contrary, in [50], the authors present a complete methodology for NCTI on two stages, where the input samples come from an actual measurement campaign of in-flight targets and the database is populated with synthetic profiles computed using the *FASCRO* prediction code. In the first stage, actual HRRPs are used as inputs to a neural network to pre-classify the input sample, where this neural network has been trained with simulated range profiles; later on, with a number of consecutive actual HRRPs they compute the ISAR image of the illuminated target and apply 1-NN to finally classify the target with

a database of simulated ISAR images. This clever approach of utilizing two steps to differentiate aircraft, had two main weak points: on the one hand, the test set was not broad enough to obtain enough ISAR images to keep validating their methodology, and on the other hand, the 1-NN algorithm utilized was very computationally intensive. In fact, in [90], the computational burden and recognition performance of the last step is evaluated with the same test set of actual ISAR images and the same synthetic database.

As seen, not many authors tend to classify actual aircraft signatures by means of synthetic databases. The main drawback found in this approach is that simulations provide a very clean signature while actual HRRPs suffer from noise and other unwanted effects. However, this makes the recognition process similar to a real situation where collected profiles could be noisier than those in the database, which adds interest to keep validating the scheme.

Thus, due to the few studies that support this latter approach, added to the ease in the database population and our lack of availability of a high number of actual HRRPs, the core of this thesis will embrace the strategy of comparing profiles of different nature. As it will be seen in the following chapters, in this thesis, *FASCRO* will be the tool employed for the retrieval of the synthetic profiles that will populate the database, while when using actual profiles as test sets, they will come from a scheduled measurement campaign.

2.4. Conclusions

The intention of this chapter was the literature review of some aspects of NCTI. The different techniques used in non-cooperative target recognition have been seen, such as JEM, ISAR images or HRRP, concluding that recognition of HRRP is the next operational NCTI system.

Under this line of thought, an overview of different feature extraction and classification methods vastly used in the literature for HRRP-based aircraft recognition have been given and finally the last section has reviewed the different approaches utilized along the years for populating a database of potential targets and therefore, for validating the developed algorithms.

As a result, we have reached the conclusion that there is no “optimal” feature extraction method or classifier that will return the best recognition performance for every identification problem. The decision on the features used for classification and the corresponding classifier is made ultimately by the system designer. After the analysis given in section 2.2.3, distance classifiers are chosen to be developed in this thesis due to their simplicity, transparency and fast implementation. Lastly, to validate the recognition methodology, a scheme where actual profiles are compared with synthetic profiles will be proposed. As said, very few researchers focused their attention on comparing profiles of different nature but in practice this approach is the most realistic one, since in reality the measured profile may be quite different than those in the database; furthermore, the poor availability of a high amount of actual HRRPs to populate a database, makes this approach the most suitable.

This way, in the following chapter a more thorough revision of range profiles will be seen, in which their definition, their generation and their extraction will be presented.

Chapter 3

Radar Range Profiles for NCTI

High Resolution Range Profiles (HRRPs) are essentially one-dimensional radar images of illuminated targets, where the contribution of their different reflecting parts, or scatterers, are projected onto the radar line of sight. The range profiles are defined as the squared magnitude of the coherent complex radar returns and normally, no phase information is stored. The minimum resolution cell within a range profile is called a range bin and it can contain the contributions of one or more scatterers combined coherently. This ability to resolve scatterers, namely the resolution of an HRRP, is inversely related to the radar bandwidth.

Before range profiles of an aircraft can be used for identification or any other purposes, they have to be measured with a high resolution radar. Figure 3.1 depicts a basic example of a radar illuminating an aircraft in motion with just 4 scatterers. The emitted wave will hit first the nose of the aircraft, and sequentially its right wing, then the stabilizer on the tail and finally, the left wing. In the same order, the echoes will arrive back to the radar and after some processing the profile will be computed. Under the same measurement conditions (aircraft orientation, weather conditions, radar parameters, etc.), different aircraft will provide different HRRPs.

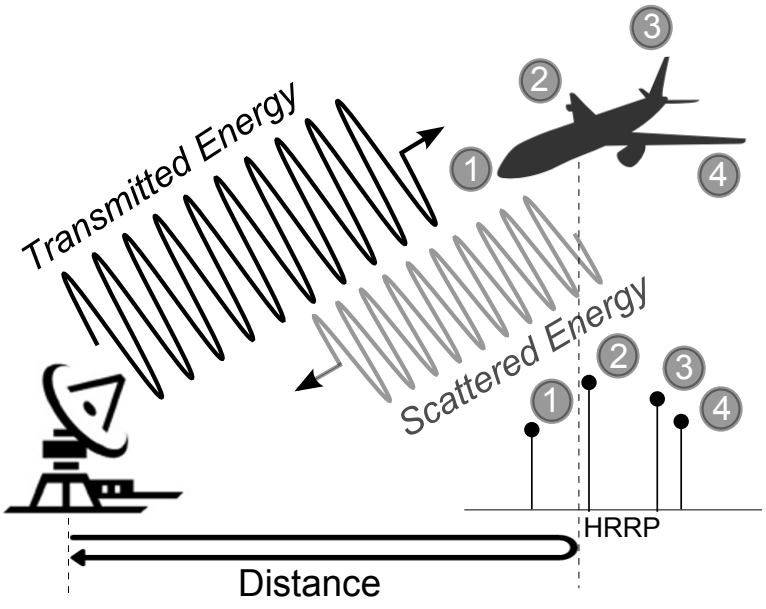

Figure 3.1: Basic radar operation

Throughout this chapter, the definition, generation and processing of HRRPs will be described. The properties and the sources that cause profiles to differ from one another are reviewed and different preprocessing techniques usually applied to palliate these effects are also described.

3.1. High Resolution Radar

The term radar stands for Radio Detection and Ranging. The basic principle of a radar is to calculate the range at which a target is located. Its operation is depicted in Figure 3.1 and it is based on the time needed by the emitted electromagnetic wave to reach the target, be scattered by its different parts and get directed back towards the radar.

With the evolution of conventional radar to high resolution radar, not only the range of the target is calculated but also, as already introduced, other aspects of the target, such as its shape, can be retrieved in form of radar images. The term high resolution is typically used to denote the ability to resolve individual scattering centers on a target, thus it is a generic term which is not linked to any particular absolute resolution. High resolution radar implies the use of wideband signals, with these having a wide bandwidth in absolute terms, the fractional bandwidth (the signal bandwidth divided by the carrier frequency) may be quite narrow.

The best known characteristic of a high resolution radar is its ability to resolve scattering sources within a target in the propagation direction, that is, in the *slant-range* dimension. This is known as the range resolution, Δ_r, which is directly related to the radar bandwidth, β, and is given by equation 3.1, where c represents the speed of light.

$$\Delta r = \frac{c}{2\beta} \tag{3.1}$$

On the other hand, there is the cross-range resolution, Δr_c, which depends on the wavelength of the emitted signal and the angular sweep made during the illumination time. Cross-range resolution is defined as the ability to resolve scatterers in the normal direction to the plane containing the radar line of sight and the target rotation angle. As it depends on the angular sweep during the illumination time, since the measured aircraft will be moving and changing its trajectory, it is not unusual when measuring flying targets from the ground, to find different measurements of the same target under the same radar with different cross-range resolution. Equation 3.2 is used to calculate the cross-range resolution where the angular sweep is given by β_a, λ_c is the radar central wavelength and f_c is its corresponding central frequency. The cross-range resolution is mainly defined for ISAR images and for cross-range profiles and as discussed earlier in previous chapters, these techniques are not the main focus of this thesis.

$$\Delta r_c = \frac{\lambda_c}{2\beta_a} = \frac{c}{2f_c\beta_a} \tag{3.2}$$

According to equation 3.1, a radar will have a better resolution in range as its bandwidth increases, that is, if two scatterers are very close and the radar has a low bandwidth, they will be detected as being only one; however, with the sufficient increment in bandwidth they will be correctly distinguished. This means that as the bandwidth gets wider, the radar will be able to discriminate scatterers with a lower separation.

The basic architecture of a high resolution radar does not differ much from the basic structure of a monostatic primary radar. However, the emitted waveform is appropriately designed to accomplish the high bandwidth and hence, the high resolution.

There exist a number of waveforms than can be used to achieve high resolution, the ideal one would be the utilization of short RF pulses, where the emitted signal consists of very narrow pulses providing a very high resolution. The width of the transmitted pulse defines the resolution of the resulting range profiles, the shorter the pulse, the better the resolution. However, the pulse width is limited by the power the radar is capable of transmitting. Unfortunately, most radars are incapable of transmitting the power required to achieve enough range resolution and a long detection range. Additionally, the transmission chain of the radar (amplifiers, mixers, etc.) may not support this type of waveform.

To achieve a high range resolution without using short pulses it is necessary to spread the radar waveform energy over time whilst still maintaining a high bandwidth. With pulse compression techniques a radar can achieve high resolution even with relatively long pulse widths. This is achieved by inner modulation of the signal and post processing of the received echoes. The following waveforms are examples where pulse compression is employed:

- Phase coded waveforms: the required bandwidth is obtained by periodically changing the phase of the waveform as a discrete step. The rate at which the phase changes is related to the bandwidth. In phase coded waveforms, the transmitted radar pulse can be seen as divided into a number of sub-pulses.
- Chirp or LFM: it is very common and consists of a linear FM coding of transmitted pulses. The chirp signal starts at a defined frequency f_1 and varies it at a constant rate until reaching the final frequency f_2. A variation is the stretch technique, in which the radar transmit an LFM signal and in the receiver, a reference chirp with a higher end frequency, f_3, is mixed with the received signal to obtain the high resolution signature of the target.
- Stepped frequency: narrow pulses are synthesized by transmitting wider pulses in different frequencies. The technique is implemented by stepping the transmission frequency in increments of Δf, from f_0 to f_{n-1} where each frequency is sequentially transmitted. If n frequency steps are utilized, n sets of amplitude and phase measurements are made, which are then used to generate the profiles.

When designing a high resolution radar, an evaluation of the requirements of the radar system should be carried out in order to select the waveform, the bandwidth and the rest of the characteristics that best satisfy the specifications. As it will be described in the following chapters, the available data for this thesis come from real measurements of actual aircraft in motion using a stepped frequency radar. Hence, in the following section an overview of the stepped frequency waveform and the retrieval of range profiles is provided. For further information about the rest of the waveforms presented here, the reader is referred to [31].

3.2. HRRP generation using a stepped frequency waveform

Instead of collecting the target scattering information in the time domain, a stepped frequency waveform collects the information in the frequency domain by emitting a number of pulses with linearly increasing frequency. The required wide bandwidth is synthesised from pulses that individually have a narrow bandwidth, but together span a large frequency range. Figure 3.2 illustrates the frequency increments in a stepped frequency waveform where the pulses can be either separated in time or sequentially emitted.

The target is illuminated by a burst of n pulses, each pulse with a duration of τ and with a frequency which is Δf higher with respect to the previous emitted pulse. If the initial frequency is known as f_0, the frequency for each transmitted pulse will be given by equation 3.3.

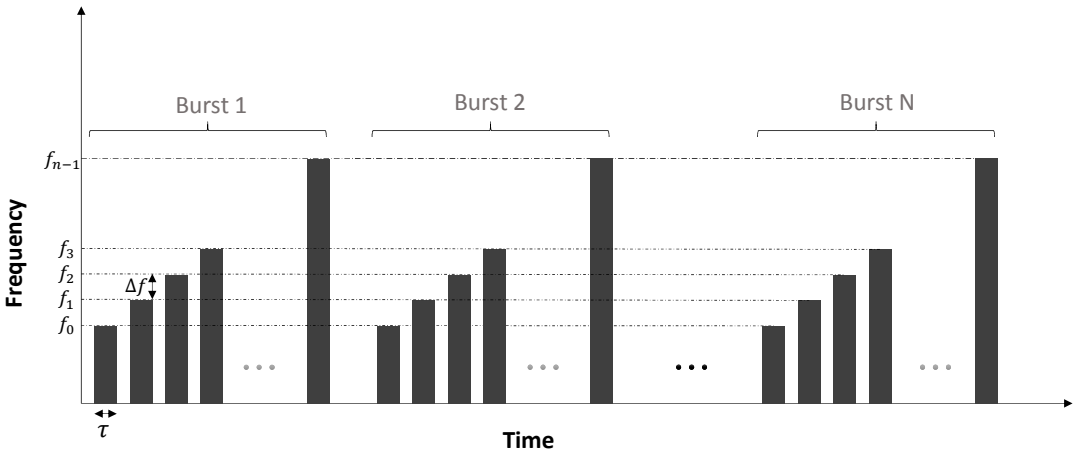

Figure 3.2: Stepped frequency waveform: frequency against time representation

$$f_i = f_0 + i\Delta f \ ; \text{with } i = 0, 1, \ldots, n-1 \tag{3.3}$$

The waveform emitted by each pulse is expressed according to equation 3.4.

$$s_i(t) = A_i \cos[2\pi(f_0 + i\Delta f)t + \theta_i] \ ; \text{with } i = 0, 1, \ldots, n-1 \tag{3.4}$$

where θ_i is the relative phase and A_i is the amplitude of the $i-th$ pulse at a f_i frequency. Accordingly, the signal scattered back from the target will be also composed of n pulses at different frequencies containing the signature of the target in terms of amplitude and phase, as illustrates Figure 3.3; this implies that in the receiver, the in-phase (I) and quadrature (Q) components of a target signature are stored for each pulse in each burst.

Frequency step sequence	Amplitude and phase
f_0	(A_0, φ_0)
f_1	(A_1, φ_1)
f_2	(A_2, φ_2)
f_3	(A_3, φ_3)
⋮	⋮
f_{n-1}	(A_{n-1}, φ_{n-1})

Figure 3.3: Stepped frequency measurements: amplitude and phase

The synthesized effective bandwidth, β_f, of the transmitted signal will be determined by the frequency step, Δf, and the number of pulses, n, of each burst, following equation 3.5.

$$\beta_f = f_{n-1} - f_0 = n \cdot \Delta f \tag{3.5}$$

The received signal belongs to the frequency domain; the corresponding radar return in the time

domain is then reconstructed by performing an *Inverse Discrete Fourier Transform (IDFT)*[1] on the n returns (equation 3.6).

$$x(t_k) = \sum_{i=0}^{n-1} X(f_i) \cdot e^{2\pi f_i t_k} \tag{3.6}$$

where $X(f_i)$ is the received signal in the frequency domain, t_k is the illumination time, f_i is the frequency of each pulse and n the total number of pulses in each burst. Once the radar returns are expressed in the time domain, the n elements that form the resulting range profile, so called range bins, are given by:

$$y = (y_0, \ldots, y_{n-1}) = |x|^2 \tag{3.7}$$

According to equation 3.7, a range profile is finally defined as the squared amplitude of the coherent complex radar returns, while the phase information is usually discarded.

From equation 3.1 and 3.5 two fundamental parameters of HRRP can be derived, which are the amount of detail that can be seen in the range profile and the largest object that fits in a profile. Firstly, the distance between two range bins, which is equivalent to the minimum distance at which two point scatterers can be resolved, that is, the range resolution, Δr of a range profile is:

$$\Delta r = \frac{c}{2\beta_f} = \frac{c}{2n\Delta f} \tag{3.8}$$

And secondly, the unambiguous range interval R_u, expressed in equation 3.9, which determines the maximum length of a target that a range profile can measure without aliasing. Targets exceeding this unambiguous range will produce range profiles that are folded over within this range window. Figure 3.4 shows an intuitive example of this aliasing effect, in which an aircraft with a length longer than the unambiguous range is shown, in that case, the scatterers related to the nose of the aircraft will overlap with the ones of the tail. The unambiguous range interval must be chosen, then, such that the size of the largest expected target does not exceed this window.

$$R_u = \frac{c}{2\Delta f} \tag{3.9}$$

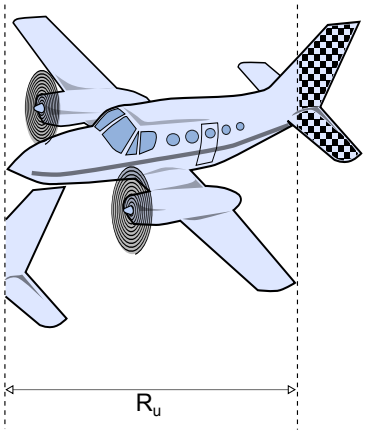

Figure 3.4: Aliasing effect when a target exceeds *Ru*

[1] To efficiently calculate the IDFT, the algorithm of *Inverse Fast Fourier Transform (IFFT)* is applied

3.3. Range profile variability

As noted, the signal processing needed to obtain the HRRP of a target is not very complex, it mainly implies a transformation of the raw data into the time domain. However, as simple as it may seem, there exist a number of obstacles in the extraction of the range profiles related to their sensitivity to the changes in aspect angle.

The energy reflected back from the scatterers comes from different physical parts of it, which are separated by a few wavelengths. As a result, there exist several constructive and destructive interference effects caused by the scatterers located in the same range bin. Each of the scatterers has its own amplitude and phase and these combine as vectors to provide the total amplitude and phase return in the associated range bin.

The aircraft orientation, or aspect angle, can be expressed as a coordinate pair (α, θ), with α being the aspect azimuth and θ the aspect elevation. Although three angles would be required to completely specify aircraft orientation, rotations of the aircraft in the plane perpendicular to the line of sight do not influence HRRP measurements [91]. Therefore, a description of aircraft pose in terms of aspect angles is sufficient. Figure 3.5 gives a graphical explanation; as seen, the aspect elevation, θ, is defined as the angle between the radar line of sight and the plane through the wing-tips and nose of the aircraft, being this $\theta = 90°$. The aspect azimuth, α, is defined as the angle between the direction of the nose of the aircraft and the direction of the radar line of sight projected on the plane through nose and wing-tips. Along this thesis, the aspect elevation will be positive if the target is viewed from above and the azimuth aspect angle will be defined as 0° when the aircraft is viewed from nose-on and 180° if it is viewed from tail-on.

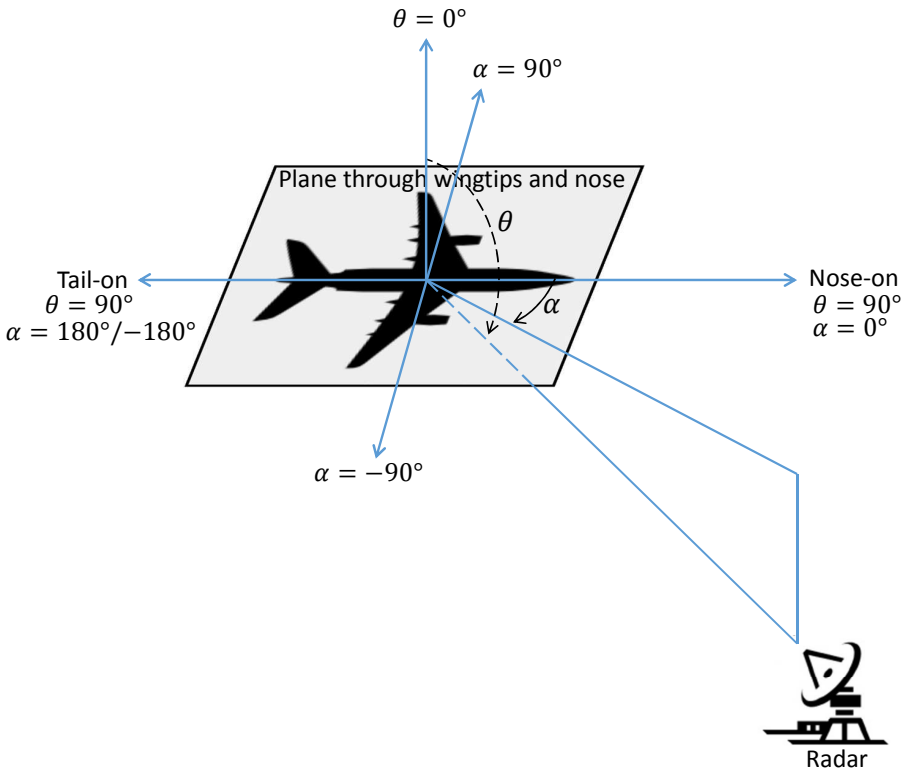

Figure 3.5: Definition of aspect angles (θ, α)

Since the aircraft will be moving while collecting range profiles, the aspect angle and the distance between radar and aircraft will change. This movement can cause interference between scatterers in the same range bin and this leads to the appearance of three main sources of variation: *Translational Range Migration (TRM)*, known as the source of time-shift sensitivity, speckle and *Rotational Range Migration (RRM)*, these latter two effects related to target-aspect sensitivity. Finally, measurement noise and occlusion can also cause variability in the measured range profiles.

3.3.1. Time-shift sensitivity

TRM is due to the translational motion of an aircraft which changes the distance between radar and target and causes scatterers to move from one range bin to the next. In this case, the relative distance between two scatterers does not change since they are all moved the same amount. This is known as the time-shift sensitivity, which causes a cyclically shift in consecutive profiles, implying that the position of the target signal within the unambiguous range window will vary with each measurement.

3.3.2. Target-aspect sensitivity

RRM is caused if HRRPs are collected during a wide rotation of the aircraft (of an order of a few degrees), making the scatterers move from one range bin to the other.

If two profiles have aspect azimuth with a difference less than:

$$\Delta\alpha_{RRM} = \frac{\Delta r}{T_D}[\text{rad}] \tag{3.10}$$

where T_D is the maximum distance between two scatterers within one resolution cell, then the profiles do not differ due to RRM in azimuth. This effect also occurs if the aspect elevation changes over a large angle. In that case, it is said that two profiles do not differ in elevation due to RRM if the variation is less than:

$$\Delta\Theta_{RRM} = \min\left(\arccos\left(1-\frac{\Delta r}{T_D}\right), \arcsin\left(\frac{\Delta r}{T_H}\right)\right)[\text{rad}] \tag{3.11}$$

where T_D is, again, the maximum distance between two scatterers within one resolution cell , T_H is the height of the aircraft and Δr the resolution. As a rule of thumb, over large rotations, the relative peak positions in the profiles will change due to RRM.

On the other hand, speckle causes range profile variability for much smaller changes in aspect angle than RRM. It occurs when the same range bin contains information about more than one scatterer. Then, a slight motion of the aircraft can cause the scatterer contribution to turn from constructive to destructive interference or vice versa causing the peak amplitudes to change rapidly between sequentially collected profiles. The intrinsic aircraft movements, yaw, pitch and roll, depicted in Figure 3.6, are the cause of this effect.

To avoid speckle, the change in aspect angle between two profiles must be smaller than:

$$\begin{aligned}\Delta\alpha_{speckle} &= \tfrac{\lambda}{4T_D} \quad [\text{rad}]\\ \Delta\Theta_{speckle} &= \tfrac{\lambda}{4T_H} \quad [\text{rad}]\end{aligned} \tag{3.12}$$

For non-zero elevations, T_H should be replaced by $T_H \cos\Theta$.

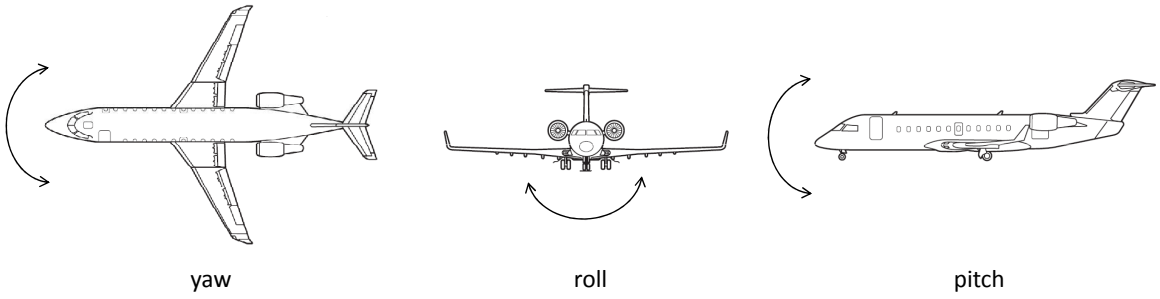

Figure 3.6: Intrinsic aircraft motions

Fluctuations of range profile amplitude due to speckle are multiplicative in nature and are usually modeled as *Swerling cases* [92].

3.3.3. Amplitude-scale sensitivity and occlusion

Amplitude-scale sensitivity appears due to the radar transmitting power, target distance, radar antenna gain, receiver gain and so on, that cause measured profiles to have different amplitude scales. Modern radars usually have *Automatic Gain Control (AGC)* systems that ensure the radar signal does not saturate the receiver. However, unless the radar data are fully calibrated, the independence of the amplitude of the range profiles with respect to the radar signal levels cannot be guaranteed.

Additionally, the measurement noise is mainly caused by thermal noise in the receiver as well as clutter (unwanted returns), although when illuminating flying targets clutter is not as accused as when measuring ground targets. The SNR and the amplitude of a HRRP, are determined mainly by the distance between radar and target since the power of the received signal is inversely proportional to the fourth power of the distance.

Occlusion of a scatterer may occur when the target is positioned in a way such that the radar does not illuminate it and thus, the scatter will not contribute to the backscattered signal, and finally, to the range profile.

An example of the differences found in range profiles with the change in aspect angle is seen in Figure 3.7. The figure shows two range profiles extracted from an actual measurement of a Fokker100; their elevation difference is almost negligible and their azimuth aspect angle differ in less than 1°. In this case, the amplitude of both profiles has been normalized for a better visualization and to deal with the amplitude-scale sensitivity, the normalization is such that their total energy equals 1; additionally, both profiles have also been aligned one respect to the other to alleviate the time-shift sensitivity. Although two main sources of variation have been reduced, still speckle, RRM, noise and occlusion may affect the profiles; this can be clearly observed in the example. For instance, at an azimuth of 54.17° a peak with a normalized amplitude of around 0.25 can be found around range bin 150. With the change in aspect azimuth, this peak has almost disappeared, as can be seen in the black profile, a fact that may be caused either by RRM or occlusion. Another evidence is the amplitude fluctuation of the scatterers located around range bins 150 and 175, they both have changed their amplitude substantially from one range profile to the other, this effect is mainly caused by speckle since it just alter the amplitude of the scatter, but not its position.

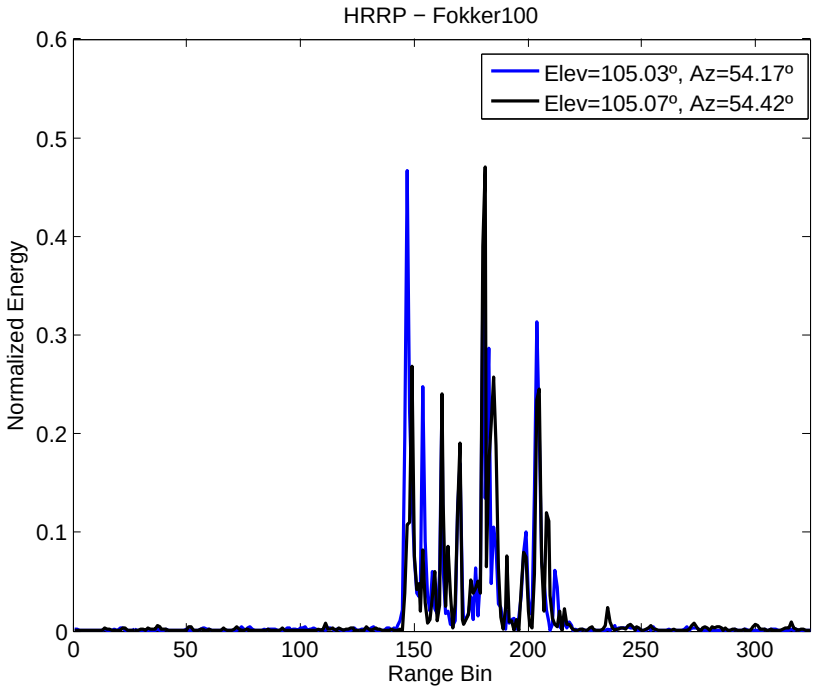

Figure 3.7: HRRP variability with aspect angle

3.4. Preprocessing of range profiles

Preprocessing techniques are mainly used to improve the quality of a range profile; on the one hand, they will be used to deal with the target-aspect, amplitude-scale and time-shift sensitivity, and on the other hand, they will be applied to lighten other effects that are intrinsic to the profiles' extraction process.

3.4.1. Windowing

Sometimes the inherent nature of the radar signal produces high sidelobes in the collected profiles that can easily obscure small returns of some scattering centers. That is the case of step frequency radars which, since they apply Fourier transformations to the raw data to obtain HRRPs, automatically apply a square window to the data, which produces high sidelobes in the range profiles. In those cases, a filter to smooth this effect, at the cost of a worsened resolution, may be implemented before the application of any Fourier transform. Many windows are available to filter the signals, but the most commonly used for HRRP preprocessing are the family of cosine windows [91,93]. Among this family, the Hamming window, defined in equation 3.13 is one of the most utilized since it can reduce the sidelobes in 43 dB, though increasing the resolution by a factor of 1.3 [94]. Figure 3.8 plots both the rectangular and the Hamming window, in time and frequency domain. As noted, the application of a Hamming window implies a poorer resolution, this fact is appreciated in the figure, since in the frequency domain, the main lobe of the Hamming window is wider than the rectangular window main lobe. On the contrary, the sidelobes of the rectangular window are located at -13dB while the sidelobes of the Hamming window drop to -43dB. The effect of applying a Hamming window to the range profiles is seen in Figure 3.9, where it is applied to a HRRP of a Fokker100. As seen, the resolution of the windowed profile may be poorer than the one without it but the range profile is now less abrupt.

$$w(n) = 0.54 - 0.46\cos\left(\frac{2\pi}{N}n\right), \; 0 \leq n \leq N-1 \tag{3.13}$$

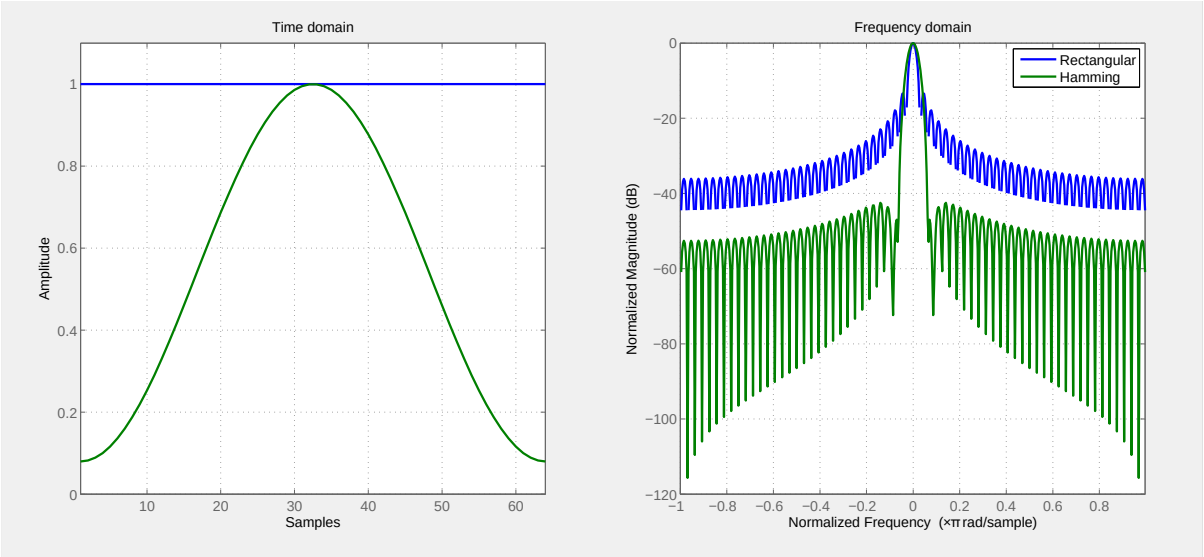

Figure 3.8: Rectangular window Vs. Hamming window

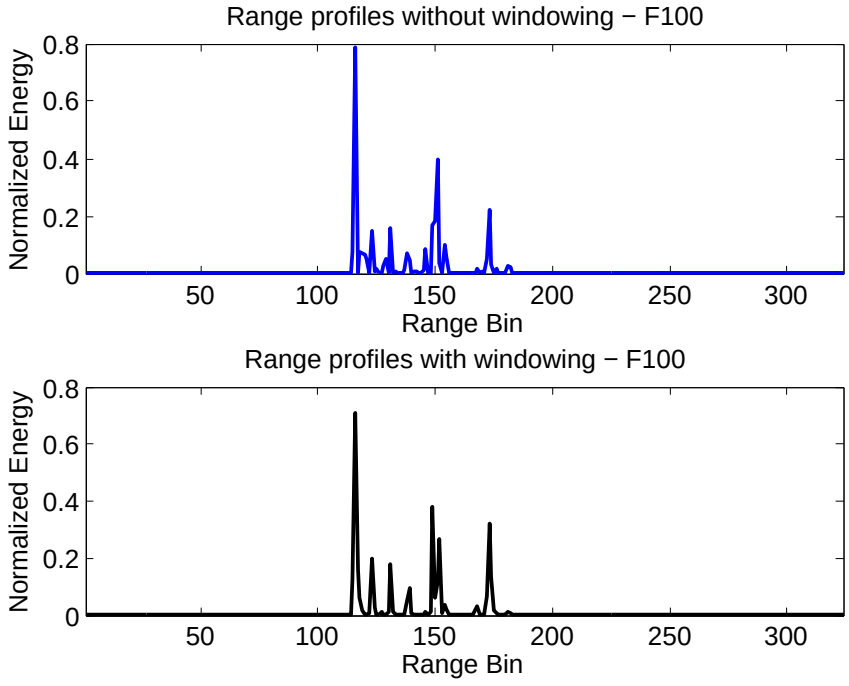

Figure 3.9: Range profiles with and without Hamming window

3.4.2. Zero-padding

After the application of a window, the dimensionality of the profiles can be increased by adding zeros to the returned signal. Sometimes dimensionality expansion may be needed to adapt the measurement

dimensions to those of the database. The application of this technique to the raw data, called zero-padding [91, 93], has the effect of interpolating the range profile by artificially increasing its number of samples (range bins). Zero-padding is a frequency interpolation technique where the resolution of an HRRP is not incremented, but allows for an easier detection of peaks. Nevertheless, it must be noted that the energy of the resulting range profile will be spread out over a higher number of samples, hence, a reduction in the HRRP magnitude is expected; moreover, the designers must be aware that an excessive zero-padding may cause peak-splitting, that is, the division of an actual amplitude peak in two or more fictitious peaks, hence, this technique should not be used arbitrarily. Figure 3.10 is an example of the effect of applying zero-padding to a range profile of a Fokker100. In the upper figure the range profile with no zero-padding is shown and in the lower figure the same range profile zero-padded to have a total number of range bins of 512 is depicted. As said, the resolution has not been incremented but the amplitude of the range profile has diminished. In this example, around range bin 240 of the zero-padded range profile seems to occur the effect of peak-splitting as Figure 3.11 shows, which is a zoomed image of the former one.

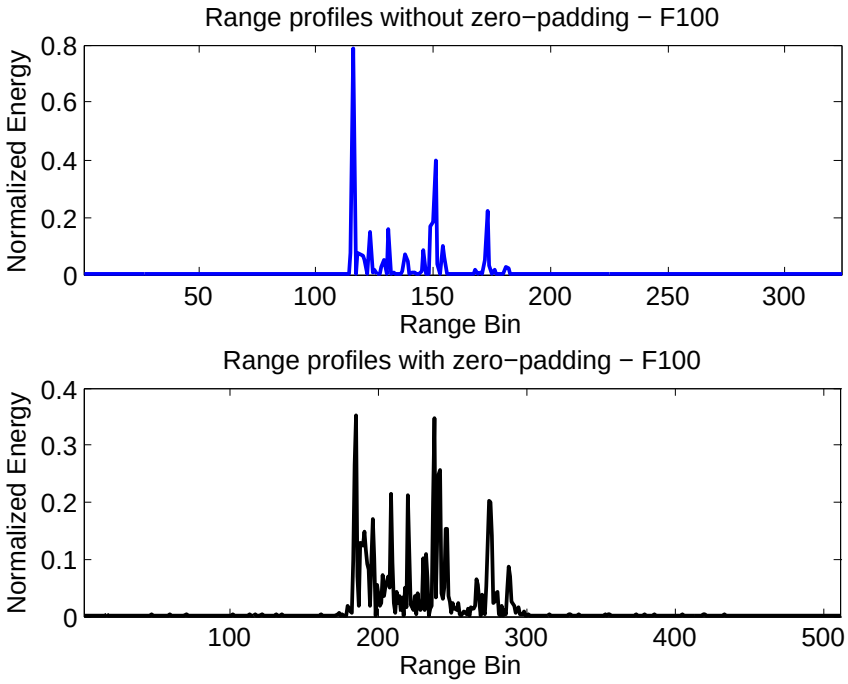

Figure 3.10: Range profiles with and without zero-padding

3.4.3. Motion Compensation

In section 3.3, it has been noted that the aircraft motion affects the shape and amplitude of the profiles. A few techniques can be applied in order to mitigate these effects.

In order to deal with target-aspect sensitivity some authors have opted for the application of non-linear transformations to range profiles [8], or to average sequences of range profiles [9], which result in a reduction of speckle and noise. To avoid the effect of RRM a small sector may be defined when analysing sequences of HRRPs such that the aircraft rotation does not produce rotational range migration [95]. Additionally, if the noise level is desired to be further reduced, thresholding techniques can be also

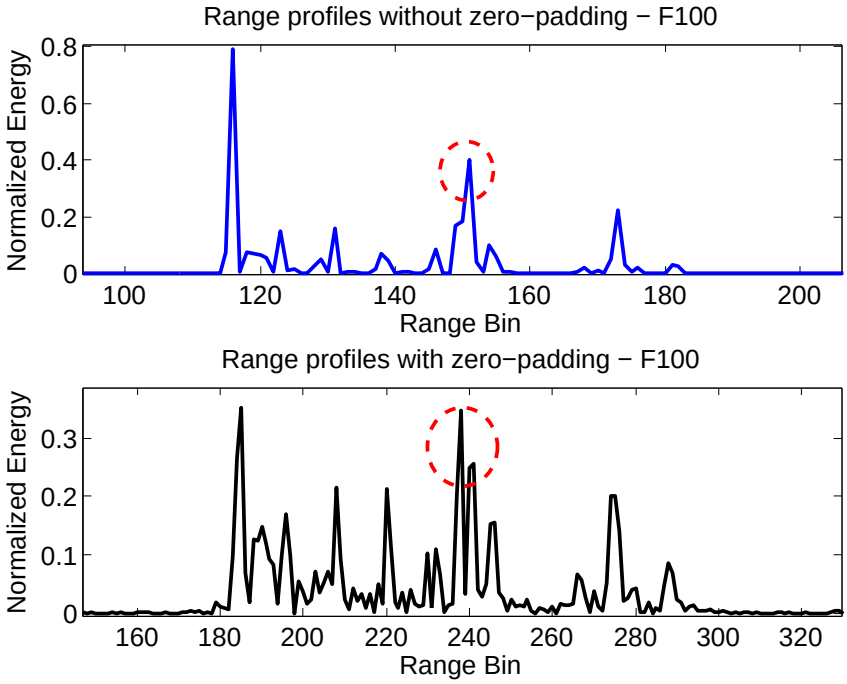

Figure 3.11: Peak-splitting of a zero-padded range profile

applied.

On the other hand, to deal with TRM, an alignment of profiles may be accomplished. HRRP alignment refers to aligning a HRRP with a particular reference position or a reference profile. There are three main reasons why HRRP alignment may be necessary: alignment for HRRP averaging, in order to reduce some effects such as speckle, alignment for ISAR processing, to retrieve target motion, or alignment for classification, because some classifiers require the target returns to be in a fixed position within the range window or because they make use of sequences of profiles and they need to be correctly aligned one respect to the others to remove aircraft motion. The alignment can be achieved by using the aforementioned compensation techniques described for ISAR in Chapter 2 (centroid tracking, envelope correlation, contrast/entropy based methods, dominant scatterer algorithm, zero phase representation, etc). Another solution to avoid TRM is to extract translation-invariant features. With invariant features the target position in the HRRP is no longer an issue and also the feature vector always has the same dimensionality regardless of the target dimensions. Translation-invariant features include the magnitude of the FFT of a range profile [59], utilization of the frequency spectra taken from the raw data obtained by the radar [63], the autocorrelation function of an HRRP [18] or computing the central moment features of range profiles produced by the MUSIC algorithm [64].

Regarding amplitude-scale sensitivity, to ensure all profiles have comparable magnitudes, range profiles normalization is usually applied. Scaling the values of range profiles so the sum of energy equals one [9, 16] or limiting the maximum amplitude to one [50, 96], are common techniques of normalization.

Finally, another common technique, which also help reduce speckle, is a gaussian normalization, a method that transforms the non-gaussian data to normalized distributed data. One of the most effective ways of transforming data to a suitable approximation of normality is to utilize a particular family of power transformations extensively applied to HRRP preprocessing: the Box-Cox transformation [97] with tunning parameter η, defined as:

$$x^{\eta} = \begin{cases} \frac{x^{\eta}-1}{\eta} & \text{if } 0 < \eta \leq 1 \\ \log x & \text{if } \eta = 0 \end{cases} \tag{3.14}$$

A power transformation, like the Box-Cox, strengthens the weak scatterers and weakens the strong ones making some characteristics of a target become clearer. The lower the η, the more the weak scatterers are amplified; this parameter should be chosen according to the range profiles SNR: for high SNR, small η is appropriate, while for low SNR it η is small the target may be submerged in the noise. Thus, for different measurements, parameter η may need a re-tune [98].

3.5. Summary

High resolution radar has the ability to resolve scatterers in the direction of propagation, being able, then, to provide signatures with information about different targets. This chapter has provided a general view of these signatures, namely the range profiles, their generation, their important parameters and the shortcomings found during their extraction.

As seen, the range profiles' extraction process using a stepped frequency waveform is quite simple since it just implies a transformation from the frequency to the time domain. Despite this simplicity, it has been seen that range profiles are very sensitive to the motion of the target. Changes of very few degrees in aspect angle can change completely the shape of a range profile.

Preprocessing techniques are needed to improve the nature of the range profiles and prepare them for a later feature extraction phase. Techniques to remove noise, such as thresholding; to reduce sidelobes, like windowing; to interpolate information, like zero padding; to normalize the inputs, such as amplitude normalization, or those for reducing the motion of the aircraft, like profile alignment, are important in the process of removing unwanted effects before classification takes place. As noted, not all the techniques will be needed in all the scenarios, the decision of which techniques to employ ultimately lies in the nature of the raw data; for example, if the input data comes from simulations, the noise removal or the motion compensation of the aircraft might be unnecessary.

In the following Chapter, the datasets used along this thesis will be presented, as well as the selected preprocessing techniques applied to further classify them.

Chapter 4

Datasets

One of the goals of this thesis lies in the development of novel algorithms for the identification of flying aircraft in a non-cooperative way. To achieve it, different datasets are needed to evaluate the proposed algorithms, hence, it is the purpose of this chapter to describe the available data utilized along this thesis.

In Chaper 2 it was already introduced the desire to evaluate the algorithms via comparison of actual measurements against simulated ones. As said, due to their military character and the difficulty of planning measurement campaigns, the availability of actual signatures is not enough to populate a complete database. On the other hand, testing a classifier in this scenario emulates the operational situation more faithfully since it may exist a significant difference between the profiles measured by an operational high resolution radar and the profiles in the database, even if this were populated also with actual profiles. Thus, both datasets, the actual and the simulated, along with the preprocessing methods applied to them will be presented in this chapter. After their description, different test cases for the experiments will be presented.

Throughout this thesis we will use the terms *input*, *training set* and *test set*. We call *training set*, for simplicity, to the data that forms the database of known potential targets, while *test set* will be the unknown data to be classified. Lastly, we call *input* to the information that enters the classifier, which will belong to the elements of the test set.

4.1. Actual data

The actual range profiles utilized throughout this text come from a civil measurement campaign that took place in 1995 called ORFEO. This campaign was held in The Hague, The Netherlands at TNO-FEL using the FELSTAR radar (a stepped frequency S-Band[1] radar) and the collected data were distributed in 2006 to the members of the NATO group RTO-SET-112 "*Advanced Analysis and Recognition of Radar Signatures for Non Cooperative Air Target Identification*".

In this section we will summarize the relevant information details on the FELSTAR radar and the extraction of range profiles from these data, but more information can be found in its technical report [99].

The ORFEO campaign was limited to civil targets of opportunity and provided measurements from 17 different types of aircraft. Measuring targets of opportunity implies that the radar illuminates any aircraft within its range, that is, non-cooperatively. Thus, estimates of the target aspect angles cannot

[1] S-Band: $2 - 4$ GHz

be obtained from on-board equipment but have to be derived from tracking data. In the case of ORFEO, during acquisition, information from a secondary radar was available providing the target type and an estimate of its flightplan (the aircraft aspect). The error on the estimated aspect angle of the aircraft did not exceed 5 degrees in both azimuth and elevation. Rapid changes in elevation, or if aircraft were making a long turn in the trajectory, would affect the profiles causing speckle and RRM, nevertheless, in the measurement campaign, only targets under conditions of no long turns nor approaching or leaving an airport runway were measured.

To minimize distortions due to radial motion, a velocity-tolerant stepped frequency waveform was used to measure the range profiles. In the velocity-tolerant waveform the pulse repetition interval decreases smoothly from pulse to pulse instead of being constant. The idea is that the times at which the pulses are transmitted are chosen such that the resulting range profiles are focused irrespective of the velocity. With this waveform not only velocity and acceleration compensation are needless[2], but also no JEM lines are observed. The specification of the main parameters of the waveform can be seen in Table 4.1.

Table 4.1: ORFEO waveform parameters

Polarization			Vertical
Carrier frequency	f_0	=	3.0738 GHz
Bandwidth	β	=	452.2 MHz
Number of pulses	n	=	324
Frequency step	Δf	=	1.4 MHz
Unambiguous range	R_u	=	107.14 m
Nominal range resolution	Δr	=	0.33 m
Minimum delay between pulses	t_{min}	=	420 μs

These parameters ensured, firstly, that targets could be measured up to a maximum range of 60 km and secondly, that any civil aircraft[3] could be contained in the unambiguous range window, R_u.

Among the 17 different types of civil aircraft that were measured in the ORFEO campaign, 7 have been selected to carry out the experimental part of this thesis. These are: Boeing 747-400, Boeing 767-300, Airbus A310, McDonnel Douglas MD-88, Boeing B737-500, Fokker 100 and Fokker 28. Each of them have been assigned a 4 digit label, which are respectively: B747, B767, A310, MD88, B737, F100 and F028. These 7 types of aircraft were chosen according to the total number of profiles that were collected along with the diversity in trajectories the aircraft described.

As noted, during the measurements a secondary radar provided the aircraft type, however, in the selected aircraft measurements there were two ambiguities that should be kept in mind:

- The system assigned the label B737 to both the Boeing 737 from the 300 and the 500 series. The two are identical apart from the length of the fuselage that differ in a couple of meters[4].

- The code MD88 was used to represent all aircraft from the McDonnell Douglas MD-80 series which includes the series MD-81/-82/-83/-87 and MD-88. Externally these are all identical except for the MD-87 which has a circa 5 meters shorter fuselage.

[2]The waveform is fairly insensitive to acceleration. The measured aircraft airliners can achieve maximum accelerations that can be tolerated by this waveform, otherwise the acceleration must be compensated

[3]The biggest expected airliner was a Boeing 747-400 with a length around 70 m

[4]The length of B737-300 is 33.4 m, while for the B737-500 is 31.1 m

Note that these two uncertainties are negligible when the aircraft is looked upon from broadside[5] but will cause additionally errors in our identification system otherwise.

The selected aircraft have the dimensions described in Table 4.2, where it is also shown the label assigned to each type of aircraft along this text. Note that the height is calculated considering the landing gear as stowed. As seen, the largest target expected is a B747-400 with an approximate length of 70 m, while the smallest will be a Fokker 28 with a length of nearly 30 m.

Table 4.2: Dimensions of selected aircraft

Aircraft	Length (m)	Wingspan (m)	Height (m)	Label
Boeing 747-400	70.66	64.44	16.79	B747
Boeing 767-300	54.22	47.52	14.77	B767
Airbus A310	46.66	43.90	12.74	A310
McDonnel Douglas MD-88	45.10	32.80	7.43	MD88
Fokker 100	35.53	28.08	6.58	F100
Boeing B737-500	31.10	28.90	9.73	B737
Fokker 28	29.61	25.07	6.62	F028

The trajectories described by each aircraft, that is, the aspect angles of each measurement, are depicted in Figure 4.1. The selected trajectories present a variety of aspect angles, they include some nose-on, tail-on and broadside aspect angles, which are representative of the different attitudes of an aircraft. As section 3.3 in Chapter 3 already introduced, nose-on aspect angles correspond to an azimuth of approximately $\alpha = 0°$, and an elevation of approximately $\theta = 90°$. As seen, all the trajectories have an elevation $75° < \theta < 110°$ while the azimuth cover a broader range. Some trajectories cover a wider azimuth range than others, due to this difference, as it will be seen in the following chapters, the trajectories will be split according to their azimuth coverage. Another important thing to be accounted for, is the number of trajectories for each aircraft. As seen in Figure 4.1a only 3 trajectories for aircraft A310 are available while for aircraft B767 for example, 6 different trajectories are considered. This implies that less profiles will be available for A310 and less input samples than other aircraft will be considered. Another noticeable characteristic of these trajectories is that some of them experience a turn in elevation or in azimuth. As said, the trajectories will be split and these abrupt changes will be avoided, that is, in the splitting process, such a change in azimuth of elevation will not be permitted and a part of a trajectory may be discarded.

4.1.1. Preprocessing of the actual data

As Chapter 3 introduced, the range profiles should be preprocessed in order to prepare them for the feature extraction and classification stages. These preprocessing methods included: windowing, zero-padding and motion compensation. As said, the nature of our data will determine the preprocessing techniques used.

The ORFEO campaign provided the in-phase (I) and quadrature (Q) components of a target signature in the frequency domain. Each measurement of the campaign comprises a frame of M profiles sequentially collected in time, with M being different for each measurement since it depends on the time the target was illuminated by the radar. As the number of pulses used by the step frequency waveform was $N = 324$,

[5] $\theta = 90°$, $\alpha = 90°$

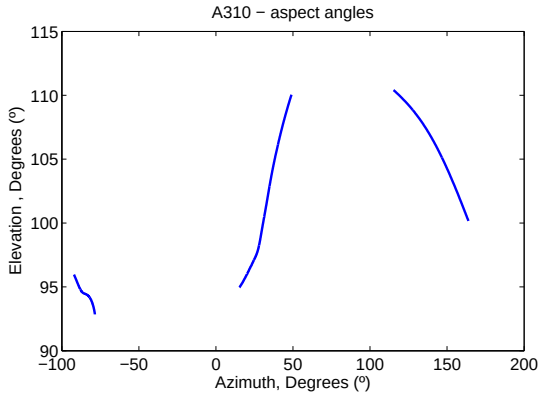

(a) A310

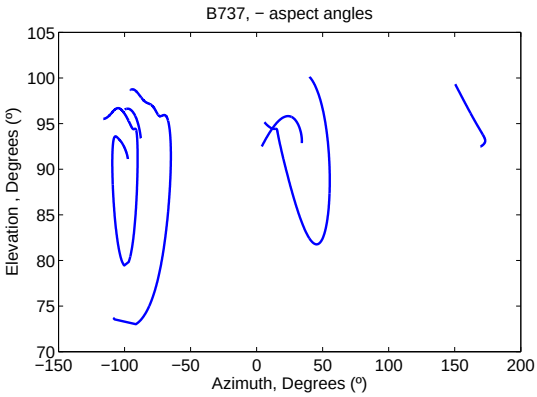

(b) B737

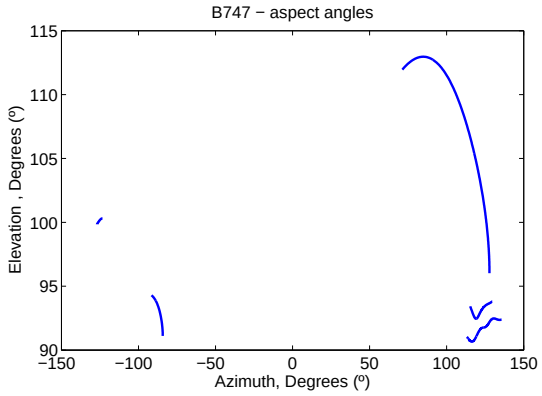

(c) B747

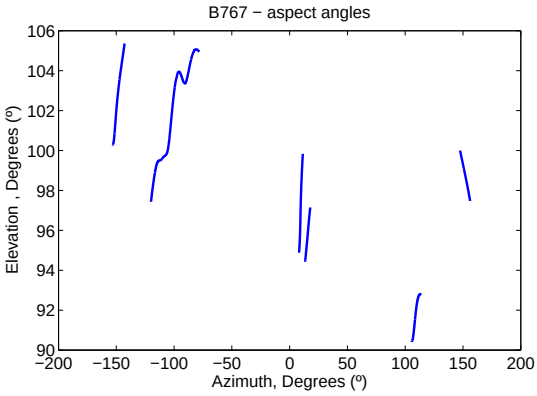

(d) B767

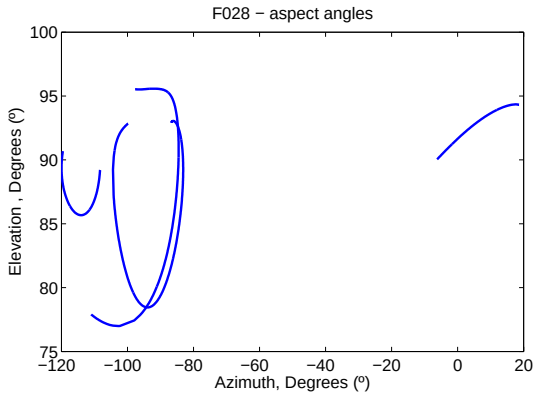

(e) F028

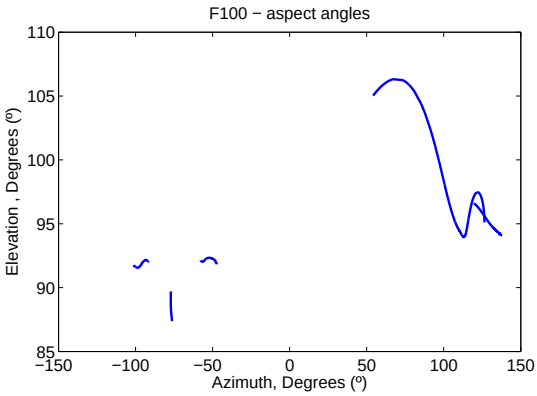

(f) F100

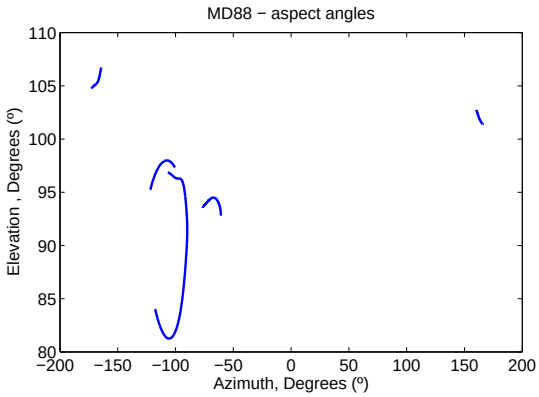

(g) MD88

Figure 4.1: Aspect angles of selected aircraft

each resulting HRRP will be composed of 324 range bins. Accordingly, each measurement will provide M profiles of N bins (matrices of dimensions $N \times M$).

The preprocessing included in the extraction of the actual range profiles used along this text is provided in the flowchart of Figure 4.2.

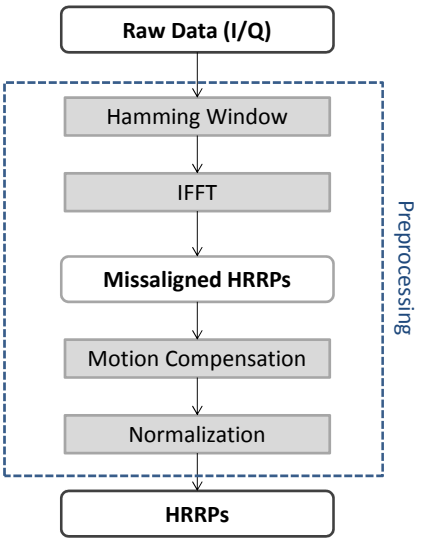

Figure 4.2: Flowchart of the preprocessing steps applied to the actual data

As seen, a Hamming window is first applied to the raw data in order to reduce the effects of the sidelobes of the stepped frequency waveform, as it was seen in the previous chapter. With this, the range resolution gets increased by a factor of 1.3, therefore, instead of a resolution of 0.33 m as Table 4.1 states, the resolution has increased to 0.43 m approximately.

After the windowing, although some authors recommend it, no zero-padding has been applied this time since it reduces the energy of the extracted range profiles and because the datasets used for recognition, as will be seen in the next section, have the same number of resolution cells. Therefore, the following step is the application of an IFFT of N samples; with this, the M range profiles of a measurement are extracted. However, these first extracted HRRPs are affected by aircraft motion and hence, this should be compensated. As previously stated, this motion can cause, on the one hand TRM, which mainly implies a shift in the profiles, and on the other hand, RRM and speckle, which are more difficult to distinguish and compensate.

To alleviate the effect of TRM, translational motion compensation is applied to the profiles via profile alignment. The algorithm used for alignment is based on the work carried out in [93], which relies on the method of envelope correlation initially described by Chen and Andrews [34]. This latter method calculates the correlation between two consecutive HRRP and estimates the shift between them. The envelope correlation procedure is robust against target oscillation and its implementation is fast and easy. The main problem lies in the fact that if one pair of profiles is not well aligned, the error propagates along the rest of the profiles in the measurement. Hence, here, a little group of profiles are taken as reference for avoiding the error propagation.

To easily understand it, the implemented alignment procedure is depicted in schematic form in Figure 4.3, and in Figure 4.4 with actual examples of a matrix of HRRPs. It follows the subsequent steps:

1. Initially (Figure 4.3a), the matrix of $N \times M$ profiles is missaligned, with N being the total number of range bins and M the total number of HRRPs.

2. A reference group is established with the first 6 profiles of a measurement. These 6 profiles are aligned pairwise one respect to the other. This alignment is made by applying circular correlation between two profiles, keeping one at a fixed position and shifting the other cyclically until the maximum correlation is found.

3. Once the 6 profiles of the reference group are aligned (Figure 4.3b), the next profile of the measurement is aligned with respect to them. In order to do that, the reference group is averaged to form a "grouped reference profile". This "reference profile" is now circularly correlated with the next profile and as in the former step, the shift between them is calculated by finding the position of maximum correlation.

4. The new aligned profile becomes part of the reference group, while the first profile of the reference group is discarded from it (Figure 4.3c).

5. Steps 3 and 4 are repeated until all the profiles in the matrix are aligned.

6. A fine alignment is completed next by aligning the profiles to a dominant scatterer (Figure 4.3d). These last two steps (step 6 and step 7) are optional, although it can improve the initial alignment carried out in the previous steps. One scatterer in a profile with maximum energy which is repeated along the rest of the aligned profiles is selected, this will be the dominant one. In the next profile, in a range of a few cells around the dominant scatterer, the scatterer with the maximum energy is found. The profile is shifted so the two dominant scatterers are aligned.

7. Now the dominant scatterer is the one of the new aligned profile and step 6 is repeated until all the profiles are finely aligned (Figure 4.3e).

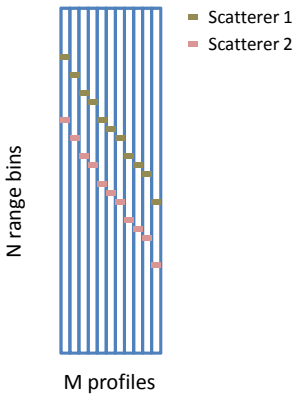

(a) Initial HRRP matrix ($N \times M$ missaligned profiles)

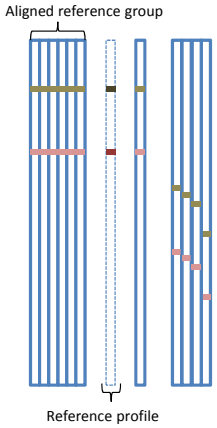

(b) Aligned reference group. New profile is aligned with respect to the reference profile.

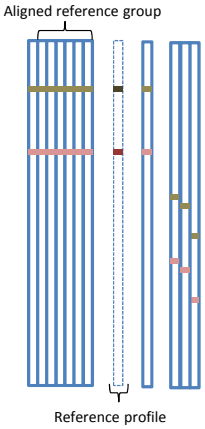

(c) New reference group: the new aligned HRRP is included while the first HRRP is discarded from it. Next profile is aligned with respect to the reference profile. Repeat this until all the matrix is aligned.

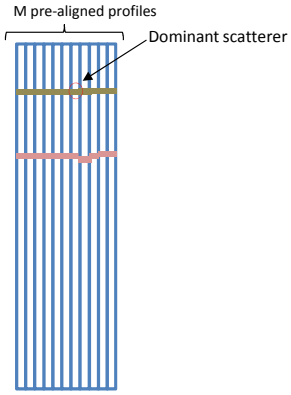

(d) Select a dominant scatterer and proceed with a fine alignment with respect to it.

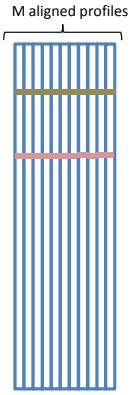

(e) The M profiles of the HRRP measurement are finally aligned.

Figure 4.3: Squematic of the process of profile alignment

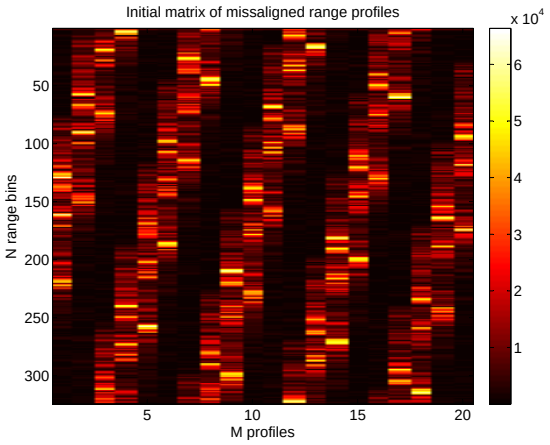

(a) Initial HRRP matrix (324×20 missaligned profiles)

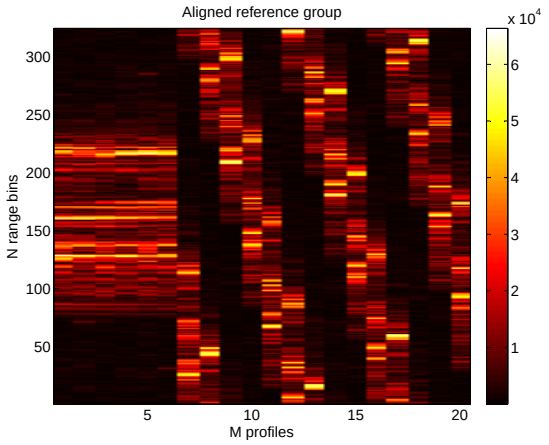

(b) Aligned reference group. New profile is aligned with respect to the reference profile.

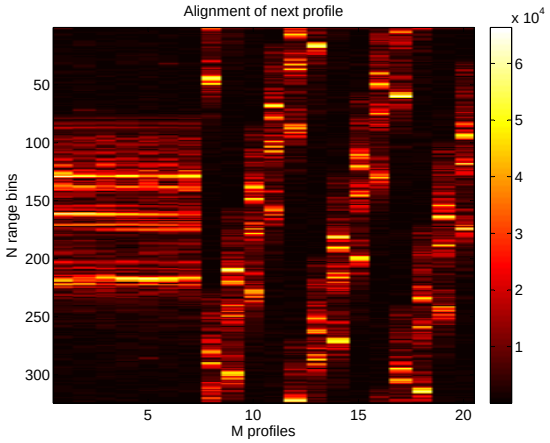

(c) New reference group: the new aligned HRRP is included while the first HRRP is discarded from it. Next profile is aligned with respect to the reference profile. Repeat this until all the matrix is aligned.

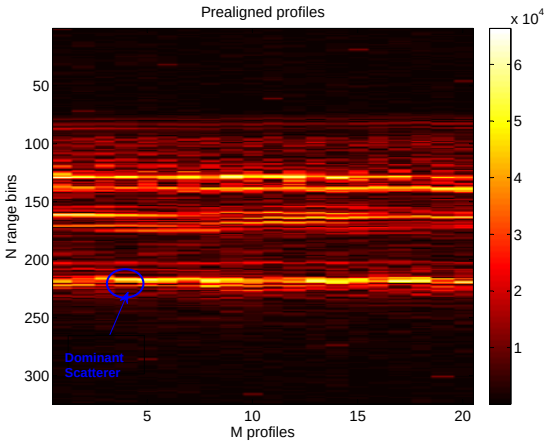

(d) Select a dominant scatterer and proceed with a fine alignment with respect to it.

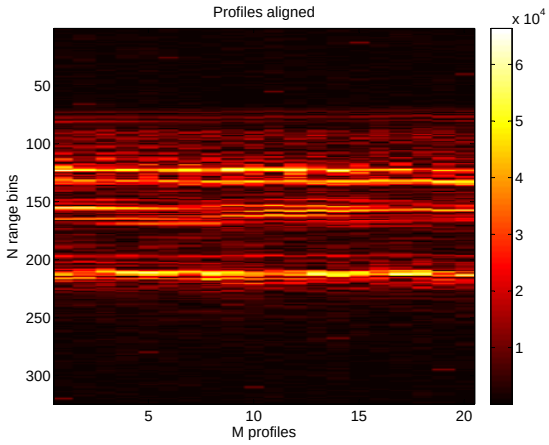

(e) The M profiles of the HRRP measurement are finally aligned.

Figure 4.4: Process of profile alignment. Actual matrix of range profiles of dimensions 324×20

In the case of RRM, small sectors will be defined where the variation in azimuth and elevation change smoothly. In the worst case, which would be that of the largest aircraft (a Boeing B747-400) with a length of 70.66 m and a height of 16.78 m, according to equations 3.10 and 3.11, the minimum aspect angle changes associated with RRM are $\Delta\alpha_{RRM} < 0.35°$ and $\Delta\theta_{RRM} < 1.46°$(remember the increase in the resolution due to the Hamming window). In order to guarantee that from one range profile to the next one there is no RRM their aspect angle difference should satisfy these constraints. Fortunately, in the measurements selected for the experiments this is satisfied.

In the case of speckle, it will be implicitly compensated in the classification process; as will be seen in the next Chapter, SVD will be used to extract the main features. The first eigenvector is equivalent to the average range profile which attenuates the speckle effect. Then, by using SVD the effect of speckle gets reduced.

Finally, the amplitude-scale sensitivity is compensated with a normalization to unit energy of each HRRP by applying a L2-norm. Then, if x represents a range profile of n range bins ($x \in \Re^n$), its normalized version, $\overline{x}$, will be given by equation 4.1. With normalization the classification should be independent on the magnitudes of the HRRPs.

$$\overline{x} = \frac{x}{\|x\|_2} = \frac{x}{\sqrt{\sum_{i=1}^{N} x_i^2}} \tag{4.1}$$

4.2. Simulated data

The training samples, that is, the known potential targets that will populate the database, are synthetically obtained with a computer software. This type of software is normally referred to as RCS-prediction codes. For decades, and still nowadays, RCS-prediction techniques have been under development for predicting the amount of energy a target is capable of reflecting under a certain aspect angle.

When the dimensions of the objects are much larger than the wavelength, high frequency techniques, as *Physical Optics (PO)*, *Physical Theory of Diffraction (PTD)*, *Shooting and Bouncing Ray (SBR)*, *Geometrical Theory of Diffraction (GTD)*, or *Uniform Theory of Diffraction (UTD)*, can be used instead of using rigorous methods, as *Finite Element Method (FEM)*, *Finite Difference Time Domain (FDTD)* or *Method of Moments (MoM)*. The high frequency methods apply simplifications of the Maxwell equations to calculate the RCS assuming that the target is electrically large, while the rigorous, or numerical methods perform a direct discretization of the Maxwell equations in their integral of differential form. Thus, the computational complexity and time consumption of these latter methods are much higher than for the high frequency techniques. In high resolution radar the target dimensions are clearly much larger than the wavelength and so, high frequency codes are adequate to predict HRRPs.

Different high frequency codes exist for the HRRP prediction, many of these codes have been developed internally for experiments, like RAPPORT [95], while others like XPATCH [100] or FASCRO [101] have been commercially distributed.

The totality of the synthetic range profiles that form the training samples of this study are generated by FASCRO, a RCS-prediction code that was first developed by *Universidad de Alcalá (UAH)* and optimized by INTA. FASCRO predicts the monostatic RCS of complex targets, which are modeled as *Non-Uniform Rational B-Splines (NURBS)* surfaces, based on PO and PTD [102, 103]. In the RCS computation, FASCRO can use the following scattering mechanisms: simple reflection, diffraction in straight edges, double and triple mechanism between planar patches and patches-edges, creeping waves and cavities.

However, it does not incorporate the diffraction mechanisms from curved edges or second order effects in curved patches.

In order to validate the code, several measurements in anechoic chamber were performed over calibrated small targets. The results showed a general good coherence between measurements and predictions, although in some cases some insubstantial discrepancies were found since, as said, not all electromagnetic effects were taken into account [104–106].

The CAD models of the 7 aforementioned aircraft have been developed at INTA. These models are defined as NURBS and can be seen in Figure 4.5. The asymptotic nature of FASCRO makes the simulation more precise as the working frequency gets higher. For this reason, FASCRO is not able to interpret either very small surfaces or resonant ones, implying that very high fidelity CAD models may provide wrong results. Therefore, the cavities, antennas and other little elements that protrude from the fuselage are not included in the CAD models; hence, it can be said that the used models are rough replicas of real aircraft. FASCRO allows the assignment of different materials to different surfaces, although it always consider them as coatings with a layer of *Perfect Electric Conductor (PEC)* underneath; in this case, the simulations have been done considering every surface as being metallic, that is, every aircraft have been considered as PEC.

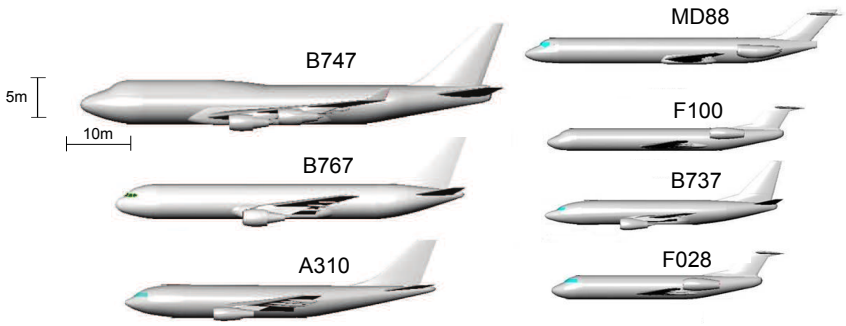

Figure 4.5: CAD models of the simulated aircraft

The synthetic profiles that comprise the training set have been predicted by FASCRO using the information of the estimated aspect angles given in the test set and the same waveform parameters that were used for the acquisition of the actual profiles (Table 4.1).

Although the synthetic data (and also the CAD models) have an intrinsically lower complexity than the measurements on real aircraft, simulated range profiles are an efficient and cheap method for obtaining large amounts of profiles describing any desired trajectory; moreover, it is clear that it is the best option when no real data are available.

4.2.1. Preprocessing of the synthetic data

In the case of predicted profiles, they do not undergo the same phenomena as a real measurement; remember that FASCRO, as it uses high frequency techniques, does not take into account all electromagnetic effects when predicting RCS, and also, although in the simulations its aspect angle changes[6], the aircraft is kept static from one measurement to the next and thus, no translational motion compensation is needed.

The RCS is transformed into the in-phase (I) and quadrature (Q) components of the energy reflected by the target. As the simulations have been performed with the same parameters as the actual measurements,

[6]The rotation axis is located in the aircraft's geometric centre

likewise, a Hamming window will be applied before the IFFT to reduce the sidelobes of the stepped frequency waveform. After the IFFT, matrices of predicted profiles of dimensions $N \times M$ for each synthetic simulation are obtained. Similarly to the actual profiles no zero-padding has been applied. As noted, in this case the TRM is not present in the simulated profiles, thus the alignment of profiles will not be needed. Regarding RRM and speckle, as the trajectories described by the actual measurements are the same as the simulations, the same properties apply.

Predicted profiles are not recorded by a real radar, hence the amplitude-scale sensitivity due to the radar system is not present. Nevertheless, since the actual profiles are normalized to unit energy by applying L2-norm, the same criteria is applied to the synthetic profiles in order to make them comparable.

In conclusion, the synthetic profiles preprocessing steps are simpler since they are just ideal simulations. These preprocessing steps include Hamming windowing, IFFT and amplitude scaling processes, while the motion compensation, which is a critical step for the actual profiles, is not necessary.

4.3. Differences between datasets

As noted, profiles that will form the test set and the training set are different in nature; the training set has been deployed using simulations of aircraft models with a RCS-prediction code, while the test set comprises a compilation of actual range profiles that were collected in a measurement campaign. This is the main difference that will produce discrepancies between simulations and actual measurements.

In this regard, Figure 4.6 shows dissimilarities between the measured profiles at a certain aspect angle and the synthetic ones obtained with FASCRO for the same aircraft with the same orientation[7].

Having a look at Figure 4.6, one can note, as expected, that the synthetic signatures may be too ideal, mainly due to the following:

CAD modeling ambiguities

Synthetic profiles have been predicted in an ideal scenario, with no noise, no clutter and no actual motion. The CAD models have been developed considering every aircraft as PEC and without little protruding elements, that is, aircraft models, though close, are not exact replicas of real aircraft. Real aircraft also have non-metallic parts, like the belly fairing, the antennas' radomes or the windows, which are made of plastic material. Additionally, the engine cavities of these models have been covered by flat plates, thus, when illuminating the aircraft from nose-on aspects, high reflection peaks are expected in the position of the engines.

CAD modeling defined as PEC is only a first approximation to the actual scattering mechanisms and is therefore, likely to produce inaccuracies in the HRRP predictions. Having this in mind, and after analyzing Figure 4.6, one can note how idealist these signatures are. Take for example Figure 4.6e which depicts a F100 illuminated at an aspect which is not near nose-on or broadside; it can be easily seen that in the measured profile a dominant scatterer exist which also exist in the simulated HRRP, however other smaller peaks appear in the measured profile that are not present in the simulated one.

Unmodeled reflective processes

Additionally, since it uses high frequency techniques, several scattering processes that occur in reality are not accounted for in FASCRO. A full wave EM software would be needed to properly run all these

[7] Aircraft B737 is not compared because that aircraft will only be used in the training set, hence no actual measurement of this aircraft will be present in the test set

effects with the associated increase in time and computer memory requirements.

The noise is another effect that is not considered in the simulations and although it is not a reflective process *per se*, it can be included into this section. Actually, actual measurements have thermal and processing noise, while the synthetic ones don't. Remember that the collected radar signals come from the real world and they must pass through the reception chain, and although its noise figure may be very low, some of it could be leaked to the final profiles.

All these unmodeled processes can be appreciated in all the subfigures of Figure 4.6 since barely no noise-power is present in the predicted profiles and more peaks are present in the actual profiles that do not exist in the simulated ones.

Amplitude difference

Although in both cases amplitude normalization is applied such that the total energy equals unity, the amplitudes of the profiles do not match very well. One of the probable causes is speckle, remember that a difference in hundredths of a degree may change the shape of the HRRP, hence if the simulated profiles are not predicted in the exact same aspect angles this effect may arise. The inaccuracies in the CAD models and in the prediction codes also affect the amplitude of the profiles; as more scattering processes occur in reality, more peaks are present in the actual HRRP and this influences the amplitudes when normalizing. Additionally, as no noise is present in the synthetic profiles its normalization pushes the signal components to higher values.

Estimation of aspects

Another very important source of error in the profiles resemblance is the target aspect estimate. As mentioned before, the synthetic profiles are simulated under the same aspect angles than the measured ones, however, the aspect angles of the actual profiles are merely predictions since the aircraft were measured non-cooperatively and their exact orientation was unknown. These estimated aspect angles had an error of 5 degrees at the most in both azimuth and elevation. So, even though the simulations have been run under the same aspect angles, this inherent error may cause additional difference between actual and simulated profiles.

Broadside vs. nose-on aspect angles

At broadside aspect angles ($\theta = 90°$, $\alpha = 90°$), unlike in nose-on and tail-on ($\theta = 90°$, $\alpha = 0/\pm 180°$) orientations, there are no reflections from cavities nor turbines; it is the aircraft fuselage which produces a very large specular return. Also, at these aspect angles, not many range cells contain multiple scatterers that give rise to inaccurate amplitudes. Figure 4.6b is a clear example of this fact. In that figure the normalized energy of a measured and simulated B747 at a near broadside aspect angle is depicted, and both the synthetic and the actual HRRP have a very high predominant peak with almost the same amplitude. On the other hand, at nose-on and tail-on aspects the radar "sees" more scattering centers and also the cavities of the engines; resonant phenomena take place around them, causing additional peaks in the HRRP. Hence, more peaks will be present in a representation of a range profile near nose-on and tail-on, as in Figure 4.6a or 4.6c. However, in the simulated profiles, the covered cavities cause high peak values and less scattering centers.

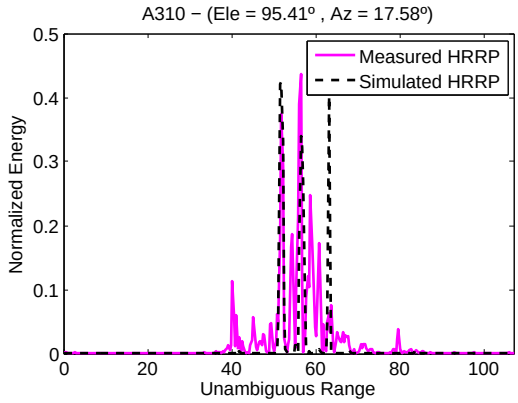

(a) A310

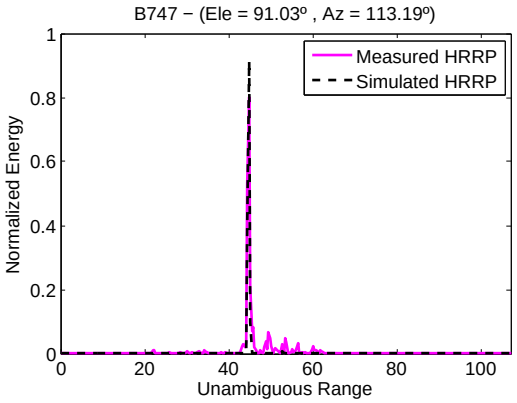

(b) B747

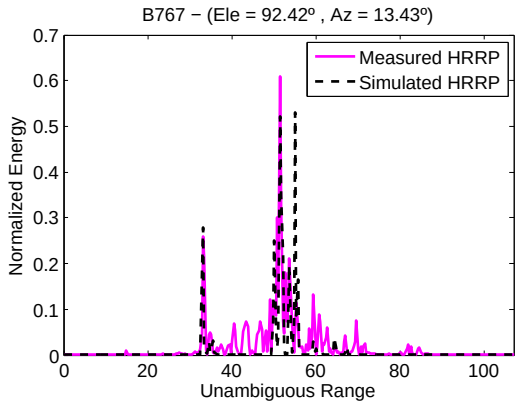

(c) B767

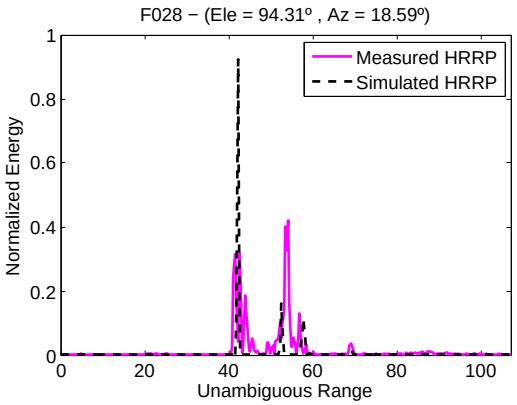

(d) F028

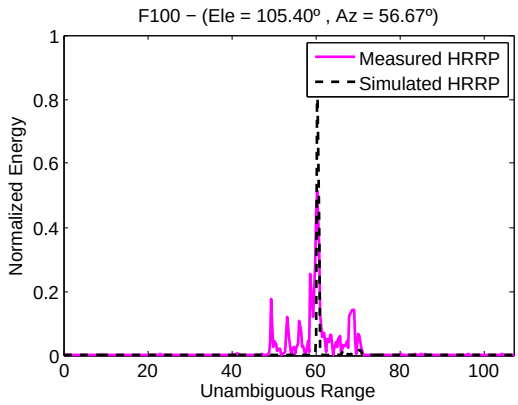

(e) F100

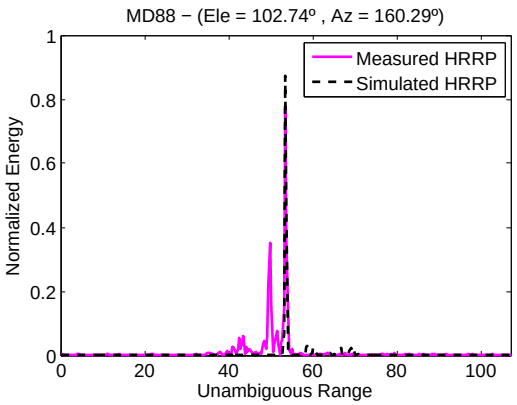

(f) MD88

Figure 4.6: Differences between actual and synthetic profiles

4.4. Discussion

In the previous sections a description of the different datasets available in this thesis has been provided. As test set, that is, the profiles that are to be classified, actual measurements of civil in-flight targets will be taken. Due to the nature of these measurements, some preprocessing is needed before the classification process. On the other hand, there are the simulated profiles, they will form the database of potential targets, the training set, and are extracted from a RCS-prediction code. Section 4.3 has described the differences between these datasets and has concluded that synthetic and actual profiles are very different in a number of ways, mainly due to the fact that predictions are just ideal approximations of actual profiles.

At this point, one can wonder, why do we want to use predicted HRRP for classification if there exist such an obvious difference?

Section 2.3 gave a discussion about this. As said, in a real scenario, the measured range profiles may have different SNR than those in the database, and thus, high similarity between them is not expected. Additionally, it would be impossible to fill the database with measurements of range profiles as the ones to be classified, mainly due to the fact that hostile nations would not permit their aircraft forces to participate in measurement campaigns, and also because it is very difficult to characterize the flying aircraft in all possible aspect angles. With a synthetic database, there is no need to perform new measurements each time a new type of aircraft has to be included in the database. With the knowledge of the CAD models, any aircraft can be simulated under any desired aspect angle. Finally, if we use a different radar or apply other waveform parameters, only a resimulation is needed instead of planning a new measurement campaign.

Taking all this into account, our final purpose will be the identification of actual profiles by means of a database of synthetic ones, despite their discrepancies. To this end, the next chapter will introduce the algorithms developed to achieve this goal.

Chapter 5

Algorithms for range profiles classification

In the preceding chapters the context of this thesis has been introduced. In Chapter 2 it was noted that a recognition system involves the tasks of : 1) data acquisition and preprocessing, 2) feature extraction and 3) classification. Following these premises, Chapter 3 gave an overview of the main properties of range profiles and Chapter 4 described the available data, their acquisition and the suitable preprocessing. Therefore, to complete the recognition system description, this chapter will deal with the feature extraction and classification stage. Chapter 2 gave an overview of different feature extraction methods and classifiers utilized along the years in the literature. Although there exist no definitive methods that can resolve the problem in the best possible way, this chapter will explain the feature extraction technique utilized for the experiments and the classifiers conceived according to it.

5.1. Feature extraction

The objective of the feature extraction techniques is to reduce the dimensionality of the problem by keeping the valuable information while discarding the redundant one. From the wide range of feature extraction methods described in Chapter 2, *Principal Component Analysis (PCA)* is the one selected in this thesis. As said in the previous section 2.2.3 of the aforementioned chapter, this technique is quite appropriate for the desired classification algorithms, additionally, it is a well known efficient technique and easy to implement. The main advantage of this feature extraction method over others is that it provides a decomposition into subspace bases that can be further used to define target classes and this will be used in the developed classifiers, which are based on subspace methods.

PCA is useful for eliminating dimensions that do not provide valuable information of the data. In general terms, PCA uses a vector space transform to reduce the dimensionality of large data sets. Using mathematical projection, the original data set, which may have a number of possibly correlated variables, can often be interpreted in just a smaller number of variables called principal components. Therefore, selecting the principal components results in a reduction of dimensionality since negligible information is being discarded.

PCA can be achieved via eigenvalue decomposition or via singular value decomposition. The fundamental difference between *Singular Value Decomposition (SVD)* and eigenvalue decomposition is that SVD uses two different bases to decompose a matrix while eigen decomposition uses just one, the eigenvectors. Singular values and eigenvalues are highly related, the nonzero singular values of a matrix X

are the positive square roots of the nonzero eigenvalues of $X^T X$ or XX^T. The bases obtained by SVD are orthonormal unlike the eigenvectors, that might not be, and finally, another important difference is that not all matrices have an eigen decomposition, even the square ones, however, all matrices, even rectangular, have a singular value decomposition [107]. For these reasons in the algorithms developed in the next sections, SVD is used to achieve matrix decomposition.

5.1.1. Singular Value Decomposition

SVD is a robust technique for the decomposition of any matrix into orthogonal basis spaces [107–109]. It is applicable to both real and complex matrices, although here it is assumed that the data is real. With SVD it is possible to find the best approximation of the original data points using fewer dimensions.

Let $X \in \Re^{N \times M}$, there exist orthogonal matrices

$$U = [u_1, ..., u_N] \in \Re^{N \times N} \tag{5.1}$$

$$V = [v_1, ..., v_M] \in \Re^{M \times M} \tag{5.2}$$

$$\Sigma = diag(\sigma_1, ..., \sigma_p) \in \Re^{N \times M} \; ; p = min\{N, M\} \tag{5.3}$$

such that

$$X = U \cdot \Sigma \cdot V^T \tag{5.4}$$

where $\sigma_1 \geq \sigma_2 \geq ... \geq \sigma_p \geq 0$ are the singular values of X, *diag* stands for diagonal matrix and vectors u_i and v_j are the ith left and jth right singular vectors of X respectively. Note that the diagonal matrix Σ has the same shape as X, while U and V are always square orthogonal matrices[1], that is $U^T \cdot U = U \cdot U^T = I$ and $V^T \cdot V = V \cdot V^T = I$. Every matrix $X \in \Re^{N \times M}$ has a singular value decomposition[2], furthermore, the singular values σ_i are uniquely determined and it can be proven that $\sigma_1 = \|X\|_2$ [108].

In the matter at hand, where $X \in \Re^{N \times M}$ is a matrix of M range profiles of N range bins, the left singular vectors in U span the orthogonal basis space in the range domain, while the right singular vectors in V span the basis space in the angle domain. Larger singular values, σ_i, imply larger contribution of the corresponding singular vector in forming the target signal. The Eckhart and Young theorem [108] guarantees that the top singular vectors with the highest singular values provide the best approximation of the data. Thus, the N-dimensional vector space (when referring to matrix U, or M-dimensional, referring to V) can be divided into two subspaces, a dominant subspace and a subdominant subspace.

The singular vectors included in the dominant subspace are defined as the bases that span the *signal subspace*, the subspace that contains valuable information about the data, while the rest of the singular vectors are the bases that span the *noise subspace*, the negligible data.

The division into *signal* and *noise* subspaces is done according to the obtained singular values, σ_i. An energy threshold, η, is set ($0 < \eta < 1$) as in equation 5.5, such that the *signal subspace* is defined as the K most significant singular vectors, that is, K is the smallest value that fulfills equation 5.5. This threshold is frequently set such that the *signal subspace* contains around the 90% of the energy [9, 110], however, this value is usually set experimentally depending on the datasets; the remaining singular vectors that are not included in the dominant subspace will be discarded as they span an unwanted subspace.

[1] Unitary matrices when working with complex matrices

[2] When computing PCA with eigenvalue decomposition the covariance matrix ($X \cdot X^T$) is decomposed into its eigenvectors and eigenvalues such that $X \cdot X^T = U \cdot \Lambda \cdot U^T$ with Λ containing the eigenvalues

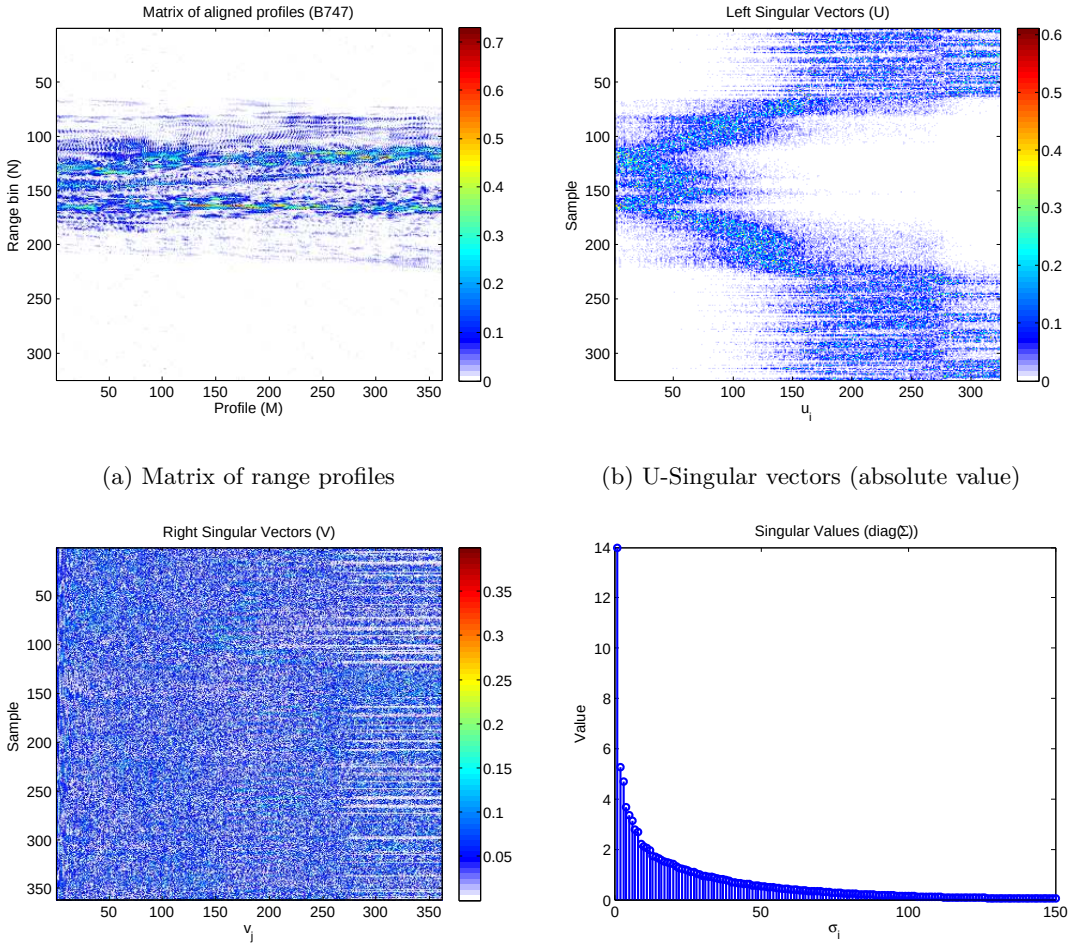

(a) Matrix of range profiles

(b) U-Singular vectors (absolute value)

(c) V-Singular vectors (absolute value)

(d) Σ-Singular values

Figure 5.1: Singular value decomposition

$$\frac{\sum_{i=1}^{K} \sigma_i}{\sum_{i=1}^{p} \sigma_i} \geq \eta \tag{5.5}$$

As an example, Figure 5.1a shows a matrix of range profiles of dimensions $N = 324, M = 361$ corresponding to a B747 measured in neither broadside nor nose/tail-on aspect angles. Applying SVD to that matrix, matrices U, V and Σ are obtained and showed in the figures 5.1b to 5.1d. As expected, the dimensions of the obtained matrices are $U \in \Re^{324\times324}$, $V \in \Re^{361\times361}$ and $\Sigma \in \Re^{324\times361}$. Note that only the first 150 singular values of Σ has been depicted for simplicity, but the decreasing tendency is clearly noticed, around the 100-th singular value, they have a negligible weight and that's the reason why a threshold to eliminate these singular values and their associated vectors is needed. Additionally, Figure 5.1b shows that the left singular vectors seem to follow a particular "shape" until a point where they look as if they were just noise, which coincidentally happens when the associated singular value has an almost zero weight. On the other hand, at first glance, the right singular vectors depicted in 5.1c do not follow any tendency and hence, they will not be used in the identification algorithms.

Additionally, the application of SVD helps to overcome the target-aspect sensitivity (RRM and speckle). The average profile of a real HRRP frame can reduce the target-aspect sensitivity of real profiles [9] and in fact, the average profile of a frame and the first left singular vector of the matrix of the same frame are similar. Accordingly, the application of SVD will help reduce the target-aspect sensitivity.

5.2. Classifiers Definitions

The selected features will be, therefore, the singular vectors that form the bases that span the *signal subspace* along with their corresponding weights, that is, their singular values. Once the features have been selected, a classifier should be designed in accordance to determine a decision boundary so the extracted features can be assigned to their true class. Three algorithms have been defined and tested along this thesis. They are presented in the following subsections such that each one presents an upgrade with respect to the previous.

Usually, the selection of the feature extraction method goes hand in hand with the classifier; therefore since PCA decompose the data into subspaces, the formulated classifiers take advantage of this property and they are defined as subspace methods with an optimization of a distance metric.

5.2.1. Classical Subspace Methods

The *Conventional Subspace Method (CSM)* [111] is a statistical pattern recognition method where each class is represented by a subspace and the belonging to a class, namely the similarity, is determined by the principal angle between a vector g, representing a test sample, and the subspace. Based on this Conventional Subspace Method, two classifiers are defined in the next section with the additional properties of accumulation and weighting.

The *Mutual Subspace Method (MSM)* presented in [71], on the contrary, defines the similarity by the angle between two subspaces where the bases of the subspaces are calculated using PCA via eigenvalue decomposition. The relationship between two subspaces, D and S, is then defined by their principal angles, so called canonical angles, which are an extension of the angle between two vectors.

A graphical explanation of both methods can be found in Figure 5.2 where Figure 5.2a shows how in CSM only one principal angle (Θ_1) is returned since the test sample is represented by one vector; and Figure 5.2b shows that MSM returns k canonical angles corresponding to the k vectors that compose the smallest subspace.

In the next lines, the focus will be on MSM and the calculation of the principal angles between subspaces. The calculation of the principal angle between vector and subspace (as in CSM) implies the same procedure when the dimension of one of the subspaces is set to one.

In MSM, the set of profiles is modeled by the subspace spanned by the principal basis vectors: in this case, if X_D is a matrix of profiles belonging to a subspace D, by applying eigen-decomposition to $X_D \cdot X_D^T$ and exploiting the eigenvectors corresponding to the K_d largest eigenvalues, the bases of subspace D are obtained as in equation 5.6:

$$X_D \cdot X_D^T = V_D \cdot \Lambda_D \cdot V_D^T \Longrightarrow \widehat{V}_D \in \Re^{N \times K_d} \tag{5.6}$$

where $V_D \in \Re^{N \times N}$ is a matrix containing the eigenvectors, $\Lambda_D = diag(\lambda) \in \Re^{N \times N}$ is a diagonal matrix containing the eigenvalues and $\widehat{V}_D \in \Re^{N \times K_d}$ is the selected basis of the subspace D.

As stated, the similarity measure between two subspaces (D and S) is defined as their canonical angles (θ_i) [112] and these are obtained recursively as:

$$\cos\theta_i = \max_{u \in D} \max_{v \in S} u^T \cdot v = u_i^T \cdot v_i \ ; \ i = 1, \ldots, k \tag{5.7}$$

such that:

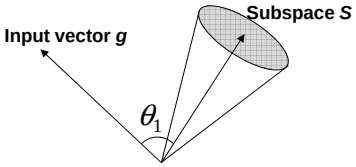

(a) Conventional Subspace Method (CSM)

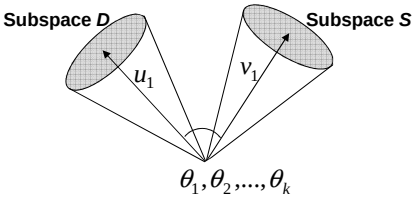

(b) Mutual Subspace Method (MSM)

Figure 5.2: Basic concepts of subspace methods

$$
\begin{aligned}
&\|u\|_2 = \|v\|_2 = 1 \\
&u^T \cdot u_i = 0 \qquad\quad i = 1, \ldots, k-1 \\
&v^T \cdot v_i = 0 \qquad\quad i = 1, \ldots, k-1 \\
&k = \min[K_d, K_s]
\end{aligned}
$$

where $[u_1, \ldots, u_k]$ and $[v_1, \ldots, v_k]$ are called the canonical or principal vectors between subspaces D and S, and K_d and K_s are the number of eigenvectors taken as bases of the subspaces D and S respectively. Note that the canonical vectors need not be uniquely defined, but the canonical angles always are. These canonical angles satisfy $0 \leq \theta_1 \leq \theta_2 \leq \cdots \leq \theta_k \leq \pi/2$.

For computing the principal angles and vectors, SVD will be the basic tool utilized [112, 113]. If the columns of $\widehat{V}_D \in \Re^{N \times K_d}$ and $\widehat{V}_S \in \Re^{N \times K_s}$ define orthonormal bases for subspaces D and S respectively, and calling $M = \widehat{V}_D \cdot \widehat{V}_S$, the singular values and singular vectors of matrix M can be characterized by:

$$\sigma_i = \max_{\|y\|_2 = \|z\|_2 = 1} (y^T \cdot M \cdot z) = y_i^T \cdot M \cdot z_i \tag{5.8}$$

subject to:

$$
\begin{aligned}
&y^T \cdot y_i = 0 \qquad\quad i = 1, \ldots, k-1 \\
&z^T \cdot z_i = 0 \qquad\quad i = 1, \ldots, k-1 \\
&k = \min[K_d, K_s]
\end{aligned}
$$

Denoting the range of a generic matrix A by $R(A)$, such that:

$$R(A) = \{u \mid Ax = u\} \tag{5.9}$$

and defining:

$$u = \widehat{V}_D y \in R(\widehat{V}_D), \quad v = \widehat{V}_S z \in R(\widehat{V}_S) \tag{5.10}$$

then, it follows that equation 5.8 is equivalent to equation 5.7, since:

$$\sigma_i = y^T \cdot M \cdot z = y^T \cdot \widehat{V}_D^T \widehat{V}_S \cdot z = u^T \cdot v \tag{5.11}$$

and therefore, σ_i are the cosines of the canonical angles θ_i. That is:

$$\cos\theta_k = \max_{u \in D} \max_{v \in S} u^T \cdot v = \max_{y \in \Re^{K_d}} \max_{z \in \Re^{K_s}} y^T \cdot (\widehat{V}_D^T \cdot \widehat{V}_S) \cdot z \tag{5.12}$$

considering $\|u\|_2 = \|v\|_2 = \|y\|_2 = \|z\|_2 = 1$ and $y^T \cdot y_i = u^T \cdot u_i = 0$, $z^T \cdot z_i = v^T \cdot v_i = 0$ just like equations 5.8 and 5.7.

Finally, assuming $K_s < K_d$ and applying SVD to matrix $\widehat{V}_D^T \cdot \widehat{V}_S$, then $k = \min[K_d, K_s] = K_s$ and:

$$\widehat{V}_D^T \cdot \widehat{V}_S = U \cdot \Theta \cdot V^T \tag{5.13}$$

where

$$\left.\begin{array}{rcl} U = [u_1, \ldots, u_{K_d}] & = & \widehat{V}_D \cdot Y \\ V = [v_1, \ldots, v_{K_s}] & = & \widehat{V}_S \cdot Z \end{array}\right\} \text{ canonical vectors}$$

$$\Theta = diag(\cos\theta_i) = diag(\sigma_i) \quad \longrightarrow \text{canonical angles' cosines ; } i = 1, \ldots, K_s$$

The similarity measure, S_{DS}, can be defined as the largest singular value σ_{max}, as the mean of the obtained singular values, as the squared sum of the canonical angles' cosines, etc. Here, it is chosen as the latter option, that is, $S_{DS} = tr(\Theta^2)$. The higher the similarity, S_{DS}, the higher the coupling between subspaces D and S as Figure 5.3 depicts. In the case that two subspaces coincide completely with each other, all canonical angles are zero and so their similarity defined as the sum of the canonical angles' cosines will be $S_{DS} = k$, with k being the dimension of the smallest subspace ($k = K_s$); on the other hand, when the two subspaces separate, the similarity will get smaller and finally, if the subspaces are orthogonal, it will become zero.

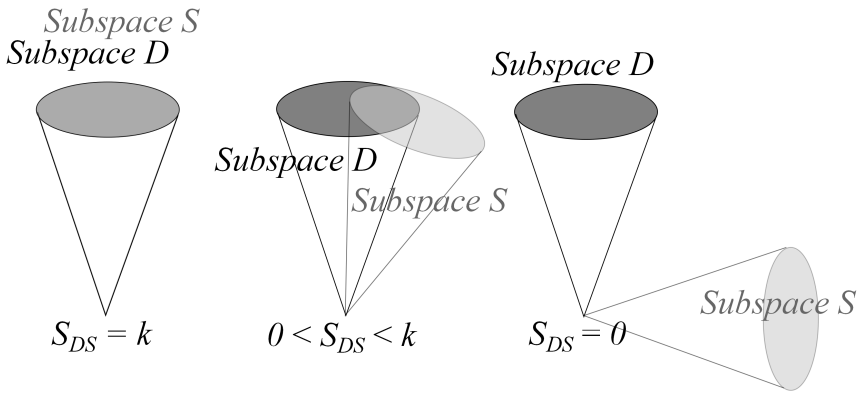

Figure 5.3: Similarity concept between subspaces

Selecting the dimensions (K_d and K_s) of the subspaces is crucial in the classification performance. These dimensions are set taking into account the eigenvalues in Λ_D and Λ_S respectively since they reveal the information gathered by each eigenvector: the higher the eigenvalue, the higher the amount of information of the target contained in its associated eigenvector.

5.2.2. Novel subspace methods

In this section, the conceived new methodology based on the previous subspace methods is explained. Three algorithms are developed, two based on the angle between vector and subspace and another based on the mutual subspace method. The added functionalities are based on the accumulation of the obtained angles and on the weighting of the subspace vectors in order to make classification in a fairly way.

5.2.2.1. Cumulative angle between subspaces

Let $X_D \in \Re^{N\times M}$ be a matrix of consecutively collected HRRPs that form the test set, and let $X_S \in \Re^{N\times M}$ be a matrix of range profiles included in the training set, that is, in the database of potential targets, with M being the total number of profiles and N the number of range bins. After applying SVD to X_D and X_S, the respective matrices of singular values and singular vectors are obtained.

$$\begin{aligned} X_D &= U_D \cdot \Sigma_D \cdot V_D^T \\ X_S &= U_S \cdot \Sigma_S \cdot V_S^T \end{aligned} \tag{5.14}$$

Since HRRPs present the target reflectivity into the range domain, only the left singular vectors, $U_D = [u_{D_1}, \ldots, u_{D_N}]$ and $U_S = [u_{S_1}, \ldots, u_{S_N}]$, will be used in the identification process. As section 5.1.1 introduced, taking into account the singular values and setting an energy threshold η as in equation 5.5, the *signal subspace* of each dataset is defined as the K most significant u_i singular vectors, while the *noise subspace* is discarded.

In order to clarify the metrics, let us graphically introduce the simplified concept of subspace division and angle between subspaces shown in the example of Figure 5.4.

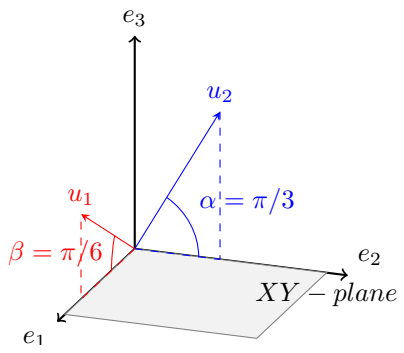

Figure 5.4: Angle between subspaces

Let vectors e_1, e_2 and e_3 in Figure 5.4 be the left singular vectors, as defined in equation 5.1, obtained after applying SVD to an input sample of the test set, $X_D \in \Re^{3\times 3}$, that is $U_D = [e_1, e_2, e_3]$. Imagine that the threshold to select the *signal subspace*, η, is set to 0.95. Assuming that according to their associated singular value the 95% of the energy is focused on e_1 and e_2 and following equation 5.5, then these are defined as the $K_d = 2$ first left singular vectors that form the bases of the *signal subspace*, while e_3 is discarded; hence, the *signal subspace* of this example corresponds to the XY plane.

Let C be the total number of aircraft classes. For an input test sample, there exist $c = 1, \ldots, C$ different aircraft to which it will be compared. Then, the training set associated with each class is defined as X_S^c. After the application of SVD to the training set $X_S^c \in \Re^{3\times 3}$, the left singular vectors

obtained for an aircraft class c are $U_S^c = [u_1, u_2, u_3]$. For the same reason as before (the energy threshold) vector u_3 is discarded and, for simplicity it is not displayed in the figure.

The angle between these remaining singular vectors of the matrices U_S^c, and the projection onto the test set *signal subspace* is obtained in order to know their level of dependency and to decide the class of aircraft, c, to which the test sample belongs. In order to do so, the principal angle between each singular vector and the test set *signal subspace* is found, as described in section 5.2.1.

In the figure, it can be seen that u_1 is closer to the XY plane than u_2, in this example the angle found for u_1 is $\beta = \pi/6$ and the angle found for u_2 is $\alpha = \pi/3$; note that the smaller the angle, the closer to the subspace.

Denoting $\widehat{X}_D \in \Re^{N \times K_d}$ as the *signal subspace* of the test set containing its K_d first left singular vectors and u_i^c as the ith left singular vector of the training set corresponding to target c; function F_u^c, given by equation (5.15), is defined as the accumulated angle between a singular vector u_i^c in the training set and the *signal subspace* of the test set, where $\angle(\widehat{X}_D, u_i^c)$ is the principal angle between the test set *signal subspace* and each singular vector of the training set [108, 112].

$$F_u^c(k) = \sum_{i=1}^{k} \angle(\widehat{X}_D, u_i^c) \text{ ; with } k = 1, \ldots, K_d \text{ and } c = 1, \ldots, C \tag{5.15}$$

The metric F_u^c shows the evolution of the angle formed by each synthetic singular vector and its projection onto the *signal subspace* resulting in a monotonically increasing function. Figure 5.5 depicts an example of the results originated by this function. In this example, the input sample is a matrix of range profiles corresponding to a B747 and 7 classes of aircraft compose the training set. The threshold taken for the selection of the *signal subspace* is in this example $\eta = 0.95$, yielding in 100 range profiles forming the signal subspace for this case[3]. As said, since F_u is a cumulative function, it has a monotonic increasing tendency clearly evident in the figure. The class of the recognized aircraft, C_r, will be that with the lowest final value of F_u^c, that is $F_u^c(K_d)$, as equation 5.16 denotes. However, in the case of the example depicted in Figure 5.5 the recognition result will be erroneous since the identified aircraft C_r is not the true class of the test sample.

$$C_r = \arg\min_c (F_u^c(K_d)) \tag{5.16}$$

5.2.2.2. Weighted cumulative angle between subspaces

In the case of function F_u^c, the projected angle of every singular vector in the training set contributes equally to the final result, *i.e.*, singular vectors are equally important, and probably that is one of the reasons that contribute to the erroneous recognition result in the previous example of Figure 5.5.

Imagine now that our training set consists of $C = 2$ different aircraft, A and B, and let vectors u_1, u_2 and u_3 in Figure 5.4 be the left singular vectors obtained for these aircraft after applying SVD to their respective matrices of range profiles, such that:

$$aircraftA = \begin{cases} U_S^A = [u_1^A, u_2^A, u_3^A] = [u_1, u_2, u_3] \\ \Sigma_S^A = diag(\sigma_1^A, \sigma_2^A, \sigma_3^A) = diag(0.8, 0.15, 0.05) \end{cases}$$

[3] In the next chapter a complete study for the threshold selection will take place, the value of $\eta = 0.95$ is selected here just as an example

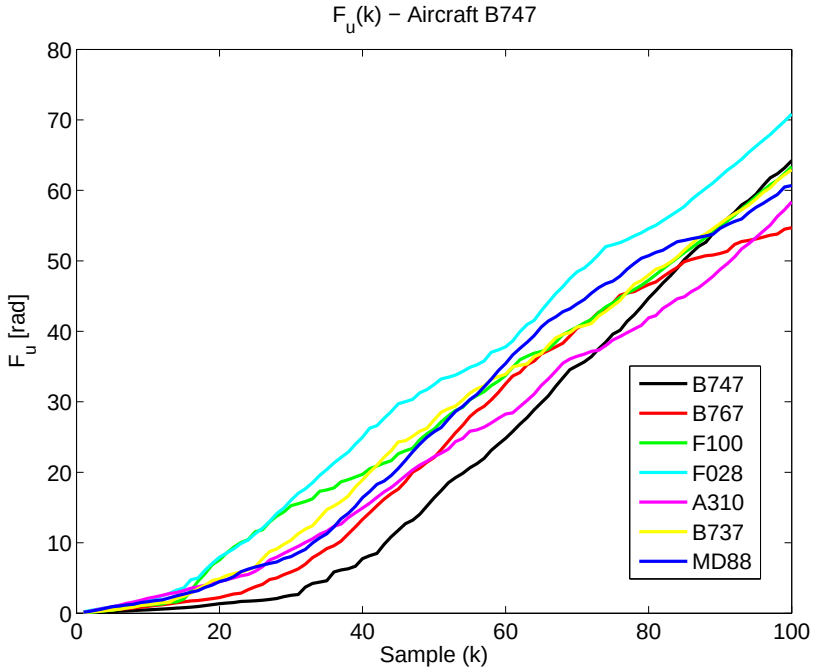

Figure 5.5: F_u results for the recognition of a B747

$$aircraftB = \begin{cases} U_S^B = [u_1^B, u_2^B, u_3^B] = [u_2, u_1, u_3] \\ \Sigma_S^B = diag(\sigma_1^B, \sigma_2^B, \sigma_3^B) = diag(0.85, 0.10, 0.05) \end{cases}$$

where the superscript represents the aircraft class c ($c = A, B; C = 2$) to which the singular vectors and singular values are related. Taking $K_d = 2$ as before, with the application of function F_u^c there would be confusion in the identification result since:

$$F_u^A(K_d) = F_u^B(K_d) = \pi/3 + \pi/6$$

However, the singular values have revealed that not all singular vectors in the training set have the same importance since the energy is focused on the top ones. This means that the obtained canonical angle between the singular vectors u_i^c and the signal subspace $\widehat{X}_D$ should be weighted in a way that the singular value, σ_i^c, associated with u_i^c sets the importance of this angle in the final solution. For instance, principal angles of $\pi/2$ mean that the singular vector is orthogonal to the subspace. Thus, obtaining results of this order when u_i^c is associated with a high singular value mean that the aircraft to be recognized will not, for sure, belong to that class. On the contrary, if an angle of $\pi/2$ is obtained with a vector with a very low singular value it will not contribute to a great extent to the final solution and therefore, it will not be involved in the identification decision. According to this, function F_u^c is modified in order to add some kind of weighting to the angles between subspaces found.

Function F_w^c given in equation 5.17 returns the accumulated weighted angle F_w^c between the *signal subspace* of the test matrix and the singular vectors u_i^c for each synthetic aircraft c in the training set.

$$F_w^c(k) = \frac{1}{\sum_{j=1}^{K_d} \sigma_j^c} \sum_{i=1}^{k} \sigma_i^c \cdot \angle(\widehat{X}_D, u_i^c) \text{ ; with } k = 1, \ldots, K_d \text{ and } c = 1, \ldots, C \tag{5.17}$$

In equation 5.17, $\sigma_{i,j}^{c}$ are the k-th first singular values associated to each synthetic aircraft in the training set and, as in equation 5.15, $\angle(\widehat{X}_D, u_i^c)$ is the principal angle between the test set *signal subspace* and each singular vector of the training set. Finally, the algorithm decides the test sample belongs to the target that minimizes the cost function 5.17, that is:

$$C_r = \arg\min_{c}(F_w^c(K_d)) \tag{5.18}$$

In the previous example, in contrast to F_u^c, the application of equation 5.17 would result in the identification of aircraft A since:

$$\left.\begin{array}{l} F_w^A(K_d) = \frac{1}{0.95} \cdot (0.8 \cdot \frac{\pi}{6} + 0.15 \cdot \frac{\pi}{3}) \\ F_w^B(K_d) = \frac{1}{0.95} \cdot (0.85 \cdot \frac{\pi}{3} + 0.10 \cdot \frac{\pi}{6}) \end{array}\right\} F_w^B(K_d) > F_w^A(K_d)$$

Figure 5.6 depicts an example of the identification curves obtained with function F_w^c for the same B747 measurement as the previous Figure 5.5. As seen, the curves also have a monotonically increasing tendency until they eventually reach a point of saturation; from that point on, the synthetic singular vector u_i^c, due to its corresponding singular value, does not add almost any new information to the recognition process and the solution stabilizes. In this case, the recognition is successful, the aircraft B747 is the one that minimizes equation 5.17.

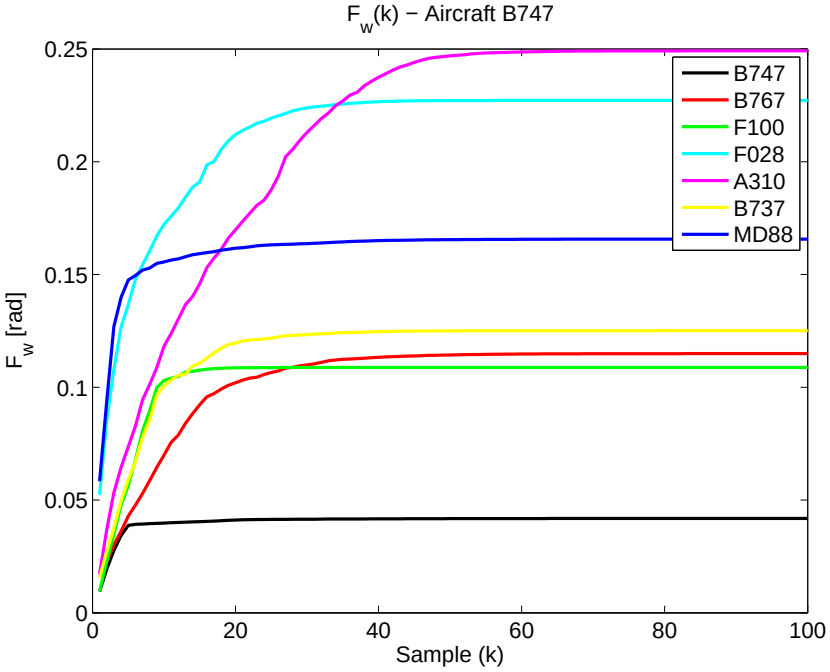

Figure 5.6: F_w results for the recognition of a B747

5.2.2.3. The generalized Mutual Subspace Method

The *generalized Mutual Subspace Method (gMSM)* is based on the MSM, which has been previously presented in section 5.2.1 and widely used along the years in image recognition.

However, the main problem of MSM (and many subspace methods, like the previous ones) is the selection of the appropriate dimension of the subspaces (K_d for algorithms F_u and F_w, and K_d and K_s

for MSM). In order to palliate this, Kobayashi [114] introduces the concept of *softweighting* for image identification and proposes a generalized Mutual Subspace Method. Contrary to his study in which gMSM is applied to static 2D images for object classification, here this method will be used for identification of flying aircraft from range profiles, which, to the author knowledge, the method is used in this thesis for the first time with this purpose.

In MSM algorithm as well as in the previous methods, when setting the dimensionality of a subspace, the eigenvalues take an important role: only the eigenvectors with the highest eigenvalues will be considered as basis and the rest will be discarded. The eigenvalues can be seen as if they had a binary weight (1/0) that affects the eigenvectors. A weight of 1 means that the corresponding eigenvector is a basis of the subspace and a weight of 0 means the opposite. That is, the subspace dimensionality is set based on a binary decision. Nevertheless, in MSM, as happened in F_u, the eigenvalue *per se* does not take part in the identification algorithm, meaning that all the eigenvectors that have been chosen as bases have the same relevance in the subspace construction.

The concept of *softweighting* tries to avoid this binary decision, that is, the selection of the subspace dimension is no longer needed. *Softweighting* gives importance to all the eigenvectors, in a way that all the eigenvectors will take part in the subspace but they will be weighted by a transformed value of their corresponding eigenvalues. This transformed value is called the *softweight*. According to equation 5.6, if $\Lambda_D = diag(\lambda)$ are the eigenvalues of matrix $X_D \cdot X_D^T$ in descending order, the design of the *softweights* is done in consonance with these eigenvalues. Let $\Omega = diag(\omega) \in \Re^{N \times N}$ be a diagonal matrix of *softweights* such that:

$$\omega = w_m(\lambda) = \min\left[\frac{\lambda}{\lambda_m}, 1\right] \tag{5.19}$$

where λ_m is the m-th eigenvalue in Λ. This *softweighting* evaluates the importance of each eigenvector as a basis in the subspace by the variance relative to λ_m. The m first values of the diagonal matrix Ω will be the unity and the rest will be proportionally decreasing with the m-th eigenvalue. Figure 5.7 illustrates an example of the resulting *softweights* of a matrix of eigenvalues when m is set to 4 and to 1. As seen, in the dashed line, the first 4 values are equal to unity while the rest slowly decrease proportionally to the 4th eigenvalue. On the contrary, the dotted line shows the decreasing tendency of the *softweights* in relation to the first eigenvalue.

By adding the *softweights* to (5.12), the importance of each eigenvector as a basis of the subspace is set. Then, the gMSM is defined as:

$$\cos\theta_k = \max_{y^T\Omega_D^{-2}y=1;\, z^T\Omega_S^{-2}z=1} \max y^T \cdot (V_D^T \cdot V_S) \cdot z \Longleftrightarrow \max_{y'^T \cdot y'=1;\, z'^T \cdot z'=1} \max y'^T \cdot (\Omega_D \cdot V_D^T \cdot V_S \cdot \Omega_S) \cdot z' \tag{5.20}$$

where $y = \Omega_D \cdot y'$, $z = \Omega_S \cdot z'$ and V_D and V_S are the eigenvectors as in equation 5.6. Eventually, the generalized canonical angles that define the similarity measure are computed by applying SVD to $\Omega_D \cdot V_D^T \cdot V_S \cdot \Omega_S$, that is:

$$\Omega_D \cdot V_D^T \cdot V_S \cdot \Omega_S = U' \cdot \Theta \cdot V'^T \Longrightarrow S_{DS} = tr(\Theta^2) \tag{5.21}$$

As in MSM, the similarity is defined as the sum of the canonical angles' cosines, and finally, the algorithm will identify the class of the aircraft as the one with the highest similarity, that is:

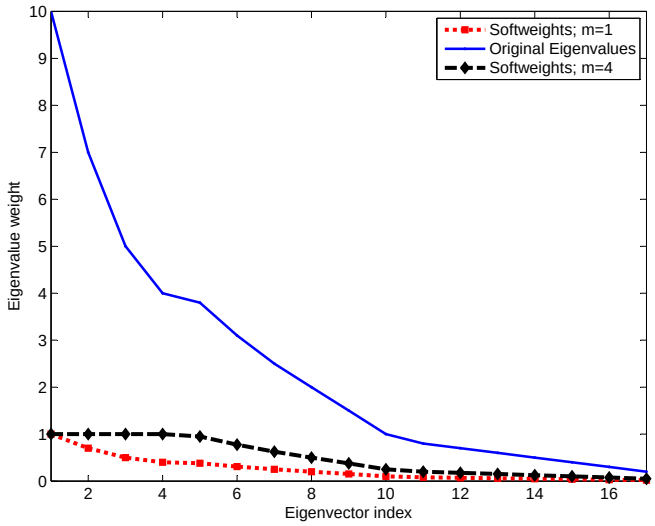

Figure 5.7: *Softweighting* of eigenvalues

$$C_r = \arg\max_c (S^c_{DS}) \tag{5.22}$$

5.3. Conclusions

In this chapter, the different algorithms that will be utilized for classification of range profiles have been deduced, F_u, F_w and gMSM. The three of them are based on the previous extraction and definition of subspaces and the angle between them. For the subspace definition it has been noted that PCA is a powerful tool which permits to extract the bases that span the signal subspace while reducing dimensionality. As said in Chapter 2, PCA can be applied via eigendecomposition or SVD. Due to the higher stability of results, SVD is mainly chosen in the three algorithms, although for gMSM both eigendecomposition and SVD are applied.

After the definition of the first algorithm, F_u, which accumulates angle between subspaces, it has been noted that the singular values have an important role in the definition of these subspaces and hence, they must be included in the recognition process. The weighted cumulative angle between subspaces (F_w) is therefore an evolution of F_u. This way, F_w introduces the singular values of the training set weighted by their total sum, in order to try to improve the results. The main issue of these algorithms lie in the selection of the dimensionality of the subspaces, which is usually defined experimentally. Therefore, finally, an upgraded method is defined, the gMSM, that makes use of the eigenvalues of both the test and training sets while no need to set the subspace dimensionality exists; in this last method, the eigenvalues are weighted to construct a matrix of *softweights* that will be involved in the recognition process. However, the definition of this matrix depends upon the m-th eigenvalue, which must be selected, therefore, although the need for the subspace dimensionality has been eliminated, a new parameter has arisen, the *softweighting* parameter m.

In the following chapter, the three algorithms will be applied to the datasets introduced in Chapter 4. As seen, although they are quite related, each algorithm has its properties and its parameters that should be tuned to obtain good results. Therefore, a study on the optimum parameters for each one will be presented and also their performance and their robustness will be evaluated.

Chapter 6

Experiments and Results

Previously, the preprocessing steps carried out for the improvement of actual range profiles, the extraction of their main features and the algorithms developed for their classification have been explained. In the present chapter, all this knowledge will be applied to different experiments defined in order to validate the algorithms developed in this thesis.

Chapter 4 introduced the different datasets available for the experiments, these datasets were divided into two groups, range profiles coming from the ORFEO measurement campaign, that is, the actual range profiles, and range profiles that were predicted in the same trajectories as the actual profiles using a CAD model and an RCS-prediction code, that is what we have called, the synthetic profiles.

One of the goals of this thesis is to develop algorithms able to determine with fidelity the aircraft type of an actual flying target using only a database of synthetic range profiles. Then, as noted in the previous chapters, the given datasets (actual and synthetic) will exhibit many discrepancies. In order to accomplish this task three algorithms have been developed and explained in Chapter 5, hence, the purpose of this chapter is to define a series of experiments to check the validity of the algorithms and to select the best parameters for our study. However, before proceeding to the classification of actual aircraft, it is recommended a first study on the identification of predicted profiles. Therefore, here, for a complete study, incremental test cases will be defined: first, the ideal test case where synthetic profiles are identified is analyzed; after that, the identification of synthetic profiles corrupted with unwanted effects that may occur in an actual scenario is performed, and lastly, the results for the identification of actual profiles are provided. The intention of this incremental study is the validation of the proposed algorithms, this way, if recognition performance is not acceptable at some point before the recognition of actual profiles, the algorithm can be discarded straightaway.

Once again, it should be remembered that for simplicity, the database of potential targets is called here training set, while the test set comprises the samples to be identified.

6.1. Test Cases Definitions

In this section, as said, the definition of the different test cases and subcases proposed to validate the algorithms are explained.

6.1.1. Test Case I

Test Case I consists of 20 trajectories taken from the ORFEO measurement campaign, depicted in Figure 6.1a. As seen, the selected trajectories present a variety of aspect angles, they include some nose-on, tail-on and broadside aspect angles, which are representative of the different attitudes of an aircraft.

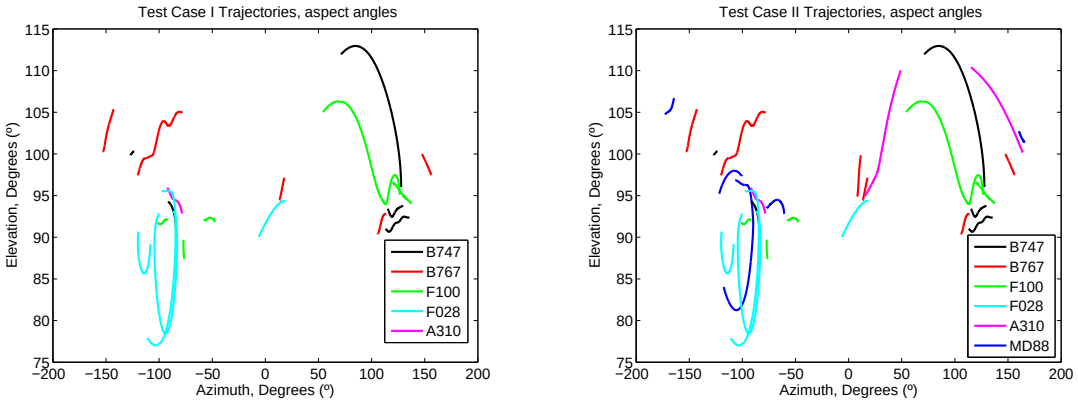

(a) Test Case I - Trajectories of the test set

(b) Test Case II - Trajectories of the test set

Figure 6.1: Sets of aircraft trajectories

These trajectories have been divided into 48 frames, which comprise from 100 up to 300 range profiles consecutively collected in time and amplitude normalized. The criteria for dividing the trajectories was that the aircraft cannot have a change of more than 4° in elevation. These frames will compose the test set and will be classified as a whole, and the training set, will be divided the same way.

The experiments carried out under Test Case I will have as test set the aircraft A310, B747, B767, F100 and F028; the training set will consist of aircraft A310, B747, B767, F100, F028 and B737. Since 5 aircraft will be compared to a database of 6 aircraft, this means that there is one aircraft in the database (the B737) that only adds confusion in the recognition problem. As seen in Chapter 4, the B737 has similar length to F028 and F100 but the distribution of its engines is like the A310 or the B767, therefore it can cause confusion in the recognition of these aircraft.

6.1.2. Test Case II

Test Case II increases the number of trajectories and aircraft to be identified. These can be seen in Figure 6.1b. In this case 28 trajectories are considered and 6 aircraft (A310, B747, B767, F100, F028 and MD88) will be classified using a database of 7 aircraft (A310, B747, B767, F100, F028, MD88 and B737).

In Test Case II the trajectories are divided into frames that cover a variation of 2.5° in azimuth at the most. A total number of 235 frames are obtained in this case. With this segmentation, more test samples are obtained so the evaluation of the algorithms gets more accurate. Even though the frames will contain less profiles than the ones of Test Case I, they still represent the evolution of the profiles in a moving target.

6.1.3. Subcases Definitions

In order to provide an incremental study of the algorithms several subcases are defined for each Test Case:

a. Synthetic profiles Vs. Synthetic profiles. The starting point for any classifier is to firstly validate it with simulations, this way, if the classifier did not provide good results, it would be worthless to continue with the process. Therefore, in this first subcase the test set will comprise exactly the same synthetic profiles as the training set.

Figure 6.2 is given as an example of the matrices of normalized range profiles that comprise both the test and training sets. In this example the test sample, a matrix of synthetic range profile from a B767 is being classified utilizing a database of 3 training samples corresponding to aircraft A310, B767 and F100. As expected, both sets comprise ideal data, the synthetic range profiles are very clean signatures of aircraft and accordingly, since both the test and the training sets are of the same high quality, the recognition results are expected to be very good, near to recognition rates of 100%.

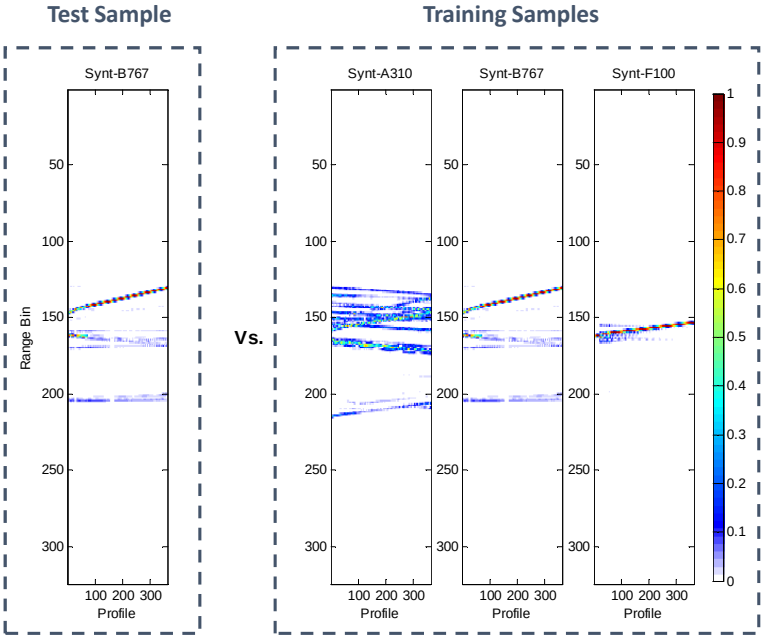

Figure 6.2: Synthetic profiles vs. Synthetic profiles

b. Synthetic profiles + *Additive White Gaussian Noise (AWGN)* Vs. Synthetic profiles. The next step will be to start degrading the synthetic profiles in the test set by adding noise. It is common the addition of complex white gaussian noise, with its modulus being Rayleigh distributed and its phase uniform distributed [115]. In order to fairly corrupt the predicted profiles given by FASCRO, the gaussian noise is added to the raw data, in the frequency domain, as if the radar would have collected the noisy signal. That is, as Figure 6.3 depicts, before the Hamming windowing and IFFT transformation.

The addition of noise implies that the HRRPs in the test set will still be ideal since they still are synthetic profiles, but they will start differing from those in the database as in an actual scenario. Hence, this is the first step to approach the final purpose of this text, which is the comparison of very different HRRPs.

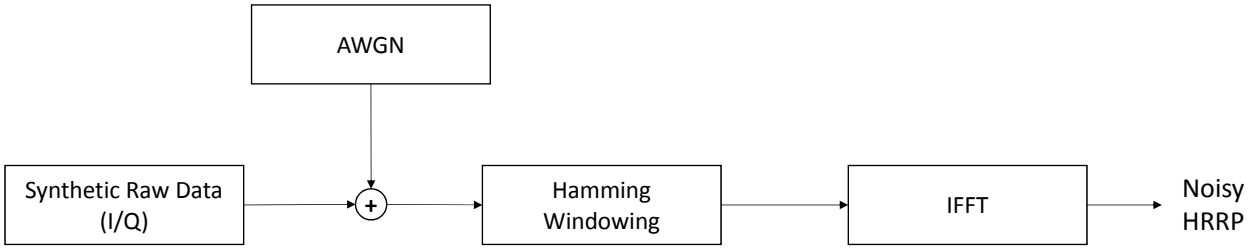

Figure 6.3: Noise addition to synthetic range profiles

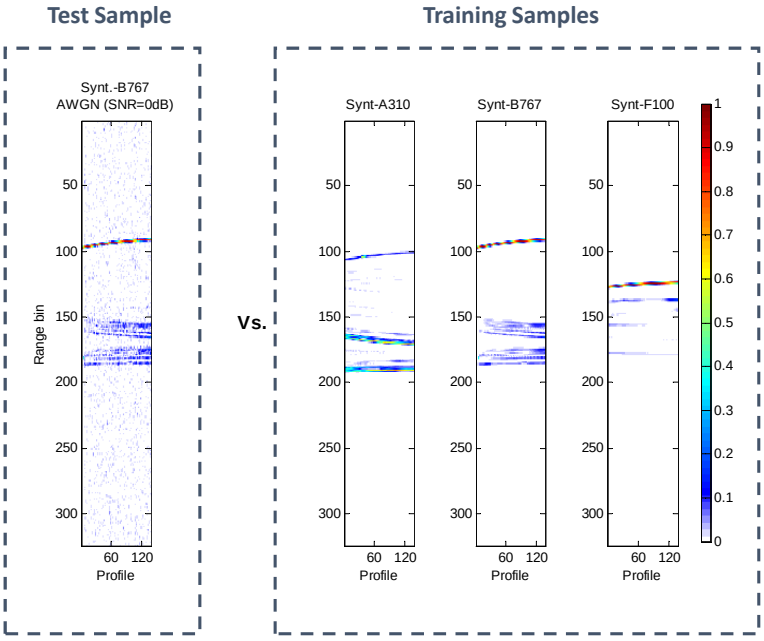

Figure 6.4: Synthetic noisy profiles vs. Synthetic profiles

Figure 6.4 depicts an example of the matrices of normalized range profiles that comprise both the test and training sets. In this example a synthetic matrix of range profiles with additional noise such that SNR = 0 dB is being compared with a database of three synthetic matrices of range profiles, all of them normalized such as their energy equals 1. The idea of this experiment is to check the robustness against noise of the proposed algorithms. The values of the resulting SNR for the added noise are summarized in Table 6.1.

c. Synthetic profiles + AWGN + misalignment + alignment Vs. Synthetic Profiles. In order to simulate an even more actual scenario where profiles suffer from TRM, noisy synthetic profiles are shifted a few samples. Remember that this effect is caused by the translational motion of an aircraft, which causes a change in the distance to the radar and hence, scatterers are displaced from one range bin to the next. Therefore, in order to imitate this, each profile in a frame has been shifted 3 range bins with respect to the previous profile. After the misalignment, just as if they were actual profiles, they need to be further aligned again, as subsection 4.1.1 described, to compensate this synthetic translational motion. The flow chart of this procedure is depicted in Figure 6.5, and an example of how a matrix of range profiles with an SNR = 5 dB has been misaligned and further aligned before normalization takes place is illustrated in Figure 6.6.

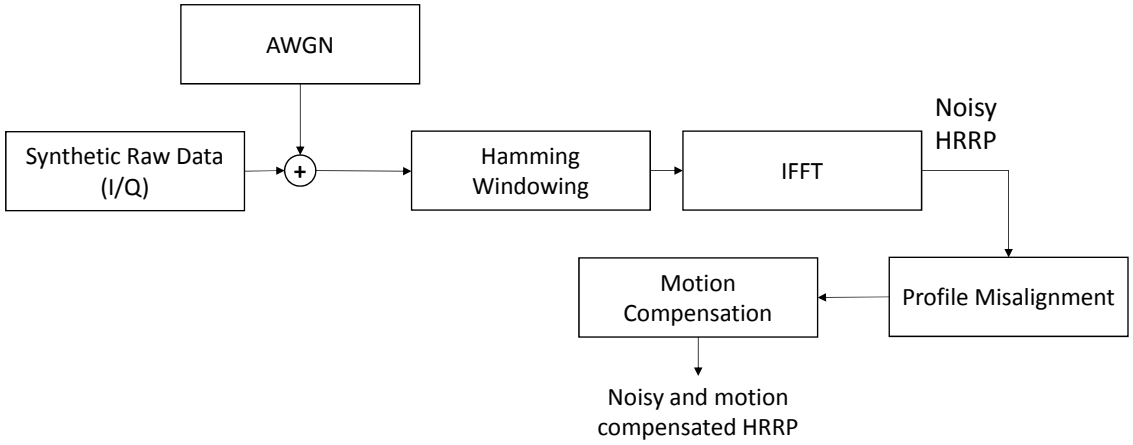

Figure 6.5: Noise addition, misalignment and motion compensation of synthetic range profiles chart

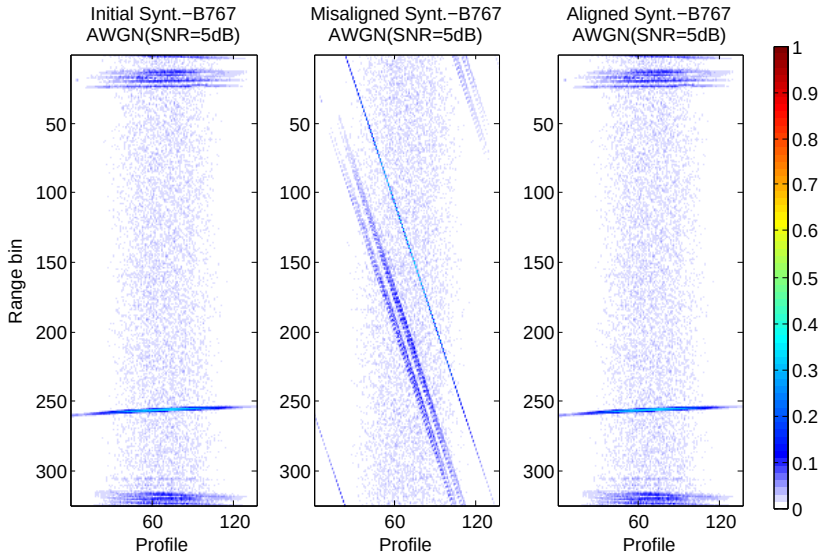

Figure 6.6: Example of noise addition, misalignment and motion compensation of a matrix of synthetic range profiles

d. Actual profiles Vs. Synthetic profiles. Finally, after checking with the previous subcases the preliminary robustness against noise and TRM of the different algorithms, the actual profiles from the ORFEO measurement campaign are classified using a database of synthetic profiles.

Figure 6.7 is an example of the comparison of a matrix of normalized actual range profiles of a B767 with a database of normalized synthetic profiles which comprises three different aircraft in the same trajectory. One more time, the difference in nature of the profiles is clearly noticeable in the figure, while actual profiles are corrupted with noise, speckle, TRM, etc., synthetic profiles are much more clear since they are the ideal signature of an aircraft. Finally, Table 6.1 summarizes the properties of all the defined subcases.

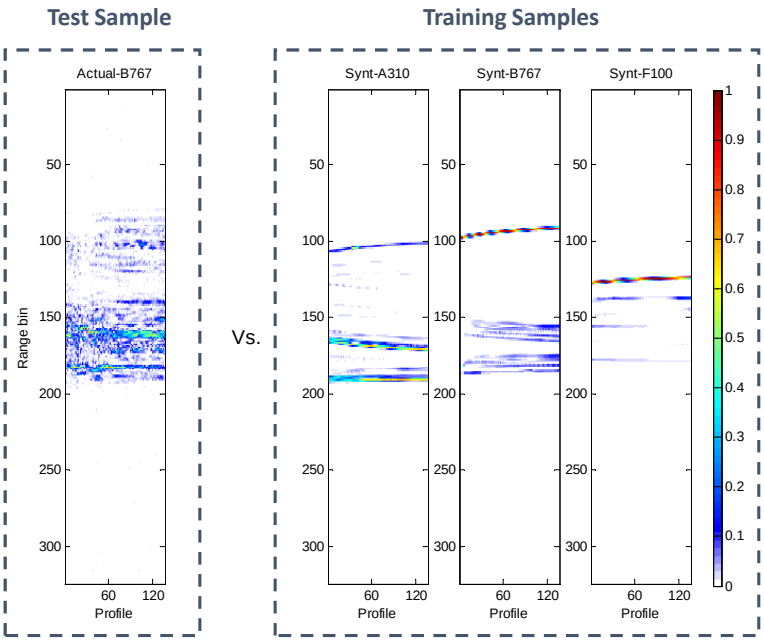

Figure 6.7: Actual profiles vs. Synthetic profiles

Table 6.1: Subcases specifications

	Test Set	Added effects	Training Set
Subcase a	Synthetic	None	Synthetic
Subcase b	Synthetic + AWGN	AWGN(SNR(dB)): 10;5;0;-5;-10	Synthetic
Subcase c	Synthetic + AWGN + TRM	AWGN(SNR(dB)): 10;5;0;-5;-10	Synthetic
Subcase d	Actual	None	Synthetic

6.2. Experiments Definitions

6.2.1. Energy Threshold

The proposed algorithms presented in Chapter 5, are all based on a distance metric, the angle between subspaces. The first two proposed algorithms, the cumulative angle between subspaces, F_u, and the weighted cumulative angle between subspaces, F_w, since one is an evolution of the other, have in common the need of setting the subspace dimensionality in advance according to a defined threshold, η, as equation 5.5 showed and reproduced here as equation 6.1 for clarity.

$$\frac{\sum_{i=1}^{K} \sigma_i}{\sum_{i=1}^{p} \sigma_i} \geq \eta \tag{6.1}$$

The threshold is set experimentally according to the energy provided by the singular values of the test set, therefore, a study of the evolution of the recognition results when varying the energy threshold is needed to select the appropriate one for the best results. Remember that when the energy threshold is modified, the *signal subspace* changes accordingly: the higher the threshold η, the higher the value of K, that is, the higher the number of singular vectors that form the *signal subspace* and the smaller the number of singular vectors discarded since they are considered as *noise subspace*. Thus, it is expected

that if a very low threshold is selected (near to 0), the signal subspace will not have enough information to properly classify the profiles, while if it is very near to 1, the signal subspace will wrongly include too many vectors that do not provide information for a good classification but include unwanted noise.

In this experiment, the energy threshold, η, is varied from 0.1 to 0.99, with steps of 0.1 for $\eta = 0.1, \ldots, 0.8$, and 0.05 for $\eta = 0.85, \ldots, 0.99$. Normalization of the profiles is accomplished by applying a L2-norm, just as said in Chapter 4 and both metrics, F_u and F_w are analyzed.

In the following subsections, the recognition results for these metrics for test cases I and II and their respective subcases when the energy threshold, η is varied, are presented.

6.2.1.1. Test Case I. Results

In this test, 48 frames are classified; in the case of Test Cases I.a to c, since we have simulations for the 5 input aircraft, then 240 input samples[1] will be available for classification; on the contrary, the test set of Test Case I.d will comprise only 48 frames of different aircraft (the ones that were truly measured in the ORFEO campaign among the 5 aircraft that form the test set). A matrix of HRRPs consecutively collected in time or synthetically obtained (depending on the subcase), motion compensated and normalized (L2-norm) will be the input of the classifier, while the database (the training set), will comprise the prediction of the range profiles of 6 aircraft for the very same trajectory.

In order to provide examples of the partial results obtained before the final recognition rates are presented, a given trajectory is selected. This trajectory, taken from the ORFEO measurement campaign, is the one depicted in Figure 6.8, named as trajectory p14.0 which belongs to a Fokker28. As seen, this trajectory covers a nose-on aspect angle[2] and comprises a total number of 226 profiles of 324 range bins each (matrices of 324×226). Along this chapter, all the provided partial results will be referred to this aircraft in this trajectory.

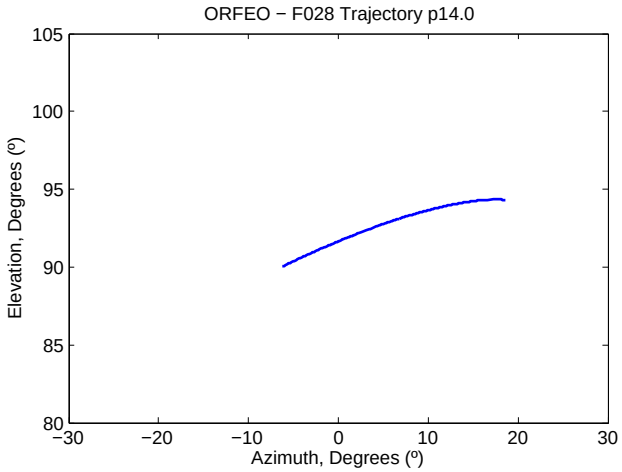

Figure 6.8: Trajectory p14.0 used as example

Test Case I.a. Synthetic Profiles Vs. Synthetic Profiles

The first step for any research is the study of an ideal case, here this translates into the classification of synthetic profiles with a database of profiles of exactly the same nature. Figure 6.9a shows the matrix of synthetic profiles of the Fokker28 taken as example and, since the feature extraction for F_u and F_w

[1] 48 frames $\times$ 5 aircraft = 240 matrices of range profiles
[2] Nose-on aspect angle: azimuth $\alpha \sim 0°$; elevation $\theta \sim 90°$

involves the extraction of singular values and singular vectors, figures 6.9b to 6.9d depict its SVD. Note that only the first 100 singular values have been depicted for simplicity, but the decreasing tendency is clearly noticed. As said, the left singular vectors in matrix U will be those utilized along with their associated singular values.

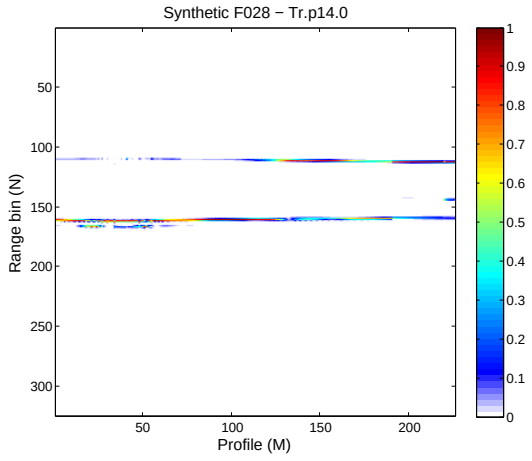

(a) Matrix of range profiles

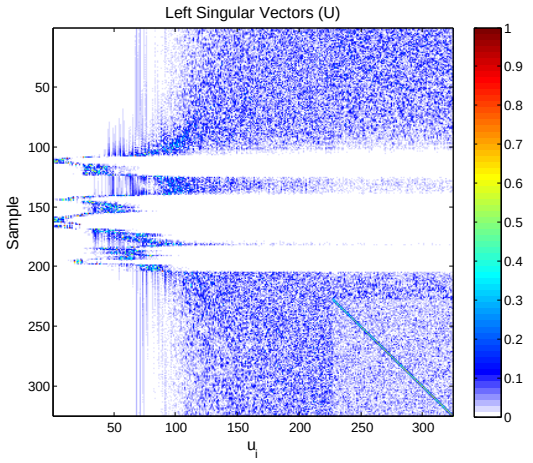

(b) U-Singular vectors (absolute value)

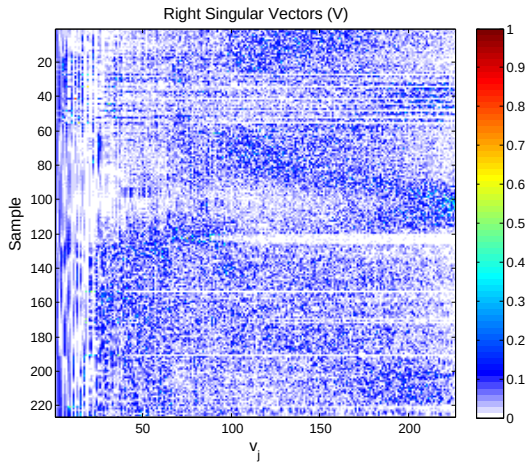

(c) V-Singular vectors (absolute value)

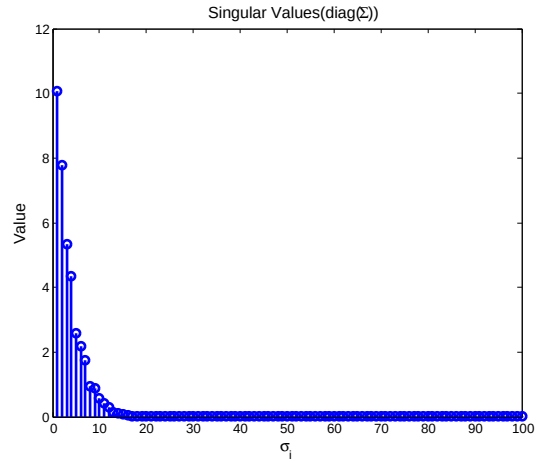

(d) Σ-Singular values

Figure 6.9: Test Case I.a. SVD of trajectory p14.0

The singular values in Figure 6.9d show that, at first glance, the energy is concentrated approximately around the first 15 or 20 singular vectors with the rest having a negligible value. Indeed, as matrix U depicts in Figure 6.9b, only the first 15 or 20 vectors u_i show a clean behaviour, while the rest seem to be very noisy. The goal of the energy threshold η is therefore, to select the number, K, of singular vectors, u_i, that focus a specific amount of energy, in order to define the *signal subspace*. As noted in Chapter 5, matrix V, showed in Figure 6.9c will not be used along this experiments.

Thus, when changing the energy threshold, the singular vectors of the test set that will form the *signal subspace* will change accordingly. As an example, Table 6.2 shows, for the F028 in the example trajectory, the evolution of the number of vectors taken as subspace for both algorithms, F_u and F_w. The 99% of the total energy is focused on the 13 first singular vectors and according to the table, the first singular vector holds approximately the 20% of the total energy in this example. Note that for each input matrix, these values will be different since each aircraft has a different SVD.

Subcase a. is clearly special since the test set and training set are exactly the same; this means that

Table 6.2: Test Case I.a. Evolution of the signal subspace dimensionality with η. Trajectory p14.0

Energy Threshold (η)	**0.99**	**0.95**	**0.9**	**0.85**	**0.8**	**0.7**	**0.6**	**0.5**	**0.4**	**0.3**	**0.2**	**0.1**
Dimensionality (K)	13	9	7	6	6	4	3	3	2	2	1	1

profiles of exactly the same SNR and highly ideal are compared to each other and therefore, very high recognition rates are expected. Table 6.3 shows these recognition rates obtained for metric F_u changing the energy threshold of the *signal subspace*; exactly the same recognition results are obtained for F_w. Taking a look at the results on the table, it is noticed that even if the energy threshold changes and the number of vectors taken as *signal subspace* varies, the totality of the test set input matrices is correctly classified to their corresponding aircraft and this is due to the high idealism of both sets. Therefore, both algorithms have passed the first test, if they had not obtained 100% of success rates, it would be worthless to continue with their assessment.

Table 6.3: Test Case I.a. F_u and F_w Recognition rates

Test Case II.d. Recognition rates varying η (%)		
η	F_u	F_w
0.99	100	100
0.95	100	100
0.9	100	100
0.85	100	100
0.8	100	100
0.7	100	100
0.6	100	100
0.5	100	100
0.4	100	100
0.3	100	100
0.2	100	100
0.1	100	100

Remember that in F_u and F_w the angle between each singular vector of the training set and the selected *signal subspace* of the test set is computed; Figures 6.10a and 6.10b depict the evolution of this angle for trajectory p.14.0 and an energy threshold $\eta = 0.9$. The recognised aircraft will be the one with the minimum final value of each metric, and as Figure 6.10 shows for both metrics, with $\eta = 0.9$, this aircraft is the Fokker28. In the case of selecting other value of η the curves will differ, but as seen, due to the idealism of this subcase, the right recognition is always achieved (the F028). As previously said, these curves tend to increase, but as seen in the preceding chapter, the evolution of F_w saturates due to the appearance of the singular values as weighting elements in the function, making the results more stable.

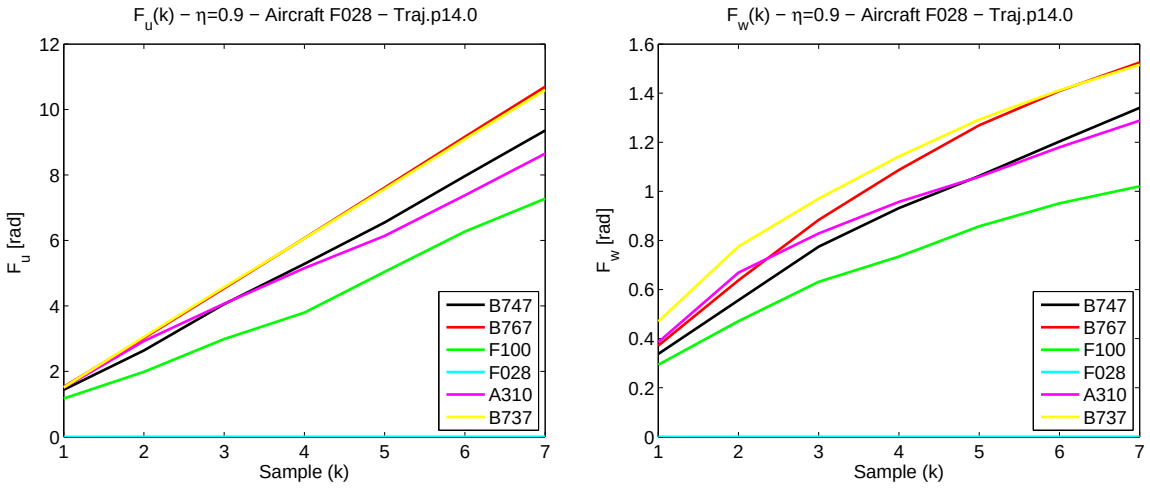

(a) F_u results for p14.0

(b) F_w results for p14.0

Figure 6.10: Test Case I.a. F_u and F_w partial results for F028; trajectory p14.0; $\eta = 0.9$

Test Case I.b. Synthetic Profiles with AWGN Vs. Synthetic Profiles

As the results of the preceding subcase have shown, due to the idealism of the scenario, the obtained recognition rates are also ideal, that is, the 100% of the input samples have been correctly classified. The present subcase tries to simulate a first approach where the test and training sets differ; therefore the expected recognition rates will not be as high as the ones obtained for Test Case I.a.

Figure 6.11a shows the matrix of synthetic profiles of the Fokker28 taken as example (trajectory p.14.0) with AWGN such that the resulting SNR = -5 dB and figures 6.11b to 6.11d its SVD. As appreciated in Figure 6.11a, around profile number 100 the noise is apparently more prominent, however, this effect is caused by the normalization of the profiles, which causes a normalization in the energy of each profile. As noted, not only the addition of noise has affected the shape of the matrix of range profiles, but also its SVD has changed. The singular values have been degraded and apparently, the singular vectors have also been distorted by the noise; this distortion has caused an increase in the value of those singular values that without noise had a nearly null weight, while decreasing the weight of the first ones. This will cause a change in the division into *signal* and *noise subspaces* as illustrates Table 6.4. Similar to the previous subcase, the evolution of the number of vectors taken as subspace for both metrics F_u and F_w is shown in the table; note that the results are shown for SNR = -5 dB and this noise is added randomly, so here it is presented just an example of the values to illustrate the variation of the *signal subspace* dimensionality with the addition of noise.

Due to the degradation of the range profiles, the *signal subspace* has also been corrupted. Taking a look at both Table 6.2 and Table 6.4 it is clearly seen that, with a low SNR (SNR = -5 dB), if the chosen energy threshold is the highest ($\eta = 0.99$), the number of vectors taken as signal subspace has been increased from 13 to 198; this indicates that the selection of the energy threshold is very important, since taking 198 singular vectors as subspace may actually imply the introduction of noise in the test set *signal subspace*.

As the SNR gets higher, the subspace dimensionality gets more similar to the initial example without noise, as depicts Figure 6.12. According to this assumption, the lower the SNR, the worse the recognition rates expected for both algorithms, F_u and F_w. This can be seen in Figure 6.13 and 6.14 where the evolution of the recognition rates for both metrics according to the change in the energy threshold (η) with different values of SNR are depicted. The figures show, on the one hand, that the selection of the

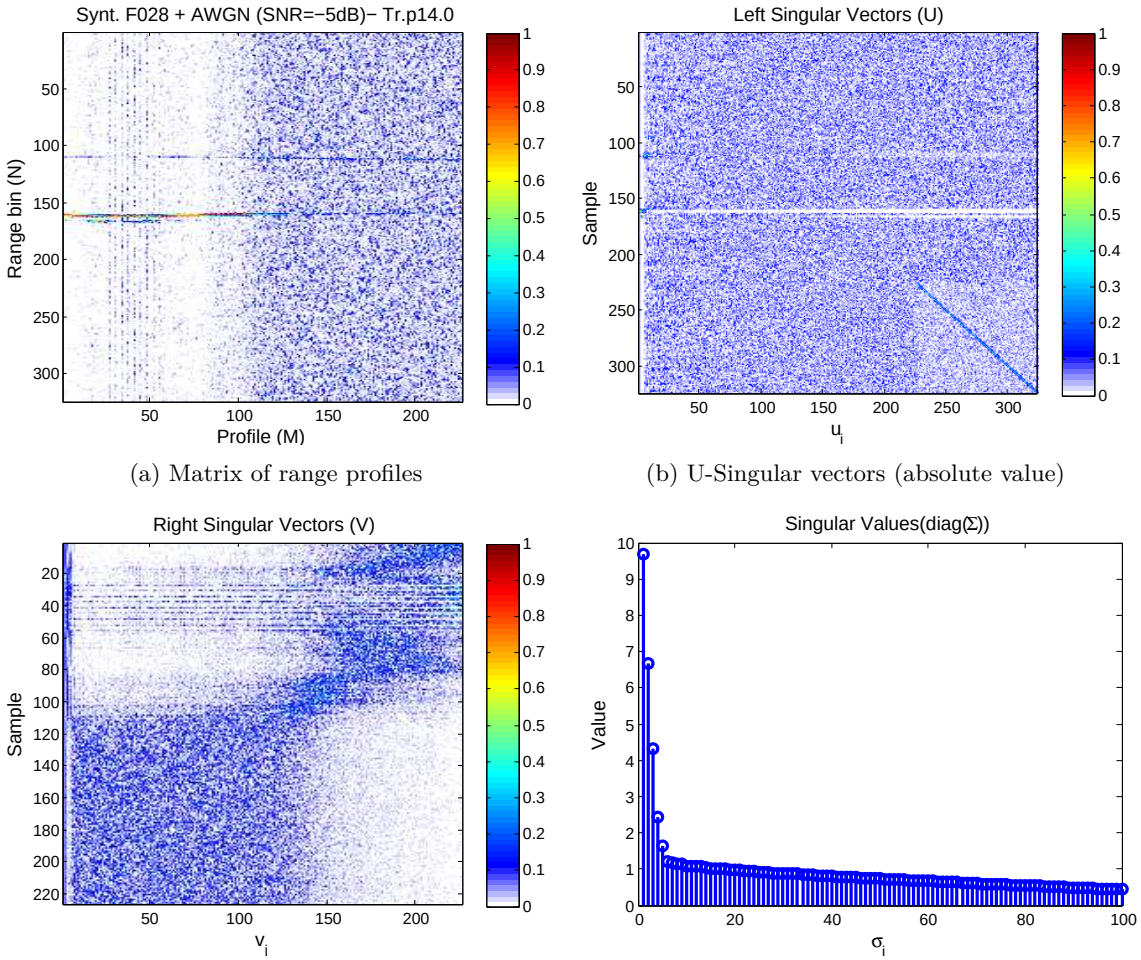

(a) Matrix of range profiles

(b) U-Singular vectors (absolute value)

(c) V-Singular vectors (absolute value)

(d) Σ-Singular values

Figure 6.11: Test Case I.b. SVD of trajectory p14.0; SNR = -5 dB

subspace dimensionality is not a trivial issue and on the other hand, that the addition of noise to the test set has clearly degraded the recognition rates.

Regarding the noise, obviously the higher the SNR the better the returned results. This fact is clearly seen in the cyan plot on Figures 6.13 and 6.14. However, at this point, a remark can be made: F_u is highly affected by the noise added to the test set, such that when the SNR is very low, only good results are obtained for very low values of η. Figure 6.13 shows the evolution of the recognition rates of F_u with the noise: with a SNR of 10 dB the results are very good even with a high η, while when the SNR takes values of 5 dB and 0 dB, it is seen that not only the recognition rates have been reduced but also, the energy threshold needed to obtain fair results also reduces. On the contrary, F_w presents an elevated robustness against the noise for any value of η, although of course, as the SNR gets lower, the recognition rates returned also degrade as Figure 6.14 illustrates.

In Test Case I.a. where no noise was added, the change of dimensionality provided by the energy threshold did not affect the recognition rates, and for any value of η the recognition rate was ideally 100%. On the contrary, the figures of the present subcase show that setting an energy threshold very near to 1 does not return such good results in this case; this is due to the added noise and the degradation of the singular values, which implies the selection of too many singular vectors as *signal subspace* and as seen in Figure 6.11, these may be corrupted by the noise. On the other hand, as the dimensionality of the subspace reduces, the recognition rates increase and even with the smallest energy threshold, both

Table 6.4: Test Case I.b. Evolution of the signal subspace dimensionality with η; SNR = -5 dB. Trajectory p14.0

Energy Threshold (η)	**0.99**	**0.95**	**0.9**	**0.85**	**0.8**	**0.7**	**0.6**	**0.5**	**0.4**	**0.3**	**0.2**	**0.1**
Dimensionality (K)	198	151	124	108	95	73	55	40	26	14	4	2

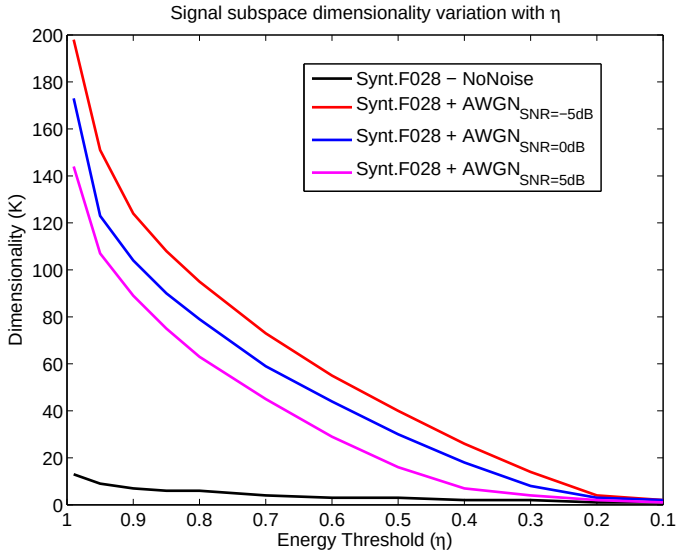

Figure 6.12: Signal subspace dimensionality evolution with η for different SNR. Trajectory p14.0

algorithms return good results, since the *noise subspace* is actually being discarded.

Table 6.5 gathers the recognition rates presented in Figure 6.13 and 6.14. As said, the best rates are obtained for high SNR and unexpectedly, very good results are returned for low values of η, especially when the SNR reaches negative values. This is because when having a poor SNR the obtained singular vectors will be so contaminated by the noise that just a very few of them will keep valuable information. For F_w the best recognition rate is 99.17%, obtained for a SNR = 10 dB and a threshold of $\eta = 0.5$ or $\eta = 0.1$, while for F_u the best recognition rate achieved is 99.58% for the same SNR and a threshold of $\eta = 0.7$ or $\eta = 0.2$, as seen, with high SNR, large energy threshold also return good results. However, as seen in the table, for algorithm F_w, even if the threshold is not optimally selected, the recognition rates are always above the 90% regardless of the value of SNR. On the other hand, F_u, even though it achieved a higher recognition rate for the optimum η and SNR than F_w, the fluctuation in recognition rates with η and the noise denotes that it lacks robustness against noise and energy threshold selection.

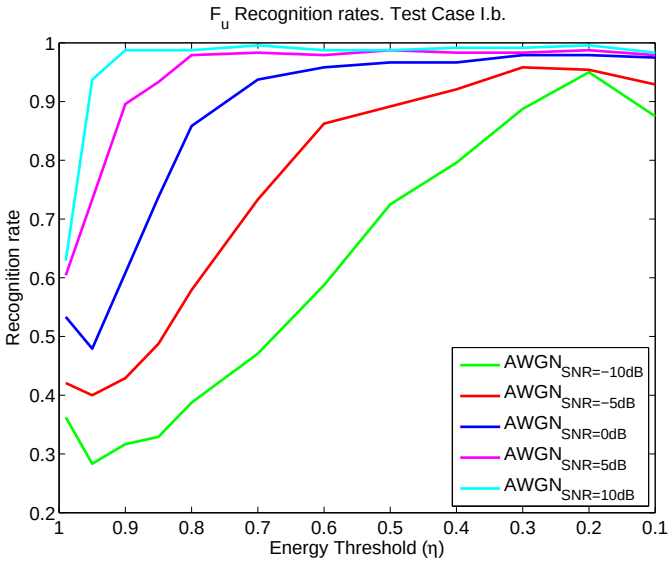

Figure 6.13: F_u - Test Case I.b. Evolution of recognition rates with η

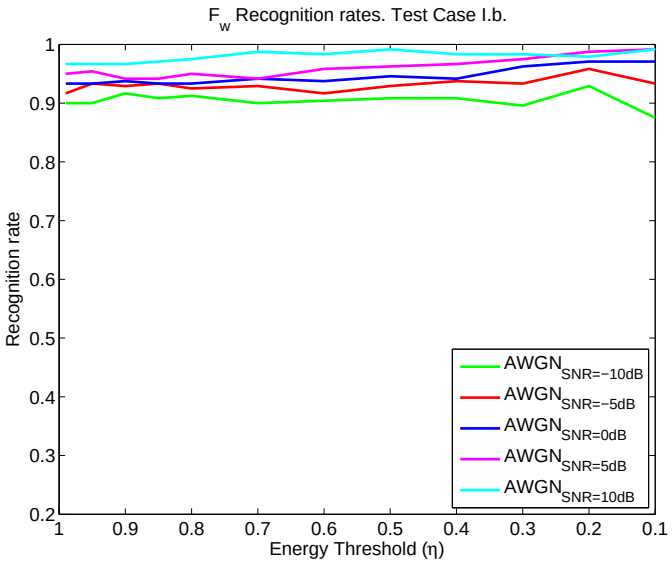

Figure 6.14: F_w - Test Case I.b. Evolution of recognition rates with η

Table 6.5: Subcase I.b. F_u and F_w Recognition rates

Test Case I.b. Recognition rates varying η (%)										
SNR	**10dB**		**5dB**		**0dB**		**-5dB**		**-10dB**	
η	F_u	F_w	F_u	F_w	F_u	F_w	F_u	F_w	F_u	F_w
0.99	62.92	96.67	60.42	95.00	53.33	93.33	42.08	91.67	36.25	90.00
0.95	93.75	96.67	73.33	95.42	47.92	93.33	40.00	93.33	28.33	90.00
0.9	98.75	96.67	89.58	94.17	60.83	93.75	42.92	92.92	31.67	91.67
0.85	98.75	97.08	93.33	94.17	73.75	93.33	48.75	93.33	32.92	90.83
0.8	98.75	97.50	97.92	95.00	85.83	93.33	57.92	92.50	38.75	91.25
0.7	**99.58**	98.75	98.33	94.17	93.75	94.17	73.33	92.92	47.08	90.00
0.6	98.75	98.33	97.92	95.83	95.83	93.75	86.25	91.67	58.75	90.42
0.5	98.75	**99.17**	**98.75**	96.25	96.67	94.58	89.17	92.92	72.50	90.83
0.4	99.17	98.33	98.33	96.67	96.67	94.17	92.08	93.75	79.58	90.83
0.3	99.17	98.33	98.33	97.50	**97.92**	96.25	**95.83**	93.33	88.75	89.58
0.2	**99.58**	97.92	**98.75**	98.75	**97.92**	**97.08**	95.42	**95.83**	**95.00**	**92.92**
0.1	98.33	**99.17**	97.92	**99.17**	97.50	**97.08**	92.92	93.33	87.50	87.50

Test Case I.c. Synthetic misaligned Profiles with AWGN Vs. Synthetic Profiles

The previous subcase showed that F_w is quite robust against the noise while F_u fails when the SNR is very poor. Moreover, it was also seen that the energy threshold should be set according to this SNR and preferably to a relatively low value. Now, the robustness of the algorithms against both the noise and the profiles motion compensation is studied in this subcase.

Figure 6.15 shows an example of a matrix of range profiles that has been shifted in order to emulate a wrong alignment, first it is shown the initial aligned matrix, and then the misaligned matrix of range profiles. In Figure 6.16 their obtained left singular values are depicted, and as seen, the shape of the matrix of singular vectors has slightly changed due to the profiles misalignment and also the weights of the singular values have been reduced as Figure 6.17 shows. Therefore, this misalignment causes a decrease in the quality of the range profiles and the SVD. However, the impact of the addition of noise is higher, such that apparently the misalignment has negligible influence when AWGN is added. This is illustrated in Figure 6.18, which depicts the obtained singular vectors of the misaligned matrix of range profiles where SNR = 10 dB.

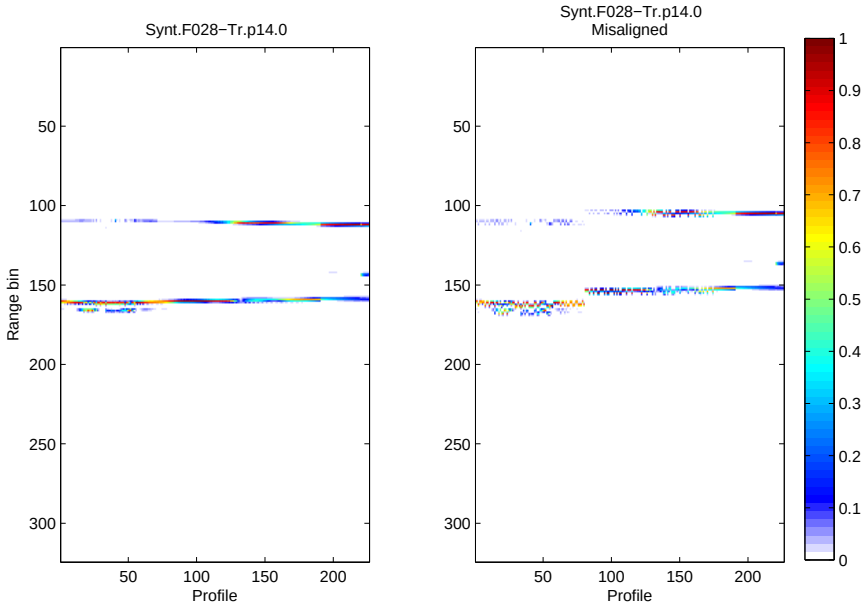

(a) Initial HRRPs (b) Misaligned HRRPs

Figure 6.15: Misaligned synthetic range profiles

Even though after the example it can be thought that the misalignment of range profiles will not affect the recognition rates, Figures 6.19 and 6.20 and Table 6.6, which contains the recognition rates obtained for this test case, shows that indeed, misalignment of range profiles does affect the identification process. Thus, the alignment of range profiles is very important and a bad alignment will produce poor recognition rates.

Again, in Table 6.6 the best results are highlighted in bold and as previously demonstrated in Test Case I.b, F_u is quite noise and energy-dependent while F_w keeps the recognition rates at a high level with little variation with η. As expected, additional distorting effects lead to worse recognition rates, while the best result for Test Case I.b for F_w was 99.17%, now the best result obtained for a SNR = 10 dB is 94.17% with an energy threshold of $\eta = 0.4$. Thus, it can be observed that not only the success rates have been reduced, but also the energy threshold for the best result has been decreased. Note that

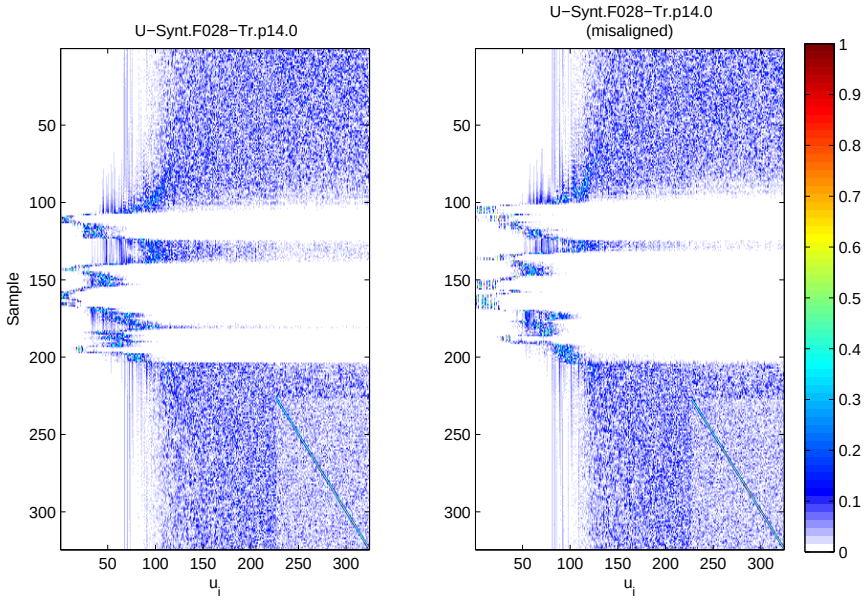

(a) Matrix U - Initial HRRPs (b) Matrix U - Misaligned HRRPs

Figure 6.16: Left singular vectors of misaligned range profiles

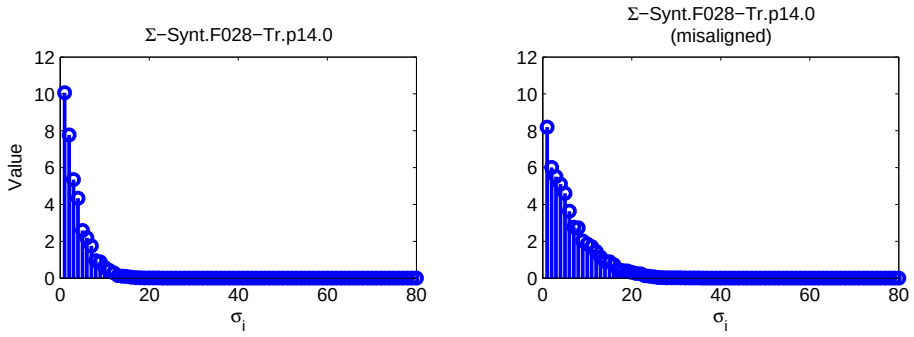

(a) Σ - Initial HRRPs (b) Σ - Misaligned HRRPs

Figure 6.17: Singular values of misaligned range profiles

when the SNR is very poor, the best results are obtained with $\eta = 0.1$, while in the previous example it was enough with $\eta = 0.2$; with higher SNR, the previous example showed that good results are achieved with η between 0.5 and 0.2, in this subcase the optimum energy threshold would be between 0.4 and 0.2 when the SNR has a high level. The reason for this reduction in the energy threshold is the high noise level added to the misalignment of range profiles; the more noise corrupts our profiles, the noisier will get the left singular vectors, furthermore, as the previous figures have shown, the incorrect profiles alignment also causes a degradation of the singular vectors and singular values, therefore, the *signal subspace* dimensionality must be set accordingly. In conclusion, F_w is still more robust than F_u although the misalignment has slightly degraded the results, in fact, this effect translates into both algorithms suffering more with a demanding SNR.

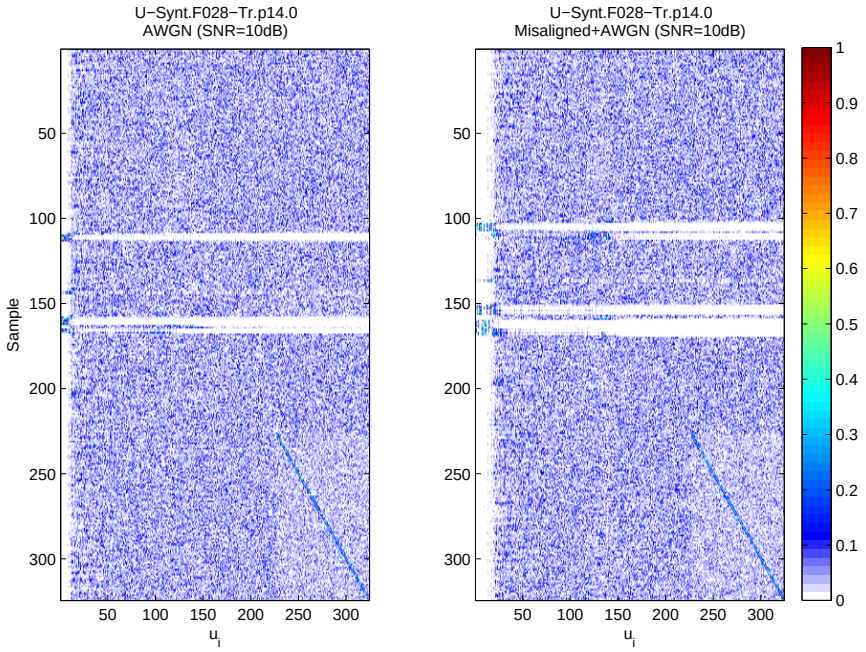

(a) Matrix U - Initial HRRPs (b) Matrix U - Noisy Misaligned HRRPs

Figure 6.18: Left singular vectors of misaligned range profiles with SNR = 10 dB

Table 6.6: Subcase I.c. F_u and F_w Recognition rates

Test Case I.c. Recognition rates varying η (%)										
SNR	**10dB**		**5dB**		**0dB**		**-5dB**		**-10dB**	
η	F_u	F_w	F_u	F_w	F_u	F_w	F_u	F_w	F_u	F_w
0.99	57.92	88.75	54.58	89.58	46.25	89.58	37.08	86.67	26.25	73.33
0.95	85.42	88.33	64.17	89.58	43.75	89.17	34.17	86.25	21.67	75.00
0.9	88.75	89.58	79.58	89.58	55.42	88.75	37.08	86.25	24.17	73.75
0.85	90.83	90.42	82.92	89.17	65.42	88.75	45.42	86.67	21.25	73.75
0.8	89.58	90.42	86.67	89.17	74.17	89.58	50.83	86.67	25.42	72.50
0.7	92.50	91.67	88.75	90.00	80.83	89.17	62.92	87.08	26.67	72.92
0.6	93.75	93.75	89.58	90.00	83.33	90.42	69.17	86.67	32.08	73.75
0.5	93.75	93.75	93.75	92.50	85.42	89.17	75.00	86.67	41.67	73.75
0.4	93.33	**94.17**	93.33	92.50	91.25	89.58	76.67	86.25	51.67	75.83
0.3	93.75	93.75	92.92	91.67	**92.92**	**92.50**	86.67	87.08	61.67	76.67
0.2	**94.58**	93.75	**94.58**	92.08	90.83	92.08	**89.58**	88.33	77.50	79.58
0.1	92.92	92.50	93.75	**92.92**	92.08	**92.50**	**89.58**	**89.17**	**80.42**	**80.83**

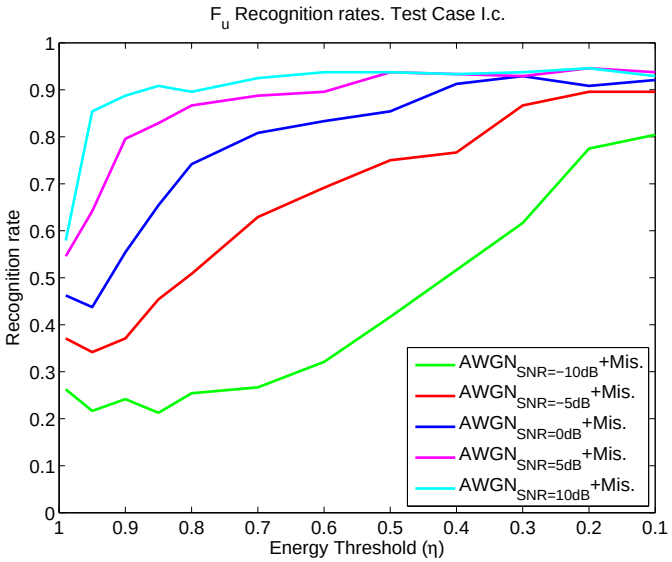

Figure 6.19: F_u - Test Case I.c. Evolution of recognition rates with η

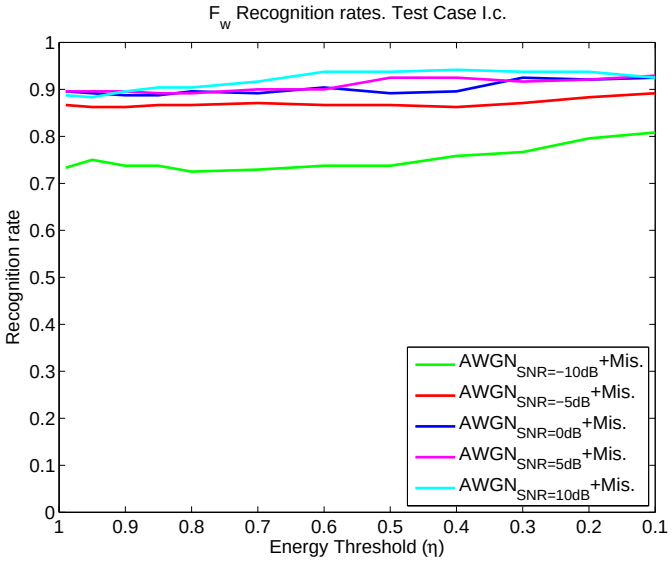

Figure 6.20: F_w - Test Case I.c. Evolution of recognition rates with η

Test Case I.d. Actual Profiles Vs. Synthetic Profiles

Lastly, this test case will validate the recognition rates and the conclusions drawn in the previous subcases and will assess the validity of the scenario proposed in this thesis, that is the non-cooperative recognition of actual range profiles by means of a synthetic database. In the previous subcases, it has been proven that F_w is quite robust against noise and incorrect motion compensation, and also that the selection of an energy threshold highly affects the recognition rates, especially those provided by F_u, unlike F_w, which, although also affected by this energy threshold, it keeps high average recognition rates. Following with the example, Figure 6.21 depicts the actual range profiles of trajectory p14.0 and their SVD. Note that the SNR of this matrix of range profiles is not as poor as the ones that have been simulated in the previous subcases b and c, since both the range profiles and the obtained matrices of singular vectors are clearer. Therefore, according to the previous results, high recognition rates are expected for metric F_w in almost any η, while for F_u only good results are expected with low η. To illustrate this, Figure 6.22 provides the graphical evolution of the obtained recognition rates while Table 6.7 collects its numerical results.

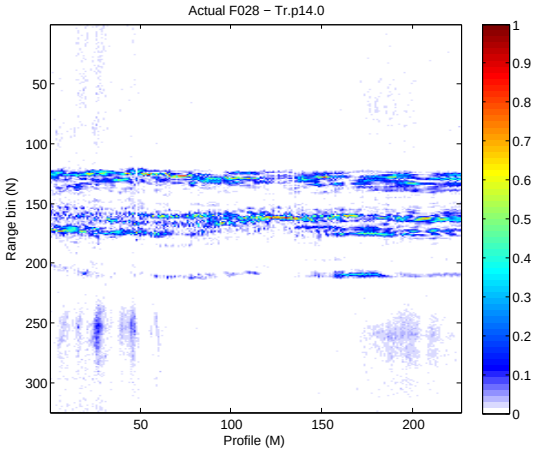

(a) Matrix of range profiles

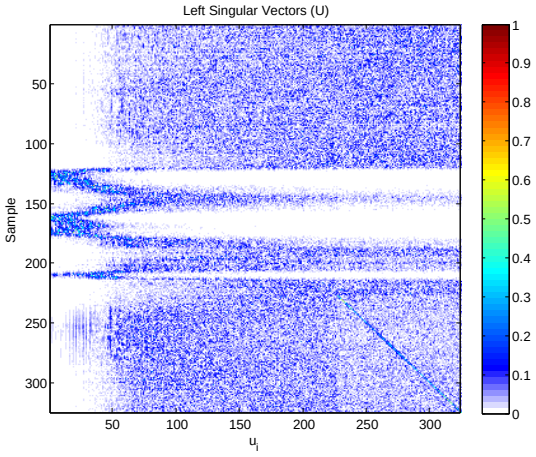

(b) U-Singular vectors (absolute value)

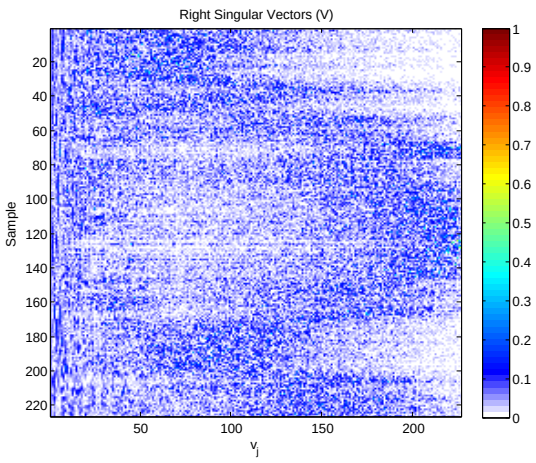

(c) V-Singular vectors (absolute value)

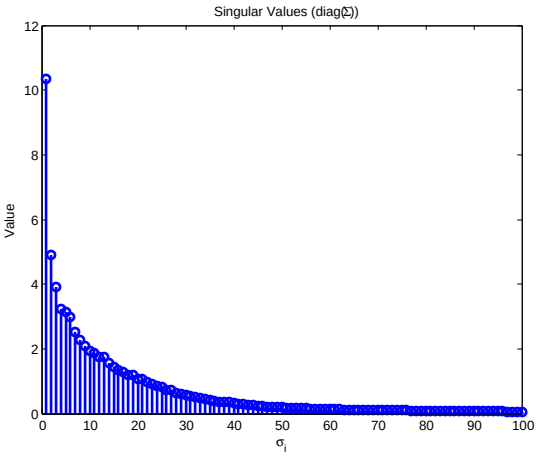

(d) Σ-Singular values

Figure 6.21: Test Case I.d. SVD of trajectory p14.0

Note that the recognition rates obtained in this Test Case I.d where actual profiles are classified by means of a synthetic database, are not as good as the ones obtained in the previous subcases. This

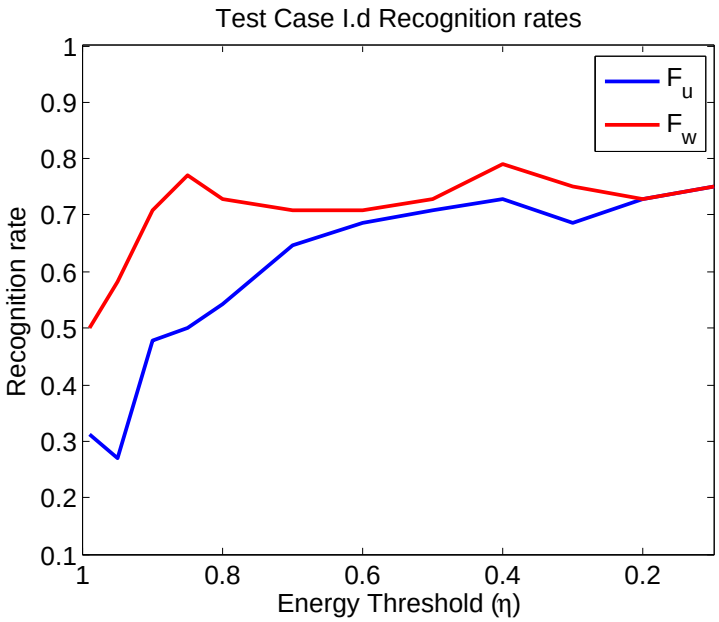

Figure 6.22: F_u and F_w - Test Case I.d. Evolution of recognition rates with η

is obvious since even though in Test Cases I.b and c unwanted effects are added to the test set, both test and training sets come from the same ideal simulations and here, on the contrary, the nature of the profiles is different. Additionally, just as section 4.3 in Chapter 4 introduced, there exist a number of facts that produce disagreement between actual and synthetic profiles. Remember that the CAD models used to generate the training set considered every aircraft as PEC and they were just rough replicas of real aircraft since small elements were not modelled. Additionally, FASCRO does not take into account all the reflective processes that occur in reality and thus, synthetic profiles are highly ideal in comparison with the actual ones. Another very important source of difference between range profiles is the target aspect estimate; recall that even though the input profiles are compared to the profiles in the database which belong to the same trajectory, these trajectories are mainly predictions since the actual aircraft were measured non-cooperatively. The error of the estimated aspect angles can be at the most of 5 degrees in both azimuth and elevation and as seen in Chapter 3, a small variation in the aircraft aspect can cause occlusion of scattering centres. Thus, synthetic profiles may not be extracted exactly in the same trajectory described by the actual aircraft and therefore, the comparison is not carried out accurately, unlike the cases where test and training sets comprised synthetic profiles. Additionally, although in principle of less importance, there also exist amplitude differences between actual and synthetic profiles, mainly due to idealism of the latter. And also, the speckle effect, although tried to be compensated with the use of SVD, may not be totally removed. These discrepancies justify the fact that the recognition rates obtained for both algorithms, F_u and F_w, do not reach the high values of the previous test cases, although the obtained rates can also be considered as good ones since in a real scenario, the collected range profiles may not have the same SNR of those in the database and may not be oriented in exactly the same aspect angles.

Regarding F_u, similarly to the prior cases, the algorithm is highly dependent on the noise and the energy threshold, and the reduction of η translates into a better recognition rate, reaching the highest value of 75% when $\eta = 0.1$. As for F_w, the recognition rates obtained, as expected after the study of Test Cases I.a to c, are more or less maintained constant around a level near to 80%, where the highest value,

Table 6.7: Subcase I.d. F_u and F_w Recognition rates

Test Case I.d. Recognition rates varying η (%)		
η	F_u	F_w
0.99	31.25	50.00
0.95	27.08	58.33
0.9	47.92	70.83
0.85	50.00	77.08
0.8	54.17	72.92
0.7	64.58	70.83
0.6	68.75	70.83
0.5	70.83	72.92
0.4	72.92	**79.17**
0.3	68.75	75.00
0.2	72.92	72.92
0.1	**75.00**	75.00

79.17%, is obtained for $\eta = 0.4$. This agrees with the results of the optimum energy threshold already seen in the above test cases where the best recognition rates were obtained for $\eta = 0.5$ and $\eta = 0.4$.

Figure 6.23 shows the evolution of F_w with the samples (k)[3], for different η; in Figure 6.23a is presented the one that achieved the best recognition rate, $\eta = 0.4$, and in Figure 6.23b the one with the second best recognition rate, $\eta = 0.85$. Note that, as expected the dimensionality of the *signal subspace* is different according to the selected η, such that for this example, $K_d = 7$ for $\eta = 0.4$ and $K_d = 37$ for $\eta = 0.85$.

The examination of these figures leads to question the accuracy of the results when $\eta = 0.4$ because as Figure 6.23a illustrates, even though the aircraft is correctly classified as a Fokker28, the confidence degree between the winner and the next aircraft is very small. A good classifier will be that which not only achieves a high recognition rate but also that has the capability to unambiguously separate the targets; therefore, with such a low energy threshold the latter condition seems to be not accomplished. On the contrary, for a threshold of $\eta = 0.85$ the obtained recognition rate is 77.08%, (very near to 80%) and also, as seen in Figure 6.23b, there is greater class separation. The issue of class separation was not of great importance in Test Cases I.a to c, since due to the idealism of both sets of profiles, both low and high energy thresholds provided good class separation.

There is a trade-off between recognition rates and class separation and it is the task of the designer to choose the best η for his system. To give an idea of the confidence degree of this test case, Figure 6.24 presents the mean difference of the final value of the metric F_w between the winner aircraft and the second one for the 48 input samples and its standard deviation; as seen, with high energy thresholds the distinction between aircraft will be less clear but with thresholds between 0.7 and 0.5 this mean difference is greater[4]. According to this, the chosen threshold for the case where matrices of actual profiles are classified utilizing a database of synthetic profiles will be $\eta = 0.5$, since it provides one of the best recognition results, 72.92% of success, and also a fair confidence interval between the recognised aircraft. Table 6.8 shows the results of F_w for the selected energy threshold in form of a confusion matrix, where the rows represent the true type of the test samples and the columns represent the recognition made

[3]Remember that $k = 1, \ldots, K_d$ with K_d being the test set *signal subspace* dimensionality

[4]Figure 6.23a showed a bad class separation between winning aircraft, however, this is just a particular case, since the results of Figure 6.24 include the results of all the trajectories in the test set

by the algorithm. For example, one element c_{ij} of the confusion matrix is the number of the members of type i that were recognized as type j by the algorithm. According to this, aircraft B767 is the one with the highest partial success rate, followed by the B747. On the other hand, the two Fokker, F028 and F100, due to the similarity between them and their smaller dimensions, provide the worst success rates. However, 48 input samples is not enough to draw firm conclusions, although it is a first step to predict the behaviour of F_w algorithm .

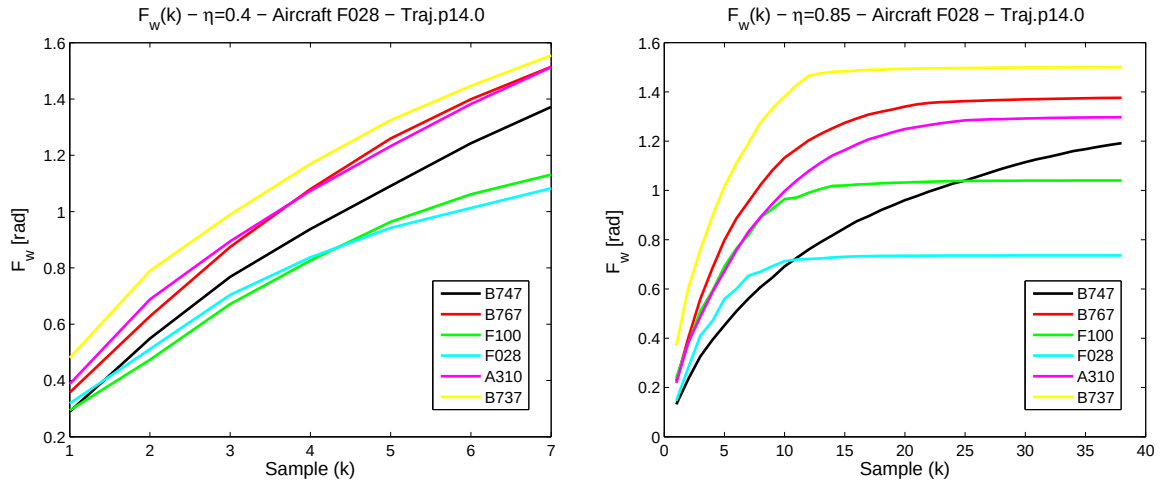

(a) $F_w; \eta = 0.4$ (b) $F_w; \eta = 0.85$

Figure 6.23: Test Case I.d. F_w partial results for F028. Trajectory p14.0

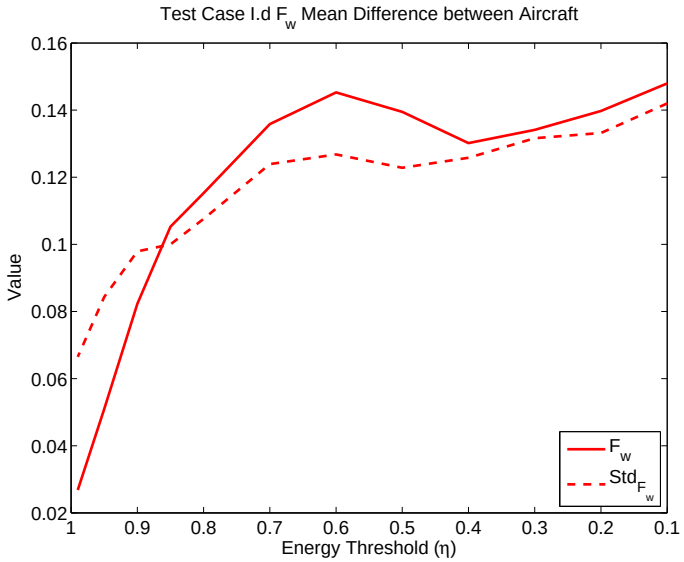

Figure 6.24: Test Case I.d. F_w Mean difference between aircraft with η

Table 6.8: Subcase I.d. F_w Confusion matrix; $\eta = 0.5$

	A310	**B747**	**B767**	**F028**	**F100**	**B737**	**Success (%)**	**Error (%)**
A310	3	1	0	0	0	0	**75.00**	**25.00**
B747	0	8	2	0	0	0	**80.00**	**20.00**
B767	1	0	9	0	0	1	**81.82**	**18.18**
F028	0	0	0	9	1	2	**69.23**	**30.77**
F100	0	1	0	1	6	2	**60.00**	**40.00**
Average rates							**72.92**	**27.08**

Test Case I. Discussion

In Test Case I, 5 aircraft classes have been classified utilizing a database of 6 aircraft classes synthetically generated. In order to have information about the change in the range profiles due to the variation in the orientation of the aircraft along the different trajectories, matrices of range profiles have been utilized as input samples instead of individual range profiles; these matrices comprise a number of HRRPs that vary from 100 up to 300.

The study of the energy threshold of Test Case I has been completed sequentially along 4 subcases, whose conclusions are summarized here:

- First, the ideal study of Test Case I.a, where 240 matrices of synthetic profiles have been compared with synthetic profiles, has provided ideal results with recognition rates reaching 100% for both metrics and for any value of energy threshold. Result that was expected since the same ideal matrices of range profiles were compared to each other.

- Test Case I.b has studied the robustness of both metrics, F_u and F_w, against noise by applying additive white gaussian noise to the 240 matrices of range profiles that formed the test set. It has been demonstrated that the addition of noise not only has caused a degradation of the HRRPs, but also a deterioration of the *signal subspace*, broadening it for any selected η and hence, including undesired information in the classification process. With this test case it has been proven that the selection of the energy threshold is crucial in these metrics and it should not be set to values very near to the unity, otherwise all the unwanted noise will take part in the *signal subspace*. Additionally, F_u has shown to be highly affected by the noise and the threshold, while F_w has shown more stability, providing high recognition rates above 90% for any value of SNR and any η. However, the optimum threshold found is different for each metric, F_u provides the best results with low η, near to 0.2 or even 0.1, while for F_w, although reaching good results with any value of η, the best rate is obtained for an energy threshold between 0.2 and 0.5.

- The next subcase in this increasing model comprised the evaluation of the robustness of both metrics with noise and TRM, which is compensated via alignment of range profiles. For this study, the 240 matrices of noisy range profiles from Test Case I.b have been misaligned and further aligned to simulate the motion compensation. It has been seen that the incorrect alignment of profiles causes, similarly to the addition of noise, a change in the singular vectors and singular values; however, the addition of noise has more influence. Test Case I.c. has shown that, for both metrics, supplementary distorting effects result in a reduction of the necessary energy threshold for obtaining the best results (now the optimum threshold found for F_w is between 0.1 and 0.4) and in poorer recognition rates;

although these rates are still around 90% for F_w and this metric has shown robustness, now with a demanding SNR, it has slightly lost robustness.

- Test Case I.d finally classified actual range profiles by means of a synthetic database. Unlike the previous subcases, where 240 matrices of range profiles where classified, now only 48 matrices of actual range profiles are available for classification[5]. As expected after the evaluation of the prior subcases, F_u is highly affected by the selection of the energy threshold, reaching the best recognition rates when $\eta = 0.1$ as in Test Case I.c. On the other hand, and as predicted, F_w has a more constant tendency and it is not as noise and energy-dependent as F_u, reaching the highest recognition rates when the threshold is set to 0.4, similarly to Test Case I.c. However, the additional problem of the confidence in the results has arose, and a trade-off between recognition rates and confidence interval should be considered. Finally, the best option for Test Case I.d is the selection of $\eta = 0.5$, which provides good agreement between success rate and confidence degree. Nevertheless, the recognition rates obtained in this Test Case I.d are not as high as the ones obtained in the previous test cases, since the same effects that actual profiles undergo cannot be exactly reproduced in the simulations. Despite this, F_w is still quite robust, obtaining recognition rates up to 80%.

Thanks to the use of singular values as weights, F_u has been upgraded to F_w, achieving more robustness against noise, against the selection of the *signal subspace* dimensionality and also against the discrepancies between test and training sets. However, still the issue of setting the dimensionality is present; not only η should be set such that the best recognition rates are obtained, but also the ability of good class separation should be taken into account when choosing this threshold.

Even though good recognition rates have been achieved with these metrics and a conclusion about the energy threshold has been reached, Test Case I is just a first approach since the number of input samples that have been classified is not high enough to draw firm conclusions about the classifier's robustness. Hence, next Test Case II will try to further validate the conclusions of Test Case I by increasing the number of trajectories and aircraft to be identified.

6.2.1.2. Test Case II. Results

In this test, a new aircraft model is added to both the test and training sets, hence the identification problem consists now in the classification of 6 aircraft with a database of 7 aircraft models. Moreover, a few more trajectories are considered and also, these are divided into smaller frames, covering a variation of 2.5° in azimuth. So now, in total, instead of 48 frames, 235 frames corresponding to 6 different aircraft are available to be classified. As in Test Case I, regarding Test Cases II.a to c, since they study predictions, the 6 aircraft of the test set have been simulated, and therefore, 1410 matrices[6] of range profiles will be classified. For Test Case II.d, only the actual 235 matrices of measured range profiles will be available for classification. With this upgrade in both the input samples and the database, an improvement in the confidence of the results is expected.

Equally to Test Case I, trajectory p14.0 is used as example, but now this trajectory is divided into 10 frames and among these frames, for simplicity, frame 1 is taken, containing a total number of 15 HRRPs covering the portion of trajectory that corresponds to nose-on aspect angles.

[5] Remember that the actual range profiles are extracted from the ORFEO measurement campaign and it collected profiles of targets of opportunity

[6] 235 frames × 6 aircraft = 1410 matrices of range profiles

Test Case II.a. Synthetic Profiles Vs. Synthetic Profiles

As the prior Test Case I, the ideal scenario is studied here, where matrices of synthetic range profiles are compared with matrices of synthetic range profiles. The matrix of HRRPs of the example trajectory is shown in Figure 6.25a, and in Figures 6.25b to 6.25d its SVD is depicted. Note that now, as the matrix only contains 15 range profiles of 324 range bins, the dimensions of the matrices of singular vectors and singular values will be $U \in \Re^{324\times324}$, $V \in \Re^{15\times15}$ and $\Sigma \in \Re^{324\times15}$. However, even if matrix U has such size, only the 15 first left singular vectors (u_i) are truly singular vectors with information about the target; the rest, as no information exist to calculate them, have been obtained automatically, explaining the strange shape of matrix U[7].

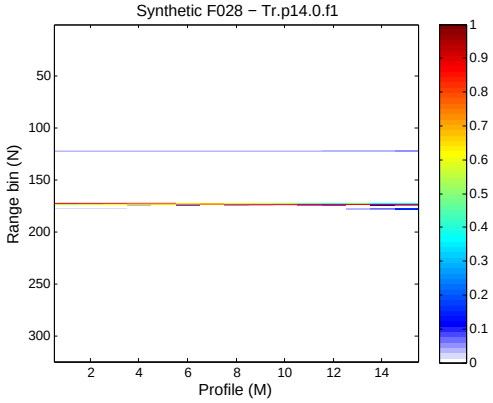

(a) Matrix of range profiles

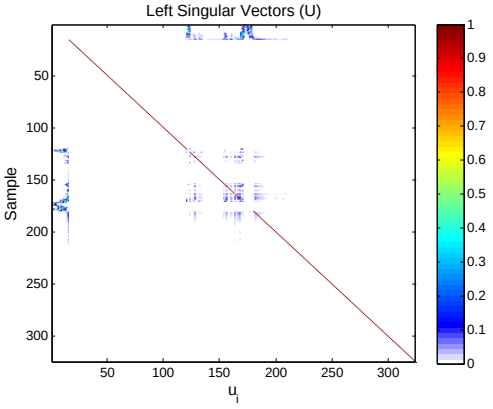

(b) U-Singular vectors (absolute value)

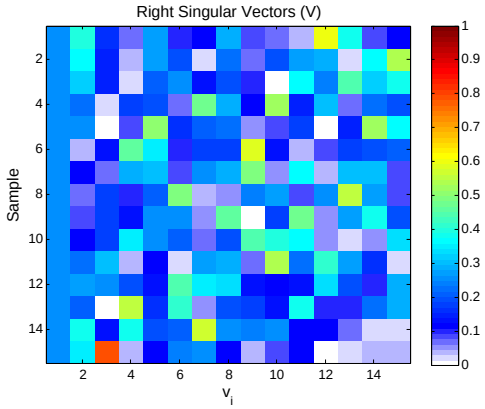

(c) V-Singular vectors (absolute value)

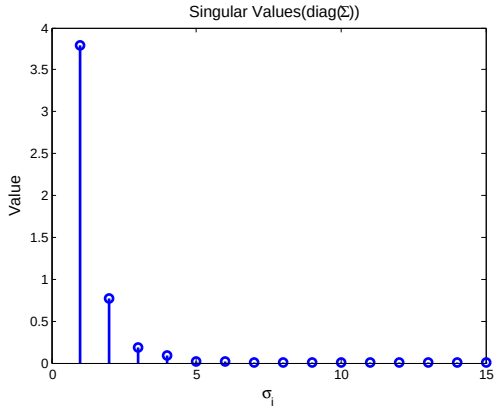

(d) Σ-Singular values

Figure 6.25: Test Case II.a. SVD of trajectory p14.0, frame 1

Regarding the variation of the subspace dimensionality when changing the value of the energy threshold, for the frame 1 of trajectory p14.0, the number of vectors that form the test set *signal subspace* is presented in Table 6.9 as an example. As seen, from $\eta = 0.7$ to $\eta = 0.1$ the signal subspace comprises only 1 singular vector and hence the results of the identification will be the same in that range. In any case, as happened in Test Case I.a, due to the idealism of this study, the 100% of the matrices of range profiles are correctly classified[8], that is, the average recognition rates obtained for Test Case II.a are 100% for both metrics F_u and F_w for any value of η.

[7] Additionally these extra u_i do not have an associated σ_i, therefore they will not take part in the classification process in any case.

[8] The table of recognition rates is not presented here for this test case but is exactly the same as Table 6.3

Table 6.9: Test Case II.a. Evolution of the signal subspace dimensionality with η. Trajectory p14.0, frame 1

Energy Threshold (η)	**0.99**	**0.95**	**0.9**	**0.85**	**0.8**	**0.7**	**0.6**	**0.5**	**0.4**	**0.3**	**0.2**	**0.1**
Dimensionality (K)	4	3	2	2	2	1	1	1	1	1	1	1

Test Case II.b. Synthetic Profiles with AWGN Vs. Synthetic Profiles

The previous subcase, still with an enlarged database, returns ideal results, just as was expected after the examination of Test Case I.a. In this section, the influence of the addition of noise to both metrics is studied, with the difference that now the trajectories are divided into smaller groups and comprise a few number of range profiles.

Test Case I.b proved that the addition of noise affected both the shape of the matrix of HRRP and its SVD (by degrading the weight of the obtained singular values and the shape of matrix U). Therefore, the noise will also cause a change in the *signal subspace* extraction; since now both test and training sets differ, the recognition rates achieved will not reach the 100%. The dimensionality of the *signal subspace* for frame 1 of trajectory p14.0 with an added noise resulting in SNR = -5 dB is presented in Table 6.10 and as foreseen, this dimensionality has been worsened. In Test Case I.b, the addition of noise was of great impact: the number of vectors that composed the target signal was 13 when no noise was present in Test Case I.a for $\eta = 0.99$, and it changed to 198 vectors when SNR = -5 dB. Now, as the initial dimensionality of the matrices of range profiles is lower than Test Case I, the effect of the noise in the subspace dimensionality is not as pronounced, changing from 4 vectors (in Test Case II.a), to 15 for $\eta = 0.99$ and SNR = -5 dB. Therefore, as a first approach, it can be said that the effect of noise will not be as high as for the previous test case.

Table 6.10: Test Case II.b. Evolution of the signal subspace dimensionality with η; $SNR = -5dB$. Trajectory p14.0, frame 1

Energy Threshold (η)	**0.99**	**0.95**	**0.9**	**0.85**	**0.8**	**0.7**	**0.6**	**0.5**	**0.4**	**0.3**	**0.2**	**0.1**
Dimensionality (K)	15	12	8	6	3	2	1	1	1	1	1	1

Table 6.11 and Figures 6.26 and 6.27 gather the results of the obtained recognition rates when varying η and the added noise. It should be noted that now the highest recognition rates obtained are of lower value than those of Test Case I.b, although a higher robustness in this Test Case II was expected. However, it should be remembered that now the number of aircraft classes to be identified has increased, hindering the identification process. In any case, the rates still maintain the similar high levels of the previous test case, for F_w, above 95% of success when the noise is minimum and around 85% when the noise is too high. In the case of F_u, although still noise and threshold dependent, a change in the energy threshold does not have such a high influence in the success rates due to the fact that, as said before, studying smaller matrices of range profiles provides more robustness against subspace dimensionality and noise. Indeed, in the previous Test Case I.b, taking the worst scenario where SNR = -10 dB and $\eta = 0.99$, the success rate of F_u was only 36.25% while now, the resulting rate is 54.54%. With regard to the optimum η, in this Test Case II.b, it gets slightly different values as Test Case I.b, where for F_w the optimum energy threshold took values of $\eta \leq 0.5$ and for F_u, $\eta \leq 0.7$, and on the present case for F_w the best rates are obtained for $\eta \leq 0.8$, while for F_u, $\eta \leq 0.2$. That is, in the case of function F_w the optimum

Table 6.11: Subcase II.b. F_u and F_w Recognition rates

Test Case II.b. Recognition rates varying η (%)										
SNR	10dB		5dB		0dB		-5dB		-10dB	
η	F_u	F_w	F_u	F_w	F_u	F_w	F_u	F_w	F_u	F_w
0.99	91.49	97.94	85.60	96.60	76.45	94.89	66.10	89.65	54.54	87.23
0.95	94.47	98.37	88.65	96.31	79.57	93.62	69.29	90.28	56.45	86.24
0.9	95.39	98.09	91.35	96.45	81.84	94.26	71.42	90.92	59.50	85.04
0.85	95.53	98.01	92.62	96.60	84.82	94.04	73.19	90.14	60.14	86.45
0.8	96.03	**98.65**	92.70	97.02	86.17	93.97	74.96	91.13	63.12	86.03
0.7	96.24	98.44	95.46	97.30	88.23	94.40	78.79	90.07	66.24	85.74
0.6	96.60	98.01	95.39	**97.66**	91.63	94.61	81.56	91.35	69.43	86.74
0.5	97.23	98.58	96.31	97.16	93.26	**95.39**	87.02	91.42	72.84	**86.81**
0.4	98.01	98.44	96.38	96.81	93.55	94.61	88.58	90.92	76.31	**86.81**
0.3	**98.09**	97.80	**97.30**	97.23	**94.89**	95.11	89.50	91.21	80.92	86.60
0.2	**98.09**	98.01	97.16	96.60	94.82	94.68	90.14	**91.49**	**83.97**	84.18
0.1	97.52	97.45	96.31	96.31	94.18	94.33	**90.57**	90.07	82.27	81.77

threshold has increased while for F_u it has been decreased.

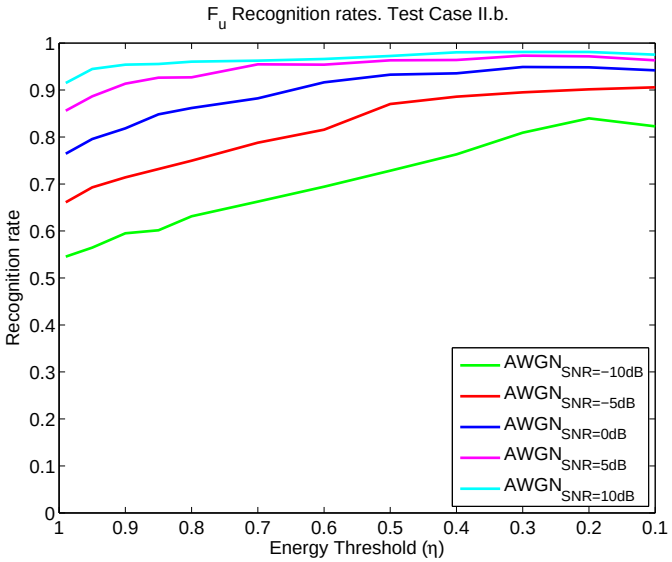

Figure 6.26: F_u - Test Case II.b. Evolution of recognition rates with η

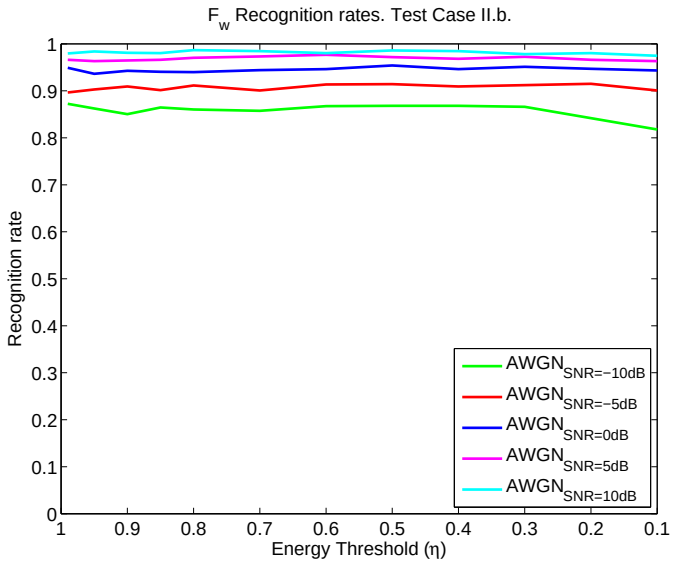

Figure 6.27: F_w - Test Case II.b. Evolution of recognition rates with η

Test Case II.c. Synthetic misaligned Profiles with AWGN Vs. Synthetic Profiles

The previous subcase showed that, even if additional aircraft classes are involved, working with smaller matrices of HRRPs results in higher robustness against noise and energy threshold, mainly for F_u. As before, this subcase c will go further into the degradation of range profiles in order to study the evolution of the obtained average recognition rates; with this purpose, after adding AWGN to the range profiles, a misalignment of 3 samples with respect to the previous profile is applied to each profile in the test set and before classification, the motion compensation technique of section 4.1.1 is employed to eliminate the misalignment. As was concluded in Test Case I.c, the impact of the addition of noise is higher, but a wrong alignment will also affect negatively the identification process.

Table 6.12 and Figures 6.28 and 6.29 show the recognition rates obtained for the different values of energy threshold and SNR. Equally to the previous subcase, F_u is more robust against the energy threshold now in comparison with Test Case I.c, although still not as robust as F_w. In both metrics, to obtain the best results, η should be set to a value between 0.4 and 0.2, depending on how corrupted the input matrix is. That is, equally to Test Case I.c, the introduction of the misalignment causes a decrease in the optimum energy threshold.

As seen in the previous test case and in the table, by including additional misalignment, the recognition results deteriorate for both metrics, the recognition rates for the best case (SNR = 10 dB) with the optimum η are 96.17% for F_u, and 96.81% for F_w, while for the worst case (SNR = -10 dB), are 75.46% for F_u, and 81.35% for F_w. The study of Test Case I resulted in a decay of an average of 5 percentage points from Test Case I.b to Test Case I.c, now this decay from Test Case II.b to Test Case II.c is, on average, of 3 percentage points. This agrees with the fact that smaller matrices provide more robustness, not only against noise and energy threshold, but also against errors in the profile alignment; this was quite easy to infer, since the lesser the number of profiles that compose a matrix, the smaller the probability of wrong alignment between them.

Table 6.12: Subcase II.c. F_u and F_w Recognition rates

Test Case II.c. Recognition rates varying η (%)										
SNR	**10dB**		**5dB**		**0dB**		**-5dB**		**-10dB**	
η	F_u	F_w	F_u	F_w	F_u	F_w	F_u	F_w	F_u	F_w
0.99	89.86	96.38	82.13	93.76	73.55	90.78	61.42	87.02	46.52	80.00
0.95	92.34	96.38	85.39	93.69	75.11	90.71	63.40	87.45	46.95	79.86
0.9	93.33	96.31	86.81	93.83	78.16	90.57	65.25	87.30	49.29	80.50
0.85	93.76	95.89	87.30	93.97	79.65	90.71	66.95	87.09	51.99	79.93
0.8	93.83	95.74	88.87	94.18	80.85	90.71	67.80	87.16	53.26	**81.35**
0.7	94.26	96.03	89.93	93.55	82.98	90.99	71.49	86.81	57.02	80.50
0.6	94.33	95.82	91.21	94.18	84.54	90.99	74.47	87.23	60.50	80.57
0.5	94.82	96.03	91.91	94.47	87.94	91.35	77.94	87.87	63.33	81.06
0.4	95.60	96.45	92.48	94.89	90.00	**92.20**	81.49	**88.16**	68.16	**81.35**
0.3	95.89	**96.81**	94.61	95.39	**91.21**	91.56	83.12	87.45	71.77	80.35
0.2	**96.17**	96.38	**95.18**	**95.46**	**91.21**	91.99	**85.04**	87.16	**75.46**	79.36
0.1	95.67	95.60	93.97	94.04	90.28	90.28	83.26	83.33	69.50	69.50

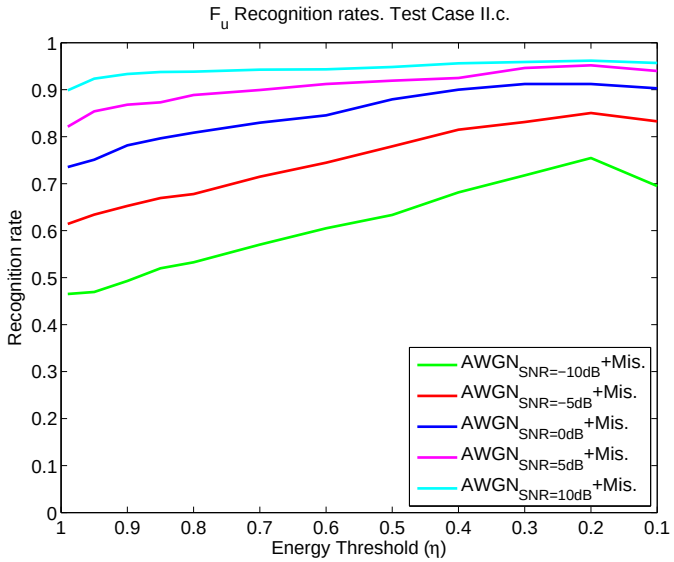

Figure 6.28: F_u - Test Case II.c. Evolution of recognition rates with η

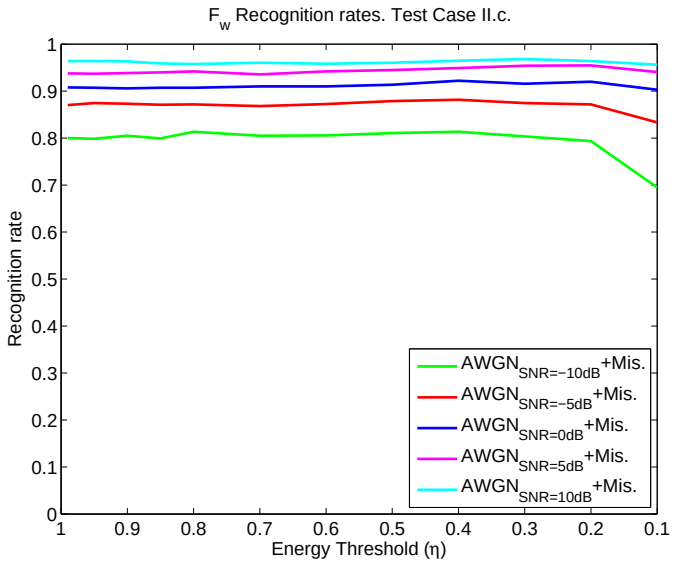

Figure 6.29: F_w - Test Case II.c. Evolution of recognition rates with η

Test Case II.d. Actual Profiles Vs. Synthetic Profiles

Finally, the classification of the 235 matrices of actual range profiles is studied in this section. In the previous subcases it has been seen that, equally to Test Case I, F_w is less affected by the addition of noise and misalignment than F_u. Additionally, it was shown that the use of small matrices of range profiles not only enlarge our database of both test and training samples, but also these matrices still have enough information to provide good recognition results. Indeed, the range profiles' misalignment and further alignment had little effect in comparison with the previous case where the matrices of range profiles comprised between 100 and 300 profiles. According to the results seen in the previous sections, high recognition rates are expected for F_w in almost any η, but the best are expected with a threshold between 0.4 and 0.2. As for F_u, Test Case II has returned more stable results than Test Case I, yet the the results are still highly dependent on the noise and the energy threshold and good recognition rates are expected only for very low η.

The results obtained for this subcase are summarized in Table 6.13 and Figure 6.30.

Figure 6.30: F_u and F_w - Test Case II.d. Evolution of recognition rates with η

As predicted, F_w achieves the best results when $\eta = 0.4$, 84.26%, while F_u increases its recognition rates from 45.53% when $\eta = 0.99$ to 84.26% when $\eta = 0.1$. As already explained, the recognition rates of this subcase do not reach the very high values of the cases where synthetic profiles are compared to each other, even though these synthetic profiles had been noticeably corrupted; the reason is, again, that profiles of different nature are compared here, and there exist some discrepancies between simulations and measurements of actual aircraft that affect the identification. In spite of that, high success rates are achieved in this section for metric F_w and F_u, although the latter needs a more precise energy threshold selection; F_w maintains recognition rates around $80 - 84\%$, higher average rates than Test Case I.d with more aircraft classes and input samples to identify; therefore, it is proven that it is better to divide trajectories into small sectors than having frames with too many HRRPs.

In Test Case I.d, it was seen that the difference between the result of the winner aircraft and the following one for the optimum energy threshold ($\eta = 0.4$) was not sufficient to guarantee a certain confidence degree, therefore, a similar analysis is given here to evaluate the optimum threshold for this test case. Figure 6.31 shows for trajectory p14.0 frame 1, the evolution of F_w for different energy

Table 6.13: Subcase II.d. F_u and F_w Recognition rates

Test Case II.d. Recognition rates varying η (%)		
η	F_u	F_w
0.99	45.53	66.81
0.95	51.49	68.51
0.9	57.87	72.34
0.85	59.57	74.04
0.8	60.85	75.32
0.7	69.36	78.30
0.6	71.06	82.55
0.5	76.17	83.83
0.4	81.70	**84.26**
0.3	82.13	82.98
0.2	83.40	**84.26**
0.1	**84.26**	**84.26**

thresholds. As seen, unlike Test Case I.d, here, with the optimum threshold ($\eta = 0.4$) the winner aircraft is clearly separated from the rest with a high confidence, and the same happens for other η. Nevertheless, this is an specific example, hence to study the confidence of the results, Figure 6.32 shows the mean difference of F_w between the winning aircraft and the next one for all the 235 input samples for every energy threshold and its standard deviation. As seen, the best results are obtained for a value of η around 0.4 or 0.3, although between 0.7 and 0.4 the difference between the standard deviation and the mean difference is a bit lower. Anyway, as the standard deviation is quite high for almost any η, it can be said that in this case a threshold of $\eta = 0.4$ is appropriate for obtaining very good results as Table 6.14 shows in form of a confusion matrix.

As seen in this confusion matrix, aircraft B747 is the one with the highest success rate, mainly due to its bigger dimensions, and on the other hand the two Fokker, just as Test Case I.d, are the ones with the lowest success rate, due to the similarity between their fuselages and dimensions that causes wrong classifications.

Table 6.14: Subcase II.d. F_w Confusion matrix; $\eta = 0.4$

	A310	**B747**	**B767**	**F028**	**F100**	**MD88**	**B737**	**Success (%)**	**Error (%)**
A310	35	0	3	0	0	0	1	**89.74**	**10.26**
B747	0	39	1	1	0	1	0	**92.86**	**7.14**
B767	2	1	30	0	0	1	0	**88.24**	**11.76**
F028	0	0	0	31	6	1	0	**81.58**	**18.42**
F100	0	0	0	7	29	1	6	**67.44**	**32.56**
MD88	1	0	1	0	3	34	0	**87.18**	**12.82**
Average rates								**84.26**	**15.74**

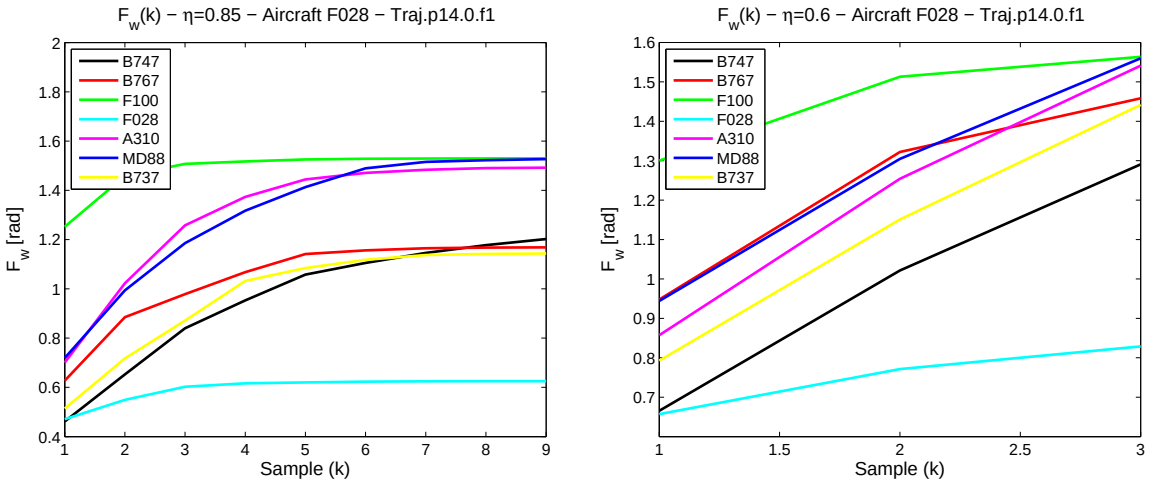

(a) $F_w; \eta = 0.4$

(b) $F_w; \eta = 0.6$

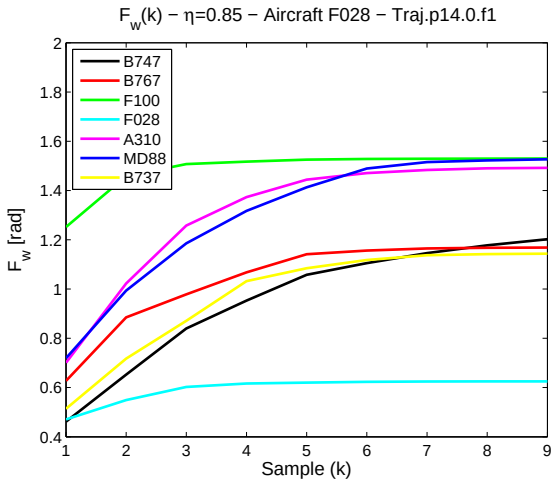

(c) $F_w; \eta = 0.85$

Figure 6.31: Test Case II.d. F_w partial results for F028

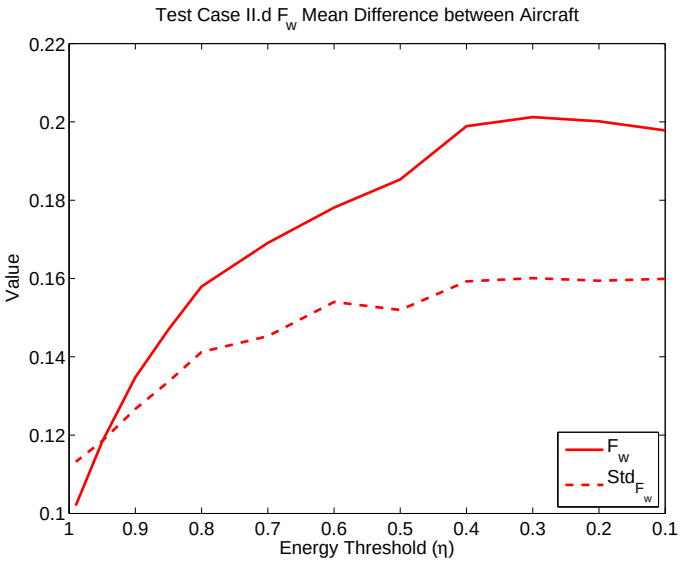

Figure 6.32: Test Case II.d. F_w Mean difference between aircraft with η

Test Case II. Discussion

In Test Case II, an additional aircraft class has been included in the classification problem in both test and training sets, resulting in an enlargement of the sets, where 6 different classes have been identified against 7 different synthetically generated aircraft classes. The trajectories described by the aircraft have been divided into small frames covering 2.5° in azimuth, so now the matrices of range profiles always contain less than 100 HRRPs, contrary to Test Case I.

As in the previous Test Case I, an incremental study has been carried out, starting from the ideal scenario to end with the most realistic one, where profiles of different nature and SNR would be compared. The conclusions reached for this test case are summarized below:

- Test Case II.a has shown that the totality of the 1410 synthetic matrices of range profiles have been correctly classified regardless of the value of the energy threshold. This was obvious after the analysis of Test Case I but it was the first step to keep evaluating the metrics with bigger sets of range profiles.

- After the ideal results obtained by Test Case II.a, the robustness of the metrics after adding white gaussian noise to the test samples has been evaluated in Test Case II.b. Now, as well as in Test Case I.b, the recognition rates have not reached 100%, since due to the noise, *the signal subspace* dimensionality has broaden for every η; this change in the *signal subspace* dimensionality produces the inclusion of information that in reality would belong to the *noise subspace*, hence degrading the results. These obtained results have proven the importance of the energy threshold selection, and as for Test Case I.b, this should not be set to high values. The best results have been obtained for a threshold of $\eta \leq 0.8$ in the case of F_w, and $\eta \leq 0.2$ for metric F_u. Similarly to Test Case I, results have shown that F_w provides high recognition rates and is more stable against the energy threshold selection while F_u is more noise and energy threshold dependent. However, in this test case, it has been proven that F_u behaves a bit better when working with smaller matrices rather than with big ones.

- Test Case II.c has studied the robustness against profiles' misalignment. As said before, the addition of noise has more effect than the wrong alignment of profiles, however, this alignment is very important and thus, its effects should be taken into account. In fact, as expected after Test Case I, the introduction of the misalignment has caused a decrease in the optimum energy threshold, which now has resulted in $0.4 \geq \eta \geq 0.2$ for both metrics. The results given in this test case have shown, especially, that working with small matrices of profiles performs better against TRM, since having less profiles translates into a reduced error in their alignment.

- Lastly, the actual scenario, where actual profiles are compared with synthetic ones, agrees with the fact that smaller matrices lead not only to better results, but also to an enlargement of the test set, providing more confidence in the results. F_u has returned more stable results than Test Case I.d, although it still is highly noise and threshold dependent. On the other hand, F_w, with more input samples and aircraft classes, has achieved higher success rates than Test Case I.d (84.26%), and also the optimum $\eta = 0.4$ provided a good confidence interval as well.

The division of trajectories into small frames with little variation in azimuth has been proven to be a wise choice; the advantages are two-fold, on the one hand, more samples are provided to check the validity of our algorithms, and on the other hand, information about the aircraft trajectory is still contained in these frames.

Test Case II has been formulated to confirm the conclusions drawn after Test Case I. After its analysis, it can be stated that F_w is an evolution of F_u, much more stable against noise, dimensionality selection, TRM and differences between test and training samples. The selection of the optimum energy threshold to define the signal subspace dimensionality needs of a thorough study as the one given here and for other sets this threshold may be different. However, F_w provides high success rates for almost any η, (although the optimum one is, as seen, around 0.4 for this study, always providing recognition rates above 80%), thus, it can be said that, F_w could be a good classifier even if the chosen threshold is not the optimum one.

6.2.2. *Softwheights* evolution with m

In the methods previously studied , as seen, setting the subspace dimensionality is always an issue, if the threshold is not properly selected, results may be degraded, although using metric F_w instead of F_u will return better results even if the threshold is not optimum.

The algorithm gMSM, introduced in section 5.2.2.3, avoids selecting the subspace dimensionality by introducing the concept of *softweighting*. In this algorithm, all the eigenvectors obtained take part in the *signal subspace* but not with the same importance since these vectors are weighted by a transformed value of their corresponding eigenvalues. With this concept of *softweighting*, there is no need to set the subspace dimensionality in advance. Nevertheless, even though this dimensionality is not literally set, there exist the need of selecting the optimum value of parameter m. Remember that this parameter provides the index of the eigenvalue that will weight the rest of the eigenvalues in order to obtain the *softweights* as equation 5.19 in Chapter 5 showed, and duplicated here as equation 6.2 for clarity.

$$\omega = w_m(\lambda) = \min\left[\frac{\lambda}{\lambda_m}, 1\right] \tag{6.2}$$

The selection of this parameter is of importance since it must be noted that the higher the m is, the more eigenvectors are treated with a *softweight* of 1. This implies, on the one hand, if m is very high, algorithm gMSM gets equivalent to MSM with large dimension of subspaces; on the other hand, and highly related to the former statement and the previous metrics, with a high value of m, eigenvectors representing the *noise subspace* may be considered as part of the *signal subspace* with the same importance; this can cause the similarity between subspaces to be very close for all aircraft classes, and thus, recognition performance can be negatively affected.

Accordingly, m is previously thought to be set to low values. In order to clarify these assumptions, a study on the parameter m should be carried out. Firstly, m is chosen dynamically for the test and training samples: if λ_i is the i-th eigenvalue out of N, m is calculated (separately for test and training sets) according to a threshold η ($0 \leq \eta \leq 1$), such that:

$$\arg\min_m \left(\left| \sum_{i=1}^{m} \lambda_i - \eta \cdot \sum_{i=1}^{N} \lambda_i \right| \right) \tag{6.3}$$

Different thresholds for test and training samples will be set (η_D and η_S respectively) and the mean value of parameter m for both sets according to these threshold will be calculated (m_D and m_S). The thresholds taken are varied equally to the study of F_u and F_w, that is, η_D and η_S will be varied from 0.1 to 0.99, with steps of 0.1 for $\eta_{D,S} = 0.1, \ldots, 0.8$, and steps of 0.05 for $\eta_{D,S} = 0.85, \ldots, 0.99$. The normalization of the profiles is also accomplished by applying a L2-norm.

6.2.2.1. Test Case I. Results

Remember that Test Case I consists on the classification of 48 different trajectories of 5 aircraft utilizing a database of 6 synthetic aircraft. As before, an incremental study is carried out along this whole subsection.

Test Case I.a. Synthetic Profiles Vs. Synthetic Profiles

As usual, a first ideal classification of a test set consisting of synthetic profiles is done with the purpose of predicting the behaviour and evolution of the algorithm under review. In Figure 6.33a the tendency of the recognition performance with the variation of m depending on η is presented for Test Case I.a where, as noted, different thresholds for test and training samples are set. Each curve in the figure depicts the evolution of the recognition rates according to a fixed threshold of the training set (η_S) while varying the threshold of the test set (η_D). The equivalence between the selected η_D and η_S and parameter m is depicted in Figure 6.33b where the mean value of the obtained parameter is given for both test and training sets (m_D and m_S respectively). As expected, a higher η means a higher m and in particular in this test case, as we are dealing with the same ideal profiles in both sets, the mean values of the respective parameters m_D and m_S are basically the same.

To clarify the results given in Figure 6.33a, the corresponding recognition rates are given also in Table 6.15. Similarly to the study of F_u and F_w, this ideal case returns a perfect recognition rate independently of the values of the *softweigths*. This result was expected due to the same ideal nature of both sets, additionally, it denotes that the algorithm should be further evaluated in the subsequent sections to draw conclusions about its performance.

Table 6.15: Subcase I.a. gMSM Recognition rates

Test Case I.a. Recognition rates varying η_D and η_S (%)												
	η_S											
η_D	**0.99**	**0.95**	**0.9**	**0.85**	**0.8**	**0.7**	**0.6**	**0.5**	**0.4**	**0.3**	**0.2**	**0.1**
0.99	100.0	100.0	100.0	100.0	100.0	100.0	100.0	100.0	100.0	100.0	100.0	100.0
0.95	100.0	100.0	100.0	100.0	100.0	100.0	100.0	100.0	100.0	100.0	100.0	100.0
0.9	100.0	100.0	100.0	100.0	100.0	100.0	100.0	100.0	100.0	100.0	100.0	100.0
0.85	100.0	100.0	100.0	100.0	100.0	100.0	100.0	100.0	100.0	100.0	100.0	100.0
0.8	100.0	100.0	100.0	100.0	100.0	100.0	100.0	100.0	100.0	100.0	100.0	100.0
0.7	100.0	100.0	100.0	100.0	100.0	100.0	100.0	100.0	100.0	100.0	100.0	100.0
0.6	100.0	100.0	100.0	100.0	100.0	100.0	100.0	100.0	100.0	100.0	100.0	100.0
0.5	100.0	100.0	100.0	100.0	100.0	100.0	100.0	100.0	100.0	100.0	100.0	100.0
0.4	100.0	100.0	100.0	100.0	100.0	100.0	100.0	100.0	100.0	100.0	100.0	100.0
0.3	100.0	100.0	100.0	100.0	100.0	100.0	100.0	100.0	100.0	100.0	100.0	100.0
0.2	100.0	100.0	100.0	100.0	100.0	100.0	100.0	100.0	100.0	100.0	100.0	100.0
0.1	100.0	100.0	100.0	100.0	100.0	100.0	100.0	100.0	100.0	100.0	100.0	100.0

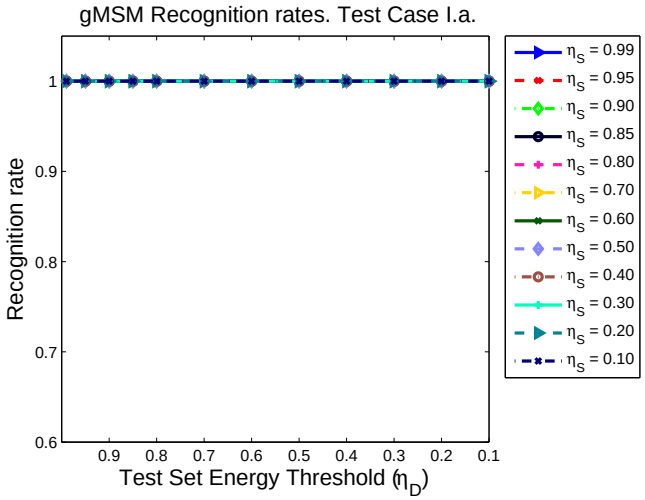

(a) gMSM recognition rates

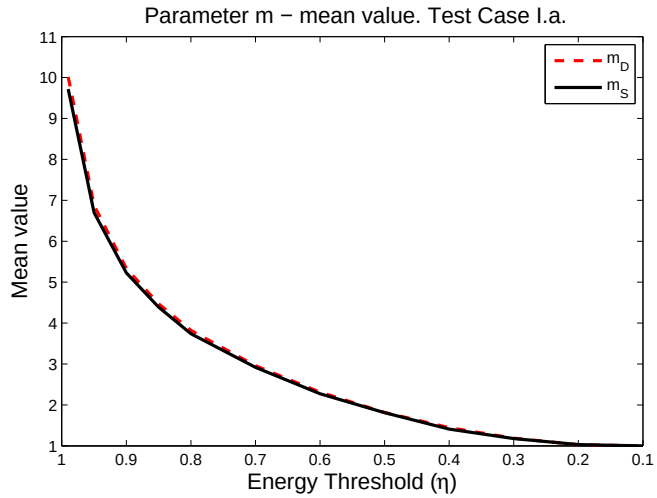

(b) Mean value of parameter m

Figure 6.33: Test Case I.a. gMSM performance with dynamic *softweights*

Test Case I.b. Synthetic Profiles with AWGN Vs. Synthetic Profiles

The previous section, just as the study of F_w and F_u when evaluating Test Case I.a and II.a, does not return a conclusion about which would be the best value of parameter m in order to create the *softweights* that will control the importance of each eigenvector in the recognition process. However, it is seen that gMSM algorithm is, at a first glance, as worth considering as F_w and F_u since when both sets of profiles are exactly the same (synthetic profiles), recognition rates of 100% are reached.

Test Case I.b is thought to evaluate the robustness of the algorithm against unwanted information that profiles may have, more specifically against noise. So, by adding AWGN to the test set and applying the same sweep of thresholds η_D and η_S as in Test Case I.a, the recognition rates obtained for this experiment are shown in Figure 6.34 and its corresponding subfigures.

The mean value of the corresponding m for each value of SNR is given in Figure 6.35 where, as can be appreciated, the noisier the test set, the higher the parameter value for a given threshold. For the training set, as it is not applied any additional effect, that is, it is just formed by the synthetic profiles,

the same mean values of m_S as the previous subcase are obtained.

As expected, the higher the value of the SNR, the best results are returned; with SNR = 10 dB, the success rates are always above 95% and the best results are obtained for thresholds $\eta_D \leq \eta_S$.

The addition of noise causes a degradation of the test set and therefore, as happened in the experiments of section 6.2.1, where for the same energy threshold, the subspace dimensionality became larger when adding noise, here, this is translated into a higher m and hence, into a bigger number of *softweights* with a value of 1, just as Figure 6.35 depicts. Therefore, selecting smaller thresholds will mean that a smaller number of *softweights* are equal to 1 and thus, their eigenvectors are not all considered equally important. When changing the SNR to 5 dB, a degradation in the recognition rates takes place, just as section 6.2.1. Figure 6.34b and Table 6.17 illustrate this fact, where now, despite this degradation, the recognition rates still maintain a very high percentage of success, overall, above 94%. As said, the thresholds should be diminished in order to prevent the effect of the noise. In any case, keeping both thresholds at the same value also returns very good recognition rates, and if the threshold of the test set is set smaller than the threshold of the training set the best recognition results can be achieved, that is, $\eta_D \leq \eta_S$.

Continuing with the noise degradation, Figures 6.34c 6.34d and their corresponding Tables 6.18 and 6.19 contain, respectively, the algorithm results for SNR = 0 dB and SNR = -5 dB. In both cases the best results are obtained for the threshold $\eta_D = 0.5$ and for different values of η_S, although, obviously the rates are a bit worse for SNR = -5 dB (97.92%). The tendency of obtaining good results when both thresholds are set to equal values still holds but apparently, when the noise is very high (negative SNR), selecting high thresholds to calculate m is not a good option (the obtained recognition rate when both η_D and η_S are 0.99 is 89.17% when the SNR is -10 dB). It seems that selecting a $\eta_D \leq \eta_S$ is more obvious in that case, and setting η_D around 0.5 is the best option. Lastly, Figure 6.34e and Table 6.20 show the results for the last value of SNR, here the profiles of the test set are highly degraded by the noise and consequently, so are their eigenvalues and eigenvectors. One more time, the effect of the noise causes the energy threshold of the test set to diminish in order to obtain the best recognition results.

After this noise evaluation, it can be said that this algorithm is quite robust against it only if the selection of parameter m is appropriate. Regarding the value of this parameter, it has been seen that the higher the contamination of the test set, the smaller its corresponding m_D should be, and regarding m_S, since the training set is not affected by the unwanted noise, the bet results are usually obtained for a value of η_S around 0.9, which corresponds to a mean value of $m_S \sim 5$.

Very good recognition rates are obtained in general for this algorithm. For this same test case, F_u and F_w achieved also really good recognition results, however, gMSM outperforms those results in the cases of poor SNR considering the appropriate energy threshold selection for each algorithm.

For example, recall the best situation where SNR = 10 dB, it was shown that the best results for these two metrics F_u and F_w were 99.58% and 99.17% respectively, on the other hand, applying gMSM as a classifier, success rates of 99.17% are reached, just as F_w. On the other hand, in the worst situation (SNR = -10 dB), F_u and F_w with their optimum energy threshold reached success rates of 95% and 92.92% respectively, good results also, but gMSM improves these results since it obtains a 97.50% of success. Therefore, apparently gMSM exhibits a higher robustness against noise than the other two algorithms. Regarding the tolerance to the threshold selection, it was shown for this very same test case, that F_u was highly affected by a wrong selection of this threshold while F_w could achieve fairly good results even with a non-optimum one. For the case being, gMSM can also reach fairly good results with non-optimum thresholds, similarly to metric F_w; however, for the best results the thresholds should follow $\eta_D \leq \eta_S$.

Table 6.16: Subcase I.b. gMSM Recognition rates - SNR = 10 dB

Test Case I.b. Recognition rates varying η_D and η_S (%) - $AWGN_{SNR=10dB}$												
	η_S											
η_D	**0.99**	**0.95**	**0.9**	**0.85**	**0.8**	**0.7**	**0.6**	**0.5**	**0.4**	**0.3**	**0.2**	**0.1**
0.99	97.08	96.25	96.25	96.67	96.67	96.67	95.42	95.83	96.67	95.42	95.83	95.00
0.95	97.92	97.50	97.92	98.33	98.33	97.92	96.67	95.83	96.67	97.08	95.83	96.25
0.9	98.75	98.33	98.33	98.33	98.33	97.92	96.67	97.08	97.50	97.50	96.25	96.67
0.85	97.50	98.75	98.75	97.92	97.92	98.33	97.50	97.50	97.08	97.08	97.50	96.67
0.8	98.33	97.92	98.33	98.33	98.33	99.17	97.50	97.50	96.67	97.08	97.92	97.50
0.7	98.75	98.75	98.75	98.33	98.33	98.33	97.92	97.50	98.33	97.92	97.50	97.92
0.6	99.17	98.75	98.33	98.33	98.33	99.17	98.33	99.17	97.50	98.33	98.33	97.50
0.5	98.75	98.75	98.75	98.75	98.75	98.75	98.75	98.75	98.75	98.33	97.50	97.50
0.4	98.75	98.75	98.75	98.75	98.75	98.75	98.75	98.75	98.75	98.75	98.33	97.92
0.3	98.75	98.75	98.75	98.75	98.75	98.75	98.75	98.75	98.75	98.75	98.33	97.92
0.2	98.75	98.75	98.75	98.75	98.75	98.75	98.75	98.75	98.33	98.33	98.33	98.33
0.1	98.75	98.75	98.75	98.75	98.75	98.75	98.75	98.75	98.75	98.33	98.33	98.33

Table 6.17: Subcase I.b. gMSM Recognition rates - SNR = 5 dB

Test Case I.b. Recognition rates varying η_D and η_S (%) - $AWGN_{SNR=5dB}$												
	η_S											
η_D	**0.99**	**0.95**	**0.9**	**0.85**	**0.8**	**0.7**	**0.6**	**0.5**	**0.4**	**0.3**	**0.2**	**0.1**
0.99	95.00	94.58	94.58	94.17	94.58	94.58	93.33	93.33	92.92	93.33	93.75	94.58
0.95	96.25	96.67	96.67	95.83	95.42	96.67	95.42	95.42	95.42	95.00	94.17	94.17
0.9	96.67	96.67	95.83	95.83	96.25	96.67	95.83	95.83	95.00	95.42	95.42	95.42
0.85	96.25	96.67	95.83	96.25	97.08	96.25	95.83	96.25	96.25	96.25	95.83	95.42
0.8	96.25	97.92	97.08	97.08	97.08	97.08	96.25	96.25	95.83	95.42	95.42	96.25
0.7	98.75	99.17	98.75	97.92	97.50	97.50	97.50	96.67	96.25	95.42	96.25	96.25
0.6	98.75	97.92	98.75	98.75	98.75	98.33	97.92	96.67	97.08	97.08	97.92	96.25
0.5	98.75	98.75	98.75	98.75	98.75	98.75	98.75	98.33	98.33	97.08	97.08	96.67
0.4	98.75	98.75	98.75	98.75	98.75	98.75	98.75	98.75	98.75	98.33	97.92	97.50
0.3	98.75	98.75	98.75	98.75	98.75	98.75	98.75	98.33	98.75	98.33	98.33	98.33
0.2	98.33	98.33	98.75	98.75	98.75	98.75	98.75	98.75	98.75	98.75	97.92	98.33
0.1	98.33	98.75	98.33	98.75	98.75	98.75	98.75	98.75	98.75	98.33	97.92	97.92

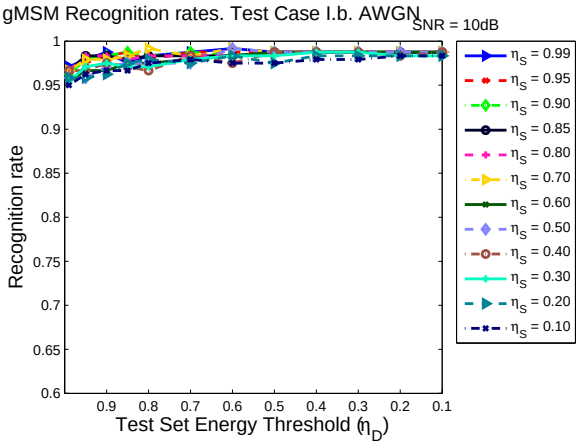

(a) SNR = 10 dB

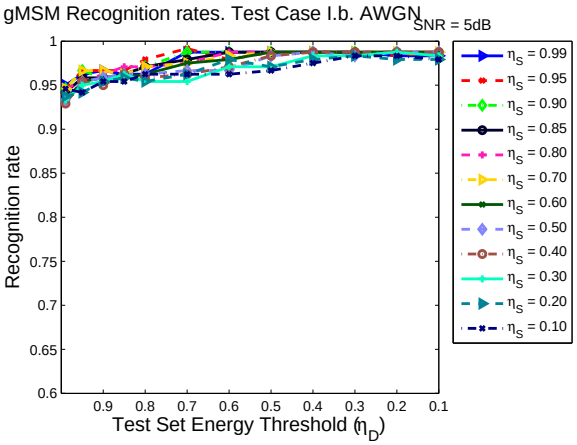

(b) SNR = 5 dB

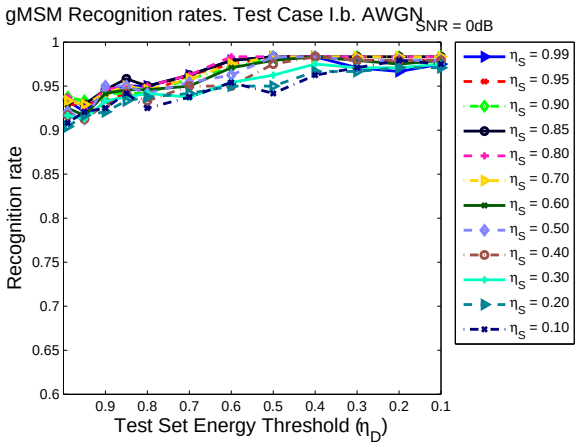

(c) SNR = 0 dB

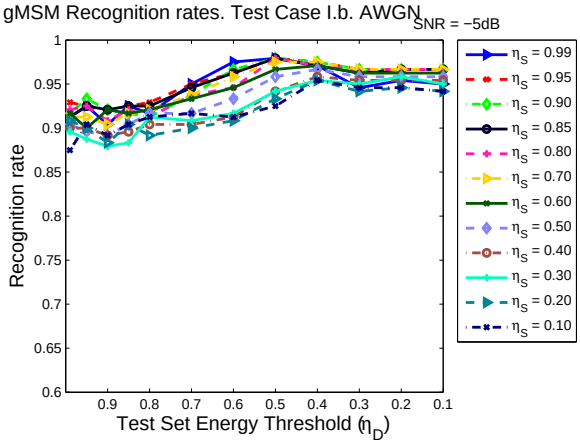

(d) SNR = -5 dB

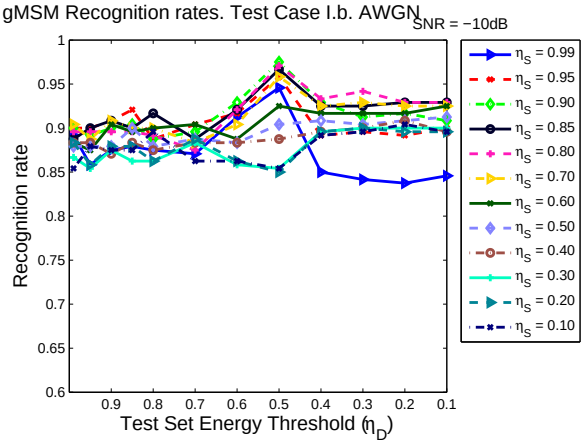

(e) SNR = -10 dB

Figure 6.34: Test Case I.b. gMSM performance with dynamic *softweights* for different SNR

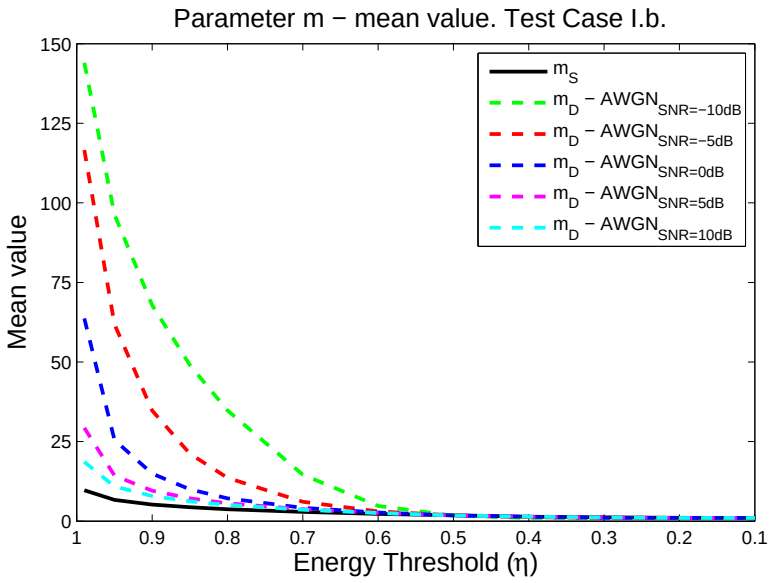

Figure 6.35: Test Case I.b. Mean value of parameter m

Table 6.18: Subcase I.b. gMSM Recognition rates - SNR = 0 dB

Test Case I.b. Recognition rates varying η_D and η_S (%) - $AWGN_{SNR=0dB}$												
	η_S											
η_D	**0.99**	**0.95**	**0.9**	**0.85**	**0.8**	**0.7**	**0.6**	**0.5**	**0.4**	**0.3**	**0.2**	**0.1**
0.99	93.33	92.92	93.75	93.33	93.75	93.33	92.50	92.08	91.67	91.67	90.42	90.83
0.95	92.08	92.92	93.33	92.92	92.50	92.92	91.67	91.25	91.25	91.25	91.67	92.08
0.9	94.58	93.33	94.17	94.58	94.58	94.17	94.17	95.00	92.92	93.33	92.08	92.50
0.85	95.00	94.17	94.17	95.83	95.00	95.00	94.58	95.00	94.17	93.75	93.33	94.17
0.8	95.00	94.17	94.17	95.00	95.00	94.58	94.58	94.17	93.33	94.17	93.75	92.50
0.7	96.25	96.25	95.83	96.25	96.25	95.83	95.00	95.42	95.00	93.75	94.17	93.75
0.6	97.92	97.50	97.08	97.92	98.33	97.50	97.08	96.25	95.00	95.42	95.00	95.42
0.5	98.33	98.33	98.33	98.33	98.33	98.33	97.92	98.33	97.50	96.25	95.00	94.17
0.4	98.33	98.33	98.33	98.33	98.33	98.33	98.33	98.33	98.33	97.50	96.67	96.25
0.3	97.08	97.92	98.33	98.33	98.33	98.33	97.92	97.92	97.92	97.08	96.67	97.08
0.2	96.67	97.92	98.33	98.33	98.33	98.33	97.50	97.92	97.92	97.08	97.08	97.92
0.1	97.50	97.92	98.33	98.33	98.33	98.33	97.92	97.92	97.92	97.50	97.08	97.50

Table 6.19: Subcase I.b. gMSM Recognition rates - SNR = -5 dB

Test Case I.b. Recognition rates varying η_D and η_S (%) - $AWGN_{SNR=-5dB}$												
	η_S											
η_D	**0.99**	**0.95**	**0.9**	**0.85**	**0.8**	**0.7**	**0.6**	**0.5**	**0.4**	**0.3**	**0.2**	**0.1**
0.99	91.25	92.92	91.67	91.25	92.08	91.25	91.67	90.42	90.00	89.58	90.83	87.50
0.95	92.50	92.50	93.33	92.50	92.50	91.25	90.00	89.58	90.00	88.75	90.00	90.42
0.9	90.42	92.08	92.08	92.08	90.83	90.42	92.08	89.17	89.17	87.92	88.33	89.17
0.85	92.50	92.50	91.67	92.50	92.08	91.67	91.67	90.42	89.58	88.33	90.42	90.42
0.8	91.67	92.92	91.25	92.50	91.25	92.08	92.08	91.67	90.42	91.25	89.17	91.25
0.7	95.00	95.00	93.75	94.58	93.75	93.75	93.33	91.67	90.42	90.83	90.00	91.67
0.6	97.50	96.25	96.67	96.25	94.58	95.83	94.58	93.33	91.25	91.67	90.83	91.25
0.5	97.92	97.92	97.92	97.92	97.92	97.50	96.67	95.83	94.17	94.17	93.33	92.50
0.4	97.08	97.50	97.50	97.08	97.08	97.50	97.08	96.67	95.83	95.42	95.42	95.42
0.3	94.58	96.67	96.67	96.25	96.67	96.67	96.25	95.83	95.42	95.00	94.17	94.58
0.2	95.42	96.67	96.67	96.67	96.67	96.67	96.25	95.83	95.42	95.83	94.58	94.58
0.1	95.00	96.67	96.67	96.67	96.67	96.67	96.25	95.83	95.42	95.00	94.17	94.17

Table 6.20: Subcase I.b. gMSM Recognition rates - SNR = -10 dB

Test Case I.b. Recognition rates varying η_D and η_S (%) - $AWGN_{SNR=-10dB}$												
	η_S											
η_D	**0.99**	**0.95**	**0.9**	**0.85**	**0.8**	**0.7**	**0.6**	**0.5**	**0.4**	**0.3**	**0.2**	**0.1**
0.99	89.17	90.00	90.00	88.75	89.58	90.42	88.33	87.92	88.33	86.67	88.33	85.42
0.95	85.83	90.00	89.17	90.00	89.58	88.75	87.50	87.92	88.33	85.42	85.83	87.92
0.9	87.50	90.83	90.00	90.83	89.58	90.83	90.42	87.92	87.08	87.50	87.92	87.50
0.85	87.92	92.08	90.42	90.00	89.58	90.00	89.58	90.00	88.33	86.25	87.92	87.50
0.8	87.50	88.75	88.75	91.67	89.17	90.00	90.00	87.92	87.50	86.25	86.25	89.58
0.7	87.08	90.42	89.58	88.75	87.50	88.33	90.42	88.75	88.33	88.33	88.75	86.25
0.6	91.25	91.67	92.92	92.08	92.08	90.42	88.75	88.33	88.33	85.83	86.25	86.25
0.5	94.58	95.83	97.50	96.67	97.08	95.83	92.50	90.42	88.75	85.42	85.00	85.42
0.4	85.00	89.17	92.92	92.50	93.33	92.50	91.67	90.83	89.58	89.58	89.58	89.17
0.3	84.17	89.58	91.25	92.50	94.17	92.92	91.67	90.42	90.00	90.00	90.00	89.58
0.2	83.75	89.17	91.67	92.92	92.92	92.50	91.67	90.83	90.83	90.00	89.58	90.42
0.1	84.58	90.00	90.83	92.92	92.92	92.50	92.50	91.25	89.58	90.00	89.58	89.58

Test Case I.c. Synthetic misaligned Profiles with AWGN Vs. Synthetic Profiles

After the evaluation of the behaviour of gMSM against noise, it was seen that even though the noise affects negatively the recognition results, keeping $\eta_D \leq \eta_S$ could bring to good recognition rates and when these are set to their optimum value, the results can outperform those obtained with the previously studied metrics, F_u and F_w. In this section, additional misalignment is applied in order to keep evaluating the effects of perturbing the profiles in the recognition performance of gMSM algorithm . As it was shown in section 6.2.1, the effect of profiles' misalignment is less relevant in the obtained results than the addition of noise, but it is really important to study it in depth since the profiles' alignment is a critical point during the recognition process.

In Figure 6.36 and its subfigures, the recognition performance of gMSM algorithm changing the value of the *softweights* according to η_D and η_S is given, and in Figure 6.37 the corresponding mean value of the obtained m_D and m_S is depicted. At fist sight, there is almost no difference in recognition performance and mean m between Test Case I.b and c. However, although slightly, the recognition results have been altered due to the profiles' misalignment. Tables 6.21 to 6.25 present this almost negligible difference in the recognition performance. As these tables illustrate, the recognition rates obtained for the optimum thresholds have experienced a reduction, and not only that, but also these optimum thresholds have changed from Test Case I.b. The analysis of Table 6.21 reveals that the addition of a little misalignment of profiles when SNR = 10 dB has caused a reduction in the best recognition rates from 99.17% to 97.8% and also, for obtaining these values, the energy thresholds have been also degraded, while Test Case I.b obtained the best success rate for $\eta_S = 0.99$ and $\eta_D = 0.6$, now, with an additional unwanted effect, the optimum thresholds are $\eta_S = 0.9$ and $\eta_D \leq 0.4$. When the SNR is 5 dB, the best success rate obtained is 96.25% with selected thresholds $\eta_S = 0.95$ and $\eta_D = 0.4$, 3 percentage points less than Test Case I.b and also with a reduction of one of the thresholds (η_D). In the case when the AWGN provides SNR = 0 dB the best recognition rates (95.42%) are obtained for an even more reduced value of thresholds ($\eta_S = 0.8$ and $\eta_D \leq 0.3$), which gives us the idea that the more corrupted the test set is, the lesser the value of parameter m should be to get the best results. Getting into the negative values of SNR, it is found that for SNR = -5 dB the results of Test Case I.b have been reduced until obtaining a success rate of 94.58% when $\eta_S = 0.7$ and $\eta_D \leq 0.3$, and finally the worst case of SNR returns a recognition rate of 89.58% of success when $\eta_S = 0.9$ and $\eta_D = 0.5$. In this last case, the effect of the profiles' misalignment is clearly significant, since even if the rule of setting $\eta_D \leq \eta_S$ is followed, the performance of the algorithm is not as good as expected, anyway, the study of metrics F_u and F_w showed a similar tendency in Test Case I.c with SNR = -10 dB, where the performance of both algorithms experienced a significant drop.

Similar to the aforementioned metrics, not only the success rates have suffered a reduction, but also the threshold for selecting the optimum m. After evaluating the behaviour of the system with ideal scenarios, it is clear that $\eta_D \leq \eta_S$, since the test set is the one with the additional unwanted information and therefore, the one with distorted eigenvalues and eigenvectors. It can be said that, generally, taking $0.4 \geq \eta_D \geq 0.1$ and $0.9 \geq \eta_S \geq 0.6$ good recognition results are expected even if the profiles in the input are very corrupted. The corresponding m_D and m_S mean values seen in Figure 6.37 would be $1.33 \geq m_D \geq 1$ and $5.23 \geq m_S \geq 2.91$ for the best case (SNR = 10 dB). As seen, the noisier the input, the closer m_D should be set to 1, which is quite related to the case of F_u and F_w. Remember that with those algorithms when the input was really corrupted, the energy threshold had to be set to very low values, meaning that very few singular vectors would form the subspace. In gMSM, it means that very few eigenvectors will have the same importance while the rest will be getting less relevance proportionally to the selected m-th eigenvalue.

Table 6.21: Subcase I.c. gMSM Recognition rates - SNR = 10 dB

Test Case I.c. Recognition rates varying η_D and η_S (%) - $AWGN_{SNR=10dB}$												
	η_S											
η_D	**0.99**	**0.95**	**0.9**	**0.85**	**0.8**	**0.7**	**0.6**	**0.5**	**0.4**	**0.3**	**0.2**	**0.1**
0.99	89.58	87.92	87.92	87.92	88.33	89.17	89.17	89.58	88.75	87.92	88.33	88.33
0.95	91.25	92.92	92.92	90.83	89.17	89.58	88.75	89.58	90.00	89.58	89.58	89.58
0.9	92.08	93.33	94.17	93.75	92.08	90.83	91.25	90.83	90.83	90.42	90.42	90.42
0.85	92.50	93.75	94.17	91.67	92.08	91.67	91.67	91.25	90.42	90.42	90.42	90.42
0.8	91.67	93.33	94.17	93.33	93.33	92.08	92.50	92.50	91.25	90.83	91.25	91.25
0.7	93.75	95.00	95.42	94.17	94.17	93.75	93.75	92.50	91.67	91.25	91.67	91.67
0.6	93.33	95.83	95.42	95.00	94.58	94.58	94.58	92.50	92.08	92.08	91.67	91.67
0.5	93.75	95.83	95.83	95.83	95.42	95.00	95.42	94.58	93.75	92.92	92.50	92.08
0.4	94.58	96.25	97.08	96.25	95.42	95.42	96.67	95.42	94.58	93.75	92.50	92.50
0.3	94.58	96.25	97.08	96.25	95.83	96.25	97.08	95.83	95.00	94.58	94.17	94.17
0.2	94.58	96.25	97.08	96.25	95.83	96.25	97.08	95.83	95.00	94.58	94.17	94.17
0.1	94.58	96.25	97.08	96.25	95.83	96.25	97.08	95.83	95.00	94.58	94.17	94.17

Table 6.22: Subcase I.c. gMSM Recognition rates - SNR = 5 dB

Test Case I.c. Recognition rates varying η_D and η_S (%) - $AWGN_{SNR=5dB}$												
	η_S											
η_D	**0.99**	**0.95**	**0.9**	**0.85**	**0.8**	**0.7**	**0.6**	**0.5**	**0.4**	**0.3**	**0.2**	**0.1**
0.99	88.75	86.67	86.67	85.83	86.25	86.25	85.42	85.83	86.67	87.08	86.67	86.67
0.95	90.42	89.17	90.00	89.17	88.33	88.75	88.33	88.75	88.33	87.92	87.50	87.50
0.9	90.83	91.25	92.08	91.25	90.00	90.00	89.58	90.42	88.75	88.75	89.17	89.17
0.85	91.67	91.67	93.33	91.67	91.25	90.83	91.25	90.83	89.58	90.00	90.00	90.00
0.8	90.83	91.67	92.08	91.67	92.08	92.50	92.50	91.67	90.83	90.83	91.25	91.25
0.7	92.08	92.50	92.50	92.08	92.92	92.08	92.92	91.25	90.83	90.00	90.42	90.42
0.6	93.75	95.00	94.17	92.92	93.75	92.50	92.50	92.50	91.25	91.25	90.83	91.25
0.5	93.75	95.42	94.58	93.75	94.17	92.92	93.33	93.75	92.50	91.67	92.92	93.33
0.4	93.75	96.25	95.00	94.17	93.75	93.33	93.75	94.58	93.33	92.08	92.92	93.33
0.3	93.33	95.83	95.00	95.00	94.58	95.42	94.58	95.00	94.17	93.33	93.33	93.33
0.2	93.33	95.42	95.00	95.00	94.58	95.42	94.58	95.00	94.17	93.33	93.33	93.33
0.1	93.33	95.42	95.00	95.00	94.58	95.42	94.58	95.00	94.17	93.33	93.33	93.33

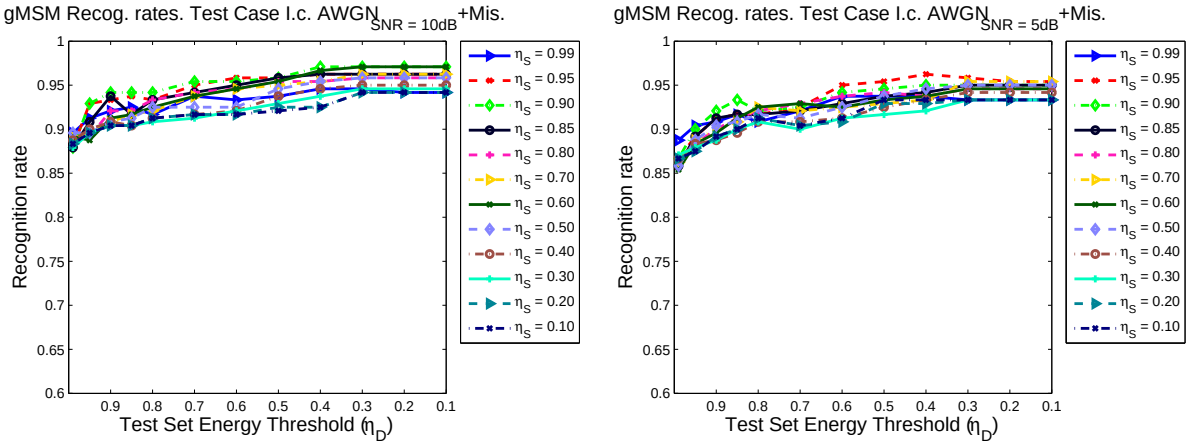

(a) SNR = 10 dB

(b) SNR = 5 dB

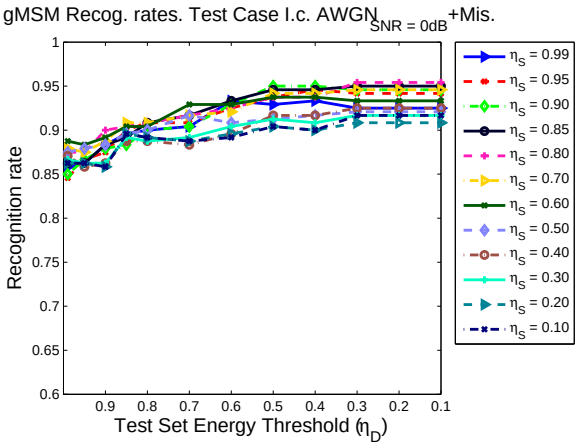

(c) SNR = 0 dB

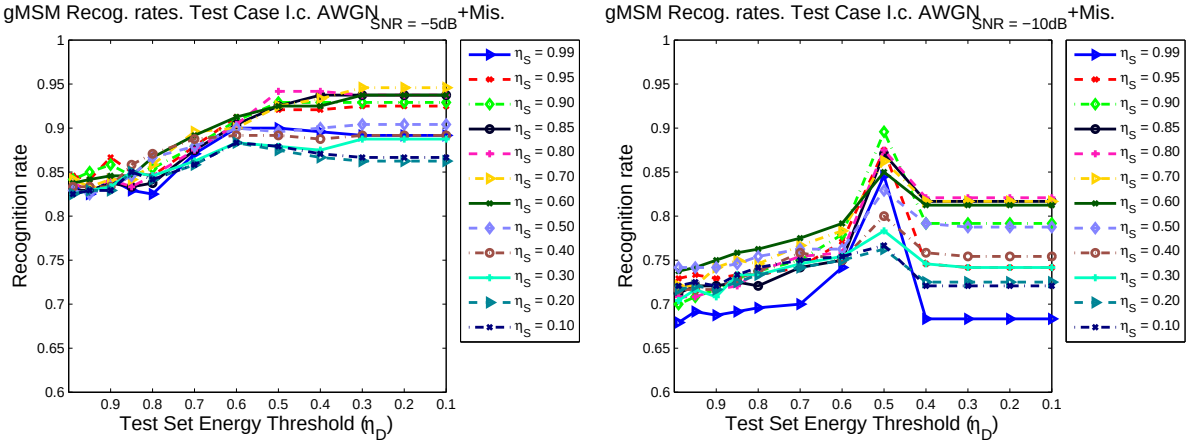

(d) SNR = -5 dB

(e) SNR = -10 dB

Figure 6.36: Test Case I.c. gMSM performance with dynamic *softweights* for different SNR

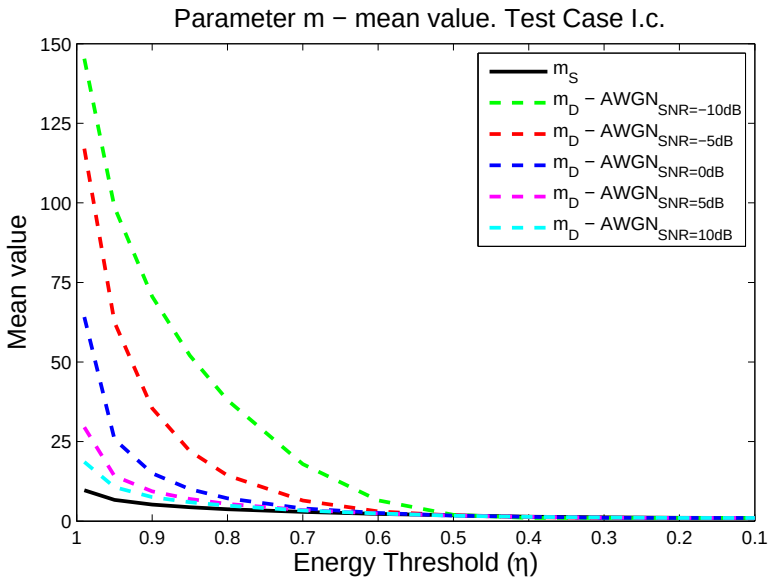

Figure 6.37: Test Case I.c. Mean value of parameter m

Table 6.23: Subcase I.c. gMSM Recognition rates - SNR = 0 dB

Test Case I.c. Recognition rates varying η_D and η_S (%) - $AWGN_{SNR=0dB}$												
	η_S											
η_D	**0.99**	**0.95**	**0.9**	**0.85**	**0.8**	**0.7**	**0.6**	**0.5**	**0.4**	**0.3**	**0.2**	**0.1**
0.99	85.83	84.58	85.00	86.25	87.50	87.92	88.75	87.50	87.08	86.67	86.25	86.25
0.95	86.25	86.67	86.67	86.25	87.50	87.50	88.33	87.92	85.83	86.25	86.25	86.25
0.9	88.33	87.50	87.92	88.33	90.00	88.75	89.17	88.33	86.25	86.25	85.83	85.83
0.85	89.58	90.00	88.33	89.17	90.42	90.83	90.42	89.58	88.75	89.17	89.58	89.58
0.8	90.00	90.83	90.00	90.83	90.83	90.83	90.42	90.00	88.75	88.75	89.17	89.17
0.7	90.42	90.83	90.42	91.67	91.67	91.67	92.92	91.67	88.33	89.17	88.75	88.75
0.6	93.33	92.50	92.92	93.33	92.50	92.08	92.92	90.83	89.58	90.42	89.58	89.17
0.5	92.92	93.75	95.00	94.58	93.75	94.17	93.75	91.25	91.67	91.25	90.42	90.42
0.4	93.33	94.58	95.00	94.58	93.75	94.17	93.75	91.67	91.67	90.83	90.00	90.00
0.3	92.50	94.17	94.58	95.00	95.42	94.58	93.33	92.08	92.50	91.67	90.83	91.67
0.2	92.50	94.17	94.58	95.00	95.42	94.58	93.33	92.08	92.50	91.67	90.83	91.67
0.1	92.50	94.17	94.58	95.00	95.42	94.58	93.33	92.08	92.50	91.67	90.83	91.67

Table 6.24: Subcase I.c. gMSM Recognition rates - SNR = -5 dB

Test Case I.c. Recognition rates varying η_D and η_S (%) - $AWGN_{SNR=-5dB}$												
	η_S											
η_D	**0.99**	**0.95**	**0.9**	**0.85**	**0.8**	**0.7**	**0.6**	**0.5**	**0.4**	**0.3**	**0.2**	**0.1**
0.99	83.33	84.58	84.17	82.92	83.75	84.17	83.75	82.92	83.33	82.50	82.50	82.50
0.95	82.50	84.17	85.00	82.92	82.92	83.33	84.17	82.50	83.33	82.92	82.92	82.92
0.9	84.17	86.67	85.83	83.75	84.17	84.17	84.58	83.33	83.33	83.33	82.92	82.92
0.85	82.92	85.00	84.58	83.33	83.33	84.17	84.58	84.58	85.83	85.00	85.00	85.00
0.8	82.50	84.58	85.42	83.75	84.58	85.83	86.67	86.67	87.08	84.58	84.17	84.17
0.7	87.08	87.92	87.92	87.50	87.50	89.58	89.17	87.92	88.75	86.25	85.83	85.83
0.6	90.00	91.25	90.83	90.42	90.42	90.00	91.25	90.00	89.17	88.33	88.33	88.33
0.5	90.00	92.08	92.92	92.50	94.17	92.50	92.50	89.58	89.17	87.92	87.50	87.92
0.4	89.58	92.08	92.92	93.75	94.17	93.33	92.50	90.00	88.75	87.50	86.67	87.08
0.3	89.17	92.50	92.92	93.75	93.75	94.58	93.75	90.42	89.17	88.75	86.25	86.67
0.2	89.17	92.50	92.92	93.75	93.75	94.58	93.75	90.42	89.17	88.75	86.25	86.67
0.1	89.17	92.50	92.92	93.75	93.75	94.58	93.75	90.42	89.17	88.75	86.25	86.67

Table 6.25: Subcase I.c. gMSM Recognition rates - SNR = -10 dB

Test Case I.c. Recognition rates varying η_D and η_S (%) - $AWGN_{SNR=-10dB}$												
	η_S											
η_D	**0.99**	**0.95**	**0.9**	**0.85**	**0.8**	**0.7**	**0.6**	**0.5**	**0.4**	**0.3**	**0.2**	**0.1**
0.99	67.92	72.92	70.00	71.25	70.83	72.08	73.75	74.17	71.67	70.42	71.67	72.08
0.95	69.17	73.33	70.83	72.08	70.83	72.08	74.17	74.17	71.67	71.67	72.08	72.50
0.9	68.75	72.92	71.67	72.08	71.67	74.17	75.00	74.17	71.67	70.83	71.67	72.08
0.85	69.17	73.33	72.92	72.50	72.08	75.00	75.83	74.58	72.92	73.33	72.50	73.33
0.8	69.58	73.33	73.75	72.08	73.75	74.58	76.25	75.42	73.75	73.33	73.33	74.17
0.7	70.00	74.17	75.00	74.17	75.42	76.67	77.50	76.25	75.83	74.58	74.17	75.00
0.6	74.17	77.08	77.92	75.00	75.83	78.33	79.17	76.25	75.00	75.42	75.00	75.42
0.5	84.58	87.50	89.58	87.08	87.50	86.25	85.00	82.92	80.00	78.33	76.25	76.67
0.4	68.33	74.58	79.17	81.67	82.08	81.67	81.25	79.17	75.83	74.58	72.50	72.08
0.3	68.33	74.17	79.17	81.67	82.08	81.67	81.25	78.75	75.42	74.17	72.50	72.08
0.2	68.33	74.17	79.17	81.67	82.08	81.67	81.25	78.75	75.42	74.17	72.50	72.08
0.1	68.33	74.17	79.17	81.67	82.08	81.67	81.25	78.75	75.42	74.17	72.50	72.08

Test Case I.d. Actual Profiles Vs. Synthetic Profiles

As previously done with F_u and F_w in section 6.2.1.1, the evaluation of gMSM algorithm in a more realistic scenario is evaluated in this section. In the preceding subsections, it has been seen that just as F_w, gMSM is quite robust against noise but unlike this metric, the energy threshold that controls the *softweighting* parameter, m, should be selected more carefully. Indeed, the thresholds should follow the rule: $\eta_D \leq \eta_S$, and just as the previous subcase c showed, good recognition results will be expected for $0.4 \geq \eta_D \geq 0.1$ and $0.9 \geq \eta_S \geq 0.6$ despite having corrupted profiles as input samples.

Figure 6.38a illustrates the obtained success rates for every value of η_D and η_S when classifying actual range profiles with a database of synthetic profiles and Table 6.26 gathers these success rates; their corresponding mean values of parameter m are depicted in Figure 6.38b. Just as occurred with the prior metrics, the results of this Test Case I.d noticeably differ from the ones obtained in Test Case I.a to c due to the fact that now the input samples and the database of potential targets strongly deviate. Remember that on the one hand, the electromagnetic simulation did not account for every scattering effect that may occur in an actual measurement and the models utilized to run these simulations are rough replicas of real aircraft, and on the other hand, the aspect angles of the actual measurement and the ones utilized for the synthetic profiles may not be exactly the same since these angles have been predicted from the measurement.

Nevertheless, the gMSM algorithm reaches recognition rates of almost 80% when actual profiles are compared with synthetic ones, like metrics F_u and F_w. More specifically, for example, setting both thresholds to 0.5 returns a success rate of 79.17%. The statement that η_D should be set such that its value is equal of smaller than η_S to obtain good results remains true. As expected, good recognition results are obtained for $0.4 \geq \eta_D \geq 0.1$ but on the contrary, the best results are not returned for $0.9 \geq \eta_S \geq 0.6$ but for $\eta_S \leq 0.6$ which translates, according to Figure 6.38b in a mean value of parameter m of $1.06 \geq m_D \geq 1$ and $m_S \leq 2.27$. That is, the higher the difference between input and database, the lower the value of parameter m should be set.

Table 6.26: Subcase I.d. gMSM Recognition rates

Test Case I.d. Recognition rates varying η_D and η_S (%)												
	η_S											
η_D	**0.99**	**0.95**	**0.9**	**0.85**	**0.8**	**0.7**	**0.6**	**0.5**	**0.4**	**0.3**	**0.2**	**0.1**
0.99	68.75	72.92	72.92	72.92	77.08	75.00	72.92	72.92	70.83	70.83	70.83	70.83
0.95	70.83	72.92	72.92	72.92	72.92	70.83	68.75	68.75	68.75	68.75	68.75	68.75
0.9	70.83	75.00	72.92	72.92	70.83	72.92	72.92	75.00	75.00	75.00	75.00	75.00
0.85	70.83	79.17	72.92	79.17	72.92	75.00	72.92	77.08	72.92	75.00	75.00	75.00
0.8	68.75	77.08	75.00	75.00	70.83	70.83	70.83	68.75	66.67	72.92	72.92	72.92
0.7	64.58	79.17	75.00	75.00	75.00	70.83	75.00	79.17	70.83	75.00	75.00	75.00
0.6	62.50	70.83	72.92	75.00	75.00	68.75	72.92	72.92	64.58	72.92	70.83	70.83
0.5	60.42	60.42	66.67	72.92	75.00	72.92	75.00	79.17	70.83	75.00	75.00	75.00
0.4	60.42	60.42	66.67	70.83	70.83	68.75	72.92	79.17	72.92	75.00	77.08	77.08
0.3	60.42	60.42	66.67	70.83	70.83	68.75	72.92	79.17	72.92	75.00	77.08	77.08
0.2	60.42	60.42	66.67	70.83	70.83	68.75	72.92	79.17	72.92	75.00	77.08	77.08
0.1	60.42	60.42	66.67	70.83	70.83	68.75	72.92	79.17	72.92	75.00	77.08	77.08

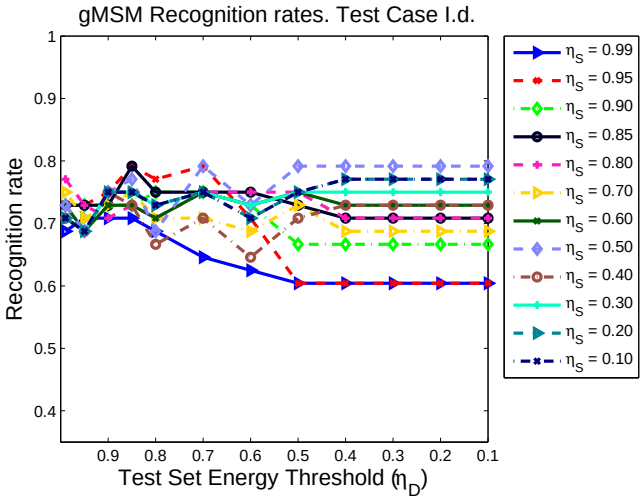

(a) gMSM recognition rates

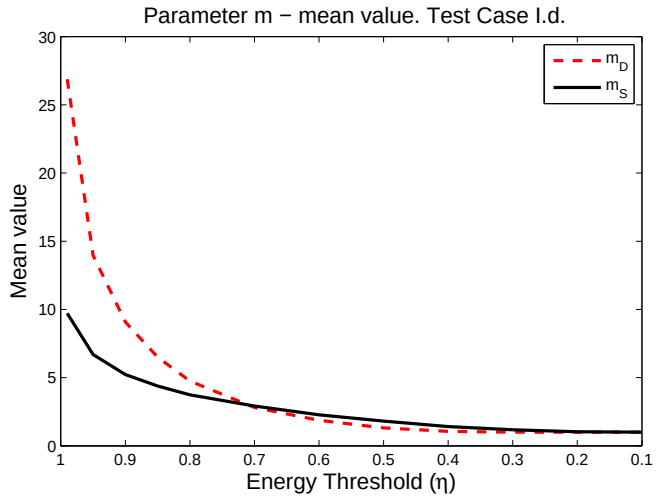

(b) Mean value of parameter m

Figure 6.38: Test Case I.d. gMSM performance with dynamic *softweights*

Regarding the confidence in the recognized aircraft, as before, Figure 6.39 depicts the mean difference between the similarities of the winning aircraft, calculated taking into account the maximum value that gMSM can reach for each threshold. As the graphic presents, the highest mean difference between the winner aircraft and the next is achieved for the thresholds $\eta_S \leq 0.4$ and $\eta_D = 0.8$; however, these thresholds do not meet the rule $\eta_D \leq \eta_S$. Checking the values of η_D and η_S which return the best recognition rates, the combinations that not only achieve the best recognition rate, but also an acceptable confidence degree in the results is $\eta_S \leq 0.4$ and $\eta_D \leq \eta_S$, which corresponds to a mean value of both parameters m_D and m_S very close to 1. Thus, as said, the higher the difference between input and database, the lower the value of parameter m should be set.

The tuning of parameter m adds computational cost to the algorithm, thus, in order to present a faster and more general algorithm with no need to be tuned every time a new test/training sample is introduced, m is eventually wished to be set to a fixed value for all the input samples and the database. Thus, according to the study made along this whole section, the best option would be to select $m_D = m_S = 1$, and with these values the algorithm gives the following results, presented in Table 6.27 in form of a

confusion matrix. As usual, the aircraft with the worst recognition rates are the two Fokker and the best rates are obtained for the two bigger aircraft, B747 and B767. The total average recognition rate obtained for gMSM in this Test Case I.d is 77.08%, in contrast, the confusion matrix of Table 6.8, seen in section 6.2.1 showed that with its optimum energy threshold ($\eta = 0.5$), F_w algorithm returned a total average recognition rate of 72.92%. Therefore, gMSM seems to outperform F_w, especially in the identification of aircraft A310 and F100 where it has achieved a better recognition rate. Nevertheless, as only 48 input samples are present, the results are only a first prediction of the algorithm performance.

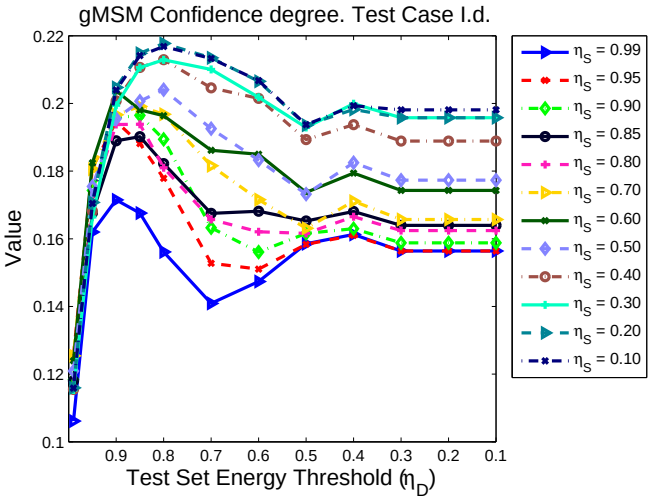

Figure 6.39: Test Case I.d. gMSM mean difference between aircraft similarities

Table 6.27: Subcase I.d. gMSM Confusion matrix; $m_D = m_S = 1$

	A310	**B747**	**B767**	**F028**	**F100**	**B737**	**Success (%)**	**Error (%)**
A310	4	0	0	0	0	0	**100.0**	**0.00**
B747	1	8	1	0	0	0	**80.00**	**20.00**
B767	2	0	9	0	0	0	**81.82**	**18.18**
F028	0	0	0	9	3	1	**69.23**	**30.77**
F100	0	0	0	0	7	3	**70.00**	**30.00**
Average rates							**77.08**	**22.92**

Test Case I. Discussion

Along this Test Case I, the behaviour of gMSM when classifying large sets of range profiles as input samples has been reviewed. Note that only 48 different frames of different aircraft have been utilized along the experiments of this test case, where for the first three subcases the input samples ascend to 240, since 48 frames of 5 synthetic aircraft are considered, while for the last subcase only 48 input samples are classified, each belonging to a specific actual flying aircraft. However, just as said in the discussion of section 6.2.1.1, the number of input samples utilized for these experiments is not enough to draw firm conclusions about the quality of an algorithm, but it helps us understand its operation. Therefore, after the study of Test Cases I .a to .d, the following observations can be made:

- First, Test Case I.a has studied the ideal case of classifying synthetic profiles by means of a database populated with the same synthetic profiles. After the study of algorithms F_u and F_w, that returned a 100% of success rates independently of the energy threshold selected, the achievement of the same ideal results was expected. As foreseen, gMSM has also classified every test sample correctly.

- Taking into account the previous result, for Test Case I.b, where now the input samples have been modified with noise, poorer average recognition rates were expected. Note that the addition of noise causes a degradation of the test set samples and therefore, their eigendecomposition will differ from the ideal case, corrupting the eigenvectors with unwanted information and also the eigenvalues, in fact, it has been seen that the noisier the test set gets, the higher m_D[9] is for a given threshold.

  In this subcase it was observed that when adding noise a degradation of the recognition rates is experienced, just as the previous metrics, but contrary to what was previously thought, better recognition rates are obtained in general for this algorithm in comparison with F_u and F_w considering the appropriate energy threshold for each of the algorithms. However, gMSM is still affected by the *softweighting*, since in contrast to F_u and F_w two thresholds control the value of the *softweights*. As seen, as long as $\eta_D \leq \eta_S$ the results show a high level of success even if the thresholds are not the optimum, similar to F_w. This translates into trying to keep m_D similar to m_S and hence, into having a similar number of eigenvectors in the subspaces with a *softweight* of 1.

- After checking the robustness against noise and seeing that gMSM can be quite robust against it as long as $\eta_D \leq \eta_S$ in principle, Test Case I.c has evaluated an additional corrupting effect, the slightly wrong alignment of the range profiles of the test set, that is, the effect of TRM. It has been seen that even though the effect of noise is more relevant, a little misalignment in the range profiles causes also a degradation in the obtained results. However, a great reduction is not experienced in the recognition rates but in the optimum thresholds, and hence, in the optimum m_D and m_S. One more time, this is due to the fact that the eigenvectors and eigenvalues get more distorted and setting the same threshold as before means a different value of parameter m_D; as noted earlier, the tendency of this algorithm is keeping m_D similar to m_S.

  In comparison with F_u and F_w, since they are all based in the same principles, gMSM keeps the tendency of these metrics of reducing the thresholds η_D and η_S as the input gets sequentially distorted. Nevertheless, the gMSM algorithm seems to slightly outperform the recognition rates, not only for the optimum thresholds but also for the thresholds that follow the rule $\eta_D \leq \eta_S$.

- Lastly, the final evaluation of gMSM facing the recognition of actual profiles by means of a synthetic database has been provided in Test Case I.d. As expected, since the datasets are highly dissimilar, just as happened in the evaluation of F_u and F_w the results have been not as high as the other test cases. Nevertheless, it reaches recognition rates of almost 80%, similarly to F_w evaluated in the same test case, although gMSM outperforms the latter.

As before, Test Case I has provided a first evaluation of gMSM algorithm, showing that good recognition results can be achieved with a proper value of *softweights*. The gMSM algorithm can be highly affected by the *softweights* value, but it has been noted that η_D should be set such that its value is equal to or smaller than η_S to obtain good results and also that the higher the difference between the database and the test set, the smaller these values should be set.

Next Test Case II will provide more confidence in the results since the database and the number of test samples will be expanded. However, after this study it can be concluded that gMSM seems to be robust against noise, achieving high success rates.

[9] m_S will not change with respect to Test Case I.a since no noise is added to the synthetic profiles of the training set

6.2.2.2. Test Case II. Results

In order to keep evaluating gMSM, a new aircraft model is added to both the test and training set, so now the test set comprises profiles of 6 different aircraft while the database is composed of profiles of 7 aircraft models. Remember also that now more trajectories are included in the study and they are divided into small frames that cover a variation of 2.5° in azimuth, resulting in a total number of 235 frames available for classification. As in section 6.2.1.2, Test Cases II.a to c contain 1410 matrices of simulated range profiles in the test set while Test Case II.d, contains only the actual 235 matrices of measured range profiles.

Test Case II.a. Synthetic Profiles Vs. Synthetic Profiles

The ideal case of identifying test samples that come from simulations, that is, synthetic profiles with a database of profiles of the same nature, returned in Test Case I.a the ideal result of a 100% of success rate regardless of the selected thresholds (η_D and η_S). Therefore, for this subcase the same ideal results are expected. Indeed, with the expansion of samples in this Test Case II.a. those results are achieved as Table 6.28 and Figure 6.40a shows. This fact denotes that expanding the database and the samples do not influence negatively in the results but still provide the perfect recognition performance.

Note that, in comparison with Test Case I.a. the mean value of parameter m for the different thresholds has been reduced, Figure 6.33b showed a mean value of both m_S and m_D very near to 10 when their respective thresholds were set to 0.99, and now for the same thresholds, as Figure 6.40b depicts, the returned mean values are around 4. The reason for this reduction is simple, the number of profiles that compose a frame in this test case is much lower than the previous test case, therefore, the application of the eigendecomposition will return less eigenvectors and hence, their energy will be distributed differently.

The analysis of this first ideal subcase shows that by reducing the number of profiles that compose a frame, the recognition performance of the algorithm still return the ideal good recognition rates as the previous Test Case I.a. This way, it encourages the further study of the different subcases to keep assessing the algorithm and the conclusions drawn in the previous test cases.

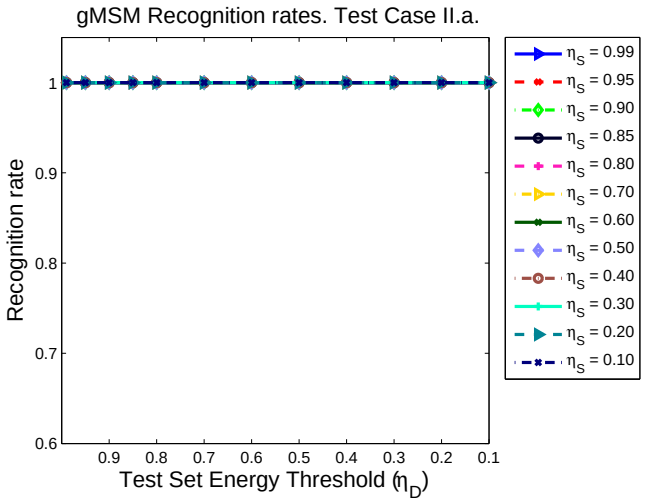

(a) gMSM recognition rates

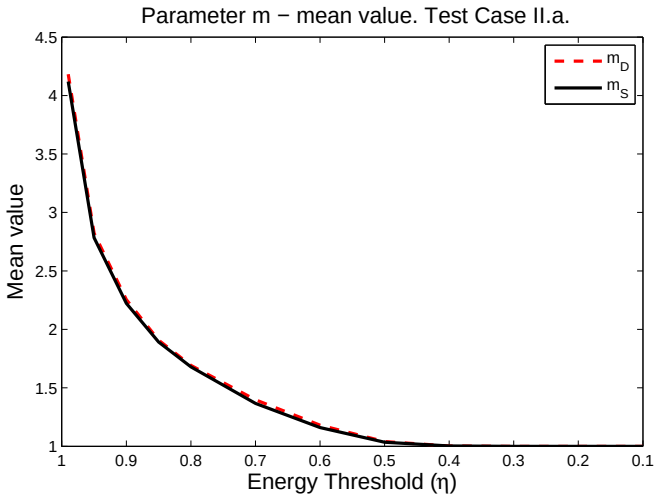

(b) Mean value of parameter m

Figure 6.40: Test Case II.a. gMSM performance with dynamic *softweights*

Table 6.28: Subcase II.a. gMSM Recognition rates

Test Case II.a. Recognition rates varying η_D and η_S (%)												
	η_S											
η_D	**0.99**	**0.95**	**0.9**	**0.85**	**0.8**	**0.7**	**0.6**	**0.5**	**0.4**	**0.3**	**0.2**	**0.1**
0.99	100.0	100.0	100.0	100.0	100.0	100.0	100.0	100.0	100.0	100.0	100.0	100.0
0.95	100.0	100.0	100.0	100.0	100.0	100.0	100.0	100.0	100.0	100.0	100.0	100.0
0.9	100.0	100.0	100.0	100.0	100.0	100.0	100.0	100.0	100.0	100.0	100.0	100.0
0.85	100.0	100.0	100.0	100.0	100.0	100.0	100.0	100.0	100.0	100.0	100.0	100.0
0.8	100.0	100.0	100.0	100.0	100.0	100.0	100.0	100.0	100.0	100.0	100.0	100.0
0.7	100.0	100.0	100.0	100.0	100.0	100.0	100.0	100.0	100.0	100.0	100.0	100.0
0.6	100.0	100.0	100.0	100.0	100.0	100.0	100.0	100.0	100.0	100.0	100.0	100.0
0.5	100.0	100.0	100.0	100.0	100.0	100.0	100.0	100.0	100.0	100.0	100.0	100.0
0.4	100.0	100.0	100.0	100.0	100.0	100.0	100.0	100.0	100.0	100.0	100.0	100.0
0.3	100.0	100.0	100.0	100.0	100.0	100.0	100.0	100.0	100.0	100.0	100.0	100.0
0.2	100.0	100.0	100.0	100.0	100.0	100.0	100.0	100.0	100.0	100.0	100.0	100.0
0.1	100.0	100.0	100.0	100.0	100.0	100.0	100.0	100.0	100.0	100.0	100.0	100.0

Test Case II.b. Synthetic Profiles with AWGN Vs. Synthetic Profiles

The behaviour of algorithm gMSM under an ideal scenario with test samples consisting on frames of a few profiles has been evaluated in the previous subcase where very good recognition rates have been obtained. Now it is the turn to evaluate the operation of the algorithm under the effect of noise and check if the success rates deteriorate with the same tendency as Test Case I.b or if, on the contrary, the reduction of the number of profiles that form a frame influences positively in these results.

Equally to the previous Test Case I.b, AWGN is added to the test set resulting in different values of SNR, and both parameters m_D and m_S are varied according to their corresponding energy thresholds η_D and η_S. The recognition rates obtained for the different values of SNR of this experiment are shown in Figure 6.41 and its corresponding subfigures. The mean value of the corresponding m_D and m_S for each value of SNR is also given in Figure 6.42, where as expected, the mean value of the *softweighting* parameters increases with the increment of the noise; as it can be seen in the figure, the value of both m_S and m_D rapidly reach the mean value of 1 with the decrease of their respective energy threshold.

A first glance of Figures 6.41a to 6.41e leads to the idea that a reduction in the size of the test samples have resulted in very good recognition rates independently of the selected energy thresholds; these figures show, for a given value of η_S a quite uniform tendency with the change of η_D, and when SNR is positive these rates are always above 90%. As expected, the more noise added to the test set, the worse the recognition performance of the algorithm, as Figure 6.41e and its corresponding Table 6.33 show where the added noise is very corrupting (SNR = -10 dB). In fact, the best recognition results drop from 98.37% for a SNR = 10 dB to 88.01% for the worst case (SNR = -10 dB), while the worst recognition rates obtained reach the values 97.09% for the best case and 77.38% for the worst case, as Tables 6.29 and 6.33 show respectively.

One interesting property is appreciated, since now the results seem to be less influenced by the value of the thresholds, the rule $\eta_D \leq \eta_S$ still holds for good results, however when the noise is highly corrupting (SNR = -10 dB), the best results are not achieved under that assumption but for $\eta_D \geq 0.6$, independently of η_S, as Figure 6.41e and its corresponding Table 6.33 portray. The assumption that $\eta_D \leq \eta_S$ was of great importance in the previous Test Case I since, as in that case more profiles are considered in each frame of a test sample, an increment in η_D implied a high increment in m_D, especially when SNR = -10 dB. Here, as there are less profiles in a test sample, there are less eigenvectors and hence, although an increment in η_D also implies an increment in m_D, this change in the value of m_D is not so pronounced and neither is the change in the obtained recognition rates.

The best results are obtained generally for $0.7 \geq \eta_D \geq 0.6$ and $0.99 \geq \eta_S \geq 0.95$, which translates into both m having a mean value between 2 and 4. Certainly, with SNR = 10 dB the best recognition rate (98.51%) is obtained for $\eta_D = 0.7$ and $\eta_S = 0.99$, with SNR = 0 dB a 95.67% of success rate is obtained for $\eta_D = 0.6$ and $\eta_S = 0.9$ and for SNR = -10 dB, the best result (88.01%) is obtained for $\eta_D = 0.6$ and $\eta_S = 0.95$. Nevertheless, it must be noted that Test Case I.b reached higher best values of recognition performance when selecting the proper value of both thresholds, however, it should be remembered that Test Case II has expanded the number of test samples that take place in the recognition along with the number of potential aircraft existing in the database. So, considering this, and that now the impact of the thresholds is not as important, it can be said that gMSM applied to small frames of consecutive range profiles is quite robust against an improper selection of parameter m, and even though the addition of noise clearly affects the performance, as expected, the recognition rates still maintain a good level of success. Actually, the behaviour of this algorithm is quite similar to F_w under these first two subcases, reaching very similar success rates.

Table 6.29: Subcase II.b. gMSM Recognition rates - SNR = 10 dB

Test Case II.b. Recognition rates varying η_D and η_S (%) - $AWGN_{SNR=10dB}$												
	η_S											
η_D	**0.99**	**0.95**	**0.9**	**0.85**	**0.8**	**0.7**	**0.6**	**0.5**	**0.4**	**0.3**	**0.2**	**0.1**
0.99	97.52	98.23	97.87	97.73	97.80	98.09	97.09	97.45	97.38	98.01	97.45	97.73
0.95	97.66	98.16	97.94	97.94	97.94	98.44	97.16	97.38	97.59	98.01	97.73	97.87
0.9	97.80	98.37	98.23	98.01	97.80	98.37	97.38	97.52	97.73	98.16	97.87	97.87
0.85	98.09	97.59	97.94	97.80	98.23	97.73	98.23	97.87	97.80	98.23	98.09	97.66
0.8	98.09	98.16	97.80	98.16	98.23	98.09	98.44	98.09	98.16	98.44	98.23	98.16
0.7	98.51	98.37	98.16	98.16	98.01	97.80	97.80	98.09	98.01	98.23	97.59	97.66
0.6	98.30	98.01	98.09	98.37	98.16	98.01	97.73	97.73	97.94	97.94	98.01	97.66
0.5	97.59	97.52	97.45	97.59	97.59	97.80	97.66	97.30	97.09	97.30	97.38	97.38
0.4	97.23	97.59	97.52	97.66	97.66	97.45	97.38	97.80	97.45	97.45	97.23	97.38
0.3	97.30	97.59	97.38	97.73	97.73	97.73	97.38	97.87	97.45	97.30	97.45	97.45
0.2	97.30	97.45	97.45	97.38	97.52	97.52	97.52	97.38	97.66	97.38	97.45	97.59
0.1	97.45	97.38	97.52	97.38	97.66	97.45	97.38	97.73	97.52	97.52	97.59	97.66

Table 6.30: Subcase II.b. gMSM Recognition rates - SNR = 5 dB

Test Case II.b. Recognition rates varying η_D and η_S (%) - $AWGN_{SNR=5dB}$												
	η_S											
η_D	**0.99**	**0.95**	**0.9**	**0.85**	**0.8**	**0.7**	**0.6**	**0.5**	**0.4**	**0.3**	**0.2**	**0.1**
0.99	95.67	96.52	96.67	96.10	95.96	96.60	96.52	95.60	95.89	96.03	96.31	96.17
0.95	96.67	97.02	96.60	96.38	96.31	95.96	96.03	96.03	96.31	96.03	96.24	95.89
0.9	96.52	96.74	96.81	96.10	96.81	96.45	96.60	96.31	96.45	96.52	95.96	96.52
0.85	96.95	96.60	96.52	96.60	96.38	96.17	96.88	96.17	96.31	96.31	96.81	95.82
0.8	96.74	97.09	96.60	96.60	96.95	96.88	97.16	96.60	96.67	96.38	96.60	96.60
0.7	97.16	97.23	96.60	96.45	96.38	96.52	96.88	96.38	97.09	96.17	96.67	96.67
0.6	97.30	97.23	96.88	97.02	96.81	97.09	96.24	96.31	96.67	96.88	96.60	96.74
0.5	96.17	96.17	96.38	96.10	95.96	96.38	96.10	96.52	96.10	96.17	96.24	96.03
0.4	96.10	96.31	96.60	96.17	96.38	96.31	95.96	96.60	96.38	96.10	96.45	96.45
0.3	96.24	96.52	95.96	96.17	96.88	96.38	96.17	96.31	96.45	96.31	96.45	96.24
0.2	96.03	96.45	96.31	96.31	96.31	96.38	96.52	96.74	96.38	96.60	96.52	96.38
0.1	95.89	96.24	96.03	96.17	96.60	96.81	96.60	96.74	96.60	96.17	96.60	96.45

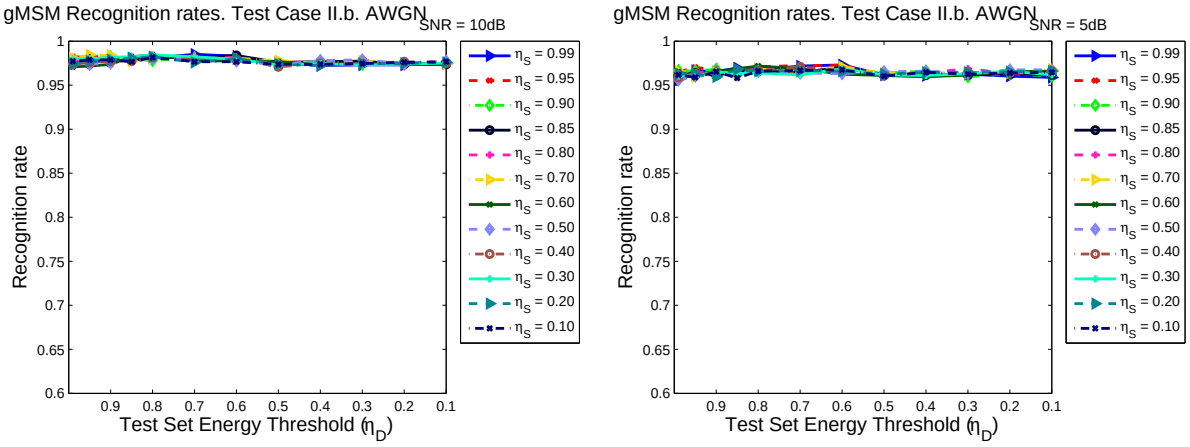

(a) SNR = 10 dB

(b) SNR = 5 dB

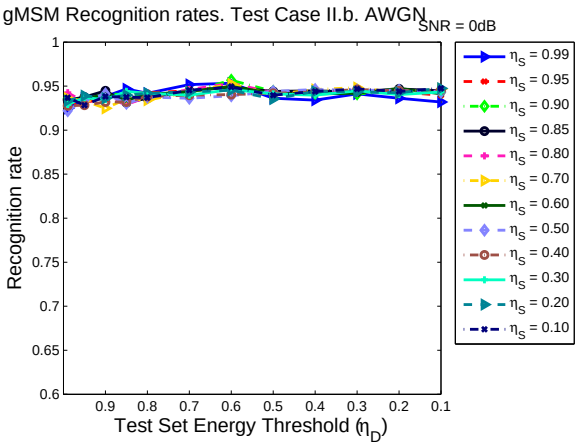

(c) SNR = 0 dB

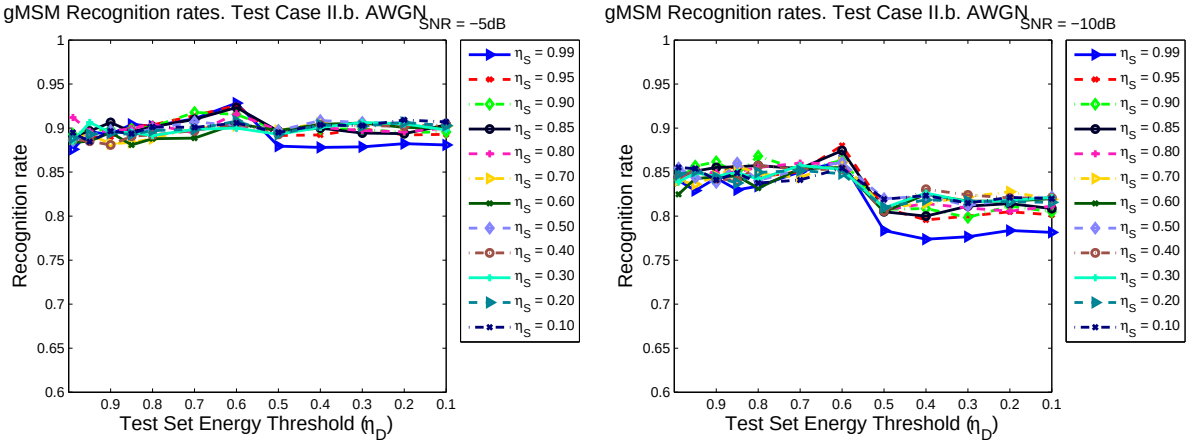

(d) SNR = -5 dB

(e) SNR = -10 dB

Figure 6.41: Test Case II.b. gMSM performance with dynamic *softweights* for different SNR

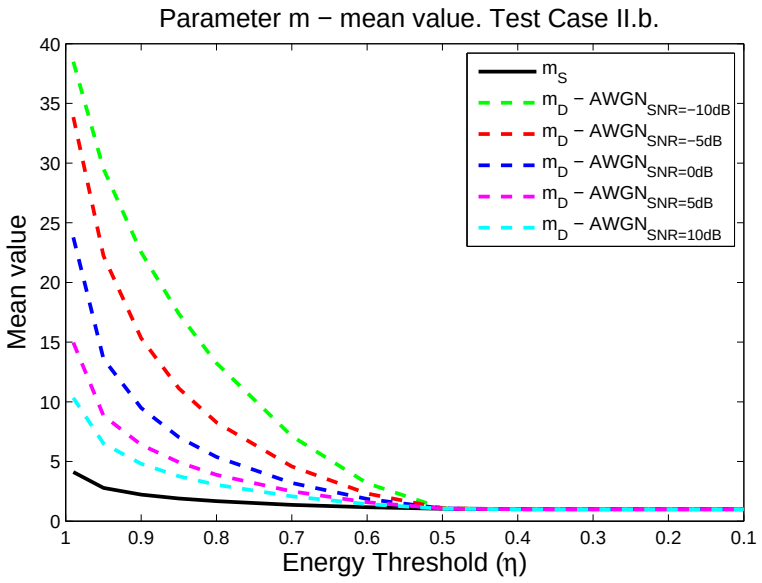

Figure 6.42: Test Case II.b. Mean value of parameter m

Table 6.31: Subcase II.b. gMSM Recognition rates - SNR = 0 dB

Test Case II.b. Recognition rates varying η_D and η_S (%) - $AWGN_{SNR=0dB}$												
	η_S											
η_D	**0.99**	**0.95**	**0.9**	**0.85**	**0.8**	**0.7**	**0.6**	**0.5**	**0.4**	**0.3**	**0.2**	**0.1**
0.99	92.48	93.05	93.55	93.40	94.26	93.62	93.19	92.20	92.77	92.91	93.33	93.69
0.95	93.62	93.19	93.55	93.76	93.19	93.33	93.40	93.40	92.84	93.69	93.90	92.84
0.9	93.83	93.48	94.11	94.47	93.62	92.48	94.18	94.11	93.19	93.48	93.62	93.83
0.85	94.68	94.26	94.04	93.12	92.91	93.55	93.40	93.05	93.19	94.40	93.97	93.76
0.8	94.18	94.26	93.83	93.62	93.76	93.40	94.04	93.76	93.83	94.18	94.18	93.69
0.7	95.18	94.47	94.33	94.47	94.61	94.33	94.40	93.62	93.97	93.97	94.33	94.54
0.6	95.32	94.96	95.67	94.89	95.32	95.25	94.96	93.90	94.04	94.61	94.54	94.89
0.5	93.62	94.18	94.40	94.40	94.26	94.04	94.18	94.40	94.18	94.11	93.55	93.97
0.4	93.40	94.11	94.18	94.47	94.33	94.61	94.11	94.61	94.33	93.97	94.40	94.40
0.3	94.11	94.33	94.11	94.33	94.47	94.82	94.18	94.54	94.61	94.47	94.33	94.68
0.2	93.62	94.33	94.40	94.68	94.18	94.26	94.75	94.54	94.47	94.04	94.26	94.40
0.1	93.19	93.97	94.33	94.47	94.47	94.68	94.11	94.33	94.54	94.33	94.75	94.75

Table 6.32: Subcase II.b. gMSM Recognition rates - SNR = -5 dB

Test Case II.b. Recognition rates varying η_D and η_S (%) - $AWGN_{SNR=-5dB}$												
	η_S											
η_D	**0.99**	**0.95**	**0.9**	**0.85**	**0.8**	**0.7**	**0.6**	**0.5**	**0.4**	**0.3**	**0.2**	**0.1**
0.99	87.59	89.08	89.29	88.87	91.21	88.79	88.37	88.58	88.72	88.51	88.87	89.50
0.95	89.57	88.94	89.72	89.65	89.65	89.29	88.51	89.15	88.51	90.64	89.29	88.44
0.9	89.29	89.01	89.86	90.64	89.65	88.23	89.50	89.72	88.09	89.50	89.43	89.65
0.85	90.43	90.14	89.86	89.57	89.93	88.37	88.09	89.36	89.08	89.50	89.29	89.36
0.8	90.21	90.35	90.14	90.14	90.43	88.79	88.79	89.93	89.22	89.15	89.72	90.14
0.7	91.06	91.42	91.77	90.99	89.43	90.00	88.87	90.71	89.72	89.86	89.86	90.07
0.6	92.84	92.55	91.56	92.34	91.63	90.28	90.50	90.28	90.50	90.00	90.78	90.57
0.5	87.94	89.15	89.72	89.65	89.72	89.72	89.72	89.72	89.29	89.29	89.29	89.50
0.4	87.80	89.22	89.93	90.00	90.07	90.57	90.43	90.85	90.35	90.07	90.35	90.35
0.3	87.87	89.93	89.86	89.43	89.72	90.35	90.57	90.64	90.28	90.64	90.21	90.28
0.2	88.23	89.22	89.50	89.36	89.57	90.35	90.07	90.57	90.21	90.50	90.64	90.92
0.1	88.09	89.29	89.57	90.35	90.00	90.21	90.00	90.28	90.35	89.79	90.28	90.71

Table 6.33: Subcase II.b. gMSM Recognition rates - SNR = -10 dB

Test Case II.b. Recognition rates varying η_D and η_S (%) - $AWGN_{SNR=-10dB}$												
	η_S											
η_D	**0.99**	**0.95**	**0.9**	**0.85**	**0.8**	**0.7**	**0.6**	**0.5**	**0.4**	**0.3**	**0.2**	**0.1**
0.99	84.04	84.26	84.18	84.40	84.26	84.04	82.48	85.46	84.40	83.90	84.75	85.53
0.95	82.91	85.32	85.67	85.11	85.25	83.62	84.26	84.40	85.18	84.89	85.11	85.39
0.9	84.33	84.61	86.17	85.53	84.89	84.54	84.47	83.83	84.26	84.54	84.40	84.11
0.85	82.98	85.89	84.75	85.60	85.04	85.67	84.54	86.03	84.04	84.96	83.76	84.89
0.8	83.40	84.47	86.81	85.74	85.53	84.82	83.19	84.04	85.74	84.18	84.96	83.76
0.7	85.04	85.04	85.25	85.39	86.03	84.40	85.39	85.32	85.32	85.74	85.18	84.11
0.6	86.24	88.01	86.31	87.45	85.96	86.10	85.53	86.10	85.32	85.32	84.82	85.46
0.5	78.37	80.92	80.78	80.50	80.71	80.92	80.50	81.99	80.57	80.92	80.99	81.91
0.4	77.38	79.57	80.85	80.00	81.42	81.49	82.48	82.27	83.05	82.62	81.84	82.34
0.3	77.66	80.00	79.86	81.13	80.92	82.20	81.70	81.21	82.41	81.63	81.70	81.49
0.2	78.37	80.50	81.13	81.42	80.57	82.77	81.70	81.91	82.06	81.77	81.63	82.13
0.1	78.16	80.14	80.50	80.85	81.13	81.91	81.99	82.20	82.06	82.13	81.56	81.99

Test Case II.c. Synthetic misaligned Profiles with AWGN Vs. Synthetic Profiles

Next step in the process of evaluating gMSM is the addition of the effect of TRM on the profiles by introducing a small misalignment between some consecutive profiles although, as happened in the previous section 6.2.1, this effect is expected to be less relevant in the final results than the addition of noise.

Figures 6.43a to 6.43e summarize the recognition performance of this test case given in Tables 6.34 to 6.38. As expected, the rates have experienced a slight degradation due to the effect of TRM, and the degradation is more prominent when more noise is present, that is, when the SNR is negative (especially when it is -10 dB). Indeed, the maximum degradation that the recognition rates have suffered from the previous Test Case II.b to this one when SNR = 10 dB is only of 4 percentage points, while when SNR = -10 dB the recognition rates can experiment a degradation up to 13 percentage points.

Similar to the previous section, where only noise was added, the evolution of the recognition rates has the same nearly uniform tendency with the change of energy thresholds, except for the case where SNR = -10 dB, as can be appreciated in the Figures 6.43a to 6.43e; however, despite this uniformity, in order to obtain the best recognition results, generally, the value of η_D should be set lower or equal to the value of η_S, although when the noise increments (negative SNR), better results are obtained for $\eta_D \geq 0.6$ and $0.5 \geq \eta_S \geq 0.1$. More specifically, and like the previous subcase, the best results are obtained generally for $\eta_D = 0.6$ and $0.95 \geq \eta_S \geq 0.9$, which according to Figure 6.44 means that the mean m_D is between 1 and 3 depending on how corrupted with noise are the profiles, and the mean m_S is around 2. Indeed, for the best case (SNR = 10 dB), as Table 6.34 shows, the best rate (97.87%) is obtained for these values of energy thresholds, but even if the thresholds are not set to their optimum values, due to the aforementioned uniformity, the rates obtained are still very high, always around 95%. On the other hand, when the test set is highly corrupted (SNR = -10 dB), the best rate (82.48%) differs in around 15 percentage points from the worst rate (65.39%) with an unsuitable threshold selection. Therefore, it can be concluded that the selection of the threshold is not as important as having clear and well aligned test samples. That is, if the test samples are highly corrupted and misaligned, the selection of a proper threshold is of high importance, while if the test samples are quite clear and well aligned, a proper threshold will of course return the best results, but the results are not so threshold dependent.

Table 6.34: Subcase II.c. gMSM Recognition rates - SNR = 10 dB

Test Case II.c. Recognition rates varying η_D and η_S (%) - $AWGN_{SNR=10dB}$												
	η_S											
η_D	**0.99**	**0.95**	**0.9**	**0.85**	**0.8**	**0.7**	**0.6**	**0.5**	**0.4**	**0.3**	**0.2**	**0.1**
0.99	95.11	94.33	94.40	94.40	94.89	95.53	95.89	96.31	96.31	96.31	96.31	96.31
0.95	95.89	95.18	94.61	94.04	94.40	95.11	95.89	96.31	96.45	96.45	96.45	96.45
0.9	96.38	96.10	95.60	94.89	95.25	95.18	95.89	96.45	96.60	96.60	96.60	96.60
0.85	96.67	96.67	96.24	95.53	95.46	95.74	96.31	96.52	96.67	96.67	96.67	96.67
0.8	97.02	96.74	96.67	96.17	96.10	96.10	96.31	96.60	96.74	96.74	96.74	96.74
0.7	97.09	97.45	97.45	97.09	97.16	96.95	96.95	97.30	97.23	97.23	97.23	97.23
0.6	97.66	97.80	97.87	97.30	97.45	97.30	97.02	97.23	97.16	97.16	97.16	97.16
0.5	96.38	96.60	96.31	95.89	96.03	96.24	95.82	95.96	95.82	95.82	95.82	95.82
0.4	96.24	96.52	96.45	96.17	96.17	96.31	95.89	96.10	95.96	95.96	95.96	95.96
0.3	96.24	96.52	96.45	96.17	96.17	96.31	95.89	96.10	95.96	95.96	95.96	95.96
0.2	96.24	96.52	96.45	96.17	96.17	96.31	95.89	96.10	95.96	95.96	95.96	95.96
0.1	96.24	96.52	96.45	96.17	96.17	96.31	95.89	96.10	95.96	95.96	95.96	95.96

Table 6.35: Subcase II.c. gMSM Recognition rates - SNR = 5 dB

Test Case II.c. Recognition rates varying η_D and η_S (%) - $AWGN_{SNR=5dB}$												
	η_S											
η_D	**0.99**	**0.95**	**0.9**	**0.85**	**0.8**	**0.7**	**0.6**	**0.5**	**0.4**	**0.3**	**0.2**	**0.1**
0.99	92.06	92.13	91.28	90.78	91.06	91.84	92.77	93.40	93.69	93.69	93.69	93.69
0.95	93.12	93.33	91.84	91.77	91.99	92.20	93.05	93.26	93.62	93.62	93.62	93.62
0.9	93.76	93.97	92.84	92.48	92.62	92.41	93.33	93.83	94.04	94.04	94.04	94.04
0.85	94.04	94.47	93.69	93.19	93.26	93.05	93.55	94.04	94.26	94.26	94.26	94.26
0.8	94.47	95.11	94.54	93.76	93.83	93.40	93.69	94.04	94.33	94.33	94.33	94.33
0.7	95.32	95.32	94.96	94.40	94.68	94.04	94.33	94.61	95.11	95.11	95.11	95.11
0.6	96.38	95.82	95.46	95.18	95.60	94.82	94.82	94.89	95.46	95.46	95.46	95.46
0.5	94.89	95.04	94.96	94.61	94.89	94.54	94.47	94.54	94.61	94.61	94.61	94.61
0.4	94.54	94.96	94.96	94.54	94.68	94.61	94.54	94.54	94.47	94.47	94.47	94.47
0.3	94.54	94.96	94.96	94.54	94.68	94.61	94.54	94.54	94.47	94.47	94.47	94.47
0.2	94.54	94.96	94.96	94.54	94.68	94.61	94.54	94.54	94.47	94.47	94.47	94.47
0.1	94.54	94.96	94.96	94.54	94.68	94.61	94.54	94.54	94.47	94.47	94.47	94.47

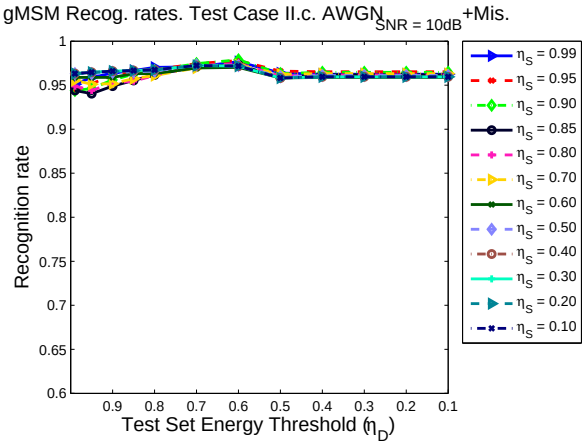

(a) SNR = 10 dB

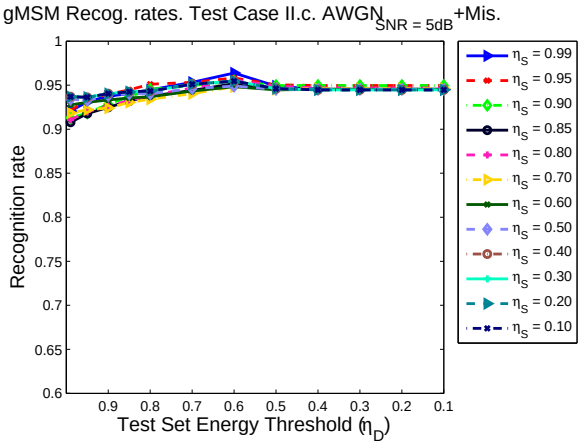

(b) SNR = 5 dB

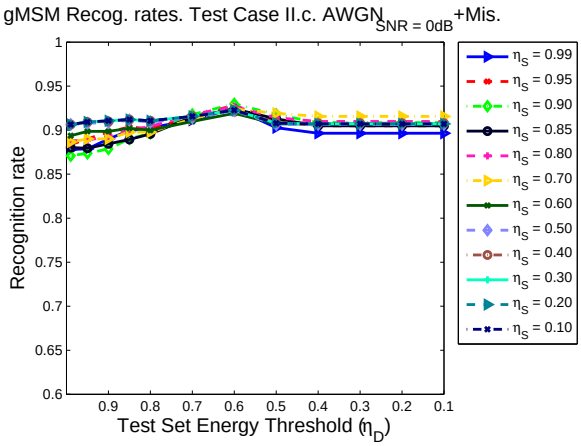

(c) SNR = 0 dB

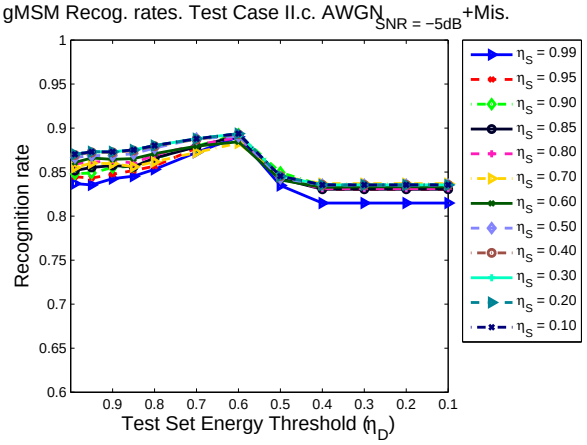

(d) SNR = -5 dB

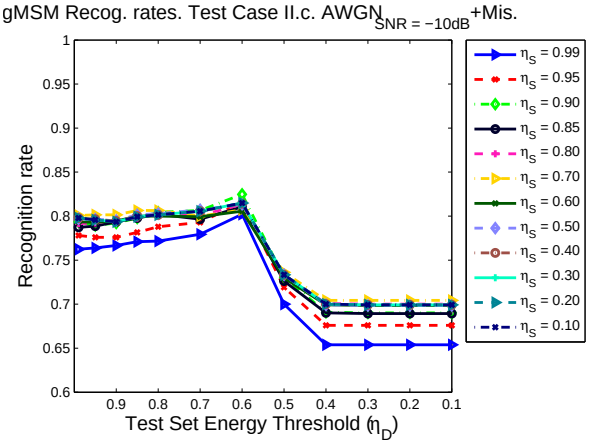

(e) SNR = -10 dB

Figure 6.43: Test Case II.c. gMSM performance with dynamic *softweights* for different SNR

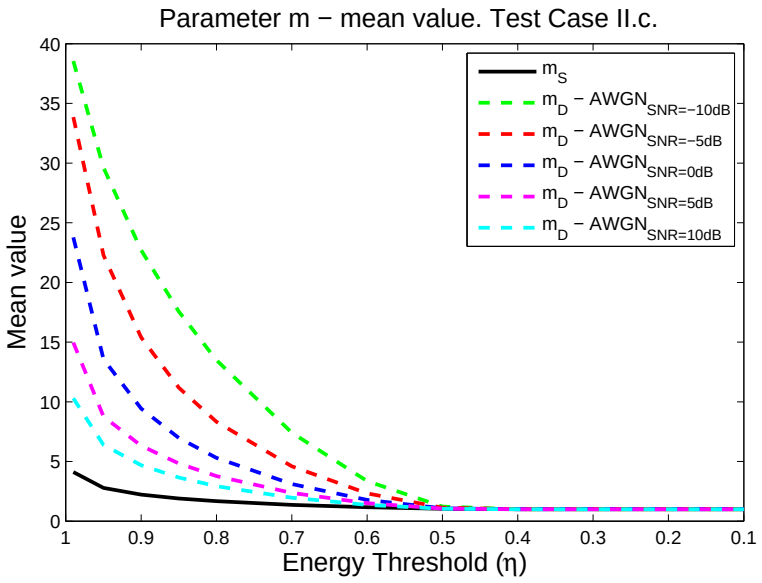

Figure 6.44: Test Case II.c. Mean value of parameter m

Table 6.36: Subcase II.c. gMSM Recognition rates - SNR = 0 dB

Test Case II.c. Recognition rates varying η_D and η_S (%) - $AWGN_{SNR=0dB}$												
	η_S											
η_D	**0.99**	**0.95**	**0.9**	**0.85**	**0.8**	**0.7**	**0.6**	**0.5**	**0.4**	**0.3**	**0.2**	**0.1**
0.99	87.80	88.37	87.09	88.01	88.79	88.65	89.36	90.64	90.64	90.64	90.64	90.64
0.95	87.87	89.01	87.38	87.94	88.87	89.01	89.86	90.78	90.92	90.92	90.92	90.92
0.9	89.01	89.79	87.87	88.44	89.29	89.01	89.86	90.85	90.99	91.06	91.06	91.06
0.85	89.93	90.35	89.01	88.94	90.00	89.79	90.21	91.13	91.21	91.21	91.21	91.21
0.8	90.28	90.14	89.65	89.57	90.43	89.79	90.00	90.92	91.06	91.06	91.06	91.06
0.7	91.13	91.56	91.77	91.49	91.77	91.28	90.99	91.42	91.56	91.56	91.56	91.56
0.6	92.48	92.84	92.98	92.41	92.70	92.41	91.91	92.20	92.27	92.27	92.27	92.27
0.5	90.28	90.99	91.77	91.28	91.42	91.91	90.71	90.64	90.85	90.78	90.78	90.78
0.4	89.65	90.50	90.85	90.50	90.99	91.56	90.71	90.64	90.78	90.71	90.71	90.71
0.3	89.65	90.50	90.85	90.50	90.99	91.56	90.71	90.64	90.78	90.71	90.71	90.71
0.2	89.65	90.50	90.85	90.50	90.99	91.56	90.71	90.64	90.78	90.71	90.71	90.71
0.1	89.65	90.50	90.85	90.50	90.99	91.56	90.71	90.64	90.78	90.71	90.71	90.71

Table 6.37: Subcase II.c. gMSM Recognition rates - SNR = -5 dB

Test Case II.c. Recognition rates varying η_D and η_S (%) - $AWGN_{SNR=-5dB}$												
	η_S											
η_D	**0.99**	**0.95**	**0.9**	**0.85**	**0.8**	**0.7**	**0.6**	**0.5**	**0.4**	**0.3**	**0.2**	**0.1**
0.99	83.69	84.47	84.82	85.18	85.96	85.53	86.10	86.67	86.95	87.02	87.02	87.02
0.95	83.55	84.33	84.89	85.53	86.10	86.03	86.60	86.88	87.23	87.30	87.30	87.30
0.9	84.26	84.75	85.53	85.74	86.31	85.96	86.45	86.88	87.23	87.30	87.30	87.30
0.85	84.54	85.18	85.67	85.60	86.03	85.60	86.52	87.09	87.45	87.52	87.52	87.52
0.8	85.32	85.67	86.52	86.60	86.95	86.17	87.09	87.73	87.94	88.01	88.01	88.01
0.7	87.23	87.73	87.94	87.87	88.09	87.23	87.94	88.79	88.72	88.79	88.79	88.79
0.6	89.01	89.36	89.29	89.15	88.94	88.30	88.44	89.08	89.29	89.36	89.36	89.36
0.5	83.48	84.47	84.96	84.26	84.33	84.54	84.11	84.33	84.54	84.54	84.54	84.54
0.4	81.49	83.05	83.48	83.05	83.12	83.69	83.26	83.55	83.55	83.55	83.55	83.55
0.3	81.49	83.05	83.48	83.05	83.12	83.69	83.33	83.55	83.55	83.55	83.55	83.55
0.2	81.49	83.05	83.48	83.05	83.12	83.69	83.33	83.55	83.55	83.55	83.55	83.55
0.1	81.49	83.05	83.48	83.05	83.12	83.69	83.33	83.55	83.55	83.55	83.55	83.55

Table 6.38: Subcase II.c. gMSM Recognition rates - SNR = -10 dB

Test Case II.c. Recognition rates varying η_D and η_S (%) - $AWGN_{SNR=-10dB}$												
	η_S											
η_D	**0.99**	**0.95**	**0.9**	**0.85**	**0.8**	**0.7**	**0.6**	**0.5**	**0.4**	**0.3**	**0.2**	**0.1**
0.99	76.24	77.80	79.36	78.72	79.15	80.07	79.36	79.72	79.79	79.79	79.79	79.79
0.95	76.38	77.59	78.94	78.87	79.22	80.14	79.29	79.65	79.65	79.57	79.57	79.57
0.9	76.67	77.59	79.22	79.36	79.57	80.14	79.43	79.50	79.43	79.36	79.36	79.36
0.85	77.09	78.16	79.79	79.79	79.79	80.64	80.00	80.14	80.00	79.93	79.93	79.93
0.8	77.16	78.79	80.43	80.21	80.28	80.64	80.00	80.28	80.14	80.14	80.14	80.14
0.7	77.94	79.29	80.64	79.65	80.07	80.00	79.93	80.71	80.57	80.57	80.57	80.57
0.6	80.21	81.56	82.48	81.06	81.35	80.71	80.57	81.35	81.42	81.49	81.49	81.49
0.5	70.00	71.91	73.05	72.62	73.33	73.62	72.98	73.33	73.33	73.33	73.33	73.33
0.4	65.39	67.59	69.08	69.01	70.07	70.43	69.93	69.93	70.00	70.00	70.00	70.00
0.3	65.39	67.59	69.01	68.94	70.00	70.43	69.86	69.86	69.93	69.93	69.93	69.93
0.2	65.39	67.59	69.01	68.94	70.00	70.43	69.86	69.86	69.93	69.93	69.93	69.93
0.1	65.39	67.59	69.01	68.94	70.00	70.43	69.86	69.86	69.93	69.93	69.93	69.93

Test Case II.d. Actual Profiles Vs. Synthetic Profiles

To finally complete the assessment of gMSM algorithm , the classification of actual profiles by means of a synthetic database is taking place in this last subcase, where 235 matrices of actual range profiles belonging to 6 different aircraft form the test set, and matrices of synthetic profiles of 7 potential aircraft compose the database, so called the training set. The results expected will obviously be worse than the previous ones obtained using synthetic profiles as test set (even if they had been corrupted with noise) due to the unmodelled effects of a real scenario and to the prediction of the trajectories that the aircraft described while acquiring their signatures.

According to the previous results, the selection of an appropriate value of parameter m to control the *softweights* is important but with a certain degree of freedom since the results have shown a quite uniform tendency in the recognition rates with the variation of parameters η_D and η_S. Now, as can be seen in Figure 6.45a, due to the difference in nature of the range profiles, this quite uniform tendency is not as pronounced as in the test cases that classified synthetic profiles, but it is still visible. Nevertheless, in the previous subsections it was said that generally, with a value of η_D lower or equal to η_S quite good recognition results are obtained, even though in some cases where the profiles were so corrupted this property did not apply, in this case, that statement is still obeyed.

The previous subcases concluded that the best results were obtained for values $0.7 \geq \eta_D \geq 0.6$ and $0.95 \geq \eta_S \geq 0.9$, which was translated into mean values of the respective m parameters around 1 and 3 approximately. Keeping this results in mind, the results for those η_D and η_S in this case return recognition rates between 74% and 80% according to Table 6.39, which is moderately good, considering the previous results. Nevertheless, in order to obtain the best results, the selected values should be $\eta_S \leq 0.7$ and $\eta_D \leq \eta_S$, corresponding to mean values of parameters $m_D \leq 1.65$ and $m_S \leq 1.36$, that is, these values have been decreased due to the dissimilarity between actual and synthetic profiles, just as happened in Test Case I.d, where it was seen that the higher the difference between test and training samples the lower the value of parameters m. The highest recognition rates obtained are 83.83% for a quite wide range of η_D and η_S, although not only the highest recognition rate is important but also the confidence in the result; here, this confidence has been measured as the previous Test Case I.d, by calculating the mean difference between the similarities of the winning aircraft taking into account the maximum value that the algorithm can reach for each threshold.

In agreement with this, Figure 6.46 depicts the evolution of this confidence degree for Test Case II.d, where according to the figure, the highest confidence degree will be returned for thresholds $\eta_D = 0.8$ and $\eta_S = 0.5$, which although they do not return bad recognition rates (around 82%), they do not obey the rule $\eta_D \leq \eta_S$ that has been followed along the study of the *softweights*. However, selecting $\eta_S \leq 0.5$ and $\eta_D \leq \eta_S$ the average confidence degree is stable in an acceptable value and also the recognition rate. Therefore, just as Test Case I.d, if parameters m are desired to be set to a fixed value for all the test and training samples, according to this last conclusion and Figure 6.45b, the best would be to select both values $m_D = m_S = 1$.

Table 6.40 shows the confusion matrix of the obtained recognition results selecting both m to the value of unity. As usual, Fokker100 and Fokker28 are the two aircraft with the worst recognition rates due to their mutual similarity, however, Fokker100, which obtained rates under 70% for the previous subcases and algorithms, has experienced an increment in success rate using gMSM. This indicates a better discrimination between similar aircraft of gMSM algorithm.

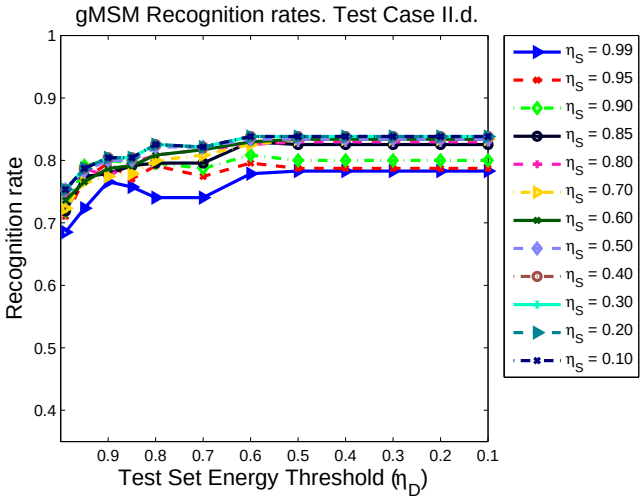

(a) gMSM recognition rates

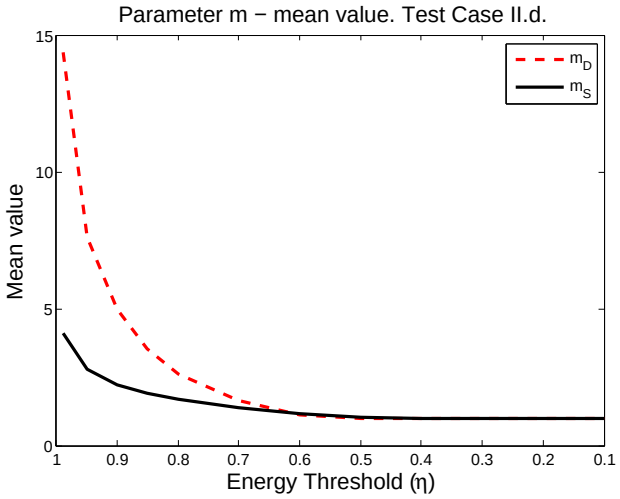

(b) Mean value of parameter m

Figure 6.45: Test Case II.d. gMSM performance with dynamic *softweights*

Table 6.39: Subcase II.d. gMSM Recognition rates

Test Case II.d. Recognition rates varying η_D and η_S (%)												
	η_S											
η_D	**0.99**	**0.95**	**0.9**	**0.85**	**0.8**	**0.7**	**0.6**	**0.5**	**0.4**	**0.3**	**0.2**	**0.1**
0.99	68.51	71.06	71.91	71.91	74.47	72.34	73.62	75.32	75.32	75.32	75.32	75.32
0.95	72.34	77.02	79.15	77.45	78.72	76.60	76.60	78.30	78.72	78.72	78.72	78.72
0.9	76.60	79.57	80.00	77.87	77.45	77.45	78.72	80.00	80.43	80.43	80.43	80.43
0.85	75.74	77.02	79.57	79.15	79.57	77.87	79.15	80.00	80.43	80.43	80.43	80.43
0.8	74.04	79.15	79.57	79.57	80.85	80.00	80.85	82.13	82.55	82.55	82.55	82.55
0.7	74.04	77.45	78.72	79.57	81.70	80.85	81.70	82.13	82.13	82.13	82.13	82.13
0.6	77.87	79.57	80.85	82.98	82.55	82.55	82.98	83.40	83.83	83.83	83.83	83.83
0.5	78.30	78.72	80.00	82.55	82.98	83.40	83.40	83.40	83.83	83.83	83.83	83.83
0.4	78.30	78.72	80.00	82.55	82.98	83.40	83.40	83.40	83.83	83.83	83.83	83.83
0.3	78.30	78.72	80.00	82.55	82.98	83.40	83.40	83.40	83.83	83.83	83.83	83.83
0.2	78.30	78.72	80.00	82.55	82.98	83.40	83.40	83.40	83.83	83.83	83.83	83.83
0.1	78.30	78.72	80.00	82.55	82.98	83.40	83.40	83.40	83.83	83.83	83.83	83.83

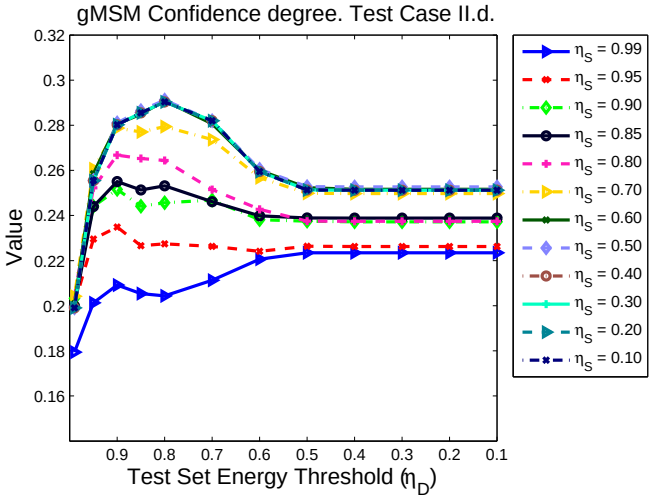

Figure 6.46: Test Case II.d. gMSM mean difference between aircraft similarities

Table 6.40: Subcase II.d. gMSM Confusion matrix; $m_D = m_S = 1$

	A310	**B747**	**B767**	**F028**	**F100**	**MD88**	**B737**	**Success (%)**	**Error (%)**
A310	35	0	2	1	0	0	1	**89.74**	**10.26**
B747	5	35	0	2	0	0	0	**83.33**	**16.67**
B767	2	0	32	0	0	0	0	**94.12**	**5.88**
F028	0	0	0	31	6	1	0	**81.58**	**18.42**
F100	0	0	0	5	31	1	6	**72.09**	**27.91**
MD88	2	0	2	0	2	33	0	**84.62**	**15.38**
Average rates								**83.83**	**16.17**

Test Case II. Discussion

Finally, this Test Case has provided a more complete study of the behaviour of gMSM by introducing new aircraft and new test samples. Just as the previous study of the energy threshold for algorithms F_u and F_w, along this whole Test Case II, it has been proven that the reduction of the number of profiles forming a frame achieves better recognition results in comparison with Test Case I. Additionally, due to the increment in the test samples, the results are more representative of the actual behaviour of the algorithm; bearing this in mind, the observations made along this test case are summarized bellow.

- Firstly, and as done before, the ideal scenario has been studied taking a test set of synthetic profiles that are equal to those in the database. As expected, very high recognition rates (100%) are accomplished, independent of the value of the selected thresholds just like Test Case I.a predicted.

- After the ideal subcase, the addition of noise has been studied in Test Case II.b. Similar to Test Case I, the noisier the test set, the higher the value of m_D is for a given threshold, however now it must be noted that the mean values of both paramaters m_D and m_S have been lower than in Test Case I[10]. It has been shown that the property $\eta_D \leq \eta_S$ is still valid for very good results and the best ones are obtained for mean values of both m between 2 and 4, so, as seen, the tendency is to set both to low values. In conclusion, the addition of noise has provided more robust recognition rates than in Test Case I.b, hence confirming that classifying small frames is easier and more reliable than working with bigger frames of profiles. Furthermore, when the noise is not very pronounced the recognition rates keep an approximately uniform tendency and even though the thresholds are not set to the optimum values, very good recognition rates can be achieved; therefore, one of the main conclusions of this test case is that gMSM presents a certain robustness against noise and selection of the *softweighting* parameters.

- Test Case II.c has studied the effect of TRM on the recognition rates. As happened in all the previous subcases, the effect of noise covers up the effect of profiles misalignment, mainly because this misalignment is not very prominent, but anyway the recognition rates undergo a degradation which is important to consider. Just like before, it has been observed that the rates have an approximately uniform tendency with the selection of the energy thresholds, and with low noise the recognition rates maintain very high values even with the wrong threshold. It has been proven, one more time, that η_D should be smaller or equal to η_S in order to achieve the best recognition results and also it has been seen that when the best results are considered, m_S should be kept around 2 just as before, but m_D varies its value between 1 and 3, that is, the more different the test samples and the training samples are, the optimum values of their respective m turn to lower values.

- Finally, and after the ideal study of the algorithm, the identification of actual profiles has taken place in the last Test Case II.d. Considering all the above test cases, good recognition performance was expected for a wide range of η_D and η_S, although obviously a bit worse than the ideal cases. Eventually, it has been confirmed the rule $\eta_D \leq \eta_S$, and also, a property that was observed in Test Case II.c, has been more noticeable here; the optimum values for η_D and η_S have been decreased in comparison with the prior ideal cases, resulting in lower respective mean values of parameters m_D and m_S, that is, similar to what happened in Test Case I.d, the higher the difference between range profiles in test and training set, the lower their respective m. The recognition performance obtained for a fixed value of $m_D = m_S = 1$ has provided recognition rates up to almost 85%, which

[10]Recall that since the number of profiles that compose a frame now is smaller than previously studied, the number of eigenvectors and eigenvalues will also be smaller and their energy will be differently distributed

are similar results than those obtained with F_w[11]. The fact that both algorithms return similar results seems to be useful for noting that they both are valid for recognition of range profiles of actual aircraft by means of a synthetic database.

The division of the aircraft trajectories into small frames of little variation in azimuth has provided better recognition performance to gMSM, just as algorithms F_u and F_w. After the assessment of Test Case II, it can be stated that gMSM is quite robust against noise and TRM.

The selection of the optimum threshold for the *softweighting* parameters needs of an exhaustive analysis like the one provided here; the initial idea of using *softweights* was to eliminate the need of selecting a subspace dimensionality in advance, therefore, the subspaces of both the test and training set are fully considered in the identification algorithm but it is the task of the *softweights* to assign the importance of each of the vectors composing the subspace.

This study was made with the purpose of assessing the optimum value of parameter m. Selecting m dynamically for each sample in the test and the training sets just adds computational cost to the algorithm, furthermore it was found that the higher the difference between datasets, the lower the value of their respective m should be set, thus, when identifying actual profiles by means of a synthetic database, selecting the first eigenvalue as the one that weights the rest, that is, selecting $m_D = m_S = 1$ is the best option for obtaining very good recognition results.

6.3. Algorithm comparison

The present chapter was focused on the results obtained with the algorithms developed in Chapter 5. As concluded, very good recognition results are obtained for a certain value of their respective parameters, however, every algorithm presented here provided an evolution with respect to the previous one. Indeed, the F_w algorithm is an evolution of F_u, more robust against noise and energy threshold selection, and the gMSM algorithm improves them by eliminating the subspace dimensionality selection; anyway, the 3 algorithms developed here are based on PCA and angle between subspaces, and are an advance of the *Mutual Subspace Method (MSM)* algorithm.

The final purpose of this thesis is to develop algorithms able to classify range profiles coming from actual measurements with a database of range profiles coming from simulated aircraft models. As seen, the obtained final recognition rates provided recognition performances around 85% of success, these rates are thought to be very good considering the difficulties found in the study with the different nature of the profiles; however, one way to emphasize the validity of these results is to compare them with other algorithms found in the literature and/or with other datasets. The latter option is more complicated since we are dealing with datasets that are not easy to obtain freely, in fact, many datasets belong to the military and are hardly accessible. Thus, validation by comparison with mature algorithms is carried out here.

For this comparison, only the results of Test Case II.d will be evaluated, since, as seen, on the one hand the utilization of small matrices of range profiles provides better recognition results, and on the other hand, because the evaluation of the actual vs. synthetic profiles case is desired. Nevertheless, due to the instability of F_u, it can be directly discarded from this assessment since, as seen, the confidence in the results are highly dependent on the energy threshold selection and F_w provides an improvement.

[11] F_w returned an 84.26% of success against the obtained 83.83% of success achieved by gMSM; this difference is caused by the wrong classification of just one frame.

The algorithms selected to take part in this comparison are also related somehow to PCA and subspaces, in fact, the first of these algorithms is the MSM, previously explained in section 5.2.1 and in [71]. The second algorithm is the one presented in [9], which is called the PCA-based minimum reconstruction error approximation, for simplicity we will call it PCA-MRE; in this algorithm, the input to the classifier is each of the HRRPs in the test set, individually; firstly, PCA is also used in the algorithm to extract the feature subspace of a frame of HRRPs belonging to the training set and once the subspaces are defined, the algorithm decides the input class considering its minimum reconstruction error in each of the previous obtained feature subspaces. The reader is referred to the cited papers for more information about the algorithms.

The algorithms presented in this thesis will be tuned to their own optimum parameters; for the case of PCA-MRE the optimum parameter proposed in its respective paper will be evaluated, while for MSM due to the similarity with both F_w and gMSM, the selected threshold parameter will be set according to both algorithms: the same energy threshold as for F_w will be selected to define the subspaces of MSM since that value also follows the same rules than gMSM for the best results, therefore MSM can be compared with both algorithms in a more fair way. Table 6.41 summarizes the parameters used in the comparison as well as their corresponding final recognition rates obtained.

Table 6.41: Algorithm comparison. Specifications

Algorithm	Parameter Value	Success Rate (%)	Confidence deg.(mean)	Confidence deg.(std)
F_w	$\eta = 0.4$	84.26	0.1989	0.1593
$gMSM$	m=1	83.83	0.2512	0.2040
MSM	$\eta_S = \eta_D = 0.4$	84.26	0.2506	0.2052
$PCA-RME$	$\eta = 0.99$	82.82	0.2522	0.2558

This comparison was made with the purpose of validating the performances of the proposed algorithms and, as seen, F_w and MSM return the same success rates, while gMSM and PCA-RME slightly lower rates. The fact of obtaining similar results for all these algorithms proves that the algorithms proposed along this thesis are also good candidates for aircraft recognition since the obtained rates fall into the same range as other algorithms seen in the literature.

Apart from the success rates, Table 6.41 also shows the mean difference between the winning aircraft and the next, and the standard deviation of these mean differences found for the algorithms and their optimum parameters. The difference is expressed normalized by the maximum value that each algorithm can reach, so the results are comparable. As seen, the confidence degrees obtained for gMSM, MSM and PCA-RME are quite similar, around 0.25, while for F_w a lower value is obtained (around 0.20). The standard deviations are quite high for their respective mean confidence degree, which denotes a great fluctuation in the results for all the algorithms. In the case of PCA-RME this is more accused, and therefore, it may denote more instability in this algorithm. Regarding gMSM, F_w and MSM, these fluctuations will be less accused, but in all cases this is caused by the dissimilarities between the test and training samples. Taking this into account, the best confidence degree found will be that of gMSM, mainly due to the lack of subspace dimensionality selection.

After the analysis of these results, it can be said that both algorithms F_w and gMSM are appropriate to perform classification of actual range profiles with a database of synthetic profiles; however, the main drawback of F_w is the need of the subspace dimensionality selection. Even though it was seen along this chapter that it is not as important as in other algorithms like F_u, a selected dimensionality far from

the optimum one can provide much lower success rates; additionally, a change in the datasets can cause the optimum dimensionality to vary, as seen along the different subcases. On the other hand, gMSM skips that step and considers the whole subspace although weighting their bases with their corresponding modified eigenvectos, so-called *softweights*, so, instead of having truncated subspaces as F_w and F_u, it works with *softweighted* ones. Obviously, the parameter that controls the *softweights* also needs of a proper selection, however, as seen along section 6.2.2, its range of variation for good results is more limited and it was proven that by setting a low value very good recognition results are achieved. In conclusion, it seems that gMSM provides a certain higher degree of confidence in the classification since it considers the whole subspace, and on the other hand if F_w were used, even though we had a very complete database and the parameter η had been tuned to find its optimum value for that case study, the introduction of new data into the database would need of a whole new process of selection of its proper value. Nonetheless, since gMSM takes the whole weighted subspace, the addition of new samples into the datasets is not that problematic.

On the other hand, the truncation of the subspaces carried out in F_w lowers the computational complexity and memory requirements of the algorithm, while for gMSM more computational resources will be needed. This way, it can be said that, even though it was concluded that gMSM provides more confidence, the selection of one or another may also depend on the nature of the database (how well populated it is and if many new aircraft will be frequently added) and the speed and available memory of our operative system.

Chapter 7

Conclusions and future research

This thesis was mainly focused on the research and definition of different algorithms for identifying flying aircraft in a non-cooperative way. The fact that identification is made non-cooperatively requires the null communication between our system and the aircraft itself; therefore, information about the target has to be gathered in other ways.

Chapter 2 reviewed the different techniques for Non-Cooperative Target Identification, like JEM, ISAR or HRRP and finally it was concluded that HRRPs are a simple and powerful tool to achieve this type of recognition since they provide information about target structure, their simplicity makes them easy to work with, and thanks to the radar properties they can be collected under adverse weather conditions even with the target being unaware of it.

Along this text, an incremental study of three different algorithms whose main purpose was the classification of HRRP has been developed. To do so, a selection of feature extraction techniques and different classifiers have been reviewed first; the problem of choosing a classifier is not trivial, in fact, there is no optimal classification rule for every problem; therefore, after the evaluation of the advantages and disadvantages of the reviewed types of feature extraction and classification techniques, it was finally decided that feature extraction will be provided by eigendecomposition and the classifiers to be developed will be included in the family of distance classifiers.

Due to the lack of high availability of measurements of in-flight aircraft in many aspect angles to populate the database of potential targets, one last decision was made in Chapter 2: the database will be populated with range profiles generated by a simulation software, that is what we have called synthetic profiles. This approach is barely seen in the literature although is very interesting since synthetic profiles can be generated at any aspect angle and aircraft configuration and any aircraft could be added to the database just by knowing its CAD model, so the database can be as wide as wanted. However, the main issue is the high idealism of the synthetic profiles that makes them differ somehow from an actual HRRP and adds difficulty to the classification process.

Chapter 3 described more accurately the properties of range profiles and the few difficulties found in their extraction that need to be compensated in a preprocessing step before classification takes place. Taking this into account, Chapter 4 presented the datasets used in this thesis along with the specific preprocessing techniques applied to them. In such manner, two datasets were proposed, the test set (the input of the classifier) and the training set (the database); the test set consists of actual range profiles coming from the ORFEO measurement campaign, while the training set contains synthetic range profiles simulated by FASCRO. As seen in the aforementioned chapter, there exist dissimilarities between actual and synthetic profiles mainly due to CAD modeling ambiguities, unmodeled reflective processes

and the estimation of aspect angles. Keeping that in mind, Chapter 5 formulated the three algorithms proposed in this thesis to achieve NCTR in an incremental way, F_u, F_w and gMSM. The three algorithms have in common the feature extraction method, Principal Component Analysis, and are based on the calculation of angle between subspaces, on the contrary, their main differences lie in how they weight their corresponding subspaces. While F_u and F_w need to set the dimensionality of the subspaces in advance according to the highest singular values, gMSM takes the complete subspaces but weights each of their bases according to a modified value of their corresponding eigenvalues; this modified value is the *softweight*.

After the definition of the proposed algorithms, Chapter 6 presented an incremental study of the performance of each of them according to their respective tuning parameters, which are: the energy threshold (η) to extract the subspaces for F_u and F_w, and for gMSM, the *softweigthing* parameter of test and training samples (m_D and m_S) that are firstly modulated by a threshold (η_D and η_S) in order to finally find their optimum value. For the incremental study, two test cases were proposed, one in which the test and training sets were divided into big frames of HRRPs and 5 aircraft were recognized utilizing a database of 6 aircraft, while in the second one the test and training sets were divided into smaller frames of HRRPs and 6 aircraft were identified with a database of 7 aircraft. Both test cases were divided into smaller subcases, beginning with an ideal case where both test and training sets comprised the same synthetic profiles; after that, the ideal case with additive white gaussian noise added only to the test set was studied, followed by the third subcase where besides the noise, the effects of TRM where also evaluated; finally, the last subcase into which the test cases were divided took the actual range profiles as test set and the synthetic range profiles as training set, in order to ensure that the conclusions made on the previous ideal subcases were on the right direction and that the recognition of actual range profiles can be achieved with a database of just synthetic profiles.

7.1. Conclusions

After this brief summary of the different chapters of this text, in this section the conclusions drawn and the lessons learned after the evaluation of the three proposed algorithms are gathered.

- First of all, after the analysis of the two test cases in Chapter 6, it has been proven that the classification of small frames of range profiles returns better recognition performance than the classification of bigger ones. As seen, Test Case II, which divided the trajectories into frames covering 2.5° in azimuth and that always had a number of profiles smaller than 100, led to much better success rates than Test Case I, that classified frames with a number of profiles up to 300.

- Among the three algorithms proposed in this thesis, F_u can be considered as invalid for the recognition of HRRPs. As seen, it is not robust against noise or TRM, and the results obtained are highly dependent on the threshold selected for the subspace dimensionality.

- The F_w and gMSM have both returned very good results which are comparable with other algorithms provided in the literature. Thus, both can be considered as proper classifiers for the problem presented here:

    - Algorithm F_w improves F_u by adding a weighting element. With this, high recognition results and robustness against noise and TRM is obtained. The subspace dimensionality should be set with an energy threshold, η, which in the ideal cases, where test and training sets do not highly differ, has a certain degree of freedom. However, when the datasets get more different,

the energy threshold should lower its value and thus, the dimensionality of the subspace will be reduced.

- In the case of gMSM, the subspace dimensionality selection is not necessary. The *softweighting* controls the importance of each eigenvector in the subspace. Now, the energy threshold is not needed to be set unlike F_w, but the selection of the *softweighting* parameter is needed for both datasets (m_D and m_S). The study has shown that these parameters should be set to small values as the datasets get more different, in particular if both m are set to 1, the algorithm has shown very good recognition results for all the test cases. Additionally, gMSM has also shown robustness against noise and TRM regardless of parameter m.

- Both F_w and gMSM yielded very similar success rates and showed robustness against noise and TRM, however each of them has their advantages and disadvantages that may make us opt for one or another.

  - F_w needs to set the subspace dimensionality, which is not a trivial issue, in fact as the datasets differ, the algorithm becomes more sensitive to this dimensionality selection. However, the advantage of choosing the dimensionality is the less computational resources needed.
  - On the other hand, the great advantage of gMSM over F_w is the absence of the step of subspace dimensionality selection. By taking the whole *softweighted* subspace, more robustness is added to gMSM, fact denoted by the higher confidence degree seen in the comparison of algorithms in Chapter 6. However, this has the drawback of needing more computational resources.

- Lastly, whatever algorithm chosen between these two, it has been proven that the recognition of actual profiles by means of a synthetic database is achievable, reaching success rates of nearly 85%.

7.2. Main Contributions

This thesis has provided a complete study about non-cooperative target identification and the previous section has summarized the conclusions drawn along its different chapters. Recognition of flying targets non-cooperatively utilizing range profiles has been long studied for years, however, there is still a lot to do to make it a reality and thus, research on this field is still essential. That is why, at this point, it is important to emphasize the main contributions made within this study.

First of all, three new algorithms have been developed for NCTI, the cumulative angle between subspaces (F_u), the weighted cumulative angle between subspaces (F_w), and the generalized Mutual Subspace Method (gMSM), all of them based on subspace methods. In the literature, this kind of methodologies are mainly used for image recognition, while here they are used for range profiles recognition, which in a way, it can be seen as a sort of image recognition.

Among the three, only one method has provided non-stable results, F_u, being very sensitive to noise and additional unwanted effects. Nevertheless, thanks to its poor results, and the thorough study of the rest of the algorithms, it has been proven that the application of weighting elements based on eigen or singular values to the metrics leads to more robust algorithms.

An incremental study has been developed to asses these algorithms. This incremental study has been conceived with the purpose of evaluating the algorithms according to different scenarios. With this, we were able to isolate the results obtained for a given scenario and to evaluate, therefore, the robustness and performance of each algorithm in each framework.

Additionally, instead of identifying each profile individually as many other authors do, the recognition of matrices of range profiles is carried out in order to know more information about the illuminated target and its trajectory. In this regard, it has been seen that matrices of too many range profiles provide worst results than smaller matrices for two main reasons: on the one hand, the bigger the matrix, the fewer the number of input samples and therefore, the final recognition results are less reliable; on the other hand, as the number of profiles in a matrix gets higher, although more information is included, the system is not able to handle it and therefore, it is not efficient. Thus, it was seen, that taking matrices up to 20 or 25 profiles provide much better and reliable results.

Finally, the identification of actual range profiles with a database of synthetic range profiles has been proven to be possible and with an acceptable level of success. As said at the beginning and along this whole thesis, the problem of NCTI encompasses also the problem of populating a database of potential targets. As seen, it is not an easy task and this is still an open field.

The database of targets should provide range profiles of all the existing aircraft in many orientations such that, when an unknown aircraft is illuminated by the radar, the system can search for its class. To obtain such a database, a measurement campaign is necessary, where all nations provide their aircraft and the trajectories are commonly defined such that they include a wide range of orientations. However, in reality, this is highly improbable, not only because of the cost it will involve, but also because of the refusal of many nations that might not be interested in providing the others with their aircraft's signatures.

Therefore, due to the difficulty in obtaining range profiles of actual flying targets and thanks to the evolution of the electromagnetic simulation tools, in this thesis the database has been populated with synthetic range profiles. Additionally, to make the study more reliable and close to reality, the range profiles utilized as input of our system comprised actual range profiles obtained in a measurement campaign. With this, a real scenario is outlined where the measured profiles are not exactly the same profiles that populate the database.

All the conclusions and contributions summarized in this chapter can be also found in different papers written by the author along the course of these years of investigation. First, the most important papers are cited below, given their inclusion in renowned scientific journals:

- **P. López-Rodríguez**, R. Fernández-Recio, I. Bravo, A. Gardel, J. L. Lázaro, and E. Rufo, "Computational burden resulting from image recognition of high resolution radar sensors", Sensors, vol. 13, no. 4, pp. 5381-5402, 2013.
- **P. López-Rodríguez**, D. Escot-Bocanegra, R. Fernández-Recio and I. Bravo, "Non-Cooperative Target Recognition by Means of Singular Value Decomposition Applied to Radar High Resolution Range Profiles", Sensors, vol. 15, pp. 422-439, 2015.
- **P. López-Rodríguez**, D. Escot-Bocanegra, R. Fernández-Recio and I. Bravo, "Non-cooperative identification of civil aircraft using a generalised mutual subspace method", IET Radar, Sonar & Navigation, vol. 10, no. 1, pp. 186-191, 2016.

Additionally, other papers related to the topic have been presented in national and international conferences including:

- **P. López-Rodríguez**, R. Fernández-Recio, I. Bravo and A. Gardel, "Tendencias actuales de la lógica reconfigurable en sistemas radar", XII Jornadas de Computación Reconfigurable y Aplicaciones (JCRA) 2012, Elche, Spain.

- **P. López-Rodríguez**, R. Fernández-Recio, I. Bravo, E. de Diego-Custodio, D. Poyatos-Martínez, D. Escot-Bocanegra, "Identificación no cooperativa de blancos reales aéreos mediante radar utilizando una base de datos sintética y descomposición en valores singulares", Congreso Nacional de I+D en Defensa y Seguridad - DESEi+d 2013, Madrid, Spain.

- **P. López-Rodríguez**, D. Escot-Bocanegra, R. Fernández-Recio and I. Bravo, "Singular Value Decomposition Applied to Automatic Target Recognition with High Resolution Range Profiles", 1st International Electronic Conference on Sensors and Applications 2014, e-conference.

- O. Hernán-Vega, **P. López-Rodríguez**, D. Escot-Bocanegra, R. Fernández-Recio and I. Bravo, "Non-Cooperative Target Identification Based on Singular Value Decomposition", International Radar Symposium (IRS) 2015, Dresden, Germany.

- O. Hernán-Vega, **P. López-Rodríguez**, D. Escot-Bocanegra, R. Fernández-Recio and I. Bravo, "Evaluación de algoritmos de identificación no cooperativa de blancos aéreos mediante perfiles de alta resolución", Congreso Nacional de I+D en Defensa y Seguridad DESEi+d 2015, Pontevedra, Spain.

- O. Hernán-Vega, **P. López-Rodrígue**z, D. Escot-Bocanegra and D. Poyatos-Martínez, " Singular Value Decomposition Applied to Non-Cooperative Target Identification", 2nd International Electronic Conference on Sensors and Applications 2015, e-conference.

- O. Hernán-Vega, **P. López-Rodríguez**, D. Escot-Bocanegra and D. Poyatos-Martínez, "On the Application of SVD to Non-Cooperative Target Identification Problems", STO - Specialists Meeting on Radar Imaging for Target Identification (SET-228), 2015, Pisa, Italy.

7.3. Future research

A doctoral thesis is not a concluded study but a living investigation that opens the door to new ideas and projects. In effect, along this text it has been proven that classification of actual range profiles with the only help of a synthetic database using subspace methods is feasible, however the path is still long and there are a number of tasks that are still pendent and even more questions will arise. Among these opened tasks we can highlight:

- **Expansion and improvement of datasets**. The datasets utilized along this thesis come from an actual measurement campaign of civil targets and from synthetic simulations, as said, the utilization of synthetic profiles to populate the database gives us the possibility to expand it as required just by obtaining the CAD model of new targets and defining their aspect angles; therefore, a few more targets could be modeled and simulated to be added to the database; additionally, these new potential targets need not have a corresponding actual measurement in the test set, hence we would be adding new obstacles to the algorithms. Regarding the actual range profiles forming the test set, new targets could be retrieved from the ORFEO measurement campaign, this way, the bigger the datasets, the more accurate the evaluation of the algorithms will be.

  It would be also highly desirable to own new measurements of the same or different targets than the ORFEO campaign; as said, finding free access measurements of HRRPs is not that easy and many of them belong to the military and cannot be published; INTA, for example, could provide new measurements of fighter planes but the results cannot be distributed and that is why those profiles were not used here. However, in order to keep validating the algorithms, those measurements could

be used. With the new datasets, it is desired to assess the optimum parameters again for the presented algorithms, that is the energy threshold for F_w and m for gMSM, this way, more robust conclusions can be drawn about them.

Even though the classification of actual profiles with synthetic ones returns good success rates for both algorithms, it is thought that these rates may be raised by making the test and training samples more similar. One way to do so could be to degrade the synthetic profiles in the database as it was done in the different subcases for the test samples; however, the question of how much noise should be added or what other effects could be added and how to deteriorate the profiles is not trivial. Another way, more feasible, could be to apply algorithms of noise reduction to the test set, improve the profiles alignment to avoid the effects of TRM or add some kind of profile averaging.

Lastly, remember that for the simulations of the synthetic range profiles, the trajectories of the actual profiles were utilized to define their aspect angles, nevertheless there was a certain degree of uncertainty since those aspect angles were just estimations of the real ones described by the aircraft and they may have an error up to 5°. This uncertainty proves that the algorithms are robust against target aspect angle to a certain extent, but the closer the aspect angle of the simulated profiles to the real ones, the higher their similarity. Thus, a point cloud of $\pm 5°$ in azimuth and elevation could be defined around the estimated aspect angles and synthetic range profiles for those could be obtained; this way when identifying, the system should also try to find the best match for the trajectories.

- **Implementing an operative demonstrator**. Every algorithm is conceived with the purpose of taking part in a real system, thus, one of the future research lines could be the efficient implementation of the algorithms developed here into a suitable platform. Should this platform be selected properly, it would be of high interest first to study the computational burden of the algorithms by means of analyzing the order of magnitude of the calculations that should be made and to see how many operations could be parallelized and optimized. First, the algorithms could be implemented into small platforms to create a demonstrator and later on, it could be embedded into a real high resolution radar.

  In addition, the option for an unknown target can be provided. This way, the classifier is not forced to assign a class to a target which returns a poor match with any database entry, instead the target would be declared as unknown. This would be the case for an aircraft which is measured for the first time and its signature is not in the database.

- **Algorithm generalization**. The algorithms proposed here are developed for the application of NCTI; however, they are just classifiers and as said, they belong to the global problem of patter recognition; as such, they can be generalized to be used in other applications such as image recognition, face detection, ground target identification, speech recognition, crop fields classification, etc. Furthermore, by generalizing the algorithms to be used in other fields of research could provide us with more datasets to keep validating and improving the algorithms; so, the advantages are two-fold: the experience of exploring new disciplines and the acquisition of new datasets which may have different properties and may challenge our algorithms.

- **Enhancing and exploring new classifiers**. According to Chapter 2 there exist a broad collection of types of classifiers and among them, due to our own experience, to the simplicity in implementation and ease in adaptation to new scenarios, distance classifiers based on subspaces are developed in this thesis. Nevertheless, as seen in the aforementioned chapter, other methods have also their advantages, so, why not try with some of them? Neural networks, support vector machines or hidden Markov models are utilized in the literature also for the classification of range

profiles, however, not many of them try to classify actual profiles with synthetic ones, so exploring new classifiers under this scenario could be of great interest. Additionally, the change in the classification method may produce also a change in the feature extraction method so it should also be revised.

Lastly, along this thesis, all the work is done with range profiles, that are a real magnitude, however, the last tendency is to keep the phase of the range profiles and try to classify the complex range profiles. Few studies deal with this option so it could be interesting to analyze the properties of the complex profiles and check the viability of classifying actual complex range profiles, whose phase will change according to the environment in which the measurement was taken, with synthetic complex range profiles, whose phase will be ideal.

As said, these are a few suggestions but more ideas will arise, since, quoting the Irish writer George Bernard Shaw:

Science never solves a problem without creating ten more.

Bibliography

[1] U. S. Congress, Office of Technology Assessment, "Who goes there: friend of foe?" June 1993.

[2] L. Bowden, "The story of IFF (identification friend or foe)," *IEE Proceedings A (Physical Science, Measurement and Instrumentation, Management and Education, Reviews)*, vol. 132, pp. 435–437(2), October 1985.

[3] P. Tait, *Introduction to Radar Target Recognition*. Institution of Engineering and Technology, 2005.

[4] http://www.indracompany.com/en/industries/defense/offering/air/air-defense.

[5] http://www.theregister.co.uk/2004/05/20/patriot_missile/.

[6] H. Borrion, "Study of processing techniques for radar non-cooperative target recognition," Ph.D. dissertation, Department of Electronic and Electrical Engineering. University College London, 2006.

[7] M. Cohen, "An overview of radar-based, automatic, noncooperative target recognition techniques," in *Systems Engineering, 1991., IEEE International Conference on*, Aug 1991, pp. 29–34.

[8] J. Zwart, R. van der Heiden, S. Gelsema, and F. Groen, "Fast translation invariant classification of HRR range profiles in a zero phase representation," *Radar, Sonar and Navigation, IEE Proceedings* -, vol. 150, no. 6, pp. 411–418, Dec 2003.

[9] L. Du, H. Liu, Z. Bao, and J. Zhang, "Radar automatic target recognition using complex high-resolution range profiles," *Radar, Sonar Navigation, IET*, vol. 1, no. 1, pp. 18–26, 2007.

[10] V. Zeljkovic, C. Tameze, and R. Vincelette, "Algorithms for radar image identification and classification," in *High Performance Computing and Simulation (HPCS), 2010 International Conference on*, June 2010, pp. 418–424.

[11] D. Pastina and C. Spina, "Multi-frame data fusion techniques for ATR of ship targets from multiple ISAR images," in *Radar Conference, 2009. EuRAD 2009. European*, Sept 2009, pp. 409–412.

[12] D. Blacknell and H. Griffiths, *Radar Automatic Target Recognition (ATR) and Non-Cooperative Target Recognition (NCTR)*, ser. Radar, Sonar, Navigation and Avionics. Institution of Engineering and Technology, 2013. [Online]. Available: http://digital-library.theiet.org/content/books/ra/pbra033e

[13] North Atlantic Treaty Organization, "Non-cooperative air target identification using radar," Systems Concepts and Integration (SCI), Research & Technical Organization (RTO), Meeting Proceedings 006, 1998.

[14] B. Borden, *Radar Imaging of Airborne Target: A Primer for Applied Mathematicians and Physicists*. Philadelpia, PA, Institute of Physics Publishing, 1999.

[15] H.-J. Li and S.-H. Yang, "Using range profiles as feature vectors to identify aerospace objects," *Antennas and Propagation, IEEE Transactions on*, vol. 41, no. 3, pp. 261–268, Mar 1993.

[16] V. Bhatnagar, A. Shaw, and R. Williams, "Improved automatic target recognition using singular value decomposition," in *Acoustics, Speech and Signal Processing, 1998. Proceedings of the 1998 IEEE International Conference on*, vol. 5, 1998, pp. 2717–2720.

[17] K. T. Kim, D.-K. Seo, and H.-T. Kim, "Radar target identification using one-dimensional scattering centres," *Radar, Sonar and Navigation, IEE Proceedings* -, vol. 148, no. 5, pp. 285–296, Oct 2001.

[18] C. Nan and X. Minghua, "Target recognition based on the self-correlation function of HRRP," in *Electrical and Control Engineering (ICECE), 2010 International Conference on*, June 2010, pp. 4787–4789.

[19] D. Zhou, X. Shen, and W. Yang, "Radar target recognition based on fuzzy optimal transformation using high-resolution range profile," *Pattern Recogn. Lett.*, vol. 34, no. 3, pp. 256–264, Feb. 2013. [Online]. Available: http://dx.doi.org/10.1016/j.patrec.2012.10.010

[20] H. Zhang, D. Ding, Z. Fan, and R. Chen, "Adaptive neighborhood-preserving discriminant projection method for HRRP-based radar target recognition," *Antennas and Wireless Propagation Letters, IEEE*, vol. 14, pp. 650–653, 2015.

[21] M. Bell and R. Grubbs, "JEM modeling and measurement for radar target identification," *Aerospace and Electronic Systems, IEEE Transactions on*, vol. 29, no. 1, pp. 73–87, Jan 1993.

[22] R. E. Gardner, "Doppler spectral characteristics of aircraft radar targets at S-band," Naval Research Laboratory Washington DC, Tech. Rep., 1961.

[23] P. Pellegrini, S. Cuomo, and S. Pardini, "Radar signals analysis oriented to target characterization applied to civilian ATC radar," in *Radar 92. International Conference*, Oct 1992, pp. 438–445.

[24] P. Pellegrini, S. Cuomo, and F. Piazza, "ATC primary radar signal analysis for target characterisation. a model validation," in *Radar Conference, 1995., Record of the IEEE 1995 International*, May 1995, pp. 516–520.

[25] S. Cuomo and E. Piazza, "Model validation for 'jet engine modulation' phenomenon," *Electronics Letters*, vol. 30, no. 24, pp. 2073–2074, Nov 1994.

[26] H. Lim, J. H. Park, J. H. Yoo, C. H. Kim, K. I. Kwon, and N. H. Myung, "Joint time-frequency analysis of radar micro-doppler signatures from aircraft engine models," *Journal of Electromagnetic Waves and Applications*, vol. 25, no. 8-9, pp. 1069–1080, 2011.

[27] H. Park, J.-H.and Lim and M. N.-H., "Modified Hilbert-Huang transform and its application to measured micro doppler signatures from realistic jet engine models," *Progress In Electromagnetics Research*, vol. 126, pp. 255–268, 2012.

[28] http://www.pw.utc.com/F100_Engine.

[29] http://www.geaviation.com/commercial/engines/cf6/.

[30] http://www.airbus.com/aircraftfamilies/out-of-production/a310/.

[31] D. R. Wehner, *High-Resolution Radar*, 2nd ed. Artech House, 1995.

[32] J. S. Son and G. T. B. Flores, *Range-Doppler Radar Imaging.* Artech House, 2001.

[33] J. M. M. Ferreras, "Enfocado de imágenes de radar de apertura sintética inversa. Nuevas técnicas y aplicaciones," Ph.D. dissertation, Universidad Politécnica de Madrid, 2008.

[34] C.-C. Chen and H. Andrews, "Target-motion-induced radar imaging," *Aerospace and Electronic Systems, IEEE Transactions on*, vol. AES-16, no. 1, pp. 2 –14, jan. 1980.

[35] M. Xing, R. u, and Z. Bao, "High resolution ISAR imaging of high speed moving targets," *Radar, Sonar and Navigation, IEE Proceedings* -, vol. 152, no. 2, pp. 58–67, April 2005.

[36] W. Brown and R. Fredricks, "Range-doppler imaging with motion through resolution cells," *Aerospace and Electronic Systems, IEEE Transactions on*, vol. AES-5, no. 1, pp. 98 –102, jan. 1969.

[37] T. Itoh, H. Sueda, and Y. Watanabe, "Motion compensation for ISAR via centroid tracking," *Aerospace and Electronic Systems, IEEE Transactions on*, vol. 32, no. 3, pp. 1191 – 1197, jul. 1996.

[38] F. Pérez-Martínez, J. Garcia-Fominaya, and J. Calvo-Gallego, "A shift-and-convolution technique for high-resolution radar images," *Sensors Journal, IEEE*, vol. 5, no. 5, pp. 1090 – 1098, oct. 2005.

[39] L. Xi, L. Guosui, and J. Ni, "Autofocusing of ISAR images based on entropy minimization," *Aerospace and Electronic Systems, IEEE Transactions on*, vol. 35, no. 4, pp. 1240 –1252, oct. 1999.

[40] F. Berizzi, M. Martorella, B. Haywood, E. Dalle Mese, and S. Bruscoli, "A survey on ISAR autofocusing techniques," in *Image Processing, 2004, International Conference on*, vol. 1, Oct 2004, pp. 9 – 12.

[41] M. Skolnik, *Introduction to Radar Systems.* McGraw-Hill, 1981.

[42] T. Sauer, K.-H. Bethke, F. Buettner, B. Roede, and A. Schroth, "Imaging of commercial aircraft by inverse synthetic aperture radar and their classification in a Near-Range Radar Network (NRN)," in *Radar Conference, 1997., IEEE National*, May 1997, pp. 19–24.

[43] J. Li and H. Ling, "Use of genetic algorithms in ISAR imaging of targets with higher order motions," *Aerospace and Electronic Systems, IEEE Transactions on*, vol. 39, no. 1, pp. 343–351, Jan 2003.

[44] H. Borrion, H. Griffiths, P. Tait, D. Money, and C. Baker, "One-dimensional model-based approach for ISAR imaging," in *Geoscience and Remote Sensing Symposium, IGARSS '05. Proceedings. 2005 IEEE International*, vol. 1, July 2005, pp. 4 pp.–.

[45] A. Aprile, D. Meledandri, T. Pellizzeri, and A. Mauri, "Translational rotational motion compensation: a single algorithm for different radar maging applications," *Signal Processing, IET*, vol. 2, no. 3, pp. 204 –215, sept. 2008.

[46] J. Muñoz Ferreras, F. Pérez-Martínez, and M. Datcu, "Generalisation of inverse synthetic aperture radar autofocusing methods based on the minimisation of the Renyi entropy," *Radar, Sonar Navigation, IET*, vol. 4, no. 4, pp. 586 – 594, aug. 2010.

[47] M. Martorella, D. Stagliano, F. Salvetti, and N. Battisti, "3D interferometric ISAR imaging of noncooperative targets," *Aerospace and Electronic Systems, IEEE Transactions on*, vol. 50, no. 4, pp. 3102–3114, October 2014.

[48] K. Rosenbach and J. Schiller, "Non-cooperative air target identification using radar imagery: identification rate as a function of signal bandwidth," in *Radar Conference, 2000. The Record of the IEEE 2000 International*, May 2000, pp. 305–309.

[49] T.-L. Chia, S.-C. Tien, and Y. Lu, "Recognize aircraft in ISAR images," *Journal of Information Science and Engineering*, vol. 23, pp. 299 – 313, 2007.

[50] A. Jurado-Lucena, B. Errasti-Alcalá, D. Escot-Bocanegra, R. Fernández-Recio, D. Poyatos-Martínez, and I. Montiel Sánchez, "Methodology to achieve accurate non cooperative target identification using high resolution radar and a synthetic database," in *Trends in Applied Intelligent Systems*, ser. Lecture Notes in Computer Science, N. García-Pedrajas, F. Herrera, C. Fyfe, J. M. Benítez, and M. Ali, Eds. Springer Berlin Heidelberg, 2010, vol. 6096, pp. 427–436. [Online]. Available: http://dx.doi.org/10.1007/978-3-642-13022-9_43

[51] M. Martorella, E. Giusti, L. Demi, Z. Zhou, A. Cacciamano, F. Berizzi, and B. Bates, "Target recognition by means of polarimetric ISAR images," *Aerospace and Electronic Systems, IEEE Transactions on*, vol. 47, no. 1, pp. 225–239, January 2011.

[52] F. Benedetto, F. Riganti Fulginei, A. Laudani, and G. Albanese, "Automatic aircraft target recognition by ISAR image processing based on neural classifier," *International Journal of Advanced Computer Science and Applications*, vol. 3, no. 8, pp. 96 – 103, 2012.

[53] E. Giusti, M. Martorella, and A. Capria, "Polarimetrically-persistent-scatterer-based automatic target recognition," *Geoscience and Remote Sensing, IEEE Transactions on*, vol. 49, no. 11, pp. 4588–4599, Nov 2011.

[54] R. Duda, P. Hart, and D. Stork, *Pattern Classification*, 2nd ed. John Wiley & Sons Inc., 2001.

[55] L. Chen and R. Chen, "A new radar target recognition method based on complex high resolution range profiles," in *Microwave and Millimeter Wave Technology (ICMMT), 2012 International Conference on*, vol. 2, 2012, pp. 1–4.

[56] B. Chen, H. Liu, and Z. Bao, "PCA and kernel PCA for radar high range resolution profiles recognition," in *Radar Conference, 2005 IEEE International*, May 2005, pp. 528 – 533.

[57] J. Pisane, M. Lesturgie, and J. Verly, "Target classification system based on the characterization of targets by subspaces," in *Radar (Radar), 2011 IEEE CIE International Conference on*, vol. 1, Oct 2011, pp. 621–625.

[58] J.-H. Jung, H.-T. Kim, and K.-T. Kim, "Comparisons of four feature extraction approaches based on fisher's linear discriminant criterion in radar target recognition," *Journal of Electromagnetic Waves and Applications*, vol. 21, no. 2, pp. 251–265, 2007.

[59] A. Zyweck and R. E. Bogner, "Radar target classification of commercial aircraft," *Aerospace and Electronic Systems, IEEE Transactions on*, vol. 32, no. 2, pp. 598–606, April 1996.

[60] D. Nelson, J. Starzyk, and D. Ensley, "Iterated wavelet transformation and signal discrimination for HRR radar target recognition," *Systems, Man and Cybernetics, Part A: Systems and Humans, IEEE Transactions on*, vol. 33, no. 1, pp. 52–57, Jan 2003.

[61] B. Huether, S. Gustafson, and R. Broussard, "Wavelet preprocessing for high range resolution radar classification," *Aerospace and Electronic Systems, IEEE Transactions on*, vol. 37, no. 4, pp. 1321–1332, Oct 2001.

[62] L. Du, H. Liu, P. Wang, B. Feng, M. Pan, and Z. Bao, "Multitask factor analysis with application to noise robust radar HRRP target recognition," in *Radar Conference (RADAR), 2012 IEEE*, May 2012, pp. 0202–0207.

[63] S. K. Wong, "Non-cooperative target recognition in the frequency domain," *Radar, Sonar and Navigation, IEE Proceedings* -, vol. 151, no. 2, pp. 77–84, 2004.

[64] D.-H. Kim, D.-K. Seo, and H.-T. Kim, "Efficient radar target recognition using the MUSIC algorithm and invariant features," *Antennas and Propagation, IEEE Transactions on*, vol. 50, no. 3, pp. 325–337, Mar 2002.

[65] P. Wang, F. Dai, M. Pan, L. Du, and H. Liu, "Radar HRRP target recognition in frequency domain based on autoregressive model," in *Radar Conference (RADAR), 2011 IEEE*, May 2011, pp. 714 – 717.

[66] L. Du, H. Liu, Z. Bao, and M. Xing, "Radar HRRP target recognition based on higher order spectra," *Signal Processing, IEEE Transactions on*, vol. 53, no. 7, pp. 2359–2368, July 2005.

[67] Z. Guo and S. Li, "One-dimensional frequency-domain features for aircraft recognition from radar range profiles," *Aerospace and Electronic Systems, IEEE Transactions on*, vol. 46, no. 4, pp. 1880–1892, Oct 2010.

[68] P. Molchanov, K. Egiazarian, J. Astola, A. Totsky, S. Leshchenko, and M. Jarabo-Amores, "Classification of aircraft using micro-doppler bicoherence-based features," *Aerospace and Electronic Systems, IEEE Transactions on*, vol. 50, no. 2, pp. 1455–1467, April 2014.

[69] H. Liu, F. Chen, L. Du, and Z. Bao, "Robust radar automatic target recognition algorithm based on HRRP signature," *Frontiers of Electrical and Electronic Engineering*, vol. 7, no. 1, pp. 49–55, 2012. [Online]. Available: http://dx.doi.org/10.1007/s11460-012-0191-1

[70] K. Copsey and A. Webb, "Bayesian gamma mixture model approach to radar target recognition," *Aerospace and Electronic Systems, IEEE Transactions on*, vol. 39, no. 4, pp. 1201–1217, Oct 2003.

[71] O. Yamaguchi, K. Fukui, and K. Maeda, "Face recognition using temporal image sequence," in *Automatic Face and Gesture Recognition, 1998. Proceedings. Third IEEE International Conference on*, 1998, pp. 318–323.

[72] X. Zeng and J. Zhong, "Semi-supervised discriminative mutual subspace method," in *Cognitive Informatics Cognitive Computing (ICCI*CC), 2011 10th IEEE International Conference on*, Aug 2011, pp. 161–166.

[73] A. Maki and K. Fukui, "Ship identification in sequential ISAR imagery," *Mach. Vision Appl.*, vol. 15, no. 3, pp. 149–155, Jul. 2004. [Online]. Available: http://dx.doi.org/10.1007/s00138-004-0140-y

[74] W. McCulloch and W. Pitts, "A logical calculus of the ideas immanent in nervous activity," *The bulletin of mathematical biophysics*, vol. 5, no. 4, pp. 115–133, 1943.

[75] A. Jurado-Lucena, I. Montiel-Sánchez, D. Escot-Bocanegra, R. Fernández-Recio, and D. Poyatos-Martínez, "Class identification of aircrafts by means of artificial neural networks trained with simulated radar signatures," *Progress In Electromagnetics Research C*, 2011.

[76] M. Rizki, M. Zmuda, and L. Tamburino, "Evolving pattern recognition systems," *Evolutionary Computation, IEEE Transactions on*, vol. 6, no. 6, pp. 594–609, Dec 2002.

[77] F. Zhu, X.-D. Zhang, Y.-F. Hu, and D. Xie, "Nonstationary hidden Markov models for multiaspect discriminative feature extraction from radar targets," *Signal Processing, IEEE Transactions on*, vol. 55, no. 5, pp. 2203–2214, May 2007.

[78] A. Paul, A. Shaw, K. Das, and A. Mitra, "Improved HRR-ATR using hybridization of HMM and eigen-template-matched filtering," in *Acoustics, Speech, and Signal Processing, 2003. Proceedings. (ICASSP '03). 2003 IEEE International Conference on*, vol. 2, April 2003, pp. II – 397 – 400.

[79] C. J. C. Burges, "A tutorial on support vector machines for pattern recognition," *Data Min. Knowl. Discov.*, vol. 2, no. 2, pp. 121–167, Jun. 1998.

[80] I. Jouny, "On SVM for classification of real and synthetic radar signatures," in *Antennas and Propagation Society International Symposium, 2005 IEEE*, vol. 1B, 2005, pp. 2–5 vol. 1B.

[81] S. Kent, N. Kasapoglu, and M. Kartal, "Radar target classification based on support vector machines and high resolution range profiles," in *Radar Conference, 2008. RADAR '08. IEEE*, May 2008, pp. 1–6.

[82] R. D. King, C. Feng, and A. Sutherland, "StatLog: Comparison of classification algorithms on large real-world problems," *Applied Artificial Intelligence*, vol. 9, no. 3, pp. 289–333, 1995.

[83] A. M. Martinez and A. Kak, "PCA versus LDA," *Pattern Analysis and Machine Intelligence, IEEE Transactions on*, vol. 23, no. 2, pp. 228–233, Feb 2001.

[84] S. Gelsema, "The desirability of a NATO-central database for non-cooperative target recognition of aircraft," in *RTO SET Symposium on Target Identification and Recognition Using RF Systems*, ser. RTO Meeting Proceedings MP-SET-080. Oslo, Norway: NATO Research & Technology Organization, October 2004.

[85] J. Schiller, "Capabilities, developments and challenges in non-cooperative target identification using radar," in *Microwaves, Radar and Remote Sensing Symposium (MRRS), 2011*, Aug 2011, pp. 24–27.

[86] A. Zyweck and R. E. Bogner, "Radar target recognition using range profiles," in *Acoustics, Speech, and Signal Processing, 1994. ICASSP-94., 1994 IEEE International Conference on*, vol. 2, Apr 1994, pp. II/373–II/376.

[87] R. Hu and Z. Zhu, "Researches on radar target classification based on high resolution range profiles," in *Aerospace and Electronics Conference. NAECON 1997., Proceedings of the IEEE 1997 National*, vol. 2, Jul 1997, pp. 951–955 vol.2.

[88] D. Zhou, X. Shen, and Y. Liu, "Nonlinear subprofile space for radar HRRP recognition," *Progress In Electromagnetics Research Letters*, vol. 33, pp. 91–100, 2012.

[89] M. Vaila, J. Jylha, H. Perala, and A. Visa, "Performance evaluation of radar NCTR using the target aspect and signature," in *Radar Conference, 2014 IEEE*, May 2014, pp. 0623–0628.

[90] P. López-Rodríguez, R. Fernández-Recio, I. Bravo, A. Gardel, J. L. Lázaro, and E. Rufo, "Computational burden resulting from image recognition of high resolution radar sensors," *Sensors*, vol. 13, no. 4, pp. 5381–5402, 2013. [Online]. Available: http://www.mdpi.com/1424-8220/13/4/5381

[91] J. P. Zwart, "Aircraft recognition from features extracted from measured and simulated radar range profiles," Ph.D. dissertation, Faculty of Science. Universiteit van Amsterdam, 2003.

[92] P. Swerling, "Probability of detection for fluctuating targets," *Information Theory, IRE Transactions on*, vol. 6, no. 2, pp. 269 –308, apr. 1960.

[93] A. J. Lucena, "Desarrollo y evaluación de algoritmos de identificación no cooperativa de blancos radar reales mediante una base de datos sintética: aproximación hacia una solución operativa," Ph.D. dissertation, Universidad de Alcalá, Departamento de Ciencias de la Computación, 2011.

[94] F. Harris, "On the use of windows for harmonic analysis with the discrete fourier transform," *Proceedings of the IEEE*, vol. 66, no. 1, pp. 51 – 83, jan. 1978.

[95] R. van der Heiden, "Aircraft recognition with radar range profiles," Ph.D. dissertation, Universiteit van Amsterdam, 1998.

[96] K. Sitler, M. Temple, R. Novack, and J. Hughes, "High range resolution profiling using phase-coded, stepped-frequency waveforms," *Electronics Letters*, vol. 38, no. 1, pp. 46–48, Jan 2002.

[97] G. E. P. Box and D. R. Cox, "An analysis of transformations," *Journal of the Royal Statistical Society. Series B (Methodological)*, pp. 211–252, 1964.

[98] X. Haili, W. Yang, Y. Wenjun, and W. Daoqing, "The performance of power transform in high resolution radar target identification," in *Radar Conference, 2009 IET International*, April 2009, pp. 1–4.

[99] R. van der Heiden and J. de Vries, "The ORFEO measurement campaign. TNO Report," 1996.

[100] D. Andersh, J. Moore, S. Kosanovich, D. Kapp, R. Bhalla, R. Kipp, T. Courtney, A. Nolan, F. German, J. Cook, and J. Hughes, "Xpatch 4: the next generation in high frequency electromagnetic modeling and simulation software," in *Radar Conference, 2000. The Record of the IEEE 2000 International*, 2000, pp. 844–849.

[101] J. Pérez and M. Cátedra, "Application of physical optics to the RCS computation of bodies modeled with NURBS surfaces," *Antennas and Propagation, IEEE Transactions on*, vol. 42, no. 10, pp. 1404–1411, 1994.

[102] G. Farin, *Curves and Surfaces for Computer Aided Geometric Design. A Practical Guide.* Morgan-Kaufmann, 2002.

[103] Y. Zhao, X.-W. Shi, and L. Xu, "Modeling with NURBS surfaces used for the calculation of RCS," *Progress In Electromagnetics Research*, vol. 78, pp. 49–59, 2008.

[104] D. Escot-Bocanegra, D. Poyatos-Martínez, R. Fernández-Recio, A. Jurado-Lucena, and I. Montiel-Sánchez, "New benchmark radar targets for scattering analysis and electromagnetic software validation," *Progress In Electromagnetics Research*, vol. 88, pp. 39–52, 2008.

[105] R. Fernández-Recio, A. Jurado-Lucena, B. Errasti-Alcalá, D. Escot-Bocanegra, and D. Poyatos-Martínez, "Study of the scattering mechanisms of a set of conospheres," in *Electromagnetic Field Computation (CEFC), 2010 14th Biennial IEEE Conference on*, May 2010, pp. 1–1.

[106] R. Fernaández-Recio, A. Jurado-Lucena, B. Errasti-Alcalá, D. Poyatos-Martínez, D. Escot-Bocanegra, and I. Montiel-Sánchez, "RCS measurements and predictions of different targets for radar benchmark purpose," in *Electromagnetics in Advanced Applications, 2009. ICEAA '09. International Conference on*, Sept 2009, pp. 443–446.

[107] L. N. Trefethen and D. Bau, *Numerical Linear Algebra.* Philadelphia, PA, USA: Society for Industrial and Applied Mathematics, 1997.

[108] G. H. Golub and C. F. Van Loan, *Matrix computations*, 3rd ed. Johns Hopkins University Press, 1996.

[109] V. Klema and A. Laub, "The singular value decomposition: Its computation and some applications," *Automatic Control, IEEE Transactions on*, vol. 25, no. 2, pp. 164–176, Apr 1980.

[110] A. Shaw, A. Paul, and R. Williams, "Eigen-template-based HRR-ATR with multi-look and time-recursion," *Aerospace and Electronic Systems, IEEE Transactions on*, vol. 49, no. 4, pp. 2369–2385, October 2013.

[111] E. Oja, *Subspace Methods of Pattern Recognition*, ser. Electronic & Electrical Engineering Research Studies: Pattern Recognition and Image Processing Series. Research Studies Press, 1983, vol. 6.

[112] A. Bjoerck and G. H. Golub, "Numerical methods for computing angles between linear subspaces," *Mathematics of Computation*, vol. 27, pp. 579–594, 1973.

[113] P. Zhu and A. V. Knyazev, "Angles between subspaces and their tangents," *ArXiv e-prints*, Sep. 2012.

[114] T. Kobayashi, "Generalized mutual subspace based methods for image set classification," in *Computer Vision ACCV 2012*, ser. Lecture Notes in Computer Science, K. Lee, Y. Matsushita, J. Rehg, and Z. Hu, Eds. Springer Berlin Heidelberg, 2013, vol. 7724, pp. 578–592.

[115] R. G. Pita, "Sistemas de clasificación de blancos radar mediante métodos estadísticos y de inteligencia artificial," Ph.D. dissertation, Universidad de Alcalá, 2006.

Appendix A

Computational Burden of an ISAR image identification system

In operational systems the analysis of the computational burden is important in order to examine whether the systems meet the requirements and whether some elements can be improved with the selection of a specific technology or implementation platform.

This Appendix presents the study published in [90], which addresses the computational burden needed in an ISAR-based NCTI system. After a brief introduction about high resolution radar systems and the algorithms used to obtain ISAR images, the computational complexity calculation is divided in two stages: ISAR image extraction and ISAR image recognition.

Sensors **2013**, *13*, 5381-5402; doi:10.3390/s130405381

OPEN ACCESS

sensors

ISSN 1424-8220

www.mdpi.com/journal/sensors

Article

Computational Burden Resulting from Image Recognition of High Resolution Radar Sensors

Patricia López-Rodríguez [1,*], Raúl Fernández-Recio [1], Ignacio Bravo [2], Alfredo Gardel [2], José L. Lázaro [2] and Elena Rufo [2]

[1] National Institute for Aerospace Technology (INTA), Torrejón de Ardoz, 28850 Madrid, Spain; E-Mail: fernandezrr@inta.es

[2] Department of Electronics, University of Alcalá, Alcalá de Henares, 28871 Madrid, Spain; E-Mails: ibravo@depeca.uah.es (I.B.); alfredo@depeca.uah.es (A.G.); lazaro@depeca.uah.es (J.L.L.); elena.rufo@depeca.uah.es (E.R.)

* Author to whom correspondence should be addressed; E-Mail: lopezrp@inta.es; Tel.: +34-915-202-127; Fax: +34-915-202-021.

Received: 21 February 2013; in revised form: 12 April 2013 / Accepted: 12 April 2013 / Published: 22 April 2013

Abstract: This paper presents a methodology for high resolution radar image generation and automatic target recognition emphasizing the computational cost involved in the process. In order to obtain focused inverse synthetic aperture radar (ISAR) images certain signal processing algorithms must be applied to the information sensed by the radar. From actual data collected by radar the stages and algorithms needed to obtain ISAR images are revised, including high resolution range profile generation, motion compensation and ISAR formation. Target recognition is achieved by comparing the generated set of actual ISAR images with a database of ISAR images generated by electromagnetic software. High resolution radar image generation and target recognition processes are burdensome and time consuming, so to determine the most suitable implementation platform the analysis of the computational complexity is of great interest. To this end and since target identification must be completed in real time, computational burden of both processes the generation and comparison with a database is explained separately. Conclusions are drawn about implementation platforms and calculation efficiency in order to reduce time consumption in a possible future implementation.

Keywords: high resolution radar; radar imagery; ISAR; target recognition; computational burden; NCC

1. Introduction

Radar systems are key components in military and civilian schemes. Different applications have emerged since World War II related to this kind of sensor. A **R**adio **A**id to **D**etection **A**nd Ranging (radar [1]) is an electromagnetic sensor used for the detection and location of energy scattering objects. These systems not only have the ability to detect targets and show their position, but also to generate images and carry out certain electronic attack tasks, among many other applications. The basic principle of radar sensors is based on the time needed by the emitted electromagnetic wave to reach a target and back.

This principle is depicted in Figure 1, and can be divided into the following phases [1,2]:

1. The radar emits an electromagnetic energy which travels through space.
2. If the transmitted energy hits a target, it will be scattered in all directions.
3. Part of the scattered energy travels back to the radar and it will be sensed by the receiving antenna.
4. In the receiver, energy is amplified and with the aid of signal processing techniques the presence of a target may be determined. Not only the existence of targets can a radar detect but also other parameters such as its range, its radial velocity, or even the shape and size of the target if the radar has enough resolution to resolve closely spaced points within a target.

Figure 1. Basic principle of a radar system.

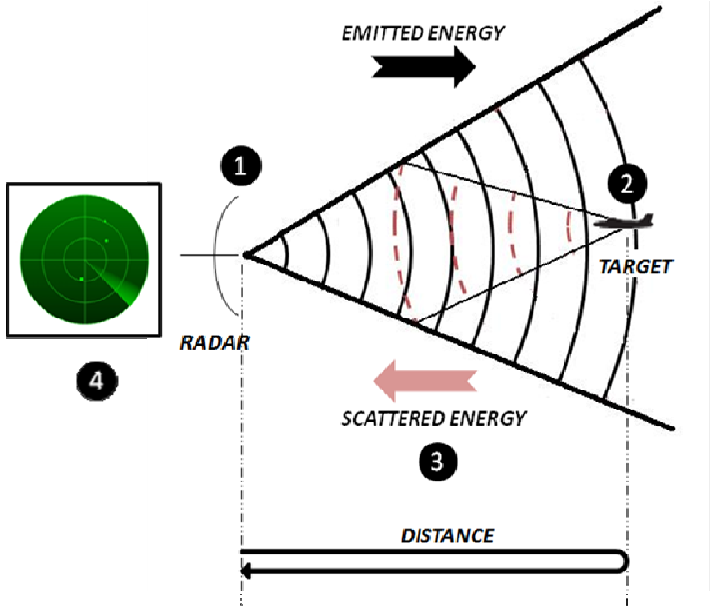

In the last decades, radar technology has experienced a change in its focus. Whereas in the beginning only the detection and tracking of targets was necessary, with the advance of technology the

need to obtain higher spatial resolution has emerged. Consequently, radars have evolved into more flexible devices with the ability to generate high resolution imagery for mapping purposes or target identification [3]. Radars are the most suitable sensors for a rapid and reliable recognition of targets as they can operate in scenarios where visibility is very poor, such as bad weather conditions, smoky and dusty environments, *etc.* Their ability to resolve targets at a long range as well as their operation under any weather conditions makes them differ from other sensors like thermal or optical ones [2].

Target recognition using radar sensors can be divided into two techniques: cooperative and non-cooperative [1]. Cooperative techniques, known as identification friend or foe (IFF), require the communication between target and radar, while non-cooperative techniques, so-called non-cooperative target identification (NCTI), do not establish any communication with them but rely on the comparison of the measured targets with a reference database. This database is usually populated with actual target measurements obtained in scheduled measurement campaigns [4]; however, it implies the collection of information from a great number of flying targets in different aspect angles and configurations and even so, the main problem lies in the fact that not all existing aircrafts may be measured. For this reason, other methods have been deployed to populate the database. These methods include measurements in anechoic chamber and electromagnetic simulations [5]. The latter is of great interest due to its low cost and the simplicity of obtaining a vast number of CAD aircraft models for electromagnetic simulations.

In this paper a target recognition methodology based on high resolution radar imagery is presented. Algorithms related to high resolution radar image creation and the problems found are introduced, as well as a target recognition methodology based on image cross correlation. High resolution radar image generation and target recognition processes are complex and time consuming. The goal of a NCTI system is the reliable recognition of targets in real time; therefore, studies on the computational burden of the whole process are of great interest. These studies will make it easy to identify the computationally critical points of the system in order to previously choose an implementation platform that could perform these operations efficiently. Accordingly, the computational burden of the proposed system is revised distinguishing the complexity of image generation from the complexity of target recognition. With these results conclusions about implementation platforms and calculation efficiency are drawn in order to reduce time consumption in a possible future implementation.

The article is organized as follows: Section 2 introduces high resolution radars as image sensors bringing into focus inverse synthetic aperture radars (ISAR). Section 3 presents the methodology used in this study for ISAR image generation from actual flying aircrafts data and its recognition, based on the previous work by [6]. The methodology presented requires complex computations implying a high computational burden as it is explained in Section 4. Finally, Section 5 discusses the results and conclusions, calling for further work and research in the area.

2. High Resolution Radars

To high resolution radars (HRRs) targets appear as comprised of individual scattering points, also called *scattering centers*, *backscatter sources* or *scatterers* [7]. Figure 2 shows an example of these scattering centers projected on the radar line of sight direction. At a given viewing angle (*target aspect*

angle), each *scatterer* reflects energy at a certain amplitude and phase. High resolution radars have the ability to discern the different scattering centers of a target in both the propagation and the transversal direction of the transmitted energy; being able, therefore, to identify the geometry of a target. Thus, resolution of these radars is defined in two dimensions, on the one hand there is the *slant-range* resolution which depends on the radar bandwidth and is defined as the ability to resolve *scatterers* in the direction of the radar line of sight; on the other hand, there is the *cross-range* resolution which depends on the wavelength of the emitted signal and the angular sweep made during the illumination time. *Cross-range* resolution is defined as the ability to resolve *scatterers* in the normal direction to the plane containing the radar line of sight and the target rotation angle.

Figure 2. Example of scattering centers in a target.

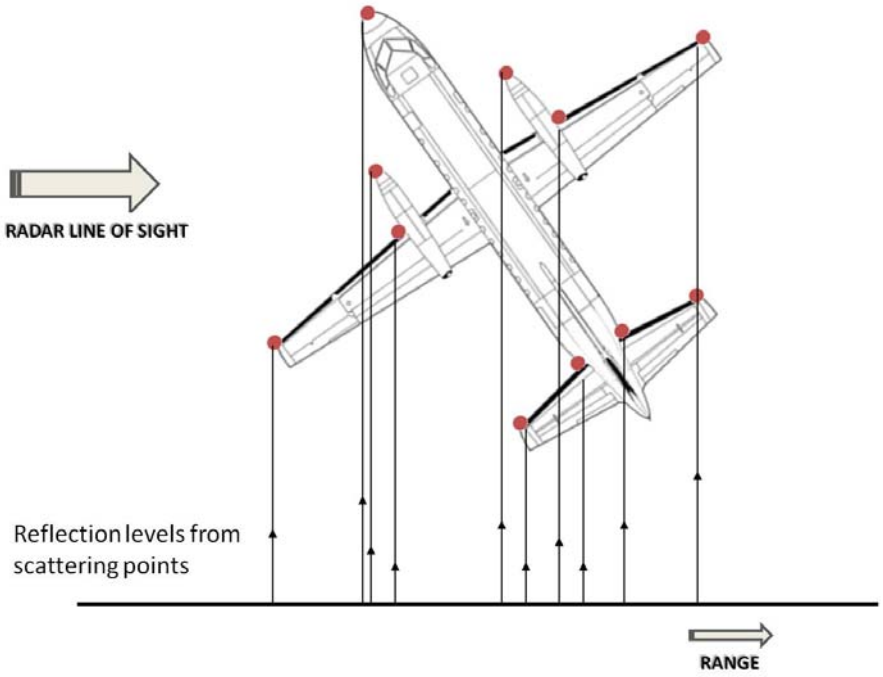

There exist mainly two different types of HRR: *synthetic aperture radars* (SAR) and *inverse synthetic aperture radars* (ISAR). Both make use of the relative motion of target and radar to achieve high resolution in the cross-range direction.

SAR radars achieve high resolution in the cross-range dimension by taking advantage of the motion of the vehicle carrying the radar to synthesize the effect of a large antenna aperture [2,7,8]. These sensors are usually used for imaging the Earth's surface to provide maps for military or civilian reconnaissance, measurements of sea state, geological and mineral explorations and other sensing applications. SAR requires coherence between signals and the means necessary for the storing and subsequent processing of the received echoes. ISAR imagery is based on the same principle as SAR imagery, but in contrast it is the target rotational motion which will generate the necessary information for obtaining the image while the radar remains stable [8,9].

2.1. Inverse Synthetic Aperture Radar

High resolution radar imagery obtained by ISAR radars can be 1-dimensional or 2-dimensional. On the one hand, 1D images present the *scatterers* of a target projected on the dimension of the radar line of sight (LOS) that is in *slant-range,* or the *scatterers* of a target projected on the *cross-range* dimension. 1D images projected on *slant-range* are called *high resolution range profiles (HRRP)* while those projected on the *cross-range* dimension are called cross-range profiles [7,9].

Usually the stop & go assumption is held, which means that the target is assumed stationary during the transmission and the reception of a pulse. Sometimes however, this statement cannot be assumed valid because the pulse repletion time is too long or because the target moves very fast. In such cases an autofocusing technique is also needed to form HRRP [10,11]. The cross-range profiles are obtained by exploiting the target motion with respect to the radar and by using the aspect angle changes to synthesize the aperture. Obviously an auto-focusing step is needed first. This paper works with range profiles (HRRP) instead of cross-range profiles and the stop & go approximation is assumed to be valid so no autofocusing technique is needed to obtain HRRP.

HRRP represent the energy reflected by every *scatterer* in a moving target as a function of distance. Each profile is comprised of *range bins* that can contain energy from different *scattering centers*. Figure 3 depicts how high resolution range profiles present the energy reflected by the *scatterers* of a target in the dimension of the radar line of sight. Signal processing needed to obtain the HRRPs of a target is not very complex; however, they are very sensitive to the target viewing angle (aspect angle) due to occlusion of *scatterers* or other unwanted effects such as speckle or rotational range migration (RRM) [4].

Figure 3. High resolution range profile.

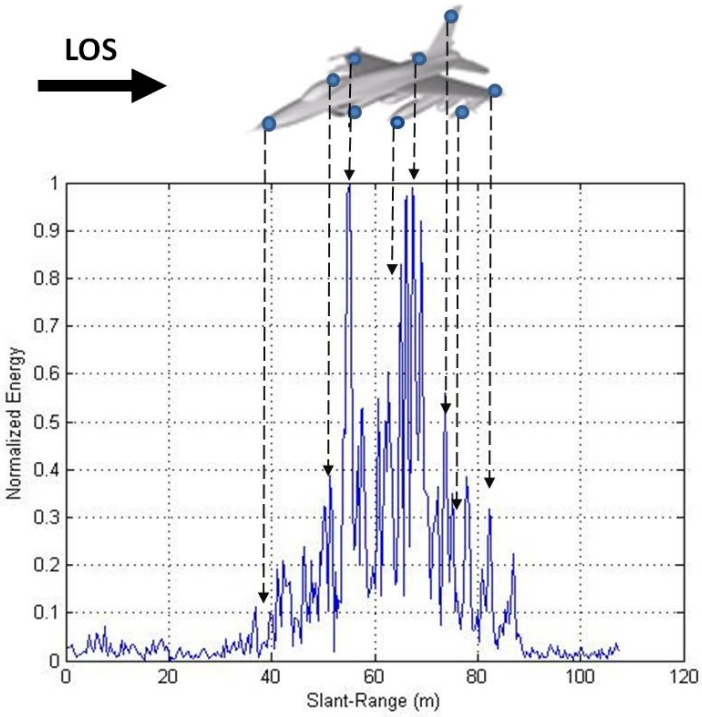

The resolution of a range profile is dependent on the bandwidth of the emitted signal; the shorter the emitted pulse, the wider the bandwidth and the finer the resolution [2,7]. Unfortunately, there are

limitations in the reduction of the width of the emitted pulse since it is limited by the energy the radar is capable of transmitting. Most radars are not able to transmit the power needed to achieve high resolution with a pulse waveform. Nevertheless, the *pulse compression* [8] technique allows radars to obtain high resolution using long pulse widths. This technique consists of modulating the frequency of the emitted waveform along the total pulse width. The receiver is in charge of the quadrature demodulation of the received signal using a matched filter to maximize the Signal-to-Noise Ratio (SNR). Typical waveforms used in pulse compression techniques are *chirp* [12] and *stepped-frequency* [13]. Radars using pulse compression technique sense the total radar returns in the frequency domain; hence, HRRPs are obtained by applying an inverse Fourier transform to the radar complex returns [9].

On the other hand, 2D images, named ISAR images, represent the geometry of a target in both *slant-* and *cross-range.* ISAR images contain information of consecutive HRRPs with small angular variation; these images display the distribution of scattering centers within a target in the perpendicular direction of the target's rotation plane [14]. Figure 4 depicts the fact that ISAR images present the scattering centers of a target in two dimensions. The aircraft displayed in this figure correspond to a Fokker-100.

Figure 4. Scattering centers in an ISAR image.

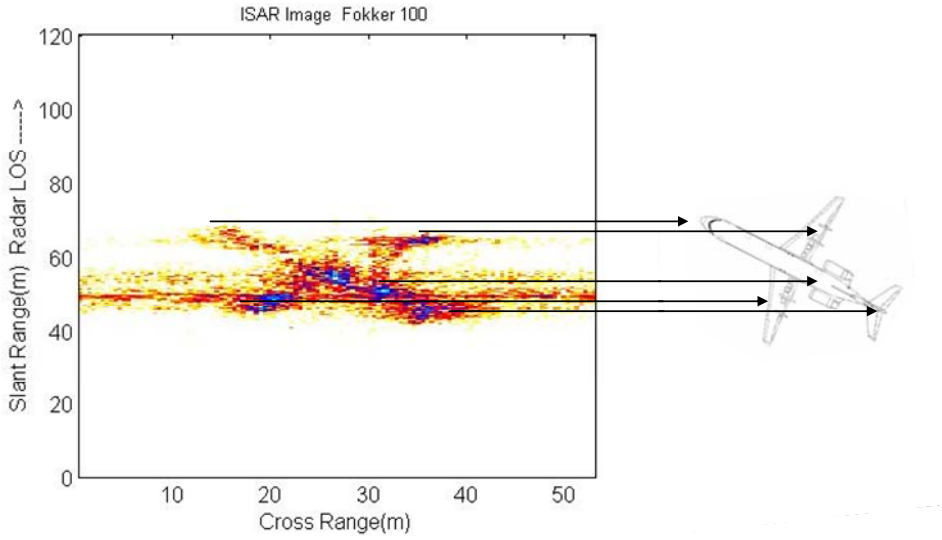

Signal processing needed to achieve ISAR images is complex and implies higher computational burden than that needed for the generation of HRRPs. There are several methods used in literature to form ISAR images including back-projection methods [15] or range-instantaneous Doppler algorithms (RID), such as Radon-Wigner transform (RWT) method [16], joint time-frequency analysis method [17], reassigned smoothed pseudo Wigner-Ville distribution [18], fractional Fourier Transform [19], *etc.* The algorithm used in this paper for the creation of ISAR images is called range-Doppler algorithm (RDA) [7,9]. This technique is the most common since it is the simplest one. It mainly consists in the application of a double Fourier transformation; first, an inverse Fourier transform is applied to the quadrature demodulated data (I/Q samples) in order to obtain a matrix filled with high resolution range profiles and second, a Fourier transform is applied to every range bin of these profiles in order to acquire information of the *scatterers* in the *cross-range* dimension. The basic

approach of this algorithm is depicted in Figure 5 where A denotes the profiles matrix and A^T is its transpose.

Figure 5. RDA Algorithm.

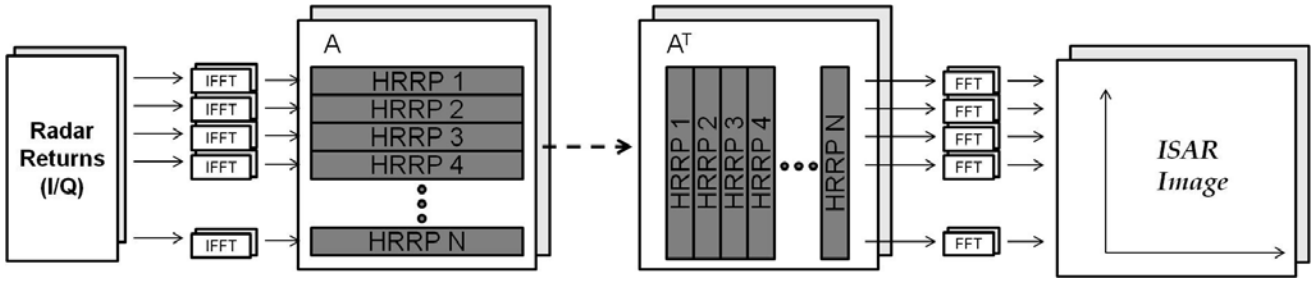

Target motion with respect to the radar makes it possible to achieve ISAR images; nevertheless, not every movement is desired and this may cause blurring in the obtained images. In order to avoid this defocusing, motion compensation techniques must be applied [9,20].

Generally speaking, target motion can be decomposed into translational and rotational [14,21,22]. In order to get focused images both the translational and rotational motion must be compensated. Translational motion causes consecutive HRRPs to be misaligned, so in order to compensate it an alignment of profiles must be completed, this procedure is also called *range bin alignment*. In addition to profile alignment, a *phase adjustment* procedure must be applied in order to refer every measurement to the same origin [9]. In the past decades, translational motion compensation has been of great interest and now it has become a well-established technology. Range bin alignment methods are rather standard, including centroid tracking [23,24], envelope correlation [14], contrast/entropy based methods [25], prominent point processing or dominant scatterer algorithm [26], *etc.*

On the other hand, rotational motion causes *motion through resolution cells* (MTRC) [27] which produces the *scatterers* to move from bin to bin in *slant-* or *cross-range*. However, it can be ignored provided that the target is small or the required resolution is coarse [22].

Many algorithms have been proposed in the literature for motion compensation in ISAR imaging. What is presented here is the computational complexity analysis of a combination of translational motion compensation methods (envelope correlation and dominant scatterer algorithm) in order to get a focused ISAR image. The driving idea is to achieve an affordable processing chain, in terms of computational burden which is the mandatory requirement for a future possible implementation in real time.

3. ISAR Generation and Target Recognition System

The complete system under study is implemented in Matlab® (R2008a) and consists, firstly, of the generation of an ISAR image from a dataset of flying aircrafts. To that end, motion compensation of high resolution range profiles must be implemented. Secondly, after an ISAR image is obtained, the comparison with a database of ISAR images is carried out with the final purpose of aircraft recognition. This database is populated with ISAR images generated synthetically with electromagnetic software. Figure 6 depicts the flowchart of this procedure.

Figure 6. System identification flowchart.

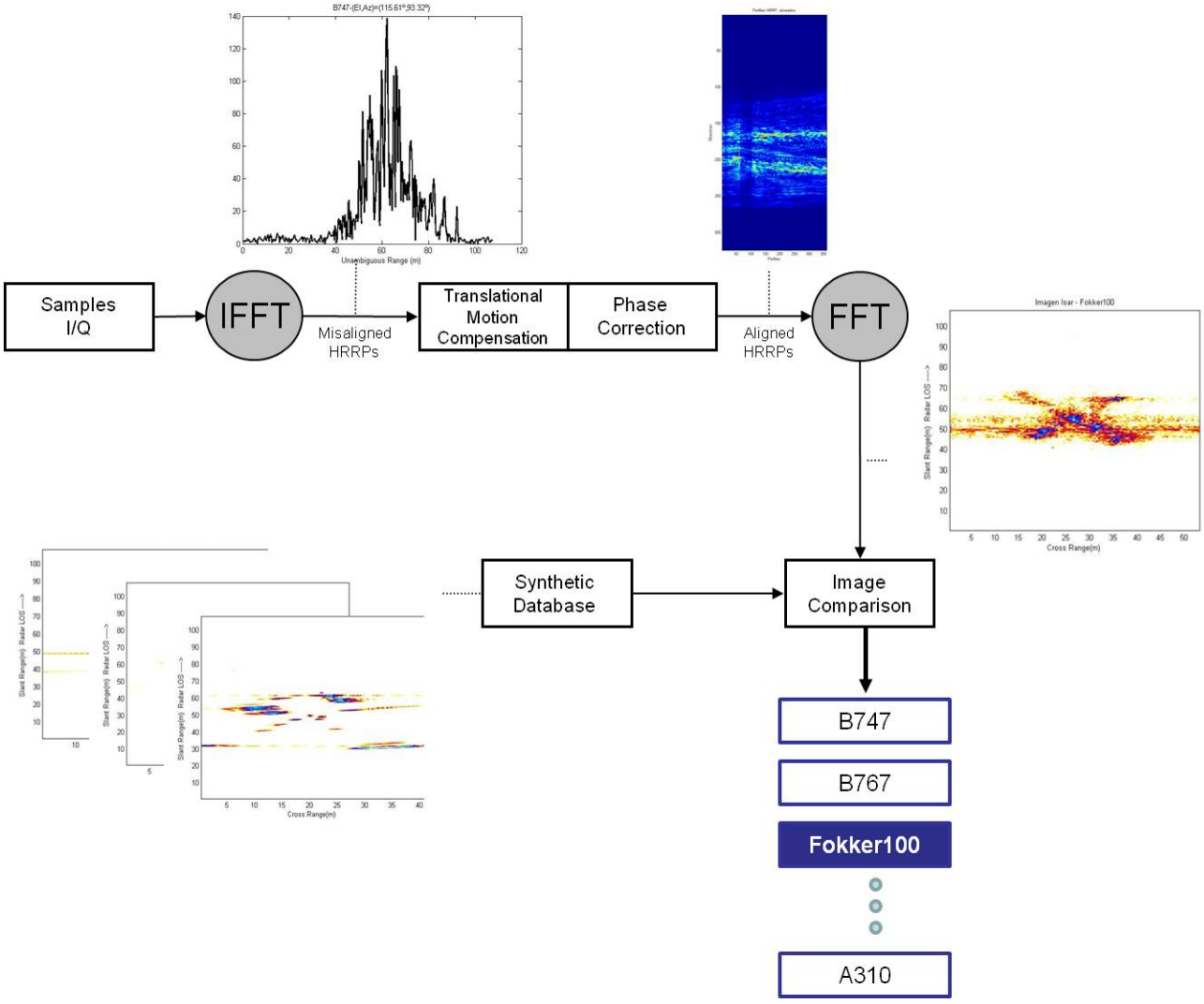

3.1. Data Set

The use of actual data in the generation of ISAR images is of great importance since it is possible to obtain realistic images that could not be obtained by any other means. However, it must be noted that actual data is not usually accessible and not easy to measure since the use of high level technology resources is required.

The North Atlantic Treaty Organization (NATO) performs different activities under its Research and Technology Organization (RTO). Data used in this work comes from the ORFEO civilian airliner measurement campaign, held in 1995 and obtained with the FELSTAR radar. FELSTAR is a stepped-frequency S-band radar owned by TNO-FEL and located in The Hague, The Netherlands [28]. This measurement campaign was carried out as part of the RTO-SET-040 Task Group activity and up to 17 different civilian aircrafts were measured as targets of opportunity. By using actual data from the ORFEO campaign and applying the RDA algorithm explained in previous sections, ISAR images of different civilian aircrafts are obtained.

3.2. ISAR Image Formation

This section describes the algorithm used for the generation of an ISAR image from actual data using Matlab®; this procedure is based on the flowchart in Figure 7. As mentioned above, for the generation of a focused ISAR image, in addition to the implementation of RDA the implementation of a motion compensation method is also necessary.

Figure 7. ISAR image formation flowchart.

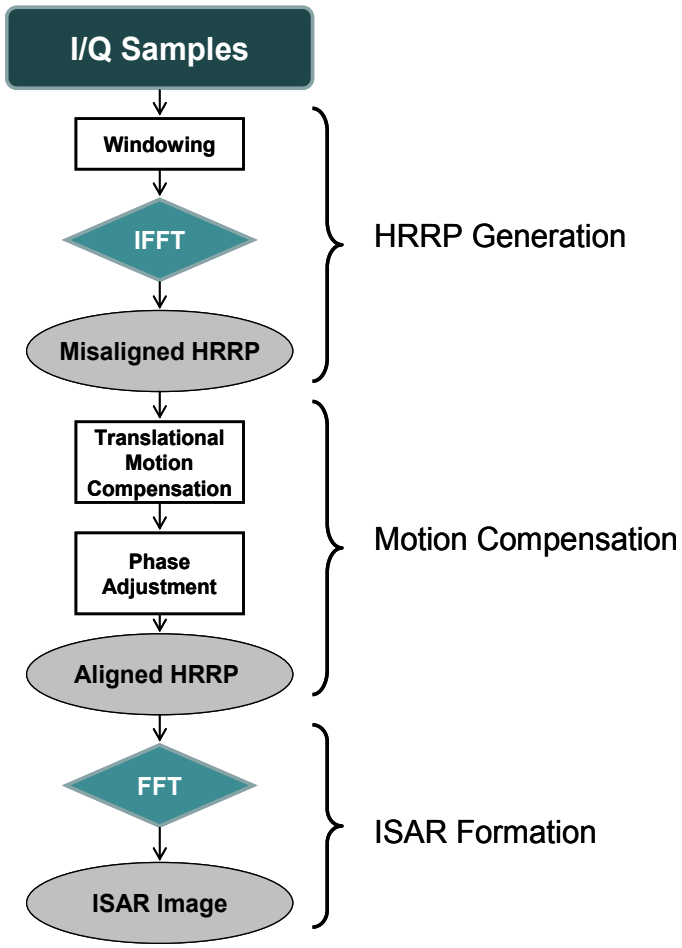

In order to acquire a more focused image a Hamming window [4,29] is first applied to the samples since it reduces sidelobes in 43 dB. In case a Hamming window was not employed, with the inverse Fourier transform needed to obtain the profiles, a rectangular window would be automatically applied which has high sidelobes that can produce the occlusion of scattering centers [30].

The next step after windowing and application of inverse Fourier transformations (using the IFFT algorithm) is the translational motion compensation of the obtained HRRPs. To align the profiles an algorithm based on the envelope correlation method [14,31] is applied first. In the case covered in this article, a reference profile is first established defined as a sum of six aligned profiles after applying correlation between them. The remaining profiles will then be aligned by correlating them to the reference one. Note that the reference profile must be updated after a new profile is aligned by including the new one to the reference profile and discarding the oldest one. After pre-alignment using envelope correlation (coarse alignment), a fine alignment is applied. This fine-alignment comprises three steps: first, a prominent *scatterer* must be selected; second, profiles are re-aligned by tracking the prominent *scatterer* along the profiles matrix; to do so, profiles maxima are found within a small band

from the prominent *scatterer* and, when necessary, profiles are realigned. Finally, phase adjustment is carried out by using the dominant scatterer algorithm (DSA) [26,32] where the phase of the dominant *scatterer* previously selected is subtracted from the phase of the rest of the profiles already aligned. Figure 8 shows the whole translational motion compensation process; Figure 8(a) presents the initial 10 HRRPs of a measured Boeing-767, and as can be seen, these profiles are completely misaligned. By employing envelope correlation profiles are pre-aligned as shown in Figure 8(b). Lastly, after phase adjustment profiles are finally aligned as in Figure 8(c).

Figure 8. Profile alignment process; (**a**) initially misaligned HRRP; (**b**) pre-aligned HRRP; (**c**) aligned HRRP after translational motion compensation.

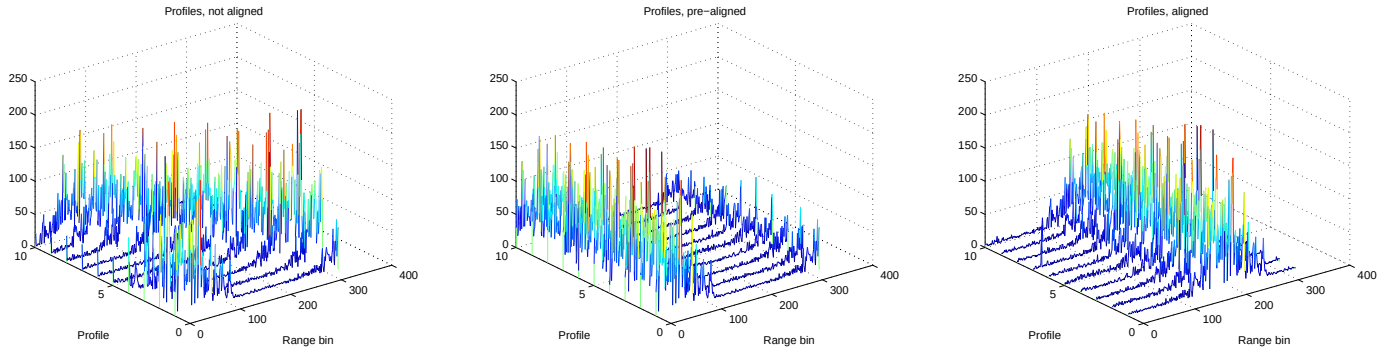

(**a**) (**b**) (**c**)

Figure 9(a) shows the initially misaligned profiles as in Figure 8(a), but in a 2D plot. This figure presents the whole set of profiles of a measured Boeing-767 in the ORFEO campaign. Figure 9(b) shows the resulting aligned profiles as in Figure 8(c) in 2D. With this last figure it is easy to observe the evolution from a misaligned set of HRRPs to an aligned set.

Regarding rotational motion compensation [9,33], it has already been noted that it would only be necessary when the resolution needed is very fine or target rotation is very high. Neither case is present in this study; hence, this step is omitted.

Finally, application of Fourier Transformation (using the FFT algorithm) to the range bins of the aligned profiles is applied and an ISAR image is obtained. Examples of different ISAR images obtained by means of the procedure described in this section are displayed in Figure 10. As expected, ISARs obtained are not of great quality if compared to a video or an IR sensor image although they have enough quality to discern the existence of an aircraft with certain geometry and dimensions.

As observed in Figure 10, a blurred band exists approximately in the middle of every image. This blurring is due to the fact that these images were produced using actual data and some noise and clutter could not have been completely removed. This will probably affect in the identification stage, resulting in a degradation of the final result.

Figure 9. Profile alignment process—2D; (**a**) initially misaligned HRRP; (**b**) aligned HRRP after translational motion compensation.

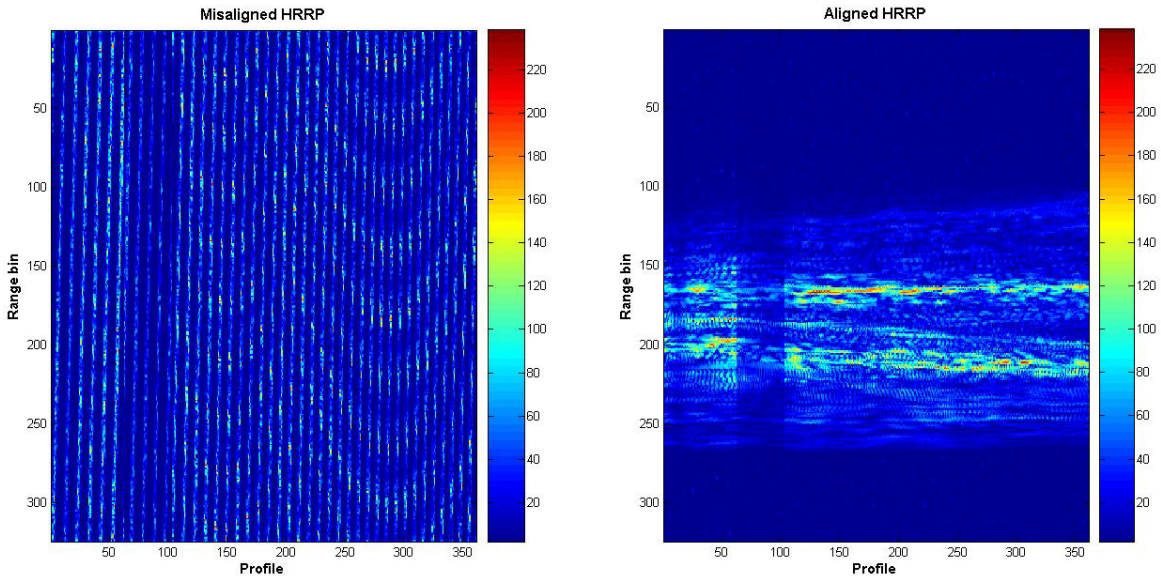

(**a**) (**b**)

Figure 10. ISAR images obtained from the ORFEO measurement campaign; (**a**) ISAR image of a Boeing 767; (**b**) ISAR image of a Fokker 100; (**c**) ISAR image of a Boeing 747.

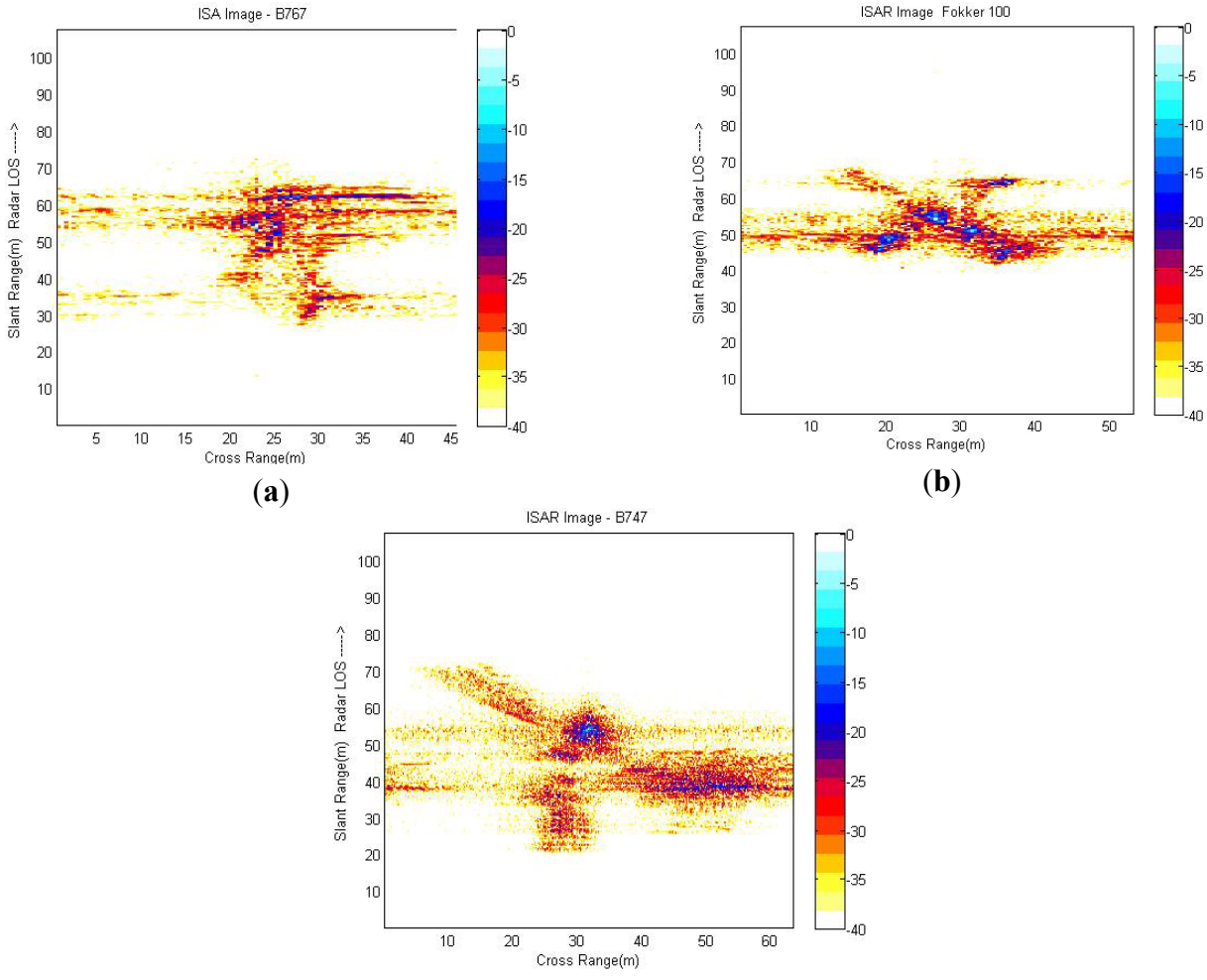

(**a**) (**b**)

(**c**)

3.3. ISAR Image Comparison (Target Recognition)

Target recognition is accomplished by applying a template-matching technique where targets are recognized based on the template that best matches the reconstructed ISAR images. The recognition is carried out by comparing ISAR images obtained from actual data to a database populated with synthetic ISAR images, that is to say images obtained with electromagnetic software. FASCRO is the tool employed in this paper in order to generate the synthetic images that will populate the database. The software is based on the work by [34,35]. Its operation lies in a combination of two high frequency techniques, physical optics (PO) and physical theory of diffraction (PTD) applied to targets modelled as non-uniform rotational B-splines surfaces (NURBS) [36,37]. Figure 11 displays some of the synthetic images that populate the database.

Figure 11. Examples of ISAR images populating the synthetic database; (**a**) Synthetic ISAR image of a Boeing 767; (**b**) Synthetic ISAR image of a Fokker 100; (**c**) Synthetic ISAR image of a Boeing 747.

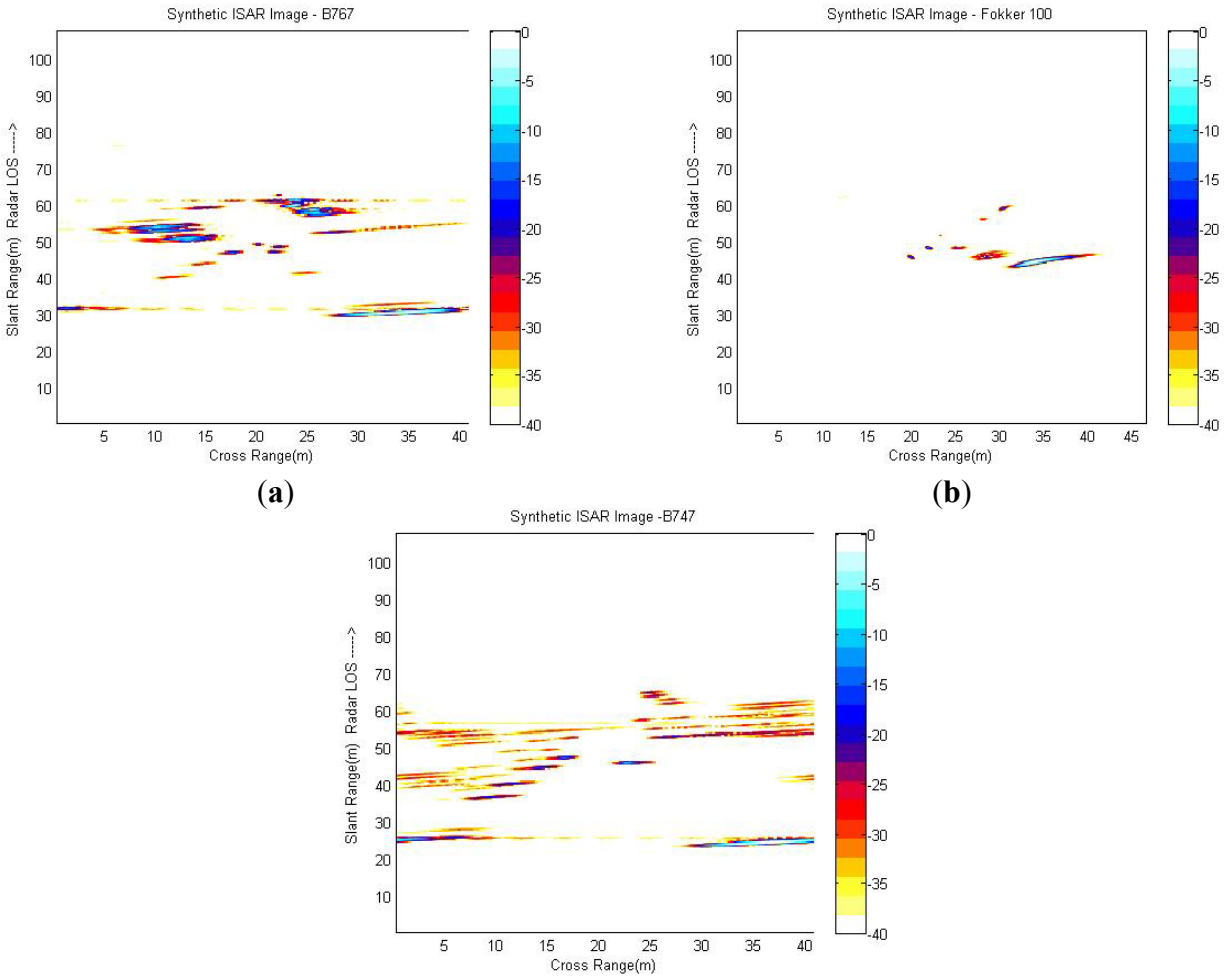

As can be easily noticed, synthetic ISAR images are in many ways different from those obtained from actual data; the images obtained synthetically are much clearer; this is due to the fact that electromagnetic software runs an ideal scheme, without considering any noise or clutter. Synthetic

ISAR images do not suffer from measurement noise, and also application of translational motion compensation to HRRPs is not needed for their generation. Moreover, all the aircrafts are considered PEC (*perfect electric conductors*) in the simulations and also CAD models are approximations of aircraft geometry. Thus, electromagnetic software cannot simulate all the effects present in a real environment. Additionally, for the construction of a good database of synthetic aircrafts the image projection plane (IPP) must be taken into account since the target reflectivity is strongly dependent on the aircraft aspect angle and can affect the recognition process. Moreover, the estimation of the angular velocity of target rotation should be carried out since cross-range scaling of the ISAR image depends on it. In [38,39] an attempt to solve the question of building a robust database can be found taking into account the image projection plane. In [40] an iterative method to estimate the angular parameters of non-cooperative targets using the estimates of the range and radial velocity of two prominent *scatterers* as inputs is addressed.

In the study presented here the flight plans of the different aircrafts are known and the database has been built according to them. This implies that the image projection plane and the angular velocity of the targets in the database used in this paper for recognition are the same as the ISAR images generated from actual data; this means that their estimation is not necessary. However, in a real application of non-cooperative target recognition flight plans are unknown and the aspect angle of the aircrafts as well as their angular velocity should be estimated. Consequently, the database should be populated with ISAR images of aircrafts in different aspect angles and trajectories and the ISAR images of the targets should only be compared to those with the same resolution and image projection plane in order to reduce computational burden. The proposed template-matching technique to compare ISAR images is the normalized cross-correlation between them [41–43] although there is no generally accepted way of performing this task. Normalized cross correlation (NCC) is one of the most robust measures for determining similarity between points in two or more images providing an accurate result. However, this method can be computationally intense, especially for large images [44]. Equation (1) presents the formula of the NCC:

$$r = \frac{\sum_{m=0}^{M-1}\sum_{n=0}^{N-1}(A_{mn}-\overline{A})(B_{mn}-\overline{B})}{\sqrt{\left[\sum_{m=0}^{M-1}\sum_{n=0}^{N-1}(A_{mn}-\overline{A})^2\right]\left[\sum_{m=0}^{M-1}\sum_{n=0}^{N-1}(B_{mn}-\overline{B})^2\right]}} \quad (1)$$

where A and B are images of size $N \times N$ and $M \times M$ respectively, and $\overline{A}$ and $\overline{B}$ denote their mean value. In the present case, both images have the same size. Table 1 summarizes some of the results obtained using normalized cross-correlation for target identification.

Table 1. Target identification results

	Synt.-B747	***Synt.-Fokker 100***	***Synt.-B767***
B-767 from actual data	0.1927	0.2473	**0.3129**

Results of the identification method show low correlation between images, even though the highest value is obtained for the aircraft to be recognized. The reason why these results are obtained lies in the fact that synthetic images are much clearer than those obtained from actual data. To improve these

correlation results further image processing should be applied to either image set. Note that this additional image processing does not have to do with RDA or motion compensation but with noise/clutter rejection techniques; however, that is not the purpose of the present work but the study of the computational cost of the generation of ISAR images from actual data and the comparison with a database.

4. Computational Burden Results

One of the requirements in an automatic target recognition method is to obtain a result in real time. Real time can be considered as the time needed to process a result sufficiently rapid in order for the radar operator to be able to make decisions. For this purpose high performance devices are usually needed to achieve these time requirements.

Prior to the selection of a device to implement a system it is of high interest to study the computational burden by means of analyzing the order of magnitude of the calculations. Matlab® Profiler [45] is an excellent tool for a preliminary study on computational cost, it was first developed to provide information for the debugging and optimization of code but it also provides information about execution time of functions, the number of times a function is called, computing time in CPU and even the memory consumed by each function. Consequently, a study of computational burden of both the generation and the comparison process is carried out using Matlab® Profiler (R2008a) in order to identify critical computational points.

In the next subsection the computational complexity of ISAR image formation is studied, establishing for each stage in which the process can be decomposed into the number of operations needed. Finally, computational complexity of ISAR image comparison for target recognition is revised.

4.1. ISAR Generation Process Computational Cost

ISAR generation process, as noted in previous sections, is comprised of the subsequent stages:

- HRRP Generation
- Motion Compensation
- ISAR Formation

Each stage comprises operations dependent on the number of high resolution range profiles (N) and the number of different frequencies in a burst of the transmitted stepped-frequency signal (M). According to the results given by Matlab® Profiler, Table 2 and Figure 12 show the operations needed and the percentage of time spent in each stage of the process. The operations grouped under "Others" in Figure 12 are those needed to plot images, load/save data or display Matlab® Profiler main window. The ISAR image generation process was run in an Intel Xeon @ 2.66GHz and 3.50 GB RAM PC and the average total time spent for the generation of an image of size 361 × 324 pixels (N = 361 profiles × M = 324 frequencies in a burst) was approximately 40 seconds.

Table 2. Operations needed to obtain an ISAR image.

Stage	Substage	Number of Operations	% Time
HRRP Generation	Windowing	N products of M complex samples	**3.24%**
	HRRP Formation	N IFFTs of M complex samples	**0.05%**
Motion Compensation	Range Bin Alignment	(N-1) circular correlation of M real samples	**86.81%**
	Scatterer Selection	N circular shifts	**0.39%**
	Phase Adjustment	N products of M complex samples	**0.10%**
ISAR Formation		M FFTs of N complex samples	**2.48%**

According to Table 2 and Figure 12 the most expensive (computationally speaking) stage is the motion compensation, and more specifically the process of the range bin alignment which involves the realization of (N − 1) circular correlation of M real samples and needs an 86.81% of the total time.

Figure 12. Time spent in the generation of an ISAR image.

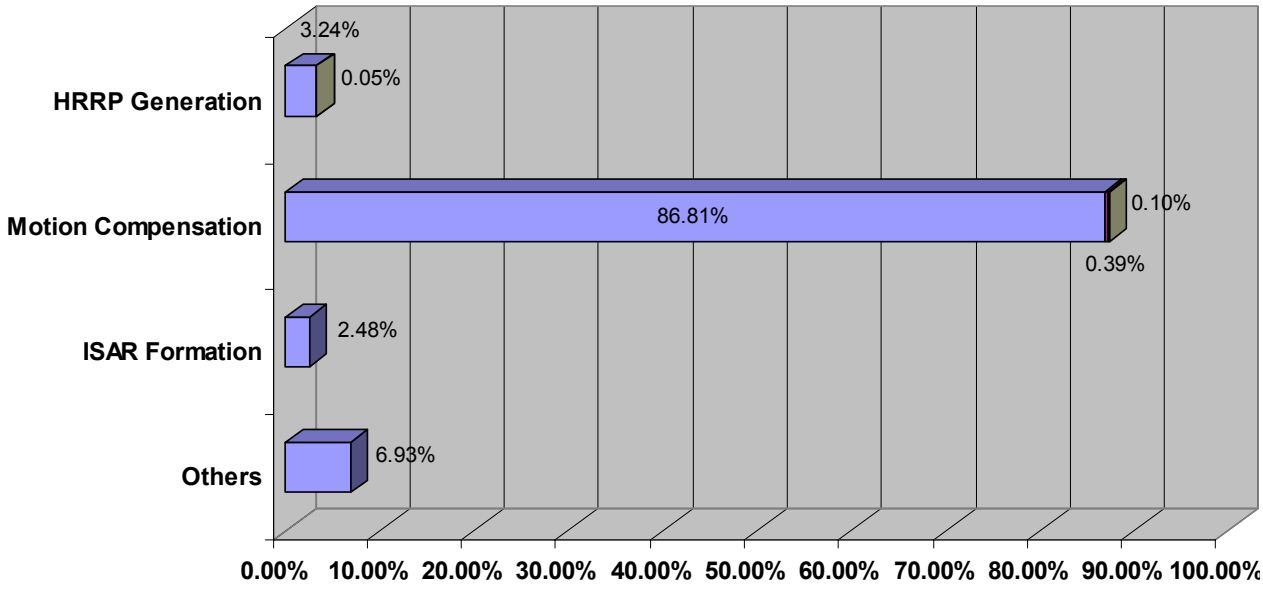

Being $x[m]$ and $y[m]$ two profiles of M samples, circular cross correlation is accomplished by applying Equation (2), where the term $x[m+k]_M$ denotes $x[(m+k) \bmod M]$, that is to say, the circular shift of $x[m]$:

$$\phi_{xy}[k] = \frac{1}{M}\sum_{m=0}^{M-1} x[m+k]_M \cdot y[m] \tag{2}$$

Analysis of Equation (2) reveals that for every circular correlation of M samples a total of M^2 products, M·(M − 1) sums and M circular shifts are employed. These operations will be complex or real depending on the nature of data. In this particular case, operations needed for circular correlations in the range bin alignment stage are real. Moreover, the normalization of the correlation is not needed since all profiles will be scaled by the same factor and it will not have effect in the alignment. It should be noticed that another technique to perform correlation between signals is through the use of FFT, which converts correlations into a product of transforms.

The method revised here for range bin alignment, based on the envelope correlation, requires the creation of an initial reference profile made up of the first six aligned HRRPs. The alignment and creation of this reference profile implies the execution of five correlations out of the (N − 1) needed to accomplish the whole alignment process. Next step is the correlation with the following profile, the alignment with it and the update of the reference profile. This process will be repeated until all profiles are aligned, therefore, it will be repeated (N − 6) times. The update of the reference profile implies 5M sums. The total number of operations needed for range bin alignment of a total number of N profiles made up of M samples is summarized in Table 3.

Table 3. Operations needed for range bin alignment.

Real Products	$(N-1)\cdot M^2$
Real Sums	$(N-1)\cdot M\cdot(M-1) + 5M\cdot(N-6)$
Shifts	$M\cdot(N-1) + 2(N-1)$

From Table 3 it can be deduced that this operation has an order of magnitude of $\mathbf{O(N\cdot M^2)}$. That means, for an image of size 361 × 324 pixels, 37,791,360 real products, 38,249,820 real sums and 117,360 circular shifts. With the implementation of the range bin alignment process in a parallel device, the computational burden could be reduced to a magnitude of order **O(N·M)**, or even further to a magnitude of **O(N)** in cases where the implementation device has enough resources.

This order of magnitude could not be further reduced, at least initially, since parallelization of more operations could not be applied due to the dependence of correlations. This means that only one correlation is done at a time because the reference profile must be computed before the next correlation can be executed.

Although FFTs/IFFTs have not been very time consuming operations compared to the range bin alignment stage, it should be noted that a high number of operations are also required. Matlab® FFT algorithm is based on a library called FFTW [46] which has a computational complexity of $O(N\cdot\log_2(N))$, where N is the number of samples. Only if the magnitude of the range bin alignment was reduced to O(N), would FFT computational cost and alignment process cost be comparable.

4.2. ISAR Image Comparison (Target Recognition) Computational Cost

The method proposed to compare ISAR images is the normalized cross-correlation between them showed in Equation (1). It is worth noting that template-matching techniques like the one proposed here are computationally expensive since ISAR images are normally of large dimensions. To speed up the recognition process other approaches have been proposed in the literature based on the comparison between a set of features extracted from the ISAR image to be recognized and a database of features [38,39,47].

In the present case both images will be squared of the same size $N \times N$, so by using normalized cross-correlation one can deduce that a computational complexity of order $O(N^2)$ is needed. Nevertheless, images are not centered at the same point so image matching should be additionally applied. This matching implies the increase of the computational complexity to an order of $\mathbf{O(N^4)}$, since additional N^2 comparisons are executed, one per pixel image. This high burden leads to an average time of 10 minutes to complete one comparison of two images of size 256 × 256 in an Intel

Xeon @ 2.66 GHz and 3.50 GB RAM PC; thus, recognition using normalized cross-correlation is clearly a bottleneck in the system and its computational complexity must be reduced. In order to do so, instead of a pixel by pixel matching, one of the images is shifted '*g*' discrete steps (pixels) in both the x and y dimensions while the other remains stable and the correlation is calculated for each position creating a correlation matrix. The following step is to find the highest correlation value in this matrix and to define a range around it in which normalized cross-correlation will be applied again by shifting images pixel by pixel.

To clarify the process Figure 13 shows blue points as the initial shifts where the "X" presents the point of maximum correlation. In red is depicted the range in which the correlation will be applied shifting images pixel by pixel.

Figure 13. Shifts applied in ISAR image comparison (g = 16 pixels).

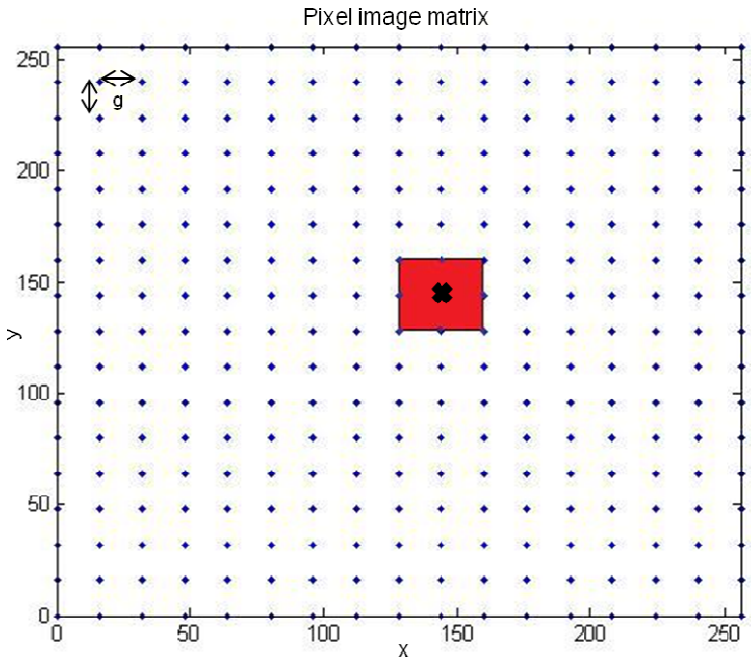

This image shifting based on the work in [48], implies the execution of *C* normalized cross-correlations instead of N^2. In Equation (3), *N* denotes the image axis size and *g* is the shift applied (16 or 32 pixels depending on the image size):

$$C = \left(\frac{N}{g} + 1\right)^2 + (2g + 1)^2 \tag{3}$$

Hence, by using this shifting scheme to carry out image comparisons the computational burden is reduced from an order of magnitude of $\mathbf{O(N^4)}$ to an order of $\mathbf{O(C \cdot N^2)}$. As an example, for the comparison of two 256 × 256 images with a shift of g = 16 pixels, from Equation (3) the number of correlations needed to obtain a result is C = 1,378 whereas if shifting was not applied a total number of N^2 = 65,536 correlations would be executed. Figure 14 compares the order of magnitude in a logarithmic scale of normalized cross-correlation when image shifting method is applied or not, with "*g*" being 16 pixels.

Figure 14. Computational complexity of normalized cross correlation.

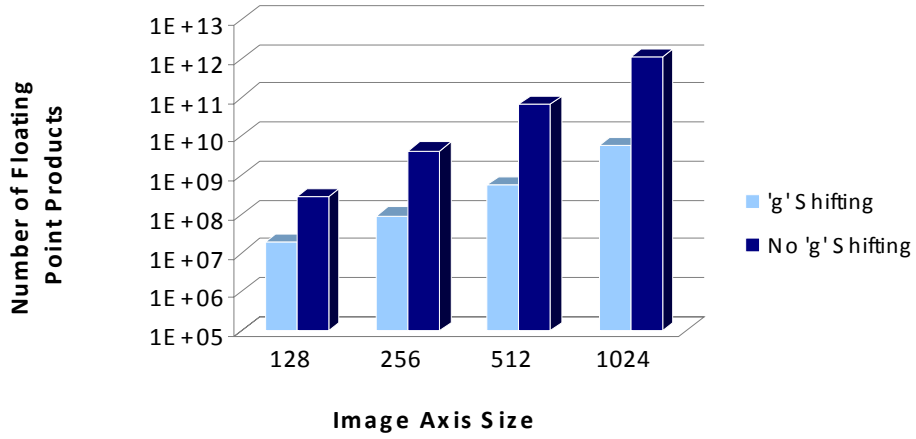

Another relatively efficient way of calculating the NCC is by using the FFT to compute the numerator of Equation (1), however, the denominator of the NCC in Equation (1) does not have a correspondingly efficient frequency domain expression [44,41]. In order to simplify computation of the denominator a sum-table of precomputed data acting as a lookup table should be used, resulting in a reduction of the computational complexity. Other methods to compute the NCC include the utilization of basis functions to approximate the image template [41].

In the method studied in this paper, as Figure 14 shows, a great reduction in the number of operations executed is achieved with this approach and hence, running time has been lowered from an average of 10 minutes to an average of 25 seconds. However, by selecting a more suitable implementation platform operations could be parallelized and execution time could be further reduced.

As already stated, in the study presented in this paper the estimation of the angular velocity of the targets is not done since the simulated aircrafts have the same trajectories than the actual measurements. However, in a real application of non cooperative target recognition angular velocity of targets should be estimated resulting in an increase of the computational complexity. As an example of how much the computational burden could be increased can be found in [40] where an iterative process to estimate the angular parameters of an aircraft is presented. That iterative method is of order $O(L^3)$ per iteration**,** with L belonging to the interval (50,150) and the iterations being a maximum of 15. Hence, considering the estimation of the angular parameters is needed, an additional computational burden of $O(L^3)$ should be added to the order of $O(C \cdot N^2)$ found in the realization of the image comparison. However, the order of magnitude in the estimation of the angular parameters is lower than the computational burden of the ISAR image comparison based on the NCC studied in this paper.

5. Conclusions

The use of radar sensors for non-cooperative target identification purposes is of great interest in civilian and military schemes. To this end a methodology for target recognition from ISAR images and the signal processing needed has been presented. It is always interesting the study of the computational complexity of any system with the aim of selecting the best implementation platform to achieve system requirements. In order to find the critical points in the target recognition system proposed in this paper, computational burden of ISAR image generation and comparison with a synthetic ISAR image have

been analyzed using Matlab® Profiler (R2008a). Results have revealed two critical points in the system presented here. On the one hand, in the ISAR generation process the bottleneck has been found in the profiles alignment. This alignment was based on the envelope correlation algorithm and had a computational complexity of $O(N \cdot M^2)$, with N and M being the number of profiles and the number of frequencies in a stepped-frequency waveform respectively. On the other hand, in the target recognition process the bottleneck is found in images cross-correlation; it has been proved that by applying a certain shifting grid the computational complexity of the normalized cross-correlation could be reduced from $O(N^4)$ to $O(C \cdot N^2)$ with the corresponding decrease in execution time.

According to the results obtained the main bottlenecks of the whole system lie in the high amount of correlations needed in both the alignment and recognition procedures. These operations can be decomposed into sums and products that can be efficiently executed in high performance parallel devices due to their high speed, internal resources and parallel execution. In conclusion, tools like programmable logic devices (FPGAs) or GPUs could be good candidates to implement and perform the system presented in this paper in real time with the additional advantage of fast reconfiguration and low cost.

Nonetheless, further investigation is being considered in the identification process where the resemblance between generated ISAR images and database images is very low resulting in poor reliable target recognition. In future work the target recognition process must be improved by adding a decision procedure based on image features which are present in both synthetic and real ISAR images. Additionally, computational burden of other recognition methods based on the comparison between image features should also be studied in order to contrast results.

Acknowledgments

This research project was funded by the Spanish Ministry of Education and Science (MEC) and the project ESPIRA (REF-DPI2009-10143). The authors would like to thank the Spanish National Institute for Aerospace Technology (INTA) for the F.P.I. grant awarded to P.L.R. and also to the members of NATO-RTO SET-112 Task Group on "Advanced analysis and Recognition of Radar Signatures for Non-Cooperative Target Identification" for providing the actual data obtained in the measurement campaigns organized in the framework of this group.

References

1. Moir, I.; Seabridge, A. *Military Avionics Systems*, 1st ed.; John Wiley & Sons, Ltd.: West Sussex, UK, 2006.
2. Skolnik, M. *Radar Handbook*, 3rd ed.; McGraw-Hill: New York, NY, USA, 2008.
3. Wei, Y.; Meng, H.; Liu, Y.; Wang, X. Extended target recognition in cognitive radar networks. *Sensors* **2010**, *10*, 10181–10197.
4. Swart, J.P. Aircraft Recognition from Features Extracted from Measured and Simulated Radar Range Profiles. Ph.D. Thesis, Universiteit van Amsterdam, Amsterdam, The Netherlands, 2003.
5. *Generation of Synthetic Databases for Non-Cooperative Air Target Identification by Radar*; Technical Reports RTO-TR-SET-040 March 2005 SET-040; Sensors & Electronics Technology

(SET) 040 Task Group 22, Research & Technical Organization (RTO): Neuilly-sur-Seine Cedex, France, 2005.

6. Jurado-Lucena, A.; Errasti-Alcalá, B.; Escot-Bocanegra, D.; Fernández-Recio, R.; Poyatos-Martínez, D.; Montiel Sánchez, I. Methodology to Achieve Accurate Non Cooperative Target Identification Using High Resolution Radar and a Synthetic Database. In *Trends in Applied Intelligent Systems*; García-Pedrajas, N., Herrera, F., Fyfe, C., Benítez, J., Ali, M., Eds.; Springer: Berlin/Heidelberg, Germany, 2010; Volome 6096, pp. 427–436.
7. Wehner, D.R. *High-Resolution Radar*, 2nd ed.; Artech House: Norwood, MA, USA, 1995.
8. Skolnik, M. *Introduction to Radar Systems*, 2nd ed.; McGraw-Hill: Singapore, 1981.
9. Son, J.S.; Thomas, G.; Flores, B.C. *Range-Doppler Radar Imaging*; Artech House: Norwood, MA, USA, 2001.
10. Giusti, E.; Martorella, M. Range doppler and image autofocusing for FMCW inverse synthetic aperture radar. *IEEE T. Aero. Elec. Sys.* **2011**, *47*, 2807–2823.
11. Cacciamano, A.; Giusti, E.; Capria, A.; Martorella, M.; Berizzi, F. Contrast-Optimization-Based Range-Profile autofocus for polarimetric stepped-frequency radar. *IEEE T. Geosci. Remote* **2010**, *48*, 2049–2056.
12. Escamilla-Hernández, E.; Ponomaryov, V.; Ikuo, A.; Endo, H. Uso de FPGA para realizar compresión del pulso de radar. *Científica* **2005**, *9*, 73–81.
13. Levanon, N. Stepped-frequency pulse-train radar signal. *IEE P. Radar Son. Nav.* **2002**, *149*, 297–309.
14. Chen, C.-C.; Andrews, H.C. Target-Motion-Induced radar imaging. *IEEE T. Aero. Elec. Sys.* **1980**, *16*, 2–14.
15. Demirci, S.; Cetinkaya, H.; Tekbas, M.; Yigit, E.; Ozdemir, C.; Vertiy, A. Back-projection Algorithm for ISAR Imaging of Near-Field Concealed Objects. In Proceedings of 2011 XXXth URSI General Assembly and Scientific Symposium, Istanbul, Turkey, 13–20 August 2011; pp. 1–4.
16. Li., W.-C.; Wang., X.-S.; Wang, G.-Y. Scaled Radon-wigner transform imaging and scaling of maneuvering target. *IEEE T. Aero. Elec. Sys.* **2010**, *46*, 2043–2051.
17. Chen, V.C.; Qian, S. Joint time-frequency transform for radar range-Doppler imaging. *IEEE T. Aero. Elec. Sys.* **1998**, *34*, 486–499.
18. Wang, R.; Jiang, Y.-C. ISAR Ship Imaging Based on Reassigned Smoothed Pseudo Wigner-Ville Distribution. In Proceedings of 2010 International Conference on Multimedia Technology (ICMT), Ningbo, China, 29–31 October 2010; pp. 1–3.
19. Liu, M.; Gao, M.; Fu, T. Real time ISAR Imaging Algorithm of Maneuvering Targets Based on the Fractional Fourier Transform. In Proceedings of APSAR 2007. 1st Asian and Pacific Conference on Synthetic Aperture Radar, Huangshan, China, 5–9 November 2007; pp. 667–670.
20. Muñoz-Ferreras, J.M. Enfocado de Imágenes de Radar de Apertura Sintética Inversa—Nuevas Técnicas y Aplicaciones. Ph.D. Thesis, Universidad Politécnica de Madrid: Madrid, Spain, 2008.
21. Delisle, G.Y.; Wu, H. Moving target imaging and trajectory computation using ISAR. *IEEE T. Aero. Elec. Sys.* **1994**, *30*, 887–899.
22. Xing, M.; Wu, R.; Bao, Z. High resolution ISAR imaging of high speed moving targets. *IEE P. Radar Son. Nav.* **2005**, *152*, 58–67.

23. Itoh, T.; Sueda, H.; Watanabe, Y. Motion compensation for ISAR via centroid tracking. *IEEE T. Aero. Elec. Sys.* **1996**, *32*, 1191–1197.
24. Perez-Martinez, F.; Garcia-Fominaya, J.; Calvo-Gallego, J. A shift-and-convolution technique for high-resolution radar images. *IEEE Sens. J.* **2005**, *5*, 1090–1098.
25. Li, X.; Liu, G.; Ni, J. Autofocusing of ISAR images based on entropy minimization. *IEEE T. Aero. Elec. Sys.* **1999**, *35*, 1240–1252.
26. Berizzi, F.; Martorella, M.; Haywood, B.; Mese, E.D.; Bruscoli, S. A Survey on ISAR Autofocusing Techniques. In Proceedings of IEEE International Conference on Image Processing (IClP), Singapore, 6–10 September 2004; Volume 1, pp. 9–12.
27. Brown, W.; Fredricks, R. Range-Doppler imaging with motion through resolution cells. *IEEE T. Aero. Elec. Sys.* **1969**, *5*, 98–102.
28. Heiden, R.V.d.; Vries, J. *The ORFEO Measurement Campaign*; TNO Defence, Security and Safety Report; The Hague, The Netherlands, 1996.
29. Oppenheim, A.V.; Willsky, A.S.; Nawab, S.H. *Signals and Systems*; 2nd ed.; Prentice Hall: New York, NJ, USA, 1997.
30. Harris, F. On the use of windows for harmonic analysis with the discrete fourier transform. *P. IEEE* **1978**, *60*, 51–83.
31. Munoz-Ferreras, J.M.; Perez-Martinez, F. Extended Envelope Correlation for Range Bin Alignment in ISAR. In Proceedings of 2007 IET International Conference on Radar Systems, Edinburgh, UK, 15–18 October 2007; pp. 1–5.
32. Steinberg, B. Microwave imaging of aircraft. *P. IEEE* **1988**, *76*, 1578–1592.
33. Munoz-Ferreras, J.M.; Perez-Martínez, F. Uniform rotational motion compensation for inverse synthetic aperture radar with non-cooperative targets. *IET Radar Son. Nav.* **2008**, *2*, 25–34.
34. Perez, J.; Catedra, M.F. Application of physical optics to the RCS computation of bodies modeled with NURBS surfaces. *IEEE T. Antenn. Propag.* **1994**, *42*, 1404–1411.
35. Conde, O.M.; Perez, J.; Catedra, M.P. Stationary phase method application for the analysis of radiation of complex 3-D conducting structures. *IEEE T. Antenn. Propag.* **2001**, *49*, 724–731.
36. Farin, G. *Curves and Surfaces for CAGD.: A Practical Guide*, 5th ed.; Morgan Kaufman Publishers: Burlington, MA, USA, 2002.
37. Zhao, Y.; Shi, X.-W.; Xu, L. Modeling with NURBS surfaces used for the calculation of RCS. *Prog. Electromagn. Res.* **2008**, *78*, 49–59.
38. Martorella, M.; Giusti, E.; Demi, L.; Zhou, Z.; Cacciamano, A.; Berizzi, F.; Bates, B. Target recognition by means of polarimetric ISAR images. *IEEE T. Aero. Elec. Sys.* **2011**, *47*, 225–239.
39. Giusti, E.; Martorella, M.; Capria, A. Polarimetrically-Persistent-Scatterer-Based automatic target recognition. *IEEE T. Geosci. Remote* **2011**, *49*, 4588–4599.
40. Munoz-Ferreras, J.M.; Perez-Martínez, F. Non-uniform rotation rate estimation for ISAR in case of slant range migration induced by angular motion. *IET Radar Son. Nav.* **2007**, *1*, 251–260.
41. Briechle, K.; Hanebeck, U.D. Template matching using fast normalized cross correlation. *Proc. SPIE* **2001**, *4387*, 95–102.
42. Wang, X.; Wang, X. FPGA Based Parallel Architectures for Normalized Cross-Correlation. In Proceedings of 2009 1st International Conference on Information Science and Engineering (ICISE), Nanjing, China, 26–28 December 2009; pp. 225–229.

43. Kincses, Z.; Voroshazi, Z.; Nagy, Z.; Szolgay, P.; Laviniu, T.; Gacsadi, A. Investigation of Area and Speed Trade-offs in FPGA Implementation of An Image Correlation Algorithm. In Proceedings of 2012 13th International Workshop on Cellular Nanoscale Networks and Their Applications (CNNA), Turin, Italy, 29–31 August 2012; pp. 1–5.
44. Hii, A.J.H.; Hann, C.E.; Chase, J.G.; Houten, E.E.W.V. Fast normalized cross correlation for motion tracking using basis functions. *Comput. Methods Prog. Biomed.* **2006**, *82*, 144–156.
45. MathWorks Documentation Center. Available online: http://www.mathworks.com/help (accessed on 14 October 2012).
46. The Faster Fourier Transform in the West (FFTW). Available online: http://www.fftw.org (accessed on 23 January 2013).
47. Martorella, M.; Giusti, E.; Capria, A.; Berizzi, F.; Bates, B. Automatic target recognition by means of polarimetric ISAR images and neural networks. *IEEE T. Geosci. Remote* **2009**, *47*, 3786–3794.
48. Jurado-Lucena, A. Desarrollo y Evaluación de Algoritmos de Identificación no Cooperativa de Blancos Radar Reales Mediante una Base de Datos Sintética: Aproximación Hacia una Solución Operativa. Ph.D. Thesis, University of Alcalá: Madrid, Spain, 2011.